Interaction of electromagnetic fields with two-dimensional materials at the interface between dielectric media

by

Asbjorn Hansen

A thesis
presented to the University of Waterloo
in fulfillment of the
thesis requirement for the degree of
Master of Mathematics
in
Applied Mathematics

Waterloo, Ontario, Canada, 2025

© Asbjorn Hansen 2025

Author's Declaration

I hereby declare that I am the sole author of this thesis. This is a true copy of the thesis, including any required final revisions, as accepted by my examiners.

I understand that my thesis may be made electronically available to the public.

Abstract

This thesis investigates the interaction of electromagnetic plane waves with two-dimensional (2D) materials approximated by infinitesimal sheets positioned at interfaces between non-magnetic, isotropic, lossless dielectrics. On their own, 2D materials offer a host of useful properties, including high carrier mobility, dopant-free tuning through the application of external electromagnetic fields or stacking, as well as significant anisotropy. When combined with the excitation of plasmon modes to enhance light-matter interactions, the range of potential applications broadens greatly, including, for example, high-speed optical computation and enhanced light trapping in solar cells.

In this thesis, a new derivation of the boundary condition for out-of-plane response is presented for a 2D material immersed in an infinite homogeneous dielectric. To account for the influence of distinct dielectric surrounding media, Fresnel coefficients are derived using a vacuum gap method. This approach yields novel dispersion relations for surface plasmons that incorporate the out-of-plane response of 2D materials. In the presence of distinct surrounding dielectrics, the out-of-plane mode hybridizes with the in-plane longitudinal plasmon mode. The hybridization is destroyed when the surrounding materials are made identical. Additionally, expressions for the conservation of energy and momentum are derived in terms of the Fresnel field amplitudes for the 2D materials described by singular current sheets. The vacuum gap method is also applied to solve the conservation equations in the presence of dielectric media, as this avoids controversial notions of electromagnetic momentum in media. The electromagnetic stress tensor derived through the vacuum gap method satisfies conservation of linear momentum, thus confirming that the forces on a 2D material can be self-consistently separated from those on surrounding dielectrics.

This theoretical framework is applied to both graphene and phosphorene. For graphene, the reflectance, transmittance, and absorption characteristics are compared with and without considering the out-of-plane response. The analysis confirms that the influence of the out-of-plane component is minimal for plasmon modes at low frequencies as is often assumed, but becomes significant at high frequencies. Forces calculated around frequencies and wavenumbers defined by the plasmon dispersion relation showed significant amplification. However, the new non-monotonic dispersion profile of the hybridized plasmon mode introduces additional resonant and antiresonant behaviour in the forces. To emphasize the in-plane anisotropy of phosphorene, only in-plane response was considered, with a focus on forces in the plasmonic regime at low frequencies. Based on numerical examples, predictions are made for possible future experimental studies of both plasmon modes in the presence of the out-of-plane response and forces on 2D materials for possible optomechanical and sensing applications.

Acknowledgements

First and foremost I have to thank Dr. Zoran Miskovic for both his insight and continued effort in keeping my feet planted on the ground, and my mind focused on task. Of course, I also have to thank my lovely parents, who have never stopped supporting me since the day I was born. I will also thank my sisters, for existing I suppose, as they do little else.

Table of Contents

List of Figures viii

1 Introduction 1

1.1 Maxwell's Equations . . . 8
1.2 Hertz Vector . . . 13
1.3 Interface Conditions . . . 16
1.4 Fresnel setting . . . 17
1.5 Transfer matrices . . . 19
1.6 2D material response functions . . . 21

2 Out-of-plane interface condition and analysis of material influence 26

2.1 Immersed Interface condition . . . 29
2.2 Distinct Dielectrics Interface Condition . . . 35
2.3 Application of vacuum gap method . . . 37
2.4 Dispersion of interface plasmons . . . 42

3 Conservation of energy and momentum 50

3.1 Basic equations . . . 51
3.2 Vacuum gap, revisited . . . 57
3.3 Conductivity models . . . 59
3.4 Energy . . . 60

3.4.1 In-plane anisotropic, no out-of-plane . . . 60
3.4.2 In-plane isotropic, with out-of-plane . . . 66
3.4.3 Numerical validation . . . 68
3.5 Linear momentum . . . 70
3.5.1 In-plane anisotropic, no out-of-plane . . . 70
3.5.2 In-plane isotropic, with out-of-plane . . . 74
3.5.3 Numerical validation . . . 76

4 Results for graphene **79**
4.1 Undoped graphene . . . 80
4.1.1 Reflectance, transmittance, and absorption . . . 81
4.1.2 Forces . . . 86
4.1.3 Comparison to [1] . . . 88
4.1.4 Comparison to [2] . . . 90
4.1.5 Comparison to [3] . . . 92
4.2 Doped graphene . . . 96
4.2.1 Plasmon dispersion . . . 99
4.2.2 Forces . . . 102
4.2.3 Comparison to [3] . . . 112

5 Results for phosphorene **115**
5.1 Plasmon dispersion . . . 117
5.2 Forces . . . 118

6 Conclusion **124**

References **127**

APPENDICES **135**

A Applications of Fresnel's formulas **136**

A.1 Total internal reflection 136

A.2 Brewster angle 137

B Additional derivations for conservation relations **139**

B.1 Conservation equations in the Fourier domain 139

B.2 A note on charge densities 143

C Additional discussion **146**

C.1 Forces on purely dielectric interfaces 146

C.2 Complex Dispersion 149

List of Figures

1.1 Example of the field profile of a surface plasmon polariton propagating along the interface between two media. 2

1.2 Dispersion relation for the bulk and surface states of a semi-infinite aluminum metal bordering vacuum. The upper solid line is the dispersion in the metal. The lower solid line is the surface dispersion. The diagonal dotted line is the vacuum light line. Plot taken from [4]. 3

1.3 Diagram of the optical path taken by an incident plane wave on a material modelled as a slab. 4

1.4 Schematic of a section of single-layer graphene showing the strong σ bonds and the weak π bonds. 5

1.5 Schematic diagram of the relationship between microscopic (left) and macroscopic (right) electromagnetic models. 9

1.6 Diagram of a plane wave interaction with a flat interface highlighting the coordinate system used in this work. 18

1.7 Diagram of a classic Fresnel style interaction between a p-polarized plane wave and the interface between two isotropic, non-magnetic dielectrics. . . 19

2.1 Diagram of a triple interface vacuum gap configuration. 28

2.2 Diagram of a classic Fresnel style interaction between a p-polarized plane wave and the interface between two identical dielectrics. 30

2.3 Vacuum gap configuration prior to evaluation of the limit. 38

3.1 Observation plane configurations for application of the vacuum gap method. Only configuration (2) is applied in this section. 59

3.2 Artificial conductivities for testing the validity of derived conservation equations. $\sigma_0 = \pi\alpha/z_0$, where α is the fine structure constant. 61

3.3 Numerical validation of the conservation of energy equations for (a) $\sigma_z = 0$ and $n_1 = n_2 = 1$, (b) $\sigma_z \neq 0$ and $n_1 = n_2 = 1$, (c) $\sigma_z = 0$ and $n_1 = 1.5, n_2 = 2$ (d) $\sigma_z \neq 0$ and $n_1 = 1.5, n_2 = 2$. $\Delta E = L.S. - R.S.$ of the energy conservation equation. 69

3.4 Numerical validation of the conservation of momentum equations for (a) $\sigma_z = 0$ and $n_1 = n_2 = 1$, (b) $\sigma_z \neq 0$ and $n_1 = n_2 = 1$, (c) $\sigma_z = 0$ and $n_1 = 1.5$, $n_2 = 2$, (d) $\sigma_z \neq 0$ and $n_1 = 1.5$, $n_2 = 2$. $\Delta F = L.S. - R.S.$ of the momentum conservation equation. 78

4.1 *Ab initio* response function of undoped graphene, digitized from [2]. $\sigma_0 = \pi\alpha/z_0$, where $\alpha = e^2/(\hbar c) \approx 1/137$ is the fine structure constant. 80

4.2 Absorbance, reflectance, and transmittance of graphene considering **TOP**: $\sigma_z \neq 0$, $\sigma_q \neq 0$ and **BOTTOM**: $\sigma_z = 0$, $\sigma_q \neq 0$. All cases considered with $n_1 = n_2 = 1$. Black lines indicate the maximum of a given spectra, and white lines indicate a minimum. 82

4.3 Absorbance, reflectance, and transmittance of graphene considering **TOP**: $\sigma_z \neq 0$, $\sigma_q \neq 0$ and **BOTTOM**: $\sigma_z = 0$, $\sigma_q \neq 0$. All cases considered with $n_1 = 1$, and $n_2 = 1.5$. Black lines indicate the maximum of a given spectra, and white lines indicate a minimum. 84

4.4 Absorbance, reflectance, and transmittance of graphene considering **TOP**: $\sigma_z \neq 0$, $\sigma_q \neq 0$ and **BOTTOM**: $\sigma_z = 0$, $\sigma_q \neq 0$. All cases considered with $n_1 = 1.5$, and $n_2 = 1$. Black lines indicate the maximum of a given spectra, and white lines indicate a minimum. 85

4.5 Forces in the $\hat{z}$ and $\hat{q}$ directions, measured in pPa, from p-polarized light on both $n_1 = n_2$ and $n_2 > n_1$ dielectric configurations both with and without out-of-plane conductivity. 87

4.6 Forces in the $\hat{z}$ and $\hat{q}$ directions, measured in pPa, from p-polarized light and dielectric surroundings defined by $n_1 = 2$ and $n_2 = 1$, both with and without out-of-plane conductivity. 88

4.7 Comparison between the absorbance of graphene for p-polarized light, $\sigma_z = 0$, $\sigma_q = \pi\alpha/z_0$, and surrounding dielectrics defined by $n_1 = 1.5$ and $n_2 = 1$. Datapoints from [1]. Datapoints represent model predictions, not measurements. 89

4.8 **LEFT**: Absorbance, reflectance, and transmittance of undoped graphene at a frequency defined by $\hbar\omega = 0.5$ eV. **RIGHT**: Difference between the absorbance, reflectance, and transmittance with and without out-of-plane response ($\Delta X = X(\sigma_z) - X(\sigma_z = 0)$). Each evaluated at $n_1 = 1$, $n_2 = 1$. . 90

4.9 **LEFT**: Absorbance, reflectance, and transmittance of undoped graphene at a frequency defined by $\hbar\omega = 0.5$ eV. **RIGHT**: Difference between the absorbance, reflectance, and transmittance with and without out-of-plane response ($\Delta X = X(\sigma_z) - X(\sigma_z = 0)$). Each evaluated at $n_1 = 1$, $n_2 = 1.5$. 91

4.10 **LEFT**: Absorbance, reflectance, and transmittance of undoped graphene at a frequency defined by $\hbar\omega = 0.5$ eV. **RIGHT**: Difference between the absorbance, reflectance, and transmittance with and without out-of-plane response ($\Delta X = X(\sigma_z) - X(\sigma_z = 0)$). Each evaluated at $n_1 = 1.5$, $n_2 = 1$. 91

4.11 Continuous curve represents absorbance calculations from this work. Data points show the results from [2]. Both results for vacuum surroundings and $\theta_i = \pi/4$. Datapoints represent model predictions, not measurements. . . . 92

4.12 Comparison of s and p-polarized reflectances digitized from measurements presented in [3], and model predictions from equations 4.3 and 4.4. Data presented for immersion in a homogeneous dielectric defined by $n = 1.4233$. The model curves overlap with the measurement curves. 94

4.13 Comparison between ellipsometric measurements of undoped graphene on a substrate with index $n = 1.4233$ from [3], and the predictions by the models of various authors. All three models predict the same result in (a). The Felderhof and Merano models predict the same result in (b). Felderhof: [5]. Merano: [3]. The harmonic mean model is defined by equations 4.3 and 4.4 through equation 4.16. 95

4.14 Schematic diagram of Otto (a) and Kretschmann (b) surface plasmon polariton excitation configurations. Blue represents some transparent dielectric, while orange represents a metal film. 97

4.15 Comparison between the analytical square root dispersion for the in-plane plasmon mode in graphene (2.99), derived in the non-retarded limit, and the numerical solutions to the lossless dispersion relation defined in equation 4.25. 100

4.16 Comparison between the numerical solutions to the lossless hybridized dispersion relation defined in equation 4.27, and the analytical solution derived in the non-retarded limit defined in equation 4.28. 101

4.17 Frequency and wavenumber scans around the plasmon dispersion relation. 103

4.18 (a) Recreation of the iso-frequency force scans considered in [6], as well as an extension to the case with dielectric surroundings (b) and out-of-plane conductivity (c). The three considered wavelengths correspond to frequencies of $\hbar\omega = 0.124$, 0.083, and 0.062 eV. All forces are in the $\hat{z}$ direction. 104

4.19 Dispersion relations for doped graphene at the material configurations used in figure 4.18. Iso-frequency scans corresponding to the three wavelengths considered in [6] are represented as horizontal lines at $\hbar\omega = 0.124$, 0.083, and 0.062 eV. 105

4.20 Dispersion relations of doped graphene for the material configurations used in the force scans of figure 4.21. The horizontal lines represent the iso-frequency scans at $\hbar\omega = 0.1$, 0.15, 0.2, and 0.25 eV. 106

4.21 Comparison between the iso-frequency force scans both with (right) and without (left) out-of-plane conductivity, for both substrate (top) and superstrate (bottom) dielectric configurations. All forces are in the $\hat{z}$ direction. . 107

4.22 Dispersion scan plots of the (a) log of the absolute $\hat{z}$ force density, and (b) $\hat{q}$ force density, (c) force density with directions, (d) dispersion relation, (e) log of the absolute amplitude spectrum, and (f) phase spectrum. All are calculated with vacuum surroundings. Force is measured in Pascals, field amplitudes are measured in V/m. 108

4.23 Dispersion scan plots of the (a) log of the absolute $\hat{z}$ force density, and (b) $\hat{q}$ force density, (c) force density with directions, (d) dispersion relation, (e) log of the absolute amplitude spectrum, and (f) phase spectrum. All are calculated with $n_1 = 2$, and $n_2 = 1$. Force is measured in Pascals, field amplitudes are measured in V/m. 109

4.24 Dispersion scan plots of the (a) log of the absolute $\hat{z}$ force density, and (b) $\hat{q}$ force density, (c) force density with directions, (d) dispersion relation, (e) log of the absolute amplitude spectrum, and (f) phase spectrum. All are calculated with $n_1 = 1$, and $n_2 = 2$. Force is measured in Pascals, field amplitudes are measured in V/m. 110

4.25 Comparison between non-retarded solutions to the coupled (4.28) and decoupled (4.49) dispersion relations for plasmon states in doped graphene. . 114

5.1 3D dispersion surface for in-plane-only phosphorene surrounded by vacuum. Iso-frequency level curves are shown in the q_x-q_y plane. 118

5.2 Iso-frequency $\hat{z}$ ((a), (c)), and $\hat{q}$ ((b), (d)) force plot. Polarization is defined by $\eta = 0$ and material rotation defined by $\phi = 0$ ((a), (b)), and $\phi = \pi/2$ ((c), (d)). All cases are calculated with vacuum surroundings. 119

5.3 Iso-frequency $\hat{z}$ force density plot for $\hbar\omega = 0.1$ eV and polarization defined by (a) $\eta = 0$, (b) $\eta = \pi/4$, and (c) $\eta = \pi/2$. All cases are calculated with vacuum surroundings. Force density measured in μPa. 120

5.4 Iso-frequency $\hat{q}$ force density plot for $\hbar\omega = 0.1$ eV and polarization defined by (a) $\eta = 0$, (b) $\eta = \pi/4$, and (c) $\eta = \pi/2$. All cases are calculated with vacuum surroundings. Force density measured in μPa. 121

5.5 Iso-frequency $\hat{z}$ force density plot for $\hbar\omega = 0.1$ eV and polarization defined by (a) $\eta = 0$, (b) $\eta = \pi/4$, and (c) $\eta = \pi/2$. All cases are calculated with $n_1 = 1.5$, and $n_2 = 1$. Force density measured in μPa. 122

5.6 Iso-frequency $\hat{z}$ force density plot for $\hbar\omega = 0.1$ eV and polarization defined by (a) $\eta = 0$, (b) $\eta = \pi/4$, and (c) $\eta = \pi/2$. All cases are calculated with $n_1 = 1$, and $n_2 = 1.5$. Force density measured in μPa. 123

5.7 Iso-frequency $\hat{z}$ force density plot for $\hbar\omega = 0.4$ eV and polarization defined by (a) $\eta = 0$, (b) $\eta = \pi/4$, and (c) $\eta = \pi/2$. All cases are calculated with $n_1 = 1$, and $n_2 = 1.5$. Force density measured in μPa. 123

C.1 Real part of q from the full complex solution to the hybridized dispersion relation shown in equation 4.27. The colour bar indicates the magnitude of the corresponding imaginary part in nm^{-1}. Calculated for the substrate case, with $n_2 = 4$ and $n_1 = 1$. Yellow line is the solution to the hybridized plasmon mode in the non-retarded limit. 149

Chapter 1

Introduction

Two-dimensional (2D) materials are, of course, not truly two-dimensional. This is a classification of materials that consist of single layers on the order of atomic thickness, with covalent bonding in-plane but only van der Waals interactions out-of-plane. Graphene is both the original and principal example of this classification; consisting of a single layer of carbon atoms bonded in a hexagonal lattice, it is the thinnest material on earth. It is this extreme thinness that gives graphene and its contemporaries the unique properties that have made them such a hotbed of new research and exciting applications. 2D materials and their properties are widely varied, though there are a number of common themes. Many such materials exhibit very high carrier mobility [7][8][9], dopant-free tuning through application of external electromagnetic fields or stacking [8][10][11], as well as significant anisotropy [12], not to mention the possibility for designer properties through the construction of layered heterostructures comprised of a stack of different 2D materials [8].

In particular, 2D materials have received much attention for their use in plasmonics. Plasmonics is the study of plasmons, and, in practice, is concerned with creation, control, and measurement. Plasmons are collective, coherent charge oscillations that can either remain localized or propagate [4]. They can couple to the electromagnetic field to form plasmon polaritons, and if excited at an interface, they are called surface plasmon polaritons (SPPs). Even though they represent a coupling between matter and the electromagnetic field, SPPs can be adequately described by classical electromagnetism by simply postulating a wave for which energy only propagates along the interface. This is done, as

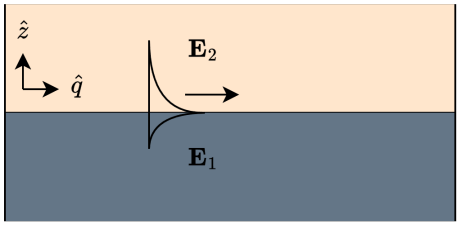


Figure 1.1: Example of the field profile of a surface plasmon polariton propagating along the interface between two media.

is shown in figure 1.1, by assuming an exponential decay into the surrounding media,

$$\mathbf{E} = \begin{cases} \mathbf{E}_{20}\, e^{-\kappa_2 z} e^{i(\mathbf{q}\cdot\mathbf{r}_\parallel - \omega t)}, & z > 0 \\ \mathbf{E}_{10}\, e^{\kappa_1 z} e^{i(\mathbf{q}\cdot\mathbf{r}_\parallel - \omega t)}, & z < 0 \end{cases}, \tag{1.1}$$

where $\kappa_{1,2}$ are the decay constants, $\mathbf{q}$ the in-plane wave vector and $\mathbf{r}_\parallel$ the in-pane position. Then, using the interface conditions, one can derive the dispersion relation on the in-plane wave vector,

$$q = \frac{\omega}{c}\sqrt{\frac{\epsilon_1(\omega)\epsilon_2(\omega)}{\epsilon_1(\omega) + \epsilon_2(\omega)}}, \tag{1.2}$$

where $\epsilon_{1,2}(\omega)$ are the frequency-dependent dielectric functions of the surrounding media. Figure 1.2 shows this dispersion relation evaluated for an interface between vacuum and a semi-infinite metal. This tells us that SPPs have shorter wavelengths for a given frequency than light in vacuum. A shorter wavelength corresponds to a higher wave number q, and, therefore, higher momentum. Having more momentum than any incident light, SPPs cannot be excited by direct illumination, so additional structures must be present to facilitate coupling. This can involve the use of diffraction gratings, surface roughness, or prism couplers; any structure that can add momentum [13].

SPPs are useful because they can provide sub-wavelength confinement and significant field enhancement [14]. The dispersion relation indicates that they can have significantly smaller wavelengths than light in vacuum, so when excited, they can confine the optical energy to a much smaller region. As indicated in equation 1.1, they also exhibit exponential decay into the surrounding media, which serves to further confine the energy to a small region surrounding the interface. The electromagnetic fields associated with SPPs are, therefore, significantly enhanced near the interface where they propagate.

Just as an interface can support SPPs, so too can 2D materials. It is this combination of unique properties that has opened up significant new opportunities and generated such

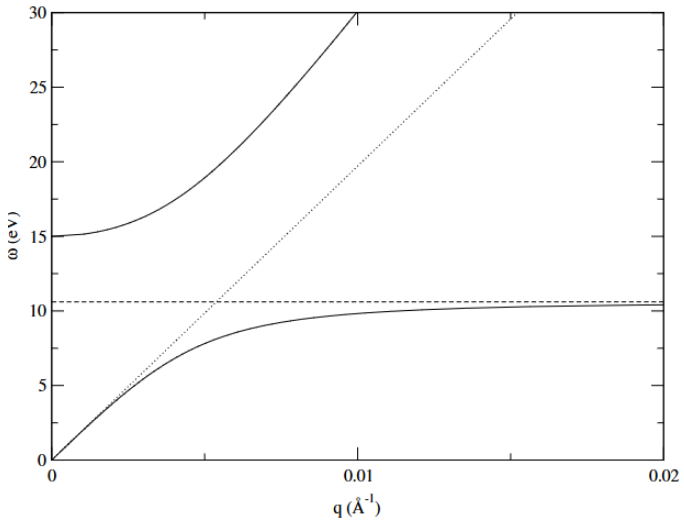


Figure 1.2: Dispersion relation for the bulk and surface states of a semi-infinite aluminum metal bordering vacuum. The upper solid line is the dispersion in the metal. The lower solid line is the surface dispersion. The diagonal dotted line is the vacuum light line. Plot taken from [4].

research interest. 2D materials have much promise on their own, however, their use is limited in many applications that involve absorption or emission, like optical sensing, solar cells, and photoluminescence, by low light-matter interaction resulting from their atomic order thickness [10]. However, this problem can be mitigated by utilizing the significant field strength enhancement of plasmons. Plasmons confine the optical energy into a much smaller region around the 2D material, thereby boosting light-matter interactions and absorption [15][16]. Among the most exciting prospects coming from the intersection of plasmonics with 2D materials is that of optical computation. It has been demonstrated that 2D heterostructures involving phosphorene and SiO_2 exhibit switchable polariton modes under excitation by an optical source in the THz regime [17]. This introduces the possibility of constructing ultrafast digital logic circuits using 2D materials [18].

To facilitate the further development of these ideas and others, it is essential to develop accurate and adaptable methods for modelling optical interactions with 2D materials. Regardless of how thin a material is, its real properties will always vary continuously across its width. Being such a small distance, however, means that the functions describing these properties can exhibit enormous gradients and large peaks [19]. In theory, thin materials would always be most accurately modelled as slabs with finite thickness and properties described by these continuously varying functions. This is a method used often in the

study of thin film optics [20], when the film thickness d is on the order of, or larger than, the wavelength of interacting light. In finite slab models, the smoothly varying properties, and thus the interaction with the electric fields, are captured by so-called material response functions. These functions generally take the form of a conductivity σ, or a susceptibility χ. Depending on the choice, the material properties will enter into the problem as either a current ($\mathbf{J} = \overleftrightarrow{\sigma}\mathbf{E}$) or a polarization ($\mathbf{P} = \epsilon_0\overleftrightarrow{\chi}\mathbf{E}$) induced by an electric field $\mathbf{E}$. Here, we indicated that functions may be tensors, and we note that they are generally related by $\sigma = -i\epsilon_0\omega\chi$ [21]. In such slab models, light interacting with the material has to travel a finite distance in the material's interior, along with internal reflections at the bounding interfaces, as shown in figure 1.3. This imparts a phase shift (ϕ_0) on the reflected and transmitted fields, along with a reduction in amplitude if the material has losses.

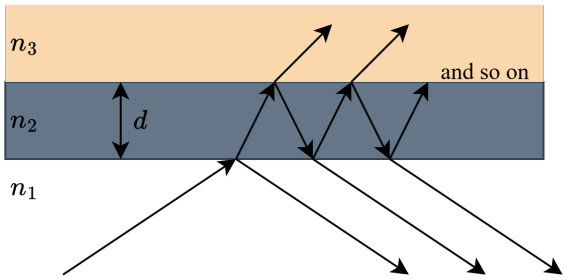


Figure 1.3: Diagram of the optical path taken by an incident plane wave on a material modelled as a slab.

Material response functions like σ and χ describe, in a general sense, how a material interacts with electromagnetic fields. In the local approximation, they are the proportionality factors that relate the electromagnetic fields to currents and polarizations in Maxwell's equations. Optical interactions occur when incident light interacts with charge carriers in a material. These interactions generally involve electronic transitions or excitations of phonon modes [22]. Material response functions, therefore, capture both the action of the fields on the charges, as well as any absorption. The nature of this absorption is dictated by the material's electronic band structure and density of states. For absorption to occur, there must be a charge carrier available to transition, as well as a destination state [22].

Determining material response functions can be done either experimentally or through *ab initio* methods. One such class of methods involves directly calculating the material properties using quantum mechanics. Density functional theory (DFT) is a popular tool for this purpose [23]. In time-dependent DFT, the system response is calculated by approximating the many-body Schrodinger equation that describes the evolution of the quantum system and its interactions. In this way, the conductivity is calculated by summation of

all available electronic transitions. For analytical or phenomenological modelling, response functions can also be described using classical or semi-classical models. The Drude model, for example, provides a straightforward way to account for free electron dynamics in metals, treating them as a gas of charged particles.

While effective for modelling the optics of many thin materials, there are some conceptual challenges associated with applying slab models to the atomically thin. Generally, slab models treat materials as perfectly smooth continua with abrupt, flat edges and material properties described by volumetric response functions. As atomically thin sheets, 2D materials at the very least cannot be thought of as having abrupt edges in the way that a material an order of magnitude thicker does. Consider graphene, a single atomic layer surrounded by weakly bonded π orbitals, as shown in figure 1.4. In this material, where exactly are the currents?

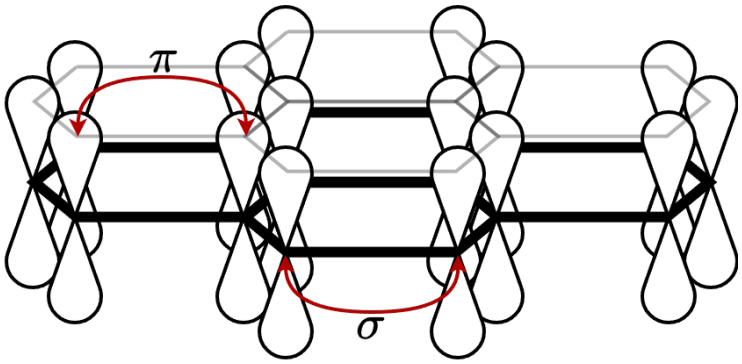


Figure 1.4: Schematic of a section of single-layer graphene showing the strong σ bonds and the weak π bonds.

At the scales present in 2D materials, the optically induced currents cannot be uniform, nor can they abruptly start or stop at the edges [24]. The concept of volumetric response functions also becomes ambiguous. Without distinct borders, the definition of width becomes a convention rather than an intrinsic property. To address these concerns, one may instead use an infinitesimal sheet model for the 2D material. In this case, the material is considered to have zero thickness, which means it appears in the model as an interface, with properties that influence the interface conditions. This infinitesimal model can be derived from the finite slab by taking the limit that the slab is optically thin [24]. Optical thinness can be defined in a number of ways, but here it is taken to mean that the phase shift (ϕ_0) imparted on light by the material is very small ($|\phi_0| \ll 1$). In sheet models, there is no need to choose a convention for the width, as the entirety of the material

response is considered to occur in one plane. The material response functions are therefore two-dimensional and can be considered the integrated volumetric parameters [25],

$$\sigma^s = \int_{-\infty}^{\infty} dz\, \sigma^v(z). \tag{1.3}$$

One of the primary challenges associated with the use of infinitesimal sheet models is capturing the out-of-plane response. In reality, 2D materials have a finite thickness, so their optical response will have a component in-plane and a component out-of-plane. In a slab model, the out-of-plane component is captured by the volumetric response function and naturally imparted on the fields as they propagate through the volume. In sheet models, however, with no volume to propagate through, there must be another way to impart the influence of the out-of-plane response on the fields. As with all other properties in the sheet model, this has to be done with an interface condition.

The out-of-plane response of a sheet is perhaps most easily characterized by polarizability. Just as a point dipole exhibits directionality and a kind of charge separation, so too can an infinitesimal sheet. However, the notion of out-of-plane response, and how to account for it, is somewhat controversial. The reason for this controversy is perhaps that 2D materials are often modelled with conductivity response functions, so they appear as currents in the relevant equations. While they are equivalent and therefore interchangeable, an out-of-plane current in an infinitesimal sheet is a much more challenging idea to accept than a polarization. Whatever the reason, the out-of-plane response is often neglected in studies of 2D materials [26][27][28][29][30]. In spite of this, among those who have embraced the idea, there is consensus on the correct form of the out-of-plane interface condition. Multiple groups have independently published unique derivations for this condition, in a range of material configurations [31][32][33][34][35][36][5]. There remains, however, some questions regarding the correct form of the out-of-plane polarization/current itself, and how it changes under the influence of surrounding materials.

In this work, we will explore electromagnetic plane wave interactions with 2D materials in a classical, infinitesimal sheet setting, with non-magnetic, isotropic, lossless dielectric surroundings. In particular, we verify the form of the out-of-plane boundary condition with a new method of derivation based on a Hertz vector formalism. We also identify the influence of surrounding materials on this condition through a transfer matrix method that permits the use of the uncontroversial vacuum boundary condition. Then, we verify the conservation of energy and momentum, paying special attention to the influence of evanescence, out-of-plane response, and dielectric material surroundings, on the reflectance (R), transmittance (T), absorbance (A), and Maxwell stress tensor. Finally, using a combination of *ab initio* and phenomenological conductivity response functions, we study R, T,

and A, as well as optical forces generated on graphene and phosphorene with and without out-of-plane response, for both vacuum and material surroundings.

1.1 Maxwell's Equations

Here we develop and justify the electromagnetic formulation that will form the basis of this work. In this section, until otherwise indicated, we will be considering a homogeneous isotropic material. In SI units Maxwell's equations are given by,

$$\nabla \cdot \mathbf{E} = \frac{\rho}{\varepsilon_0}, \tag{1.4}$$

$$\nabla \cdot \mathbf{B} = 0, \tag{1.5}$$

$$\nabla \times \mathbf{E} = -\frac{\partial \mathbf{B}}{\partial t}, \tag{1.6}$$

$$\nabla \times \mathbf{B} = \mu_0 \left(\mathbf{J} + \varepsilon_0 \frac{\partial \mathbf{E}}{\partial t} \right), \tag{1.7}$$

where ρ is the charge density, $\mathbf{J}$ is the current density, $\mathbf{E}$ is the electric field, $\mathbf{B}$ is the magnetic field, ϵ_0 is the vacuum permittivity, and μ_0 is the vacuum permeability. In a purely mathematical universe where charge and current are simply properties given to geometry, Maxwell's equations are always exact, regardless of their scale or distribution, continuous or point-like. The problems arise when trying to map this description to reality. Charge is not a property possessed by pure geometry, it is possessed by particles. And particles do not, in general, behave classically, but are instead governed by quantum mechanics. Electrons and protons are not really point-like, and materials are not really continuous. Regardless, the approximate classical forms of point charges and continuous distributions remain useful in the appropriate limits. Material models that consider charges as points are often labelled microscopic, while ones that use continuous distributions are labelled macroscopic.

In the microscopic setting, the fields are fully defined by the distribution of point charges, captured by the charge density ρ, and their dynamics, captured by the current $\mathbf{J}$,

$$\rho(\mathbf{r}, t) = \sum_{n=1}^{N} q_n \delta(\mathbf{r} - \mathbf{r}_n(t)), \tag{1.8}$$

$$\mathbf{J}(\mathbf{r}, t) = \sum_{n=1}^{N} q_n \dot{\mathbf{r}}_n(t) \delta(\mathbf{r} - \mathbf{r}_n(t)). \tag{1.9}$$

While useful in certain circumstances, the discrete nature of this model can make it difficult to simultaneously treat a large number of individual charges and their interactions through the Lorentz force. This is especially challenging when those charges constitute a

material, participate in bonding, or interact with internal potentials—not to mention cases where quantum mechanical effects become significant. These factors together make true microscopic models of large-scale materials very unwieldily.

The macroscopic picture of electromagnetism is often defined with respect to the microscopic as a smoothed or averaged version, shown schematically in figure 1.5, but it is more concretely based on the idea of continuous charge distributions[37].

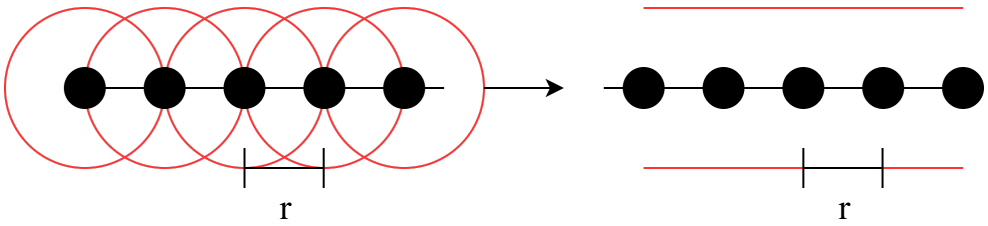


Figure 1.5: Schematic diagram of the relationship between microscopic (left) and macroscopic (right) electromagnetic models.

In practice, considering the macroscopic as a smoothed version of the microscopic is often ill-defined, making the comparison dubious [37]. As the microscopic picture is itself an approximation, the relationship between the two is largely unimportant. It is the relationship to observations that is critical. Generally, it is believed that as long as we can assume that the wavelength of the incoming plane wave is much larger than the structural details of the underlying system, characterized by r, then it is sensible to assume continuous charge distributions and work with the macroscopic picture [38]. This is manifested mathematically by the condition,

$$rk_0 \ll 1, \tag{1.10}$$

where k_0 is the wave number. In this regime, Maxwell's equations are often presented as,

$$\nabla \cdot \mathbf{D} = \rho_f, \tag{1.11}$$

$$\nabla \times \mathbf{H} = \mathbf{J}_f + \frac{\partial \mathbf{D}}{\partial t}, \tag{1.12}$$

$$\nabla \cdot \mathbf{B} = 0, \tag{1.13}$$

$$\nabla \times \mathbf{E} = -\frac{\partial \mathbf{B}}{\partial t}, \tag{1.14}$$

where $\mathbf{H} = \mathbf{B}/\mu_0$ and

$$\mathbf{D} = \epsilon_0 \mathbf{E} + \mathbf{P}_b. \tag{1.15}$$

$\mathbf{D}$ is the electric displacement field, $\mathbf{P}_b$ is called the polarization density due to bound charges, and the subscript f indicates the free charges. Often the charges in a macroscopic system are separated into bound and free. The bound are thought to remain localized, like a fixed dipole, and the free are thought to move, like conduction electrons. This separation raises a lot of questions. For instance, how is it possible to distinguish between charges in a continuous system? When we switch to the macroscopic view, we eliminate the idea of charges as occupying discrete bodies. Further complicating things is the introduction of oscillating fields. How can one possibly distinguish between bound and free charges when both oscillate in place? Any attempt to distinguish between charges that occupy the same region of space in the macroscopic picture raises more questions than it answers. Instead, throughout this work, we will abandon the notion of charges as distinguishable and instead consider only the continuous distributions as a whole. To that end, we adopt the formulation often applied in materials science, and define two distinct categorizations, external and induced. Within these two categories, we will further introduce the labels of continuous and singular. This further distinction is made because these sub-categories have intrinsic differences. For example, only continuous distributions can contribute to bulk properties like modifications to the speed of light.

There are a number of ways to define the distinction between external and induced charges and currents. Here we adopt the definition used in [37]: external charges and currents are any known *a priori*, and the induced are all others, i.e., both bound and free charges in the material of interest. We also adopt the notion that the external charges and currents are unaffected by the induced fields. The external and induced fields are therefore defined completely by their respective charges and currents,

$$\nabla \cdot \mathbf{E}_{\text{ext}} = \rho_{\text{ext}}, \tag{1.16}$$

$$\nabla \times \mathbf{H}_{\text{ext}} = \mathbf{J}_{\text{ext}} + \epsilon_0 \frac{\partial \mathbf{E}_{\text{ext}}}{\partial t}, \tag{1.17}$$

$$\nabla \cdot \mathbf{B}_{\text{ext}} = 0, \tag{1.18}$$

$$\nabla \times \mathbf{E}_{\text{ext}} = -\frac{\partial \mathbf{B}_{\text{ext}}}{\partial t}, \tag{1.19}$$

and for the induced,

$$\nabla \cdot \mathbf{E}_{\text{ind}} = \rho_{\text{ind}}, \tag{1.20}$$

$$\nabla \times \mathbf{H}_{\text{ind}} = \mathbf{J}_{\text{ind}} + \epsilon_0 \frac{\partial \mathbf{E}_{\text{ind}}}{\partial t}, \tag{1.21}$$

$$\nabla \cdot \mathbf{B}_{\text{ind}} = 0, \tag{1.22}$$

$$\nabla \times \mathbf{E}_{\text{ind}} = -\frac{\partial \mathbf{B}_{\text{ind}}}{\partial t}. \tag{1.23}$$

The total fields are then given by the addition of the two sets of equations,

$$\nabla \cdot \mathbf{E} = \rho_{\text{ext}} + \rho_{\text{ind}}, \tag{1.24}$$

$$\nabla \times \mathbf{H} = \mathbf{J}_{\text{ext}} + \mathbf{J}_{\text{ind}} + \epsilon_0 \frac{\partial \mathbf{E}}{\partial t}, \tag{1.25}$$

$$\nabla \cdot \mathbf{B} = 0, \tag{1.26}$$

$$\nabla \times \mathbf{E} = -\frac{\partial \mathbf{B}}{\partial t}, \tag{1.27}$$

where the total fields are defined by, e.g., $\mathbf{E} = \mathbf{E}_{\text{ext}} + \mathbf{E}_{\text{ind}}$.

If the external currents are known *a priori*, then it follows that the entire response of the system will be captured by the induced current. For non-magnetic materials, we can define the induced current as a function of only the electric field [39],

$$\mathbf{J}_{\text{ind}}(\mathbf{r}, t) = \frac{\partial}{\partial t} \int_0^\infty dt' \iiint_{\mathbb{R}^3} d^3\mathbf{r}' \overleftrightarrow{f} (\mathbf{r} - \mathbf{r}', t - t') \, \mathbf{E}(\mathbf{r}', t'), \tag{1.28}$$

where f is the electric field response function for an infinite, non-local, and dispersive medium exhibiting translational invariance and rotational isotropy with respect to spatial coordinates, as well as stationarity in time. For anisotropic materials it is tensorial, and in the presence of stratified media, symmetry breaking, or interfaces, it is defined piecewise. In the above equation, $\mathbf{E}$ is the total field, which is itself defined at each point, in part, by the induced field coming from all over the medium. The benefit of this picture is that while purely macroscopic, we can still account for the large-scale effects of important microscopic and quantum behaviours using an appropriately chosen response function.

We have chosen to capture the material response in the induced current, however, it is often described by the polarization density. We can relate the induced current to an induced polarization by recognizing that current is simply moving charge, and so equivalent to a changing polarization,

$$\mathbf{J}_{\text{ind}}(\mathbf{r}, t) = \frac{\partial \mathbf{P}_{\text{ind}}}{\partial t}(\mathbf{r}, t). \tag{1.29}$$

So we can relate our material response to polarization density by applying equation 1.29 to equation 1.28,

$$\mathbf{P}_{\text{ind}}(\mathbf{r},t) = \int_0^\infty dt' \iiint_{\mathbb{R}^3} d^3\mathbf{r}' \overleftrightarrow{f}(\mathbf{r}-\mathbf{r}', t-t')\mathbf{E}(\mathbf{r}', t'), \tag{1.30}$$

We will continue to refer to $\mathbf{P}_{\text{ind}}$ as the polarization density, but it is perhaps more accurately described in general terms as the electric field response. This is because, as we have defined it, $\mathbf{P}_{\text{ind}}$ captures both conduction and polarization. This is made more clear in the Fourier domain where, by convolution theorem, the integral relationship becomes multiplicative,

$$\mathbf{P}_{\text{ind}}(\mathbf{k},\omega) = \overleftrightarrow{f}(\mathbf{k},\omega)\mathbf{E}(\mathbf{k},\omega), \tag{1.31}$$

$$\mathbf{J}_{\text{ind}}(\mathbf{k},\omega) = -i\omega\overleftrightarrow{f}(\mathbf{k},\omega)\mathbf{E}(\mathbf{k},\omega), \tag{1.32}$$

where $\mathbf{k}$ is the wave vector and ω is the angular frequency. This clearly aligns with standard polarization density for bound charges when $f = \epsilon_0\chi$, and Ohm's law for free charges when $f = -\sigma/i\omega$. We can apply charge continuity to our established definition of the induced current to find an expression for the induced charge,

$$-\frac{\partial}{\partial t}\rho_{\text{ind}}(\mathbf{r},t) = \nabla\cdot\mathbf{J}_{\text{ind}}(\mathbf{r},t). \tag{1.33}$$

Note that while bound and free charges are considered indistinguishable in this work, charges that fall under each of these categories will still exist in the material, and each of these classifications of charge satisfy continuity independently, thus guaranteeing the validity of equation 1.33. We can insert into this our expression for the induced current given in equation 1.28,

$$-\frac{\partial}{\partial t}\rho_{\text{ind}}(\mathbf{r},t) = \nabla\cdot\frac{\partial}{\partial t}\int_0^\infty dt' \iiint_{\mathbb{R}^3} d^3\mathbf{r}' \overleftrightarrow{f}(\mathbf{r}-\mathbf{r}', t-t')\,\mathbf{E}(\mathbf{r}', t'), \tag{1.34}$$

$$= \nabla\cdot\frac{\partial}{\partial t}\mathbf{P}_{\text{ind}}(\mathbf{r},t), \tag{1.35}$$

which of course suggests that

$$\rho_{\text{ind}}(\mathbf{r},t) = -\nabla\cdot\mathbf{P}_{\text{ind}}(\mathbf{r},t). \tag{1.36}$$

Here is where we make the distinction between continuous and singular contributions to the induced charge,

$$\rho_{\text{ind}}(\mathbf{r},t) = -\nabla\cdot(\mathbf{P}^c_{\text{ind}}(\mathbf{r},t) + \mathbf{P}^s_{\text{ind}}(\mathbf{r},t)). \tag{1.37}$$

The singular contributions come from discontinuities in the model. For induced charges, these arise at interfaces between different materials, which may contain atomically thin 2D materials that can be considered as having zero thickness in the context of macroscopic classical electromagnetism. Using this definition of the polarization density, we can write a final form of the macroscopic Maxwell's equations,

$$\nabla \cdot \mathbf{D} = \rho_{\text{ext}} - \nabla \cdot \mathbf{P}^s_{\text{ind}}, \tag{1.38}$$

$$\nabla \times \mathbf{H} = \mathbf{J}_{\text{ext}} + \frac{\partial \mathbf{D}}{\partial t} + \frac{\partial \mathbf{P}^s_{\text{ind}}}{\partial t}, \tag{1.39}$$

$$\nabla \cdot \mathbf{B} = 0, \tag{1.40}$$

$$\nabla \times \mathbf{E} = -\frac{\partial \mathbf{B}}{\partial t}, \tag{1.41}$$

where,

$$\mathbf{D}(\mathbf{r}, t) = \epsilon_0 \mathbf{E}(\mathbf{r}, t) + \int_0^\infty dt' \iiint_{\mathbb{R}^3} d^3\mathbf{r}' \overleftrightarrow{f_c} (\mathbf{r} - \mathbf{r}', t - t') \, \mathbf{E}(\mathbf{r}', t') \tag{1.42}$$

$$= \epsilon_0 \mathbf{E}(\mathbf{r}, t) + \mathbf{P}^c_{\text{ind}}(\mathbf{r}, t), \tag{1.43}$$

where both the superscript and subscript "c" indicate that the spatial dependence of the tensor $\overleftrightarrow{f_c}$ renders the polarization, $\mathbf{P}^c_{\text{ind}}$, a continuous function of position, $\mathbf{r}$. The response of such materials is now captured by $\mathbf{D}$ and $\mathbf{P}^s_{\text{ind}}$, regardless of whether it is thought to be associated with free or bound charges. The entirety of this work will be done in regions with no external charges or currents, so the induced labels will be omitted.

1.2 Hertz Vector

In the model of electrodynamics that we have established in our homogeneous isotropic dielectric medium, most of the properties that make a given system unique are captured by the polarization density $\mathbf{P}$. This makes the use of the Hertz vector a natural choice to facilitate some of our analysis. Here the Hertz vector formulation is developed in a way not dissimilar to [34], though with additional emphasis on the relation to the Lorentz gauge. Considering a homogeneous, isotropic, non-magnetic, lossless dielectric medium, in a region with no external charges or currents, the fields can be defined in terms of the well-known vector and scalar potentials,

$$\mathbf{B} = \nabla \times \mathbf{A}, \qquad \mathbf{E} = -\nabla\phi - \frac{\partial \mathbf{A}}{\partial t}. \tag{1.44}$$

We begin with equation 1.39,

$$\nabla \times \mathbf{H} = \frac{\partial \mathbf{D}}{\partial t} + \frac{\partial \mathbf{P}^s}{\partial t} \tag{1.45}$$

$$= \frac{\partial}{\partial t}(\epsilon \mathbf{E} + \mathbf{P}^s), \tag{1.46}$$

where we assume that the source of the singular polarization, $\mathbf{P}^s$, is some 2D material immersed in the mentioned medium, characterized by a dielectric constant ϵ. In such a medium, the continuous part of the polarization in equation 1.43 can be written as $\mathbf{P}^c = \epsilon_0 \chi_c \mathbf{E}$, where χ_c is the constant susceptibility, so that $\epsilon = \epsilon_0(1 + \chi_c)$, which may be equivalently expressed in terms of the refractive index of the medium, $\epsilon = n^2 \epsilon_0$. Now we insert into equation 1.46 the definition of the potentials in equation 1.44, along with using $\mathbf{B} = \mu_0 \mathbf{H}$,

$$\frac{1}{\mu_0} \nabla \times \nabla \times \mathbf{A} = \frac{\partial}{\partial t} \left(\epsilon \left(-\nabla \phi - \frac{\partial \mathbf{A}}{\partial t} \right) + \mathbf{P}^s \right). \tag{1.47}$$

Then, using the vector identity,

$$\nabla \times \nabla \times \mathbf{A} = \nabla \left(\nabla \cdot \mathbf{A} \right) - \nabla^2 \mathbf{A}, \tag{1.48}$$

we can say,

$$\epsilon \mu_0 \frac{\partial^2 \mathbf{A}}{\partial t^2} - \nabla^2 \mathbf{A} = -\nabla \left(\nabla \cdot \mathbf{A} \right) - \epsilon \mu_0 \frac{\partial}{\partial t} \nabla \phi + \mu_0 \frac{\partial}{\partial t} \mathbf{P}^s, \tag{1.49}$$

$$= -\nabla \left(\nabla \cdot \mathbf{A} + \epsilon \mu_0 \frac{\partial}{\partial t} \phi \right) + \mu_0 \frac{\partial}{\partial t} \mathbf{P}^s. \tag{1.50}$$

This is the standard form of the vector potential wave equation. In this form, the equations for the vector and scalar potentials are coupled. We can decouple them by applying the Lorentz gauge for non-magnetic materials,

$$\nabla \cdot \mathbf{A} = \epsilon \mu_0 \frac{\partial}{\partial t} \phi. \tag{1.51}$$

The Hertz vector can then be thought of as just another way to satisfy the Lorentz Gauge. This is made clear when we exploit the continuity of $\mathbf{A}$ in time to represent it as the time derivative of another function,

$$\mathbf{A} = \epsilon \mu_0 \frac{\partial \mathbf{\Pi}}{\partial t}, \tag{1.52}$$

then simply by inserting this into the equation for the Lorentz gauge, the following relationship is found,

$$\phi = -\nabla \cdot \mathbf{\Pi}. \tag{1.53}$$

These are the standard forms of the relationship between the Hertz vector and the vector and scalar potentials [34]. To determine the relationship with the base fields, $\mathbf{E}$ and $\mathbf{B}$, we can substitute equations 1.52 and 1.53 into 1.44. First for the magnetic field,

$$\mathbf{B} = \frac{1}{v^2}\nabla \times \frac{\partial \mathbf{\Pi}}{\partial t}, \tag{1.54}$$

and then for the electric field,

$$\mathbf{E} = \nabla\left(\nabla \cdot \mathbf{\Pi}\right) - \frac{1}{v^2}\frac{\partial^2 \mathbf{\Pi}}{\partial t^2}. \tag{1.55}$$

In the above equations, we introduced the speed of light in the background medium as $v = c/n$, where $c = 1/\sqrt{\epsilon_0 \mu_0}$ is the speed of light in vacuum, and n is the refractive index of that medium. To find a wave equation for the Hertz vector, we can insert equations 1.52 and 1.53 into 1.50,

$$\nabla^2\left(\epsilon\mu_0 \frac{\partial \mathbf{\Pi}}{\partial t}\right) - \frac{1}{v^2}\frac{\partial^2}{\partial t^2}\left(\epsilon\mu_0 \frac{\partial \mathbf{\Pi}}{\partial t}\right) = -\mu_0 \frac{\partial}{\partial t}\mathbf{P}^s, \tag{1.56}$$

$$\frac{\partial}{\partial t}\nabla^2\left(\mathbf{\Pi}\right) - \frac{1}{v^2}\frac{\partial}{\partial t}\left(\frac{\partial^2 \mathbf{\Pi}}{\partial t^2}\right) = -\frac{1}{\epsilon}\frac{\partial}{\partial t}\mathbf{P}^s, \tag{1.57}$$

which of course suggests an equation of the form,

$$\nabla^2 \mathbf{\Pi} - \frac{1}{v^2}\frac{\partial^2 \mathbf{\Pi}}{\partial t^2} = -\frac{1}{\epsilon}\mathbf{P}^s. \tag{1.58}$$

To simplify some of our later analysis, we can again apply equation 1.48, along with 1.58 to equation 1.55 to find the final set of relationships,

$$\mathbf{E} = \nabla \times \nabla \times \mathbf{\Pi} - \frac{1}{\epsilon}\mathbf{P}^s, \qquad \mathbf{B} = \frac{1}{v^2}\nabla \times \frac{\partial \mathbf{\Pi}}{\partial t}. \tag{1.59}$$

Besides allowing one to define a system entirely in terms of polarization, the simple form of the governing wave equation for the Hertz vector permits a scalar Green's function solution of equation 1.58,

$$\mathbf{\Pi}(\mathbf{r}, t) = \frac{1}{4\pi\epsilon}\iiint_{\mathbb{R}^3} d^3\mathbf{r}' \frac{\mathbf{P}^s(\mathbf{r}', t - \frac{R}{v})}{R}, \tag{1.60}$$

where $R = |\mathbf{r} - \mathbf{r}'|$. This allows us to construct an equation for the total electric field as,

$$\mathbf{E}(\mathbf{r}, t) = -\frac{1}{\epsilon}\mathbf{P}^s(\mathbf{r}, t) + \frac{1}{4\pi\epsilon}\nabla \times \nabla \times \iiint_{\mathbb{R}^3} d^3\mathbf{r}' \frac{\mathbf{P}^s(\mathbf{r}', t - \frac{R}{v})}{R}. \tag{1.61}$$

In this expression, the contribution from the bulk response of the dielectric is captured in the permittivity $\epsilon = n^2\epsilon_0$, whereas the interfacial, and therefore singular, polarization is given by $\mathbf{P}^s$, and considered to describe a 2D material. According to equation 1.61, the electric field is singular at the interface due to the contribution from the singular polarization density outside the integral. It will be shown in section 2.1 that the curl terms generate additional singularities which cancel with those in the in-plane directions, leaving only a singularity in the $\hat{z}$ direction from the out-of-plane polarization component. This aligns with other published works investigating the boundary conditions on out-of-plane response [40]. In [40], it is postulated that the electric field consists of a regular part away from the interface and a singular part at the interface. The boundary conditions are then derived directly from Maxwell's equations. The method in this work arrives at the same conclusion of singular fields, though as a direct result of the singular polarization density of the 2D material rather than a postulate.

1.3 Interface Conditions

Up to this point, we have been working within infinite, isotropic, homogeneous media. With broken spatial invariance, space is defined in a piece-wise continuous manner. Electromagnetic interface conditions describe how electric and magnetic fields change across these discontinuities in the underlying medium. The specific form of these interface conditions is dictated by the geometry and composition of the media around the interface. The most familiar textbook setting is that of a flat abrupt interface between two isotropic, non-magnetic, lossless dielectrics. In this case, and in those where interfacial currents are present but purely in the plane, the standard textbook method involving integration over current loops and pill boxes spanning the interface is perfectly acceptable [41].

For example, the textbook integral method is appropriate for interfacial currents defined by,

$$\mathbf{J}^s = \mathbf{J}_\parallel \delta(z), \tag{1.62}$$

where $\mathbf{J}_\parallel$ indicates that the current is defined only parallel to the interface. The resulting interface conditions are defined by, [41]

$$\hat{z} \times (\mathbf{E}_2 - \mathbf{E}_1) = 0, \tag{1.63}$$
$$(\mathbf{D}_2 - \mathbf{D}_1) \cdot \hat{z} = \rho_{2\mathrm{D}}, \tag{1.64}$$
$$(\mathbf{B}_2 - \mathbf{B}_1) \cdot \hat{z} = 0, \tag{1.65}$$
$$\hat{z} \times (\mathbf{H}_2 - \mathbf{H}_1) = \mathbf{J}_\parallel, \tag{1.66}$$

where $\hat{z}$ is the unit normal vector, and the in-plane current density and the surface charge density satisfy the continuity equation,

$$\nabla_{\parallel} \cdot \mathbf{J}_{\parallel} + \frac{\partial \rho_{\text{2D}}}{\partial t} = 0, \tag{1.67}$$

and $\parallel$ indicates only the in-plane components are present, making $\nabla_{\parallel}$ a 2D gradient vector acting tangentially to the interface. However, this method breaks down when considering out-of-plane current, and it is not clear how it must be modified. Perhaps with a current loop flat on the interface, but interpreting this is ambiguous. A new method is necessary.

1.4 Fresnel setting

When we begin to talk about the reflection and transmission of plane waves at interfaces, it becomes convenient to adopt a coordinate system defined with respect to wave propagation. We choose the Cartesian triplet of unit vectors ($\hat{x}$, $\hat{y}$, $\hat{z}$) to represent the fixed material frame and adopt coordinates defined with respect to the incident wave vector for the waves themselves. In these coordinates, the plane of incidence is the $\hat{q} - \hat{z}$ plane, with the perpendicular direction defined as $\hat{\tau} = \hat{q} \times \hat{z}$ as shown in figure 1.6. The in-plane propagation direction $\hat{q}$ is defined with respect to the fixed material frame by rotation about the $\hat{z}$ axis, described by the angle ϕ. In all cases with broken translational invariance, we will denote the in-plane coordinates as $\mathbf{r}_{\parallel}$.

The most general case of a Fresnel-style optical interaction involves four fields, one upward and one downward propagating field on either side of an interface. This is shown schematically in figure 1.7. Labelling all upward propagating fields u and all downward propagating fields d, we will have two fields in each interface separated region given by, [38]

$$\mathbf{E}_{uj} = \begin{bmatrix} -u_{pj}\cos\theta_j \\ u_{sj} \\ u_{pj}\sin\theta_j \end{bmatrix} e^{i(\mathbf{q}\cdot\mathbf{r}_{\parallel} + k_{zj}z - \omega t)}, \; \mathbf{E}_{dj} = \begin{bmatrix} d_{pj}\cos\theta_j \\ d_{sj} \\ d_{pj}\sin\theta_j \end{bmatrix} e^{i(\mathbf{q}\cdot\mathbf{r}_{\parallel} - k_{zj}z - \omega t)}, \tag{1.68}$$

$$\mathbf{H}_{uj} = \frac{n_j}{z_0} \begin{bmatrix} -u_{sj}\cos\theta_j \\ -u_{pj} \\ u_{sj}\sin\theta_j \end{bmatrix} e^{i(\mathbf{q}\cdot\mathbf{r}_{\parallel} + k_{zj}z - \omega t)}, \; \mathbf{H}_{dj} = \frac{n_j}{z_0} \begin{bmatrix} d_{sj}\cos\theta_j \\ -d_{pj} \\ d_{sj}\sin\theta_j \end{bmatrix} e^{i(\mathbf{q}\cdot\mathbf{r}_{\parallel} - k_{zj}z - \omega t)}, \tag{1.69}$$

where $\mathbf{q} = q\hat{q}$ are the in-plane wave vectors, k_{zj} the out-of-plane wavenumbers, $z_0 = \frac{1}{\epsilon_0 c}|_{\text{SI}} = \frac{4\pi}{c}|_{cgs}$ is the impedance of free space, and n_j are the refractive indices. The in-plane and

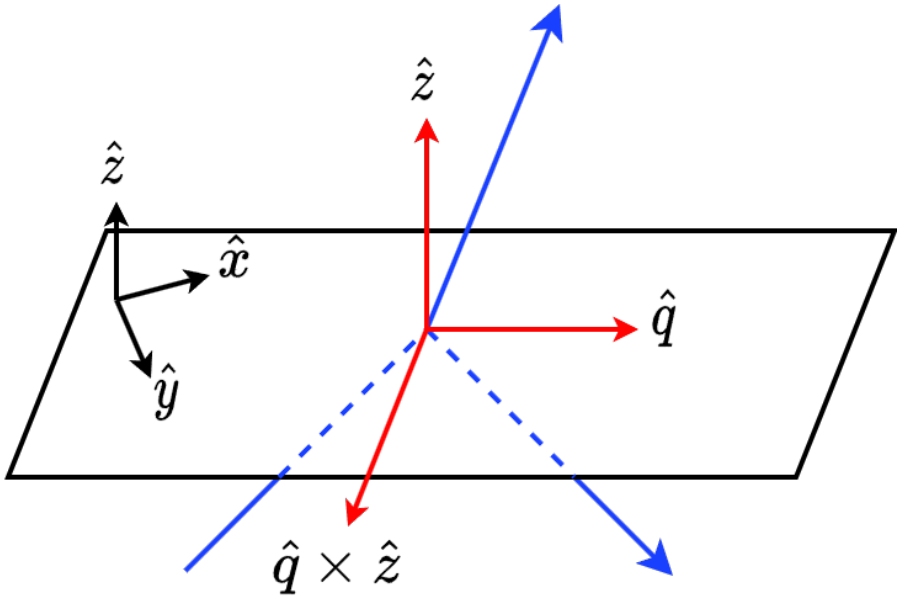


Figure 1.6: Diagram of a plane wave interaction with a flat interface highlighting the coordinate system used in this work.

out-of-plane wavenumber are related by

$$n_j^2 k_0^2 = q^2 + k_{zj}^2, \tag{1.70}$$

where $k_0 = \omega/c$ is the vacuum wavenumber, and c is the speed of light in vacuum. The transmitted wave retains the same amplitude sign convention, while the reflected wave is mirrored across $x = 0$.

The in-plane component of the wave vector is conserved across the interface[38], and so remains the same for all of the fields. This gives rise to Snell's law,

$$n_1 \sin\theta_i = n_2 \sin\theta_t, \tag{1.71}$$

or, in terms of the dielectric constants,

$$\epsilon_1 \sin^2\theta_i = \epsilon_2 \sin^2\theta_t. \tag{1.72}$$

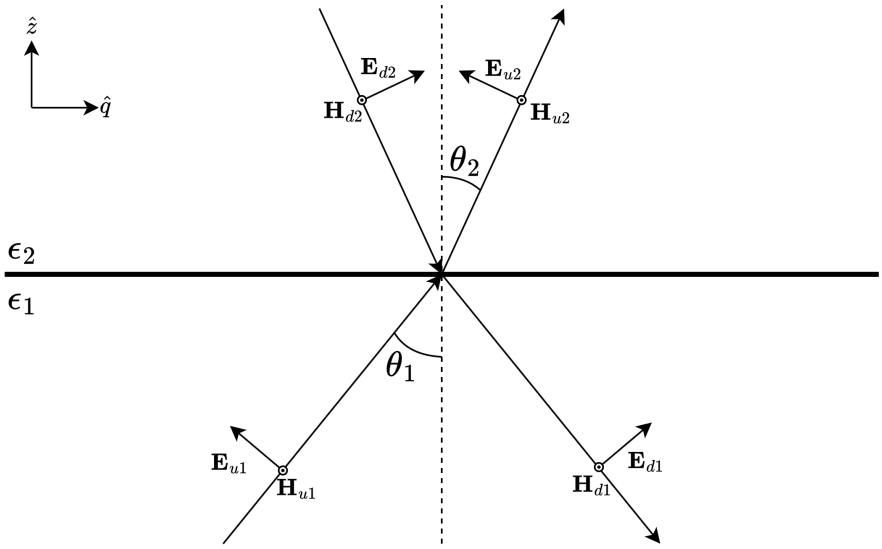


Figure 1.7: Diagram of a classic Fresnel style interaction between a p-polarized plane wave and the interface between two isotropic, non-magnetic dielectrics.

1.5 Transfer matrices

For single interfaces, it is easy to simply insert the electromagnetic fields defined in terms of Fresnel amplitudes (equations 1.68 and 1.69) and directly solve the interface conditions to relate fields on either side of a discontinuity. This problem grows substantially more tedious for systems of multiple interfaces. In these cases we adopt a transfer matrix formalism [42]. This is a method by which one converts the interface conditions into transfer matrices that can be directly applied to relate the fields on either side of the j^{th} interface as,

$$\begin{pmatrix} u_{pj} \\ u_{sj} \\ d_{pj} \\ d_{sj} \end{pmatrix} = \mathbf{M}_{j,j+1} \begin{pmatrix} u_{p(j+1))} \\ u_{s(j+1)} \\ d_{p(j+1)} \\ d_{s(j+1)} \end{pmatrix}. \tag{1.73}$$

We derive the matrices starting from the interface conditions without in-plane current, equations 1.63, and 1.66 with $\mathbf{J}_{\parallel} = 0$. Note that we do not need all four; two of the interface conditions are all that is necessary to uniquely determine all of the amplitudes. For an interface between two isotropic, non-magnetic, lossless dielectrics, equation 1.63 tells us that the in-plane components of the electric field are continuous, $\mathbf{E}_1|_{\hat{q}} = \mathbf{E}_2|_{\hat{q}}$ and

$\mathbf{E}_1|_{\hat{\tau}} = \mathbf{E}_2|_{\hat{\tau}}$. In terms of the amplitudes defined in equation 1.68, this means,

$$(u_{p1} - d_{p1})\cos\theta_1 = (u_{p2} - d_{p2})\cos\theta_2, \tag{1.74}$$

and,

$$u_{s1} + d_{s1} = u_{s2} + d_{s2}, \tag{1.75}$$

respectively. Equation 1.66 then tells us that the in-plane components of the magnetic field are continuous, $\mathbf{H}_1|_{\hat{q}} = \mathbf{H}_2|_{\hat{q}}$ and $\mathbf{H}_1|_{\hat{\tau}} = \mathbf{H}_2|_{\hat{\tau}}$. In terms of the field amplitudes defined in 1.69, this means,

$$\frac{n_1}{z_0}(u_{s1} - d_{s1})\cos\theta_1 = \frac{n_2}{z_0}(u_{s2} - d_{s2})\cos\theta_2, \tag{1.76}$$

and,

$$\frac{n_1}{z_0}(u_{p1} + d_{p1}) = \frac{n_2}{z_0}(u_{p2} + d_{p2}), \tag{1.77}$$

respectively. Now we can simply organize these four equations into a matrix that satisfies equation 1.73,

$$\mathbf{M} = \frac{1}{2}\begin{bmatrix} \frac{n_2}{n_1} + \frac{\cos(\theta_2)}{\cos(\theta_1)} & 0 & \frac{n_2}{n_1} - \frac{\cos(\theta_2)}{\cos(\theta_1)} & 0 \\ 0 & 1 + \frac{n_2\cos(\theta_2)}{n_1\cos(\theta_1)} & 0 & 1 - \frac{n_2\cos(\theta_2)}{n_1\cos(\theta_1)} \\ \frac{n_2}{n_1} - \frac{\cos(\theta_2)}{\cos(\theta_1)} & 0 & \frac{n_2}{n_1} + \frac{\cos(\theta_2)}{\cos(\theta_1)} & 0 \\ 0 & 1 - \frac{n_2\cos(\theta_2)}{n_1\cos(\theta_1)} & 0 & 1 + \frac{n_2\cos(\theta_2)}{n_1\cos(\theta_1)} \end{bmatrix}. \tag{1.78}$$

To apply this method to systems of multiple interfaces, we also need to consider the intervening bulk material. As we are considering lossless materials, this amounts to phase shifts, and is accomplished through so-called propagation matrices,

$$\mathbf{\Psi}_j = \begin{bmatrix} e^{i(k_{zj}d_j)} & 0 & 0 & 0 \\ 0 & e^{i(k_{zj}d_j)} & 0 & 0 \\ 0 & 0 & e^{-i(k_{zj}d_j)} & 0 \\ 0 & 0 & 0 & e^{-i(k_{zj}d_j)} \end{bmatrix}, \tag{1.79}$$

where d_j is the thickness of the j^{th} dielectric layer. So, one would represent the relationship between the amplitudes of the incident field at the first interface and the ultimately transmitted field at the final interface for N media separated by $N-1$ interfaces as,

$$\begin{pmatrix} u_{p1} \\ u_{s1} \\ d_{p1} \\ d_{s1} \end{pmatrix} = \Pi_{j=1}^{N-1}\mathbf{M}_{j,j+1}\mathbf{\Psi}_{j+1}\begin{pmatrix} u_{pN} \\ u_{sN} \\ 0 \\ 0 \end{pmatrix}, \tag{1.80}$$

where the N^{th} propagation matrix is the identity, $\mathbf{\Psi}_N = \mathbf{I}$. In an effort to match with commonly used conventions for Fresnel coefficients [38], in the following analysis of optical interactions with 2D materials, we will rename the parameters in the incident and ultimately transmitted media to,

$$\begin{pmatrix} a_p \\ a_s \\ r_p \\ r_s \end{pmatrix} = \Pi_{j=1}^{N-1} \mathbf{M}_{j,j+1} \mathbf{\Psi}_{j+1} \begin{pmatrix} t_p \\ t_s \\ 0 \\ 0 \end{pmatrix}. \tag{1.81}$$

This corresponds to $u_1 \to a$, $d_1 \to r$, and $u_N \to t$.

1.6 2D material response functions

Optical response functions in general terms describe how materials interact with electromagnetic fields. In a linear-response approximation for N dimensional systems, which are translationally invariant in N spatial dimensions and stationary in time, we can perform $N+1$ Fourier transforms. Then, response functions are the proportionality factors, in the Fourier domain, between electromagnetic fields and descriptions of charge redistribution like current and polarization. In a classical picture, a material can be fully characterized by one electric and one magnetic response function, each capturing how a material influences surrounding and internal electromagnetic fields [37]. In this work, we are only considering non-magnetic materials, and so each material is described by a single electric response function. In general, a susceptibility χ or a conductivity σ is used as the optical response function of a material, at a given frequency ω. Traditionally, susceptibility is related to polarizability, and thus to bound charges, while conductivity is related to electrical current, and thus to quasi-free charges. The bound charges represent those electrons that remain bound to their host atoms in the material, but they can "jump" from one to another quantum state under the influence of a harmonic EM field, thereby executing the so-called interband electron transitions. On the other hand, quasi-free charges are represented by those electrons or holes that occupy one or more partially filled energy bands in the materials and can therefore absorb energy from the EM radiation at arbitrarily small frequencies, thereby executing the so-called intraband electron transitions. In practice, however, those two functions can be combined into a single, frequency-dependent response function, either an effective susceptibility, $\chi_{\text{eff}} = \chi + \frac{i\sigma}{\epsilon_0 \omega}$, or an effective conductivity, $\sigma_{\text{eff}} = \sigma - i\omega\epsilon_0\chi$. Therefore, susceptibility and conductivity are interchangeable, $\chi = i\sigma/(\epsilon_0\omega)$, where we have dropped the subscript "eff". In this work, when implementing response function

models, conductivity will be used. This is in part because the *ab initio* data from the time-dependent DFT calculations are typically obtained for the conductivity. Those data are inherently obtained as decomposed into separate contributions from the intraband and interband electron transitions [23].

At the level of Maxwell's equations, conductivity response functions appear through a vector Ohm's law of the form,

$$\mathbf{J}(\mathbf{k},\omega) = \overleftrightarrow{\sigma}(\mathbf{k},\omega)\mathbf{E}(\mathbf{k},\omega), \tag{1.82}$$

where, in a general case with full anisotropy, spatial non-locality, and temporal dispersion,

$$\overleftrightarrow{\sigma}(\mathbf{k},\omega) = \begin{bmatrix} \sigma_{qq}(\mathbf{k},\omega) & \sigma_{q\tau}(\mathbf{k},\omega) & \sigma_{qz}(\mathbf{k},\omega) \\ \sigma_{\tau q}(\mathbf{k},\omega) & \sigma_{\tau\tau}(\mathbf{k},\omega) & \sigma_{\tau z}(\mathbf{k},\omega) \\ \sigma_{zq}(\mathbf{k},\omega) & \sigma_{z\tau}(\mathbf{k},\omega) & \sigma_{zz}(\mathbf{k},\omega) \end{bmatrix}. \tag{1.83}$$

However, for a single 2D material in the infinitesimal sheet model, the dependence on a 3D wavevector ($\mathbf{k}$), is reduced to a 2D in-plane wavevector ($\mathbf{q}$) because there can be no dependence on the out-of-plane spatial coordinate when the out-of-plane thickness is zero. This would mean for a 2D material the general conductivity takes the form,

$$\overleftrightarrow{\sigma}_{\mathrm{2D}}(\mathbf{q},\omega) = \begin{bmatrix} \sigma_{qq}(\mathbf{q},\omega) & \sigma_{q\tau}(\mathbf{q},\omega) & \sigma_{qz}(\mathbf{q},\omega) \\ \sigma_{\tau q}(\mathbf{q},\omega) & \sigma_{\tau\tau}(\mathbf{q},\omega) & \sigma_{\tau z}(\mathbf{q},\omega) \\ \sigma_{zq}(\mathbf{q},\omega) & \sigma_{z\tau}(\mathbf{q},\omega) & \sigma_{zz}(\mathbf{q},\omega) \end{bmatrix}, \tag{1.84}$$

where the in-plane wavevector is defined by $\mathbf{q} = q\hat{q} + \tau\hat{\tau}$, with $\hat{q}$ as the longitudinal direction and $\hat{\tau}$ as the transverse direction. The version of Ohm's law shown in equation 1.82 is simply the Fourier transform of equation 1.28 in both the in-plane spatial ($\mathbf{r}_{\parallel} \to \mathbf{q}$), and the temporal ($t \to \omega$) coordinates when the electric field response function $\overleftrightarrow{f}(\mathbf{q},\omega) = \frac{i}{\omega}\overleftrightarrow{\sigma}(\mathbf{q},\omega)$.

In reality, all materials have some level of non-locality and dispersion, though many can be treated in an approximate sense by dropping one or both of these dependencies [23]. In fact, given the atomistic nature of matter, all materials are truly anisotropic as well, though just as with the macroscopic picture, justifications for approximate isotropy can be made in the long wavelength limit (equation 1.10). In this work, all general derivations will be performed using a local approximation, also known as the optical limit or the long wavelength approximation whereby one sets $\mathbf{k} \to \mathbf{0}$ based on equation 1.10 with r being the physical thickness of the material. This gives a conductivity response function that only depends on frequency, which may be expressed in the material coordinate frame in a

way that exhibits both out-of-plane response and in-plane anisotropy,

$$\overleftrightarrow{\sigma}_m(\omega) = \begin{bmatrix} \sigma_x(\omega) & 0 & 0 \\ 0 & \sigma_y(\omega) & 0 \\ 0 & 0 & \sigma_z(\omega) \end{bmatrix}. \tag{1.85}$$

Here, x and y indicate coordinates directed along the principal axes in the plane of an anisotropic 2D material, such as, e.g., the armchair (AC) and the zigzag (ZZ) crystalline directions of phosphorene [43]. In general, the 2D material can be rotated with respect to the plane of incidence, which would alter the conductivity contributions along the directions of the electric fields. This is accounted for by allowing for rotation about the out-of-plane $\hat{z}$-axis,

$$R = \begin{bmatrix} \cos\phi & -\sin\phi & 0 \\ \sin\phi & \cos\phi & 0 \\ 0 & 0 & 1 \end{bmatrix}, \tag{1.86}$$

$$\overleftrightarrow{\sigma}(\omega,\phi) = R^{\mathrm{T}} \overleftrightarrow{\sigma}_m R \tag{1.87}$$

$$= \begin{bmatrix} \sigma_x(\omega)\cos^2\phi + \sigma_y(\omega)\sin^2\phi & (\sigma_y(\omega) - \sigma_x(\omega))\sin\phi\cos\phi & 0 \\ (\sigma_y(\omega) - \sigma_x(\omega))\sin\phi\cos\phi & \sigma_x(\omega)\sin^2\phi + \sigma_y(\omega)\cos^2\phi & 0 \\ 0 & 0 & \sigma_z(\omega) \end{bmatrix}. \tag{1.88}$$

To simplify the following derivations, the rotated conductivity components will be collected into new conductivity terms,

$$\overleftrightarrow{\sigma}(\omega,\phi) = \begin{bmatrix} \sigma_q(\omega,\phi) & \sigma_c(\omega,\phi) & 0 \\ \sigma_c(\omega,\phi) & \sigma_\tau(\omega,\phi) & 0 \\ 0 & 0 & \sigma_z(\omega) \end{bmatrix}, \tag{1.89}$$

where in future expressions, the frequency and angular dependence will be omitted. In terms of 2D materials, the full form of 1.89 is necessary for inherently anisotropic materials like phosphene [43], however, we are also interested in graphene, which is often modelled as isotropic [27] [44] [45]. This is an approximation valid in the long wavelength limit ($\mathbf{q} \to 0$)[46]. With no $\mathbf{q}$ dependence, graphene in the long wavelength limit is local, with $\sigma_q(\omega,\phi) = \sigma_\tau(\omega,\phi) \equiv \sigma(\omega)$ and $\sigma_c(\omega,\phi) = 0$. However, in general, when graphene is non-local, i.e., when it exhibits an in-plane spatial dispersion that gives rise to the dependence of its conductivity on the wavenumber q, in addition to the dependence on frequency, there is a difference in the conductivity between the in-plane longitudinal and transverse directions [47]. In-plane longitudinal is defined as along the $\hat{q}$ direction, while transverse is along

the $\hat{\tau}$ direction in this work. In this case, graphene would be modelled by a conductivity tensor,

$$\overleftrightarrow{\sigma}(q,\omega) = \begin{bmatrix} \sigma_q(q,\omega) & 0 & 0 \\ 0 & \sigma_\tau(q,\omega) & 0 \\ 0 & 0 & \sigma_z(q,\omega) \end{bmatrix}, \tag{1.90}$$

regardless of the material orientation, because the transverse direction $\hat{\tau}$ is by definition perpendicular to the longitudinal direction $\hat{q}$. Because of this, even when explicitly considering graphene in the local limit, all calculations will involve conductivity tensors that distinguish between longitudinal and transverse directions, like equation 1.85, so that the results remain similarly applicable to the non-local case.

Everywhere in Fresnel's formulas, conductivity contributions appear in a product $Z_0\sigma$ where $Z_0 = \sqrt{\mu_0/\epsilon_0} = \frac{4\pi}{c} \approx 376.7\ \Omega$ is the impedance of vacuum. The conductivity of a 2D material is naturally expressed in the units of the Bohr's speed $v_B = \frac{e^2}{\hbar} \approx 0.243$ mS [milli Siemens $= 1/(\text{k}\Omega)$]. Thus, we shall use/develop models for the *normalized* conductivity $\bar{\sigma} = \sigma/v_B$ and will define a *scaled* conductivity $\tilde{\sigma}$ to be used in Fresnel's formulas as

$$\tilde{\sigma} = Z_0\sigma = 4\pi\alpha\bar{\sigma}, \tag{1.91}$$

where $\alpha = \frac{v_B}{c} \approx \frac{1}{137}$ is the fine structure constant. In the optical limit (neglecting spatial dispersion in 2D materials), a conductivity $\sigma(\omega)$ is generally a complex-valued function of the angular frequency $\omega = 2\pi\nu$.

For example, at frequencies up to the visible, the optical conductivity of undoped (intrinsic) graphene is approximately constant, $\sigma_0 = v_B/4$ (a.k.a. universal conductivity of graphene), so that the corresponding scaled conductivity, $\tilde{\sigma}_0 = \pi\alpha \approx 0.029$, is quite small, whereas the conductivity of undoped phosphorene is zero at frequencies throughout its energy band gap, $\hbar\omega \lesssim 2$ eV. However, doping of graphene or phosphorene by an external gate induces quasi-free charge carriers with the density per unit area n, giving rise to a sizable increase in their optical conductivity at frequencies in a broad range around $\nu = 1$ THz (corresponding to energy $\hbar\omega \approx 4.14$ meV and the wavelength $\lambda \approx 300\ \mu$m), which is well described by the famous Drude model. This model describes the dynamic polarization of quasi-free charge carriers in a material that arises from the intra-band electronic transitions and has a firm basis in *ab initio* calculations.

The normalized form of the Drude model for an isotropic 2D electron gas (2DEG) is

$$\bar{\sigma}_D(\omega) = \frac{i}{\pi}\frac{\omega_F}{\omega + i\gamma} \tag{1.92}$$

where $\omega_F = E_F/\hbar$ is the frequency related to the Fermi energy E_F, $\gamma \equiv 1/\tau_f$ is the empirical damping rate, and τ_f is the corresponding empirical carrier lifetime. For the Dirac electrons/holes in doped graphene, one has $\omega_F = v_F k_F$, where $v_F \approx c/300$ is the Fermi speed in graphene and $k_F = \sqrt{\pi n}$ its Fermi wavenumber. Typical doping densities range from about $n = 10^{11}$ cm^{-2} to about $n = 10^{14}$ cm^{-2}, giving typical Fermi energy E_F in the range from 0.037 eV to 1.16 eV, corresponding to the frequencies $\nu_F \approx 8.9$ THz to 280 THz (mid-infrared, or MIR, range).

For an isotropic 2DEG with a single parabolic energy band, we have $\omega_F = \hbar k_F^2/(2m^*)$, where $k_F = \sqrt{2\pi n}$ is its Fermi wavenumber and m^* is the effective electron mass. For an anisotropic 2D material like doped phosphorene, we have a diagonal conductivity tensor with the x and y components taken along the AC and ZZ crystal directions, which are well described by the anisotropic Drude model at zero temperature

$$\bar{\sigma}_{Dj}(\omega) = \frac{i}{\pi}\frac{\omega_j}{\omega + i\gamma_j}, \tag{1.93}$$

where $\omega_j = \pi\hbar n/(m_j^*)$ with n being the doping density of phosphorene and m_j^* the effective electron/hole mass in the $j = x, y$ direction. For example, for electron doping with a typical density of $n = 10^{13}$ cm^{-2}, we find from *ab initio* data that $m_x^* = 0.133m_0$ and $m_y^* = 1.119m_0$, where m_0 is the free electron mass, giving $\omega_x \approx 0.180$ eV and $\omega_y \approx 0.021$ eV. The damping parameters for both graphene and phosphorene can take broad ranges of γ values, going from zero (giving undamped plasmon-polariton modes in those materials) to $1/\tau \sim 1$ THz (causing fast attenuation of those modes).

In this work, we will consider both doped and undoped 2D materials. For all doped 2D materials, we will describe the conductivities purely as Drude models, and so will only consider the aforementioned low-frequency regimes where these models are accurate. For all undoped materials, we will make use of *ab initio* response functions calculated using density functional theory (DFT).

Chapter 2

Out-of-plane interface condition and analysis of material influence

The method developed in section 1.3 is an effective and physically intuitive method of calculating jump conditions on the fields in this simplest case of planar interfaces at $z = 0$ between isotropic, non-magnetic, lossless dielectrics. If only the in-plane behaviour is considered, then the standard textbook method, based on Gaussian pill boxes and Stokesian current loops, is sufficient. However, with out-of-plane current, a different method is necessary for calculating the jump condition. Multiple groups [31] [32] [33] [34] have published distinct derivations of the interface condition on the out-of-plane response, and each agrees on the form, for vacuum surroundings, of,

$$\mathbf{E}_2(\mathbf{r}_\parallel, \omega) - \mathbf{E}_1(\mathbf{r}_\parallel, \omega) = -\frac{1}{\epsilon_0}\left[\nabla_\parallel P_z(\mathbf{r}_\parallel, \omega) + \nabla_\parallel \cdot \mathbf{P}_\parallel(\mathbf{r}_\parallel, \omega)\hat{z}\right], \tag{2.1}$$

where $\mathbf{P}_\parallel$ is an in-plane, two-component polarization vector, which is related to a three-component singular polarization vector that was introduced in the previous chapter, by

$$\mathbf{P}^s(\mathbf{r}, \omega) = \mathbf{P}^{2D}(\mathbf{r}_\parallel, \omega)\delta(z) = \begin{pmatrix} P_q(\mathbf{r}_\parallel, \omega) \\ P_\tau(\mathbf{r}_\parallel, \omega) \\ P_z(\mathbf{r}_\parallel, \omega) \end{pmatrix} \delta(z) = (\mathbf{P}_\parallel(\mathbf{r}_\parallel, \omega) + P_z(\mathbf{r}_\parallel, \omega)\hat{z})\delta(z). \tag{2.2}$$

Here, we write the position vector in 3D as $\mathbf{r} = (\mathbf{r}_\parallel, z)$ and the in-plane coordinates are defined as $\mathbf{r}_\parallel$, with $\nabla_\parallel$ denoting the in-plane gradient. Most of the derivations of this interface condition involved the reflection of light from an interface between non-magnetic, isotropic, lossless dielectrics, or vacuum, though anisotropic surroundings [35] has also been investigated.

Common across all derivations is the fact that the in-plane directions are made discontinuous by the polarization density in the out-of-plane direction. There remains a lack of consensus, however, on how to define the out-of-plane polarization density with dielectric surroundings. Assuming there is an influence on the polarization density from surrounding materials, its form will be highly dependent on the material configuration. There are four possible configurations for the interfacial polarization density,

$$\mathbf{P}_a = \begin{cases} \mathbf{P}_2, & z > 0 \\ \mathbf{P}^s, & z = 0 \\ \mathbf{P}_1, & z < 0 \end{cases}, \quad \mathbf{P}_b = \begin{cases} \mathbf{P}_2, & z > 0 \\ \mathbf{P}^s, & z = 0 \\ \mathbf{P}_1, & z \leq 0 \end{cases}, \quad \mathbf{P}_c = \begin{cases} \mathbf{P}_2, & z \geq 0 \\ \mathbf{P}^s, & z = 0 \\ \mathbf{P}_1, & z < 0 \end{cases}, \quad \mathbf{P}_d = \begin{cases} \mathbf{P}_2, & z \geq 0 \\ \mathbf{P}^s, & z = 0 \\ \mathbf{P}_1, & z \leq 0 \end{cases}. \tag{2.3}$$

While the b, c, and d configurations are technically multiply defined at zero, they symbolically represent cases in which the polarizable media at the interface (2D materials, scattered metallic particles, etc.) are immersed in one media or partially in both. These final three cases and their influence on the form of the polarization density have been investigated in [35][36][5]. Each of these groups found that when the polarization density is defined partially or fully in one of the surrounding dielectrics, its effect becomes screened by that dielectric. This can be understood by considering the Hertz vector wave equation, derived originally in equation 1.58, for an infinite dielectric,

$$\nabla^2 \mathbf{\Pi} - \frac{1}{v^2} \frac{\partial^2 \mathbf{\Pi}}{\partial t^2} = -\frac{1}{\epsilon} \mathbf{P}^s. \tag{2.4}$$

When fully immersed, the source, represented here as a singular polarization density, is effectively reduced in magnitude by $1/\epsilon$. This factor of the dielectric constant is reflected in the boundary condition as,

$$\hat{z} \times \big(\mathbf{E}_2(\mathbf{r}_\parallel, \omega) - \mathbf{E}_1(\mathbf{r}_\parallel, \omega) \big) = -\frac{1}{\epsilon} \hat{z} \times \nabla_\parallel P_z(\mathbf{r}_\parallel, \omega), \tag{2.5}$$

where the ϵ_0 in the vacuum case has been replaced by the dielectric constant (ϵ) of the medium in which the polarization density is slightly immersed. However, papers that investigate configuration $\mathbf{P}_a$ with distinct dielectrics surroundings either recognize that the polarization is modified, but do not attempt to derive this modification [40], or simply not mention it at all [48].

There is a further lack of consensus around how to define the total field at the interface in the $\hat{z}$ direction. It is undisputed that in frequency space, the singular polarization density at the interface takes the form,

$$\mathbf{P}^s(\mathbf{r}, \omega) = \epsilon_0 \overleftrightarrow{\chi} \mathbf{E}(\mathbf{r}_\parallel, \omega) \delta(z) = \frac{i}{\omega} \overleftrightarrow{\sigma} \mathbf{E}(\mathbf{r}_\parallel, \omega) \delta(z), \tag{2.6}$$

where $\mathbf{E}$ is the total field at the interface, and the conductivity tensor is in general defined for 2D materials as equation 1.84. This tensor is particular to the case of infinitesimal sheets due to its dimensionality. Equation 1.3 indicates that the sheet conductivity can be related to bulk conductivity through integration over the out-of-plane direction. This gives the conductivity of an infinitesimal sheet units of velocity in Gaussian CGS coordinates. It is similarly common for the total field at an interface to be defined as the average of the fields on either side,

$$\mathbf{E}^{\text{av}} = \frac{1}{2}(\mathbf{E}_1 + \mathbf{E}_2). \tag{2.7}$$

This is the picture adopted in many macroscopic treatments of this problem [33] [3] [49] [48] [50] [51] [52] [53]. This averaging in the macroscopic picture is widely used, though rarely with an accompanying justification. Regardless, the choice is consistent with the interface conditions. Inserting the average of the fields on either side into the standard jump conditions for a dielectric interface results in the appropriate field amplitudes. However, this averaging procedure is potentially incomplete for the out-of-plane direction. Consider the argument laid out in [35]. Imagine a sheet of conductivity inserted into a small vacuum region in between two semi-infinite dielectric media. This is shown schematically in figure 2.1. The jump condition on the electric fields normal to the dielectric interfaces is,

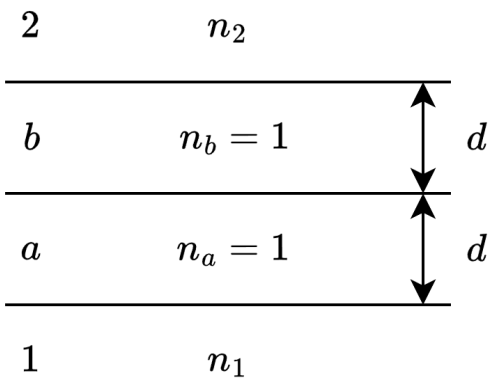


Figure 2.1: Diagram of a triple interface vacuum gap configuration.

$$(\mathbf{D}_{\text{above}} - \mathbf{D}_{\text{below}}) \cdot \hat{z} = 0, \tag{2.8}$$

where $\mathbf{D}_{\text{above}}$ and $\mathbf{D}_{\text{below}}$ are the displacement fields above and below an interface without external charges. The central regions (a & b) in figure 2.1 are vacuum, so according to

equation 2.8 the field just below the upper interface is $\epsilon_0 E_{bz} = D_{2z}$, while the field just above the lower interface is, $\epsilon_0 E_{az} = D_{1z}$. In the limit that the central vacuum region collapses ($d \to 0$), those interior fields just above and just below the dielectric interfaces become the fields that act on the 2D material. This means that the total electric field at the 2D material, modelled by the arithmetic mean,

$$E_z^{\text{av}} = \frac{1}{2}(E_{az} + E_{bz}), \tag{2.9}$$

becomes the arithmetic mean of the displacement fields in the semi-infinite dielectric media,

$$E_z^{\text{av}} = \frac{1}{2}(\frac{D_{z1}}{\epsilon_0} + \frac{D_{z2}}{\epsilon_0}) = \frac{1}{\epsilon_0} D_z^{\text{av}}. \tag{2.10}$$

The equivalence of the normal part of the electric field at an interface to the displacement field has been discussed numerous times [25] [35] [36] [54], though it has yet to see widespread acceptance. With this change, the polarization density in the out-of-plane direction would involve the average of the displacement field according to,

$$P_z(\mathbf{r}_\parallel, \omega) = \frac{i}{\omega\epsilon_0}\sigma_z(\omega) D_z^{\text{av}} = \frac{i}{2\omega\epsilon_0}\sigma_z(\omega)\left(D_{z1}(\mathbf{r}_\parallel, \omega) + D_{z2}(\mathbf{r}_\parallel, \omega)\right), \tag{2.11}$$

or by a different interpretation, something similar to a weighted average of the surrounding electric fields,

$$P_z(\mathbf{r}_\parallel, \omega) = \frac{i}{2\omega}\sigma_z(\omega)\left(n_1^2 E_{z1}(\mathbf{r}_\parallel, \omega) + n_2^2 E_{z2}(\mathbf{r}_\parallel, \omega)\right). \tag{2.12}$$

In the following sections, we will derive the appropriate boundary conditions on 2D materials with out-of-plane response, both with and without material surroundings, as well as validate the notion that the total electric field in the $\hat{z}$ direction is related to the displacement field.

2.1 Immersed Interface condition

Here we present a new derivation, though similar to that of [33] with its Hertz vector basis, for the interface condition on the out-of-plane behaviour for a 2D material suspended in vacuum, or immersed in dielectric as shown in figure 2.2. Derived initially in equation 1.61, the Hertz vector formulation can be used to write the total field electric field in terms of the singular sheet of polarization representing a 2D material immersed in a dielectric as

$$\mathbf{E}(\mathbf{r}, t) = -\frac{1}{\epsilon}\mathbf{P}^{\text{s}}(\mathbf{r}, t) + \frac{1}{4\pi\epsilon}\nabla \times \nabla \times \iiint_{\mathbb{R}^3} d^3\mathbf{r}' \frac{\mathbf{P}^{\text{s}}(\mathbf{r}', t - \frac{R}{v})}{R}. \tag{2.13}$$

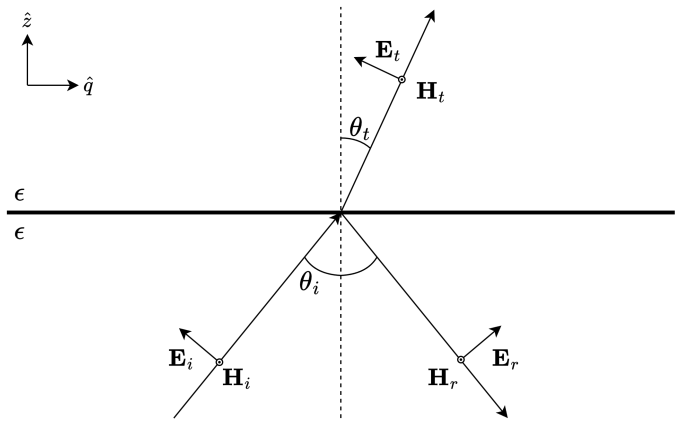


Figure 2.2: Diagram of a classic Fresnel style interaction between a p-polarized plane wave and the interface between two identical dielectrics.

We then convert to the frequency domain ($t \to \omega$),

$$\mathbf{E}(\mathbf{r},\omega) = -\frac{1}{\epsilon}\mathbf{P}^{\mathrm{s}}(\mathbf{r},\omega) + \frac{1}{4\pi\epsilon}\nabla\times\nabla\times\iiint_{\mathbb{R}^3} d^3\mathbf{r}'\,\mathbf{P}^{\mathrm{s}}(\mathbf{r}',\omega)G(\mathbf{r}-\mathbf{r}',\omega), \tag{2.14}$$

where the scalar Green's function for a homogeneous dielectric is defined by

$$G(\mathbf{r}-\mathbf{r}',\omega) = \frac{e^{ikR}}{R}, \tag{2.15}$$

where $R = |\mathbf{r}-\mathbf{r}'|$, and $k = n\omega/c$. Most studies on the optical response of 2D materials model the materials with conductivity tensors. However, here we present the derivation in terms of polarization density. The singular polarization density is defined as,

$$\mathbf{P}^{\mathrm{s}}(\mathbf{r},t) = \mathbf{P}^{\mathrm{2D}}(\mathbf{r}_\parallel,t)\delta(z), \tag{2.16}$$

where,

$$\mathbf{P}^{\mathrm{2D}}(\mathbf{r}_\parallel,t) = \begin{bmatrix} P_q(\mathbf{r}_\parallel,t) \\ P_\tau(\mathbf{r}_\parallel,t) \\ P_z(\mathbf{r}_\parallel,t) \end{bmatrix} = \mathbf{P}_\parallel(\mathbf{r}_\parallel,t) + P_z(\mathbf{r}_\parallel,t)\hat{z}, \tag{2.17}$$

where, based on figure 2.2, $\hat{q}$ is the in-plane longitudinal direction, and $\hat{\tau}$ is the in-plane transverse direction. After Fourier transforming equation 2.16 with respect to time ($t \to \omega$), and plugging it into equation 2.14,

$$\mathbf{E}(\mathbf{r}) = -\frac{1}{\epsilon}\mathbf{P}^{\mathrm{s}}(\mathbf{r}) + \frac{1}{4\pi\epsilon}\nabla\times\nabla\times\iint_{\mathbb{R}^2} d^2\mathbf{r}'_\parallel\,\mathbf{P}^{\mathrm{2D}}(\mathbf{r}'_\parallel)G(\mathbf{r}_\parallel-\mathbf{r}'_\parallel,z), \tag{2.18}$$

where here and going forward, the ω dependence has been omitted.

With this, we can construct equations for the total fields in the surrounding half spaces by choosing the observation point in the corresponding region. To evaluate the integrals, we can use convolution theorem to represent them as the inverse Fourier transform of the product of the Fourier transforms of the integrand components, in terms of the in-plane spatial coordinates ($\mathbf{r}_\parallel \to \mathbf{q}$),

$$\iint_{\mathbb{R}^2} d^2\mathbf{r}'_\parallel \, \mathbf{P}^{\mathrm{2D}}(\mathbf{r}'_\parallel) G(\mathbf{r}_\parallel - \mathbf{r}'_\parallel, z) = \frac{1}{(2\pi)^2} \iint_{\mathbb{R}^2} d^2\mathbf{q} \, e^{i\mathbf{q}\cdot\mathbf{r}_\parallel} \, \mathbf{P}^{\mathrm{2D}}(\mathbf{q}) \, G(\mathbf{q}, z), \tag{2.19}$$

where $\mathbf{q} = q\,\hat{q} + \tau\,\hat{\tau}$ is the general in-plane wavevector, with q and τ as the longitudinal and transverse components along the interface, respectively. Inserting this into equation 2.18 and bringing the curls into the integrals,

$$\mathbf{E}(\mathbf{r}) = -\frac{1}{\epsilon}\mathbf{P}^{\mathrm{2D}}\left(\mathbf{r}_\parallel\right)\delta(z) + \frac{1}{2(2\pi)^3\epsilon}\iint_{\mathbb{R}^2} d^2\mathbf{q}\,\nabla\times\nabla\times\left(\mathbf{P}^{\mathrm{2D}}(\mathbf{q})e^{i\mathbf{q}\cdot\mathbf{r}_\parallel}G(\mathbf{q},z)\right). \tag{2.20}$$

The Fourier transform of the Green's function (equation 2.15) with respect to the in-plane components ($\mathbf{r}_\parallel \to \mathbf{q}$) is, [55]

$$G(\mathbf{q}, z) = 2\pi i \frac{e^{i|z|\sqrt{k^2-|\mathbf{q}|^2}}}{\sqrt{k^2-|\mathbf{q}|^2}}. \tag{2.21}$$

If we insert this into equation 2.20 and evaluate the curls we find,

$$\begin{aligned}
\mathbf{E}(\mathbf{r}) = -\frac{1}{\epsilon}\mathbf{P}^{\mathrm{2D}}\left(\mathbf{r}_\parallel\right)\delta(z) + \frac{1}{2(2\pi)^2\epsilon}\iint_{\mathbb{R}^2} d^2\mathbf{q}\, e^{i\mathbf{q}\cdot\mathbf{r}_\parallel} e^{i|z|\sqrt{k^2-|\mathbf{q}|^2}} \\
\times\Bigg[\left(2\delta(z)P_q(\mathbf{q}) - iq\,\mathrm{sign}(z)P_z(\mathbf{q}) + i\frac{(k^2-q^2)P_q(\mathbf{q}) - q\tau P_\tau(\mathbf{q})}{\sqrt{k^2-q^2-\tau^2}}\right)\hat{q} \\
+\left(2\delta(z)P_\tau(\mathbf{q}) - i\tau\,\mathrm{sign}(z)P_z(\mathbf{q}) + i\frac{(k^2-\tau^2)P_q(\mathbf{q}) - q\tau P_\tau(\mathbf{q})}{\sqrt{k^2-q^2-\tau^2}}\right)\hat{\tau} \\
+i\left(\frac{(\tau^2+q^2)P_z(\mathbf{q})}{\sqrt{k^2-q^2-\tau^2}} - \mathrm{sign}(z)(qP_q(\mathbf{q}) + \tau P_\tau(\mathbf{q}))\right)\hat{z}\Bigg]
\end{aligned} \tag{2.22}$$

The singularities in the in-plane directions then cancel between the integrand and the

polarization density outside the integral,

$$\frac{1}{2(2\pi)^2\epsilon}\iint_{\mathbb{R}^2} d^2\mathbf{q}\, e^{i\mathbf{q}\cdot\mathbf{r}_\parallel} e^{i|z|\sqrt{k^2-|\mathbf{q}|^2}} 2\delta(z) P_{q/\tau}(\mathbf{q}) = \frac{1}{(2\pi)^2\epsilon}\iint_{\mathbb{R}^2} d^2\mathbf{q}\, e^{i\mathbf{q}\cdot\mathbf{r}_\parallel}\delta(z) P_{q/\tau}(\mathbf{q}) = \frac{1}{\epsilon}\delta(z) P_{q/\tau}(\mathbf{r}_\parallel), \quad (2.23)$$

leaving only a singularity in the out-of-plane direction,

$$\begin{aligned}\mathbf{E}(\mathbf{r}) = \frac{1}{2(2\pi)^2\epsilon}\iint_{\mathbb{R}^2} d^2\mathbf{q}\, e^{i\mathbf{q}\cdot\mathbf{r}_\parallel} e^{i|z|\sqrt{k^2-|\mathbf{q}|^2}} \\ \times\Bigg[\left(-iq\,\mathrm{sign}(z) P_z(\mathbf{q}) + i\frac{(k^2-q^2)P_q(\mathbf{q}) - q\tau P_\tau(\mathbf{q})}{\sqrt{k^2-q^2-\tau^2}}\right)\hat{q} \\ + \left(-i\tau\,\mathrm{sign}(z) P_z(\mathbf{q}) + i\frac{(k^2-\tau^2)P_q(\mathbf{q}) - q\tau P_\tau(\mathbf{q})}{\sqrt{k^2-q^2-\tau^2}}\right)\hat{\tau} \\ + i\left(\frac{(\tau^2+q^2)P_z(\mathbf{q})}{\sqrt{k^2-q^2-\tau^2}} - \mathrm{sign}(z)(qP_q(\mathbf{q}) + \tau P_\tau(\mathbf{q})) + i2\delta(z)P_z(\mathbf{q})\right)\hat{z}\Bigg] \quad (2.24)\end{aligned}$$

This expression can be used to describe the fields on either side of the 2D material by simply changing the observation point z. We can use this to form an equation for the interface condition by taking the difference $\mathbf{E}_2(\mathbf{r}_\parallel, z_2) - \mathbf{E}_1(\mathbf{r}_\parallel, z_1)$, with $z_2 > 0$ and $z_1 < 0$, then evaluating the limit as $z_1 \to 0^-$ and $z_2 \to 0^+$. The two observation points are on opposite sides of the interface; though they are not necessarily placed symmetrically, they do have opposite parity. The Green's function in equation 2.21 is even in z, so after evaluating the limit, the only terms that do not cancel are those associated with the first derivatives of $|z|$ that give rise to the sign functions in equation 2.22. This leaves us with the following expression for the electric field jump across the interface at $z = 0$,

$$\mathbf{E}_2(\mathbf{r}_\parallel) - \mathbf{E}_1(\mathbf{r}_\parallel) = -\frac{1}{(2\pi)^2\epsilon}\iint_{\mathbb{R}^2} d^2\mathbf{q}\, e^{i\mathbf{q}\cdot\mathbf{r}_\parallel}\left[iq\tilde{P}_z(\mathbf{q})\hat{q} + ip\tilde{P}_z(\mathbf{q})\hat{\tau} + \left(iq\tilde{P}_q(\mathbf{q}) + ip\tilde{P}_\tau(\mathbf{q})\right)\hat{z}\right]. \quad (2.25)$$

We can recognize equation 2.25 as the inverse Fourier transform of the derivative of polarization components. Evaluating this inverse Fourier transform,

$$\mathbf{E}_2(\mathbf{r}_\parallel) - \mathbf{E}_1(\mathbf{r}_\parallel) = -\frac{1}{\epsilon}\left[\hat{q}\cdot\nabla P_z(\mathbf{r}_\parallel)\hat{q} + \hat{\tau}\cdot\nabla P_z(\mathbf{r}_\parallel)\hat{\tau} + \left(\hat{q}\cdot\nabla P_q(\mathbf{r}_\parallel) + \hat{\tau}\cdot\nabla P_\tau(\mathbf{r}_\parallel)\right)\hat{z}\right]. \quad (2.26)$$

Finally, recognizing that the polarization components have no dependence on z,

$$\mathbf{E}_2(\mathbf{r}_\parallel) - \mathbf{E}_1(\mathbf{r}_\parallel) = -\frac{1}{\epsilon}\left[\nabla_{||} P_z(\mathbf{r}_\parallel) + \nabla_{||} \cdot \mathbf{P}_\parallel(\mathbf{r}_\parallel)\hat{z}\right], \tag{2.27}$$

where $\nabla_{||}$ represents the in-plane gradient, and $\mathbf{P}_\parallel$ is the in-plane polarization density defined in equation 2.17. We have recovered an identical boundary condition to those in [31] [33] [25] for the $\hat{z}$ and $\hat{q}$ directions. These works assumed the fields had no transverse in-plane coordinate dependence (τ) and so predicted the $\hat{\tau}$ direction would remain continuous. However, equation 2.27 matches exactly with the interface condition derived in [32], as this work also considered the general case with transverse dependence. Equation 2.27 is the boundary condition as it emerges from the integral method, though it is more common to separate the condition into in-plane and out-of-plane components. For the in-plane condition, we simply take the cross product of equation 2.27 with $\hat{z}$,

$$\hat{z} \times \big(\mathbf{E}_2(\mathbf{r}_\parallel) - \mathbf{E}_1(\mathbf{r}_\parallel)\big) = -\frac{1}{\epsilon}\hat{z} \times \nabla_{||} P_z(\mathbf{r}_\parallel). \tag{2.28}$$

For the out-of-plane condition, we take the dot product of equation 2.27 with $\hat{z}$,

$$\hat{z} \cdot \big(\mathbf{E}_2(\mathbf{r}_\parallel) - \mathbf{E}_1(\mathbf{r}_\parallel)\big) = -\frac{1}{\epsilon}\nabla_{||} \cdot \mathbf{P}_\parallel(\mathbf{r}_\parallel), \tag{2.29}$$

or equivalently, in terms of the displacement field we recover the standard boundary condition in equation 1.64,

$$\hat{z} \cdot \big(\mathbf{D}_2(\mathbf{r}_\parallel) - \mathbf{D}_1(\mathbf{r}_\parallel)\big) = -\nabla_{||} \cdot \mathbf{P}_\parallel(\mathbf{r}_\parallel), \tag{2.30}$$

where $\rho_{2\mathrm{D}} = -\nabla_\parallel \cdot \mathbf{P}_\parallel$ is the conventional form of the interfacial charge density, $\mathbf{D}_1 = \epsilon_0 n^2 \mathbf{E}_1$, and $\mathbf{D}_2 = \epsilon_0 n^2 \mathbf{E}_2$ in the present case of immersion in dielectric media defined by $\epsilon = \epsilon_0 n^2$.

It should be noted that while it appears as though the properties of the homogeneous dielectric background medium directly contribute to the in-plane boundary conditions in equation 2.28, due to the definition of the polarization density, all material coefficients cancel. The out-of-plane polarization, previously defined in equation 2.12, will look like,

$$P_z(\mathbf{r}_\parallel, \omega) = \frac{i}{2\omega}\sigma_z(\omega)\left(n^2 E_{z1}(\mathbf{r}_\parallel, \omega) + n^2 E_{z2}(\mathbf{r}_\parallel, \omega)\right), \tag{2.31}$$

$$= \frac{in^2}{2\omega}\sigma_z(\omega)\left(E_{z1}(\mathbf{r}_\parallel, \omega) + E_{z2}(\mathbf{r}_\parallel, \omega)\right). \tag{2.32}$$

The extracted factor of n^2 cancels with the dielectric screening term in equation 2.28. The consequence of this is that the jump condition on the in-plane electric fields is the same for both vacuum and identical dielectric surroundings. It will be shown in section 2.2 that the properties of surrounding dielectric materials only influence the boundary conditions when they are distinct ($n_1 \neq n_2$).

We can apply the same method to the $\mathbf{H}$ fields to ensure that no deviations from the standard result are predicted. For immersion in a homogeneous dielectric background medium, the $\mathbf{H}$ field can be similarly defined in terms of the Hertz vector in equation 1.60 through equation 1.59 as

$$\mathbf{H}(\mathbf{r},t) = \frac{1}{\mu_0}\mathbf{B}(\mathbf{r},t) = \frac{1}{4\pi}\nabla\times\frac{\partial}{\partial t}\iiint_{\mathbb{R}^3} d^3\mathbf{r}'\,\frac{\mathbf{P}^s(\mathbf{r}',t-\frac{R}{v})}{R}, \tag{2.33}$$

where $\epsilon_0\mu_0 = 1/c^2$ was used. First, we can convert to the Fourier domain in time ($t\to\omega$),

$$\mathbf{H}(\mathbf{r},\omega) = -\frac{i\omega}{4\pi}\nabla\times\iiint_{\mathbb{R}^3} d^3\mathbf{r}'\,\mathbf{P}^s(\mathbf{r}',\omega)G(\mathbf{r}-\mathbf{r}',\omega), \tag{2.34}$$

where we will again omit the frequency dependence of polarization in future expressions. We can follow the same process as was done for the electric field to find an equation for the difference in the magnetic field across the interface,

$$\mathbf{H}_2(\mathbf{r}_\parallel) - \mathbf{H}_1(\mathbf{r}_\parallel) = -i\omega\iint_{\mathbb{R}^2} d^2\mathbf{q}\,e^{i\mathbf{q}\cdot\mathbf{r}_\parallel}\left[\tilde{P}_\tau(\mathbf{q})\hat{q} - \tilde{P}_q(\mathbf{q})\hat{\tau}\right]. \tag{2.35}$$

We can then evaluate the inverse Fourier transform on the right-hand side of equation 2.35 ($\mathbf{q}\to\mathbf{r}_\parallel$), along with an additional inverse Fourier transform in frequency ($\omega\to t$) to get

$$\mathbf{H}_2(\mathbf{r}_\parallel) - \mathbf{H}_1(\mathbf{r}_\parallel) = \frac{\partial}{\partial t}P_\tau(\mathbf{r}_\parallel)\hat{q} - \frac{\partial}{\partial t}P_q(\mathbf{r}_\parallel)\hat{\tau}, \tag{2.36}$$

$$= \hat{z}\times\frac{\partial\mathbf{P}_\parallel}{\partial t}(\mathbf{r}_\parallel), \tag{2.37}$$

alternatively, in terms of current, we recover the standard boundary condition in equation 1.66,

$$\mathbf{H}_2(\mathbf{r}_\parallel) - \mathbf{H}_1(\mathbf{r}_\parallel) = \hat{z}\times\mathbf{J}_\parallel(\mathbf{r}_\parallel). \tag{2.38}$$

So, while this method predicts significant changes to the electric field interface conditions, it recreates exactly the standard form for the magnetic field interface conditions, shown originally in equation 1.66 to have the same lack of dependence on the material parameters.

2.2 Distinct Dielectrics Interface Condition

Calculating the boundary condition when the 2D material is sandwiched between two distinct dielectrics complicates the picture significantly. When fully immersed in a dielectric or vacuum, the 2D material can be considered against a continuous background. With a continuous background, there is no question as to how the 2D material is screened by its surroundings. At the level of classical electromagnetism, the screening of a source is determined by where it is defined, and against what background material. When the background itself is discontinuous, and the source is coincident with this discontinuity, there is no longer a unique solution to account for how the source is screened; a choice must be made. This issue is a consequence of considering both sharp interfaces and infinitesimal sheets. When surrounding materials are defined simply as Heaviside functions, there is, in theory, a single point of vacuum in between the two half-spaces. This is not an issue for the standard dielectric boundary conditions with an in-plane-only current sheet, as the material parameters do not enter into the boundary conditions, as shown in equations 1.63-1.66. When one adds out-of-plane response, however, the dielectric screening appears directly in the boundary condition. With the naive Heaviside definition, one could assume that the 2D material should be treated as if suspended in vacuum, however experimental evidence, and common sense, suggest otherwise. In [3], Fresnel field amplitudes identical to those calculated with the immersed boundary condition derived in section 2.1 were used to fit conductivity values to measurements taken from graphene immersed in a dielectric. The conductivities coming from their fit matched very closely with predictions by *ab initio* calculations. This means that, in the case of graphene at the very least, the dielectric screening from the surrounding materials does agree with experiment. Given that it is necessary for identical dielectric surroundings, it is not likely that the screening would suddenly be unimportant, as it would be for vacuum surroundings, when the dielectrics are distinct.

What this all indicates is that there is a need for some material definition at the interface ($z = 0$). In the non-retarded limit, a charge at an interface will experience an effective medium given by the arithmetic mean of the media on each side. However, through charge continuity, the inclusion of the out-of-plane response in the infinitesimal sheet model gives rise to a dipole layer, not a charge layer,

$$\nabla \cdot \mathbf{J}^s(\mathbf{r}, \omega) = \nabla_\parallel \cdot \mathbf{J}_\parallel(\mathbf{r}_\parallel, \omega)\delta(z) + J_z(\mathbf{r}_\parallel, \omega)\delta'(z) = -i\omega\rho(\mathbf{r}, \omega), \tag{2.39}$$

where the presence of a dipole layer is indicated by the derivative of the Dirac delta. It was shown in [36], that in the non-retarded limit, a dipole that is symmetrically placed in the out-of-plane direction at the interface between two dielectrics experiences an effective

medium given by the harmonic mean of the dielectric constants of the two surrounding media. They further stated that this is also true in the fully retarded picture, and claimed the appropriate boundary condition for the out-of-plane conductivity includes screening by the harmonic mean of the surrounding dielectric constants. While the derivation was not shown, they stated that the harmonic mean screening arises from the application of the singular fields technique [40], when used with an interfacial source defined partly in each medium, in the limit that the two components approach the interface. In this work, we are interested in symmetrical polarization densities that represent 2D materials, so this can be reinterpreted by a source given by half the polarization of the 2D material defined partly in each medium,

$$\mathbf{P}^s(\mathbf{r}) = \frac{\mathbf{P}^{\mathrm{2D}}(\mathbf{r}_\parallel)}{2}\delta(z-d) + \frac{\mathbf{P}^{\mathrm{2D}}(\mathbf{r}_\parallel)}{2}\delta(z+d). \tag{2.40}$$

Then, in the limit that $d \to 0$, the boundary condition can be derived from the singular fields method [40] as

$$\hat{z} \times \big(\mathbf{E}_2(\mathbf{r}_\parallel) - \mathbf{E}_1(\mathbf{r}_\parallel)\big) = -\frac{1}{\epsilon_0}\hat{z} \times \nabla P_z^e(\mathbf{r}_\parallel), \tag{2.41}$$

where the effective out-of-plane polarization density is defined by

$$P_z^e(\mathbf{r}_\parallel) = \frac{\epsilon_0}{2}\left(\frac{1}{\epsilon_1} + \frac{1}{\epsilon_2}\right) P_z(\mathbf{r}_\parallel) = \frac{\epsilon_0}{\epsilon_\perp} P_z(\mathbf{r}_\parallel), \tag{2.42}$$

and the harmonic mean of the surrounding dielectrics is defined by

$$\epsilon_\perp = \frac{2}{\frac{1}{\epsilon_1} + \frac{1}{\epsilon_2}}. \tag{2.43}$$

This follows directly from equation (34) of [36], where the reciprocal contributions from the dielectric constants come from the screening of the sources partially embedded in each medium, though our case differs as we use a symmetric polarization. Screening by the harmonic mean reduces to screening by the background medium ($\epsilon_\perp = \epsilon_0 n^2$) when $n_1 = n_2 = n$.

This can be equivalently interpreted as considering the source at the interface to be the average of the limit from each side — a common technique for handling source terms at interfaces. This same definition of the source can be applied to the Hertz vector method in this work, however, this requires a more careful treatment of the retarded Hertz vector Green's function, which is considered outside the scope of this work.

To summarize, the general set of unique boundary conditions, applicable to all scenarios considered in this work, becomes,

$$\hat{z} \times \big(\mathbf{E}_2(\mathbf{r}_\parallel) - \mathbf{E}_1(\mathbf{r}_\parallel)\big) = -\frac{1}{\epsilon_0}\hat{z} \times \nabla_\parallel P_z^e(\mathbf{r}_\parallel), \tag{2.44}$$

$$\mathbf{H}_2(\mathbf{r}_\parallel) - \mathbf{H}_1(\mathbf{r}_\parallel) = \hat{z} \times \mathbf{J}_\parallel(\mathbf{r}_\parallel), \tag{2.45}$$

where, according to equation 2.11, the effective out-of-plane polarization density is defined by

$$P_z^e = \frac{\epsilon_0}{\epsilon_\perp} P_z = \frac{\epsilon_0}{\epsilon_\perp}\frac{i}{\omega} J_z = \frac{i}{\omega}\frac{\sigma_z}{\epsilon_\perp} D_z^{\text{av}} = \frac{i}{\omega}\frac{\sigma_z^e}{\epsilon_0} D_z^{\text{av}}, \tag{2.46}$$

with σ_z^e being an effective out-of-plane conductivity that incorporates screening by the harmonic mean of the surrounding dielectric constants,

$$\sigma_z^e = \epsilon_0 \frac{\sigma_z}{\epsilon_\perp} = \frac{\sigma_z}{n_\perp^2}, \tag{2.47}$$

and D_z^{av} is the arithmetic mean of the perpendicular components of the surrounding displacement fields and is defined in equation 2.10. Further, the parallel component of the current in equation 2.45 is defined through Ohm's law as

$$\mathbf{J}_\parallel = \overleftrightarrow{\sigma}_\parallel \mathbf{E}_\parallel^{\text{av}}, \tag{2.48}$$

where $\overleftrightarrow{\sigma}_\parallel$ is the 2×2 sub-tensor of the full conductivity tensor defined in equation 1.84 for only the in-plane components, and $\mathbf{E}_\parallel^{\text{av}}$ is the parallel component of the arithmetic mean of the surrounding electric fields, defined originally in equation 2.7.

2.3 Application of vacuum gap method

Now, with the interface conditions on a 2D material surrounded by vacuum and dielectric media established, we move on to the verification that the total field in the $\hat{z}$ direction is proportional to the displacement field. We will do so simultaneously with calculating the Fresnel coefficients by using a vacuum gap method. This was discussed in [35], but not explored explicitly. We will expand the problem to three interfaces by including a vacuum region with width $d_1 + d_2$ around the 2D material, as shown in figure 2.3. In this configuration, we can use the vacuum condition to calculate the field amplitudes. Then, by taking the limit that the vacuum region collapses, we can emulate the case with dielectrics surrounding a true single interface. However, it is important to note that the vacuum gap

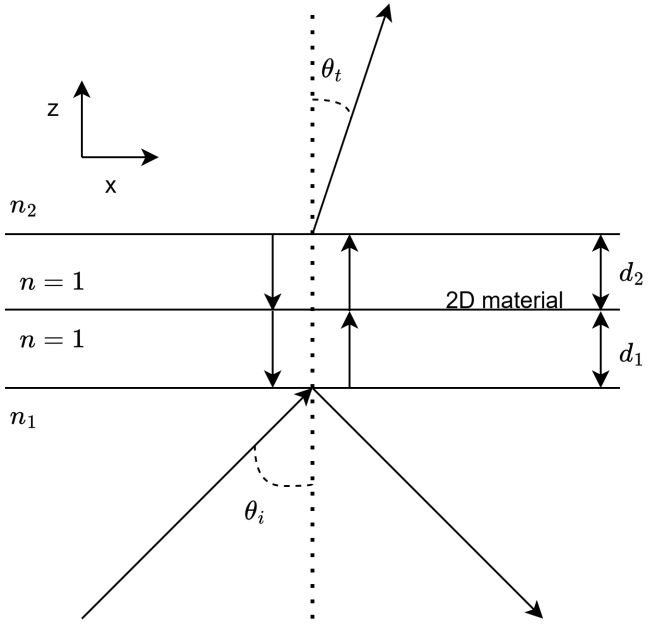


Figure 2.3: Vacuum gap configuration prior to evaluation of the limit.

method does not capture the effect of dielectric screening on the 2D material. As was discussed in the preceding section, screening in the case of distinct dielectric surroundings is not uniquely defined, and so must be introduced manually in this formulation.

Because we are interested in the limits that d_1, $d_2 \to 0$, this problem is neatly captured by a transfer matrix formulation with the propagation matrices omitted. We omit them because with zero distance between each interface, the propagation matrices, defined in equation 1.79, go to identity matrices. This way we can represent the amplitudes of the fields in the first medium in terms of the fields in the final medium as,

$$\begin{pmatrix} a_p \\ a_s \\ r_p \\ r_s \end{pmatrix} = \mathbf{M}_{1,2}\,\mathbf{M}_{2,3}\,\mathbf{M}_{3,4} \begin{pmatrix} t_p \\ t_s \\ 0 \\ 0 \end{pmatrix}. \tag{2.49}$$

$\mathbf{M}_{1,2}$ and $\mathbf{M}_{3,4}$ both describe jumps between vacuum and dielectric with inserted 2D ma-

terial, and so resemble equation 1.78,

$$\mathbf{M}_{1,2} = \frac{1}{2}\begin{bmatrix} \frac{1}{n_1} + \frac{\cos(\theta)}{\cos(\theta_i)} & 0 & \frac{1}{n_1} - \frac{\cos(\theta)}{\cos(\theta_i)} & 0 \\ 0 & 1 + \frac{\cos(\theta)}{n_1\cos(\theta_i)} & 0 & 1 - \frac{\cos(\theta)}{n_1\cos(\theta_i)} \\ \frac{1}{n_1} - \frac{\cos(\theta)}{\cos(\theta_i)} & 0 & \frac{1}{n_1} + \frac{\cos(\theta)}{\cos(\theta_i)} & 0 \\ 0 & 1 - \frac{\cos(\theta)}{n_1\cos(\theta_i)} & 0 & 1 + \frac{\cos(\theta)}{n_1\cos(\theta_i)} \end{bmatrix}, \tag{2.50}$$

and,

$$\mathbf{M}_{3,4} = \frac{1}{2}\begin{bmatrix} n_2 + \frac{\cos(\theta_t)}{\cos(\theta)} & 0 & n_2 - \frac{\cos(\theta_t)}{\cos(\theta)} & 0 \\ 0 & 1 + \frac{n_2\cos(\theta_t)}{\cos(\theta)} & 0 & 1 - \frac{n_2\cos(\theta_t)}{\cos(\theta)} \\ n_2 - \frac{\cos(\theta_t)}{\cos(\theta)} & 0 & n_2 + \frac{\cos(\theta_t)}{\cos(\theta)} & 0 \\ 0 & 1 - \frac{n_2\cos(\theta_t)}{\cos(\theta)} & 0 & 1 + \frac{n_2\cos(\theta_t)}{\cos(\theta)} \end{bmatrix}, \tag{2.51}$$

where θ_i is the incident angle, θ_t is the transmitted angle, and θ is the common vacuum angle, related to the incident and transmitted angles by Snell's law, $n_1 \sin\theta_i = \sin\theta = n_2 \sin\theta_t$. In deriving the transfer matrix for the 2D material, we are explicitly considering plane waves, so the induced current varies only in the $\hat{q}$ direction. This assumption simplifies the boundary condition on the electric fields (equation 2.44) by eliminating the jump in the $\hat{\tau}$ components. The 2D material will be modelled as an infinitesimal current sheet described, in the frequency domain, by the anisotropic conductivity defined in equation 1.89, with σ_z replaced by σ_z^e defined in equation 2.46. Through this conductivity, the material response will be included with a current density defined by Ohm's law,

$$\mathbf{J}^{\mathrm{2D}}(\mathbf{r}_\parallel, \omega, \phi) = \overleftrightarrow{\sigma}(\omega, \phi)\mathbf{E}(\mathbf{r}_\parallel, \omega), \tag{2.52}$$

where in future expressions we will omit both the frequency and ϕ dependence. Following the same process as was used in section 1.4, we calculate the transfer matrix $\mathbf{M}_{2,3}$ from the interface conditions. Because we are assuming the current varies only in the $\hat{q}$ direction, the only new condition is $(\mathbf{E}_3 - \mathbf{E}_2)\cdot\hat{q} = -i/(\omega\epsilon_0)\hat{q}\cdot\nabla_\parallel J_z^e$, which follows equation 2.44. The superscript "e" indicates that the conductivity is screened according to equation 2.46. This equation can be cast in terms of the field amplitudes as

$$(-u_{p3} + d_{p3})\cos\theta - (-u_{p2} + d_{p2})\cos\theta = -\frac{i}{\omega\epsilon_0}\hat{q}\cdot\nabla_\parallel J_z^e(\mathbf{r}_\parallel), \tag{2.53}$$

where,

$$-\frac{i}{\omega\epsilon_0}\hat{q}\cdot\nabla_\parallel J_z^e(\mathbf{r}_\parallel) = \frac{q}{\omega\epsilon_0}J_z^e(\mathbf{r}_\parallel). \tag{2.54}$$

Notice that when the current only varies along the $\hat{q}$ direction, the out-of-plane response only affects the interface condition for p-polarization. We can then recognize that the in-plane component of the wave vector can be related to the vacuum wave number as $q = k_0 \sin\theta$, so,

$$\frac{q}{\omega\epsilon_0} J_z^e(\mathbf{r}_\parallel) = z_0 \sin\theta J_z^e(\mathbf{r}_\parallel). \tag{2.55}$$

For concision in the following equations, we will absorb z_0 into the conductivity, defining $\tilde{\sigma} = z_0\sigma$. Then, inserting into equation 2.53 $J_z^e = \sigma_z^e E_z^{\text{av}}$, which follows from equation 2.46 in vacuum while retaining the dielectric screening on the conductivity,

$$(-u_{p3} + d_{p3})\cos\theta - (-u_{p2} + d_{p2})\cos\theta = \sin\theta\, \tilde{\sigma}_z^e E_z^{\text{av}}(\mathbf{r}_\parallel), \tag{2.56}$$

where E_z^{av} is, in terms of the Fresnel amplitudes defined in equation 1.68,

$$E_z^{\text{av}} = \frac{1}{2}(E_{z2} + E_{z3}) = \frac{1}{2}(u_{p2} + d_{p2} + u_{p3} + d_{p3})\sin\theta, \tag{2.57}$$

where, because the 2D material is in vacuum, the total field in the $\hat{z}$ direction is simply the electric field. Then, taken along with the other standard electromagnetic interface conditions in equations 1.63 and 1.66, we can simply arrange the resulting system of equations such that they satisfy equation 1.73,

$$\mathbf{M}_{2,3} = \begin{bmatrix} -\frac{(\tilde{\sigma}_q\cos\theta+2)(\tilde{\sigma}_z^e\sin^2\theta+2\cos\theta)\sec\theta}{\tilde{\sigma}_q\tilde{\sigma}_z^e\sin^2\theta-4} & \frac{\tilde{\sigma}_c(\tilde{\sigma}_z^e\sin\theta\tan\theta+2)}{\tilde{\sigma}_q\tilde{\sigma}_z^e\sin^2\theta-4} \\ \frac{\tilde{\sigma}_c(\tilde{\sigma}_z^e\sin\theta\tan\theta+2)}{\tilde{\sigma}_q\tilde{\sigma}_z^e\sin^2\theta-4} & \frac{2\tilde{\sigma}_q\tilde{\sigma}_z^e\sin^2\theta-\tilde{\sigma}_z^e(\tilde{\sigma}_c^2-\tilde{\sigma}_q\tilde{\sigma}_\tau)\sin\theta\tan\theta-4\tilde{\sigma}_\tau\sec\theta-8}{2\tilde{\sigma}_q\tilde{\sigma}_z^e\sin^2\theta-8} \\ \frac{-2\tilde{\sigma}_q\cos\theta+2\tilde{\sigma}_z^e\sin\theta\tan\theta}{\tilde{\sigma}_q\tilde{\sigma}_z^e\sin^2\theta-4} & \frac{\tilde{\sigma}_c(\tilde{\sigma}_z^e\sin\theta\tan\theta-2)}{\tilde{\sigma}_q\tilde{\sigma}_z^e\sin^2\theta-4} \\ -\frac{\tilde{\sigma}_c(\tilde{\sigma}_z^e\sin\theta\tan\theta+2)}{\tilde{\sigma}_q\tilde{\sigma}_z^e\sin^2\theta-4} & \frac{(\tilde{\sigma}_z^e(\tilde{\sigma}_c^2-\tilde{\sigma}_q\tilde{\sigma}_\tau)\sin^2\theta+4\tilde{\sigma}_\tau)\sec\theta}{2\tilde{\sigma}_q\tilde{\sigma}_z^e\sin^2\theta-8} \\ \frac{2\tilde{\sigma}_q\cos\theta-2\tilde{\sigma}_z^e\sin\theta\tan\theta}{\tilde{\sigma}_q\tilde{\sigma}_z^e\sin^2\theta-4} & \frac{\tilde{\sigma}_c(\tilde{\sigma}_z^e\sin\theta\tan\theta+2)}{\tilde{\sigma}_q\tilde{\sigma}_z^e\sin^2\theta-4} \\ \frac{\tilde{\sigma}_c(\tilde{\sigma}_z^e\sin\theta\tan\theta-2)}{\tilde{\sigma}_q\tilde{\sigma}_z^e\sin^2\theta-4} & -\frac{(\tilde{\sigma}_z^e(\tilde{\sigma}_c^2-\tilde{\sigma}_q\tilde{\sigma}_\tau)\sin^2\theta+4\tilde{\sigma}_\tau)\sec\theta}{2\tilde{\sigma}_q\tilde{\sigma}_z^e\sin^2\theta-8} \\ -\frac{(\tilde{\sigma}_q\cos\theta-2)(\tilde{\sigma}_z^e\sin^2\theta-2\cos\theta)\sec\theta}{\tilde{\sigma}_q\tilde{\sigma}_z^e\sin^2\theta-4} & \frac{\tilde{\sigma}_c(-\tilde{\sigma}_z^e\sin\theta\tan\theta+2)}{\tilde{\sigma}_q\tilde{\sigma}_z^e\sin^2\theta-4} \\ \frac{\tilde{\sigma}_c(-\tilde{\sigma}_z^e\sin\theta\tan\theta+2)}{\tilde{\sigma}_q\tilde{\sigma}_z^e\sin^2\theta-4} & \frac{2\tilde{\sigma}_q\tilde{\sigma}_z^e\sin^2\theta+\tilde{\sigma}_z^e(\tilde{\sigma}_c^2-\tilde{\sigma}_q\tilde{\sigma}_\tau)\sin\theta\tan\theta+4\tilde{\sigma}_\tau\sec\theta-8}{2\tilde{\sigma}_q\tilde{\sigma}_z^e\sin^2\theta-8} \end{bmatrix}. \tag{2.58}$$

With our matrices defined, we can insert them into equation 2.49. Once done, it is a simple matter of collecting terms to find the Fresnel coefficients for the triple interface configuration shown in figure 2.3, in the limit $d_1, d_2 \to 0$,

$$t_p = -\frac{2n_1\cos\theta_i\left(f_2 f_3 - \tilde{\sigma}_z\tilde{\sigma}_c^2\sin^2\theta\right)}{\Delta} a_p + \frac{4n_1\tilde{\sigma}_c\cos\theta_i\left(n_1\tilde{\sigma}_z^e\sin^2\theta + 2\cos\theta_i\right)}{\Delta} a_s, \tag{2.59}$$

$$t_s = \frac{4n_1\tilde{\sigma}_c\cos\theta_i(n_2\tilde{\sigma}_z^e\sin^2\theta + 2\cos\theta_t)}{\Delta}a_p + \frac{2n_1\cos\theta_i(f_4+4f_1)}{\Delta}a_s, \tag{2.60}$$

$$r_p = \left(1 - \frac{2n_1(4f_2\cos\theta_t + f_2(\tilde{\sigma}_\tau\tilde{\sigma}_q + 4n_2)\tilde{\sigma}_z^e\sin^2\theta - \tilde{\sigma}_z^e\tilde{\sigma}_c^2\cos\theta_t\sin^2\theta)}{\Delta}\right)a_p - \frac{4n_1\sigma_c\cos\theta_i(n_2\sigma_z\sin^2\theta + 2\cos\theta_t)}{\Delta}a_s, \tag{2.61}$$

$$r_s = \frac{4n_1\tilde{\sigma}_c\cos\theta_i(n_2\tilde{\sigma}_z^e\sin^2\theta + 2\cos\theta_t)}{\Delta}a_p + \left(-1 + \frac{2n_1\cos\theta_i(f_4+4f_1)}{\Delta}\right)a_s, \tag{2.62}$$

where we defined the following expressions for brevity,

$$f_1 = n_1\cos\theta_t + n_2\cos\theta_i + \tilde{\sigma}_q\cos\theta_t\cos\theta_i, \tag{2.63}$$
$$f_2 = n_1\cos\theta_i + n_2\cos\theta_t + \tilde{\sigma}_\tau, \tag{2.64}$$
$$f_3 = \sin^2\theta\sigma_q\tilde{\sigma}_z^e - 4 \tag{2.65}$$
$$f_4 = \sin^2\theta((n_2\cos\theta_i + n_1\cos\theta_t)\tilde{\sigma}_q + 4n_1n_2)\tilde{\sigma}_z^e, \tag{2.66}$$

and,

$$\Delta = (f_4+4f_1)f_2 - (\tilde{\sigma}_z^e\sin^2\theta(n_2\cos\theta_i + n_1\cos\theta_t) + 4\cos\theta_i\cos\theta_t)\tilde{\sigma}_c^2 \tag{2.67}$$

The factors f_1 and f_2 appear in the standard in-plane case with anisotropic conductivity [1], however, we introduce the additional terms f_3 and f_4 to simplify the additional complexities introduced by the out-of-plane current. To identify the appropriate boundary condition to be used for a true single interface surrounded by media with no gaps, we will make a comparison between the field amplitudes as a result of the triple interface vacuum gap configuration, and that of a true single interface. Through this comparison, we will identify the necessary adjustments to the boundary condition on the single interface such that it matches the result from the vacuum gap method.

In essence, we reverse engineer the appropriate condition for the single interface from the multi-interface vacuum gap result. As the point of comparison, we shall use the jump in the electric fields across the interface. Using the Fresnel amplitudes defined in equations 2.59-2.62, the jump in $\hat{q}$ component of the electric field can be cast entirely in terms of the transmitted field amplitudes,

$$\left(\mathbf{E}_2(\mathbf{r}_\parallel) - \mathbf{E}_1(\mathbf{r}_\parallel)\right)\cdot\hat{q} = -\frac{2\sin^2\theta\tilde{\sigma}_z^e\left((\cos\theta_t\tilde{\sigma}_q + 2n_2)\,t_p - t_s\tilde{\sigma}_c\right)}{\sin^2\theta\tilde{\sigma}_q\tilde{\sigma}_z^e - 4}. \tag{2.68}$$

This is the effective interface condition on the triple interface setup in the limit of zero vacuum gap. Next, we repeat the preceding Fresnel analysis, though this time for a true single interface. We calculate the Fresnel coefficients and then compare the resulting difference in fields to equation 2.68. As it turns out, the necessary condition for the single interface to match the vacuum gap method is,

$$\begin{aligned}\big(\mathbf{E}_2(\mathbf{r}_\parallel) - \mathbf{E}_1(\mathbf{r}_\parallel)\big)\cdot\hat{q} &= \frac{q}{2\epsilon_0\omega}\sigma_z^e\left(n_1^2E_{z1} + n_2^2E_{z2}\right) &(2.69)\\ &= \frac{\sin\theta}{2}\tilde{\sigma}_z^e\left(n_1^2E_{z1} + n_2^2E_{z2}\right) &(2.70)\\ &= \frac{\sin\theta}{2\epsilon_0}\tilde{\sigma}_z^e\left(\epsilon_1E_{z1} + \epsilon_2E_{z2}\right) &(2.71)\\ &= \sin\theta\tilde{\sigma}_z^e\frac{D_z^{\text{av}}}{\epsilon_0}, &(2.72)\end{aligned}$$

where in the second line $q = k_0\sin\theta$ and $z_0 = 1/(\epsilon_0 c)$ were used to introduce the scaled conductivity $\tilde{\sigma}_z = z_0\sigma_z$, and $\sigma_z^e = (\epsilon_0/2)(1/\epsilon_1 + 1/\epsilon_2)\sigma_z$ which indicates screening by the harmonic mean of the surrounding dielectric constants, as was established in section 2.2. So, we have found that the only modification to the interface condition from the inclusion of surrounding media, aside from the screening of the out-of-plane conductivity, is to modify the form of the total electric field in the $\hat{z}$ direction at the interface. This effectively replaces the arithmetic mean E_z^{av} by the arithmetic mean of the displacement fields, $D_z^{\text{av}}/\epsilon_0$ as was initially suggested in equation 2.11.

2.4 Dispersion of interface plasmons

The introduction of a new boundary condition also introduces the possibility of new interface plasmons. Plasmon states are self-sustaining electromagnetic solutions that remain confined to the interface, either propagating or remaining localized. We can solve for the dispersion relation of these interface states simply by omitting the incident wave and solving the interface conditions [4] [43]. Consider an interface like that of figure 2.2, though with surrounding electromagnetic fields given by,

$$\mathbf{E}_1 = \begin{pmatrix} E_q^{(1)} \\ E_\tau^{(1)} \\ E_z^{(1)} \end{pmatrix} e^{i(qx - k_{z1}z - \omega t)}, \tag{2.73}$$

and,

$$\mathbf{E}_2 = \begin{pmatrix} E_q^{(2)} \\ E_\tau^{(2)} \\ E_z^{(2)} \end{pmatrix} e^{i(qx+k_{z2}z-\omega t)}, \tag{2.74}$$

and magnetic fields are given by,

$$\mathbf{H}_1 = \begin{pmatrix} H_q^{(1)} \\ H_\tau^{(1)} \\ H_z^{(1)} \end{pmatrix} e^{i(qx-k_{z1}z-\omega t)}, \tag{2.75}$$

and,

$$\mathbf{H}_2 = \begin{pmatrix} H_q^{(2)} \\ H_\tau^{(2)} \\ H_z^{(2)} \end{pmatrix} e^{i(qx+k_{z2}z-\omega t)}. \tag{2.76}$$

By choosing this sign convention for the k_z components of the wavevectors, we also assert the condition that the imaginary part must be positive for any solutions to be physical. If this condition is not satisfied, the solutions would be exponentially growing.

Based on the analysis in sections 2.1 and 2.3, the interface conditions of interest for a 2D material surrounded by non-magnetic, isotropic, lossless dielectrics are,

$$\left(\mathbf{E}_2(\mathbf{r}_\parallel) - \mathbf{E}_1(\mathbf{r}_\parallel)\right) \cdot \hat{q} = \frac{q}{2\epsilon_0\omega}\tilde{\sigma}_z^e \left(n_1^2 E_{z1} + n_2^2 E_{z2}\right), \tag{2.77}$$

$$\left(\mathbf{E}_2(\mathbf{r}_\parallel) - \mathbf{E}_1(\mathbf{r}_\parallel)\right) \cdot \hat{\tau} = 0, \tag{2.78}$$

$$\mathbf{H}_2(\mathbf{r}_\parallel) - \mathbf{H}_1(\mathbf{r}_\parallel) = \hat{z} \times \mathbf{J}(\mathbf{r}_\parallel). \tag{2.79}$$

The first step in deriving the dispersion relation is to represent the boundary conditions in terms of independent field quantities. The relationships between mutually dependent field quantities can be derived through substitution of equations 2.73 to 2.76 into Maxwell's equations. In a region with no external or singular induced charges or currents, equation 1.38 becomes,

$$iqE_q^{(j)} e^{i(qx\pm k_{zj}z-\omega t)} \pm ik_{zj}E_z^{(j)} e^{i(qx\pm k_{zj}z-\omega t)} = 0, \tag{2.80}$$

$$E_z^{(j)} = \mp\frac{q}{k_{zj}} E_q^{(j)}, \tag{2.81}$$

and equation 1.41 becomes,

$$\begin{pmatrix} \mp ik_{zj}E_\tau^{(j)}e^{i(qx\pm k_{zj}z-\omega t)} \\ \pm ik_{zj}E_q^{(j)}e^{i(qx\pm k_{zj}z-\omega t)} - iqE_z^{(j)}e^{i(qx\pm k_{zj}z-\omega t)} \\ iqE_\tau^{(j)}e^{i(qx\pm k_{zj}z-\omega t)} \end{pmatrix} = i\mu_0\omega \begin{pmatrix} H_q^{(j)}e^{i(qx\pm k_{zj}z-\omega t)} \\ H_\tau^{(j)}e^{i(qx\pm k_{zj}z-\omega t)} \\ H_z^{(j)}e^{i(qx\pm k_{zj}z-\omega t)} \end{pmatrix}, \tag{2.82}$$

$$\begin{pmatrix} H_q^{(j)} \\ H_\tau^{(j)} \\ H_z^{(j)} \end{pmatrix} = \begin{pmatrix} \mp\frac{k_{zj}}{\mu_0\omega}E_\tau^{(j)} \\ -\frac{1}{\mu_0\omega}(\mp k_{zj}E_q^{(j)} + qE_z^{(j)}) \\ \frac{q}{\mu_0\omega}E_\tau^{(j)} \end{pmatrix}, \tag{2.83}$$

where k_{zj} is positive in region $j = 1$ and negative in region $j = 2$. Considering first the simpler case of vacuum surroundings with $n_1 = n_2 = 1$ and $k_{z1} = k_{z2} = k_z$, insertion of equation 2.81 into equation 2.77 yields,

$$E_q^{(2)} - E_q^{(1)} = -\frac{z_0 q^2 \tilde{\sigma}_z}{2k_0 k_z}(E_q^{(2)} - E_q^{(1)}), \tag{2.84}$$

$$\left(1 + \frac{q^2\tilde{\sigma}_z}{2k_0k_z}\right)E_q^{(2)} - \left(1 + \frac{q^2\tilde{\sigma}_z}{2k_0k_z}\right)E_q^{(1)} = 0 \tag{2.85}$$

where the substitution $\omega\epsilon_0 = k_0/z_0$ was used, and $\tilde{\sigma_z} = z_0\sigma_z$. Next, equation 2.78 gives

$$E_\tau^{(2)} = E_\tau^{(1)}. \tag{2.86}$$

The continuity of the $\hat{\tau}$ component of the electric field can be used to simplify the magnetic field condition 2.79. Applying equation 2.83 to the $\hat{\tau}$ component of equation 2.78 yields,

$$-\frac{k_z}{k_0}(E_\tau^{(2)} + E_\tau^{(1)}) = \frac{1}{2}\tilde{\sigma}_\tau(E_\tau^{(2)} + E_\tau^{(1)}), \tag{2.87}$$

where the substitutions $\mu_0 = z_0/c$ and $k_0 = \omega/c$ were applied. Application of equation 2.86 yields,

$$-\frac{k_z}{k_0}E_\tau^{(1)} = \frac{1}{2}\tilde{\sigma}_\tau E_\tau^{(1)}, \tag{2.88}$$

$$-\left(\tilde{\sigma}_\tau + \frac{2k_z}{k_0}\right)E_\tau^{(1)} = 0. \tag{2.89}$$

Then, applying equations 2.81 and 2.83 to the $\hat{q}$ component of equation 2.79,

$$\frac{k_0}{k_z}(E_q^{(2)} + E_q^{(1)}) = -\frac{\tilde{\sigma}_q}{2}(E_q^{(2)} + E_q^{(1)}), \tag{2.90}$$

$$\left(\frac{k_0}{k_z} + \frac{\tilde{\sigma}_q}{2}\right)E_q^{(2)} + \left(\frac{k_0}{k_z} + \frac{\tilde{\sigma}_q}{2}\right)E_q^{(1)} = 0, \tag{2.91}$$

where the substitutions $\mu_0 = z_0/c$, $k_0 = \omega/c$, and $q^2 + k_z^2 = k_0^2$ were applied. Between equations 2.85, 2.89, and 2.91, we have a homogeneous system of three equations and three unknowns in the field amplitudes. A system of this kind can be represented as a matrix,

$$\begin{bmatrix} 0 & 0 & -\frac{2k_z}{k_0} - \tilde{\sigma}_\tau \\ \frac{k_0}{k_z} + \frac{\tilde{\sigma}_q}{2} & \frac{k_0}{k_z} + \frac{\tilde{\sigma}_q}{2} & 0 \\ -1 - \frac{q^2\tilde{\sigma}_z}{2k_0k_z} & 1 + \frac{q^2\tilde{\sigma}_z}{2k_0k_z} & 0 \end{bmatrix} \begin{pmatrix} E_q^{(1)} \\ E_q^{(2)} \\ E_\tau^{(1)} \end{pmatrix} = \begin{pmatrix} 0 \\ 0 \\ 0 \end{pmatrix}. \tag{2.92}$$

For physically meaningful solutions, the field amplitudes need to be non-zero. The condition for non-trivial solutions on a system of homogeneous equations such as this is that the determinant of the coefficient matrix be zero. This is equivalent to the statement that the system is linearly dependent. Linear dependency means the system has infinitely many solutions with non-zero field amplitudes.

The determinant of the coefficient matrix 2.92 is,

$$\det \begin{bmatrix} 0 & 0 & -\frac{2k_z}{k_0} - \tilde{\sigma}_\tau \\ \frac{k_0}{k_z} + \frac{\tilde{\sigma}_q}{2} & \frac{k_0}{k_z} + \frac{\tilde{\sigma}_q}{2} & 0 \\ -1 - \frac{q^2\tilde{\sigma}_z}{2k_0k_z} & 1 + \frac{q^2\tilde{\sigma}_z}{2k_0k_z} & 0 \end{bmatrix} = -\frac{(\tilde{\sigma}_q k_z + 2k_0)(\tilde{\sigma}_\tau k_0 + 2k_z)(q^2\tilde{\sigma}_z + 2k_0k_z)}{2k_z^2k_0^2}. \tag{2.93}$$

So, the condition on non-trivial solutions is,

$$(\tilde{\sigma}_q k_z + 2k_0)(\tilde{\sigma}_\tau k_0 + 2k_z)(q^2\tilde{\sigma}_z + 2k_0k_z) = 0. \tag{2.94}$$

Eliminating k_z by substituting in $k_z = \sqrt{k_0^2 - q^2}$, and then solving for q yields

$$q = \pm k_0 \frac{\sqrt{\tilde{\sigma}_q^2 - 4}}{\tilde{\sigma}_q}, \pm\frac{k_0}{2}\sqrt{4 - \tilde{\sigma}_\tau^2}, \pm k_0 \frac{\sqrt{2}\sqrt{-1 \pm \sqrt{\tilde{\sigma}_z^2 + 1}}}{\tilde{\sigma}_z}. \tag{2.95}$$

This result indicates that for in-plane isotropic 2D materials suspended in vacuum, there are three distinct, decoupled, surface modes coming from each of the conductivity components. The in-plane modes are both well established [56], however, the out-of-plane mode is not. While these modes are technically allowed given the idealized geometry and classical description, any relationship to actual plasmons will depend on the properties of a particular material. Graphene, for example, only supports plasmons at low frequencies [44]. At higher frequencies, there emerge significant losses which serve to suppress plasmon resonance. However, in the appropriate low-frequency region, the plasmon dispersion relation is proportional to the square root of the wavenumber q. In section 1.6, graphene was discussed as having a conductivity, in the low-frequency regime, well described by a

Drude model. Using these facts, we can show that the derived in-plane longitudinal mode shown in equation 2.95 correctly predicts the graphene plasmon dispersion relation in the THz region.

Consider the in-plane longitudinal mode,

$$\tilde{\sigma}_q k_z + 2k_0 = 0. \tag{2.96}$$

Then, defining the in-plane longitudinal conductivity as a Drude model,

$$\tilde{\sigma}_q = \frac{i}{\pi}\frac{\omega_F'}{\omega + i\tau_f^{-1}} = \frac{i}{\pi}\frac{\omega_F}{\omega + i\tau_f^{-1}}\left(\frac{4\pi v_B}{c}\right), \tag{2.97}$$

where the substitutions $\omega_F' = 4\pi\alpha\omega_F$, and $\alpha = v_B/c$ were used, with $\omega_F = E_F/\hbar$ and v_B as the Bohr speed. We can then consider the lossless ($\tau_f \to \infty$) non-retarded limit ($c \to \infty$), where the dispersion relation simplifies to

$$-4\omega_F v_B q + 2\omega^2 = 0. \tag{2.98}$$

Solving for ω results in the famous square root relationship found across the literature [56] [44],

$$\omega = \sqrt{2v_B\omega_F}\sqrt{q}. \tag{2.99}$$

So, the longitudinal surface mode derived using the classical interface conditions matches with well-accepted plasmon behaviour for graphene, in the appropriate limits. At the same time, using the same Drude model for the transverse conductivity gives no plasmon modes.

The nature of out-of-plane response in 2D materials is something of an open problem. As a consequence, the relationship between out-of-plane response and plasmonics remains unclear. However, if one wanted to find an analytical expression for the dispersion relation of the out-of-plane mode, the first choice would be to simply follow the same process as with the in-plane mode. While there is much less research published regarding out-of-plane conductivity in graphene, and to the author's knowledge none regarding analytical models, a reasonable first guess could be a Lorentz model. Lorentz conductivity models are derived based on principles of classical oscillators, and so are associated with electrons that remain localized. In the long wavelength limit, graphene as a 2D material has essentially no out-of-plane direction for electrons to propagate. This could mean their out-of-plane behaviour is well described by a localized electron model like the Lorentzian.

In the non-retarded limit the out-of-plane dispersion relation becomes

$$2i\omega\epsilon_0 + q\sigma_z = 0. \tag{2.100}$$

Next, the out-of-plane conductivity is defined as a Lorentzian,

$$\sigma_z = \frac{i}{\pi}\frac{\omega S_b}{\omega^2 - \omega_b^2 + i\omega\tau_f^{-1}}. \tag{2.101}$$

We consider the limit that the frequency is small and define the lossless conductivity as,

$$\sigma_z = -\frac{i}{\pi}\frac{\omega S_b}{\omega_b^2}. \tag{2.102}$$

Then, substituting this conductivity into equation 2.100, the factor of ω cancels and so there is no longer a continuum of states, meaning there is no out-of-plane plasmon mode. So, the same process that produced an accurate dispersion relation for the in-plane plasmon mode, predicts that the out-of-plane mode appears to not correspond to a plasmon.

This same process for finding the interface modes can be applied to the case with material surroundings. When a 2D material is surrounded by non-magnetic, isotropic, lossless dielectrics, the system of equations describing interface states is given by,

$$\begin{bmatrix} 0 & 0 & -\frac{k_{z2}}{n_2 k_0} - \frac{k_{z1}}{n_1 k_0} - \tilde{\sigma}_\tau \\ \frac{n_1 k_0}{k_{z1}} + \frac{\tilde{\sigma}_q}{2} & \frac{n_2 k_0}{k_{z2}} + \frac{\tilde{\sigma}_q}{2} & 0 \\ -1 - \frac{n_1^2 q^2 \tilde{\sigma}_z^e}{2k_0 k_{z1}} & 1 + \frac{n_2^2 q^2 \tilde{\sigma}_z^e}{2k_0 k_{z2}} & 0 \end{bmatrix} \begin{pmatrix} E_q^{(1)} \\ E_q^{(2)} \\ E_\tau^{(1)} \end{pmatrix} = \begin{pmatrix} 0 \\ 0 \\ 0 \end{pmatrix}. \tag{2.103}$$

The determinant in this case is far more complex, though it can be collected into two primary factors,

$$\det \begin{bmatrix} 0 & 0 & -\frac{k_{z2}}{n_2 k_0} - \frac{k_{z1}}{n_1 k_0} - \tilde{\sigma}_\tau \\ \frac{n_1 k_0}{k_{z1}} + \frac{\tilde{\sigma}_q}{2} & \frac{n_2 k_0}{k_{z2}} + \frac{\tilde{\sigma}_q}{2} & 0 \\ -1 - \frac{n_1^2 q^2 \tilde{\sigma}_z^e}{2k_0 k_{z1}} & 1 + \frac{n_2^2 q^2 \tilde{\sigma}_z^e}{2k_0 k_{z2}} & 0 \end{bmatrix} = -\frac{AB}{4k_0^2 k_{z1} k_{z2}}, \tag{2.104}$$

where

$$A = k_0\tilde{\sigma}_\tau + k_{z1} + k_{z2}, \tag{2.105}$$

and,

$$B = q^2\tilde{\sigma}_q\tilde{\sigma}_z^e(n_2^2 k_{z1} + n_1^2 k_{z2}) + 4k_0(n_1^2 n_2^2 q^2 \tilde{\sigma}_z^e + k_{z1}k_{z2}\tilde{\sigma}_q) + 4k_0^2(n_2^2 k_{z1} + n_1^2 k_{z2}). \tag{2.106}$$

The solutions in this case have changed dramatically. Even before solving for q, it is clear that only the σ_τ contribution remains decoupled. Inserting in the conditions $k_{z1} =$

$\sqrt{n_1^2 k_0^2 - q^2}$, $k_{z2} = \sqrt{n_2^2 k_0^2 - q^2}$, and then solving $AB = 0$ for q results in 14 solutions. The decoupled τ part contributes two of these solutions from $A = 0$ in the form,

$$q = \pm k_0 \frac{\sqrt{-\tilde{\sigma}_\tau^4 + 2(n_1^2 + n_2^2)\tilde{\sigma}_\tau^2 - (n_1 - n_2)^2(n_1 + n_2)^2}}{2\tilde{\sigma}_\tau}. \tag{2.107}$$

The new solution for τ with material surroundings is clearly a direct modification of the vacuum case. In the limit that $n_1, n_2 \to 1$, this mode converges to the τ mode in equation 2.95. The other 12 solutions are contributed by the solutions to $B = 0$, which can be represented exactly as the roots of a 12^{th} order polynomial. It is important to note that the existence of these 12 solutions does not imply the existence of 12 new plasmon modes. Some of these solutions will correspond to unphysical combinations of signs on complex q solutions; for example, a positive real and negative imaginary part would correspond to an exponential growth along the propagation direction. Others still may in fact combine to form a single true solution branch. Regardless, the exact solutions depend on a combination of σ_z and σ_q contributions, indicating that the inclusion of dielectric surroundings serves to hybridize the in-plane longitudinal and out-of-plane modes. However, it is not simply the presence of surrounding dielectrics that induces hybridization, but the difference between the two surrounding materials. When the materials are the same, $n_1 = n_2 = n$, the two modes decouple, and B can be factored as,

$$B = (q^2\tilde{\sigma}_z + 2k_0 k_z)(2k_0 n^2 + k_z\tilde{\sigma}_q), \tag{2.108}$$

where the effective out-of-plane conductivity $\tilde{\sigma}_z^e$ was replaced by the uncontroversial value for total immersion in a dielectric, $\tilde{\sigma}_z^e = \tilde{\sigma}_z/n^2$. On the surface, this result does match with experimental findings. It is true that surface modes of 2D materials will hybridize with other nearby surface modes on 2D materials, interfaces, or even their own image in a conductor [57]. Some important questions to consider include the identification of the boundaries of this hybridization, for example under what limiting cases, besides matched materials, does decoupling return? A detailed analysis of this hybridization will be left for future work.

A final note is that the dispersion relation factors shown in equations 2.105 and 2.106 are the denominators of the Fresnel amplitudes derived in section 2.3 when the conductivity is isotropic in the plane. The denominators of the s-polarized components map to the transverse (σ_τ) dispersion relation, while the denominators of the p-polarized components map to the hybridized (σ_z & σ_q) dispersion relation. The common denominator of the general Fresnel coefficients is defined in equation 2.67. This equation simplifies in this case of isotropic in-plane conductivity with $\sigma_c = 0$ to give a common denominator Δ defined by

$$\Delta = (f_4 + 4f_1)f_2, \tag{2.109}$$

where f_1, f_2, and f_4 are defined in equations 2.63, 2.64, and 2.66, respectively.

In the numerators of the s-polarized Fresnel amplitudes defined in equations 2.59-2.62, there is a factor of $f_4 + 4f_1$, which cancels with the factor in the common denominator Δ to give a new denominator for the s-polarized components of

$$\tilde{\sigma}_\tau + n_2 \cos\theta_t + n_1 \cos\theta_i. \tag{2.110}$$

Using the substitutions $\cos\theta_i = k_{z1}/(n_1 k_0)$ and $\cos\theta_t = k_{z2}/(n_2 k_0)$,

$$\tilde{\sigma}_\tau + \frac{k_{z2}}{k_0} + \frac{k_{z1}}{k_0}, \tag{2.111}$$

and finally multiplying by k_0 we can see the relationship between the denominator and the dispersion relation in equation 2.105 is that of a scalar multiple,

$$k_0 A = \tilde{\sigma}_\tau + n_2 \cos\theta_t + n_1 \cos\theta_i. \tag{2.112}$$

The same argument can be made for the hybridized mode dispersion relation in equation 2.106. In this case, the numerators of the p-polarized components defined in equations 2.59-2.62 contain factors of f_2 which cancel with the factor in Δ to give a new p-polarized denominator of

$$\tilde{\sigma}_q \tilde{\sigma}_z^e \sin^2\theta \,(n_2 \cos\theta_i + n_1 \cos\theta_t) + 4 n_1 n_2 \tilde{\sigma}_z^e \sin^2\theta + 4\tilde{\sigma}_q \cos\theta_i \cos\theta_t + 4 n_2 \cos\theta_i + 4 n_1 \cos\theta_t. \tag{2.113}$$

Again, the similarities to the dispersion relation are immediately obvious. However, following through the same substitutions of $\cos\theta_i = k_{z1}/(n_1 k_0)$ and $\cos\theta_t = k_{z2}/(n_2 k_0)$, though this time also with $\sin\theta = q/k_0$, the relationship to the dispersion relation in equation 2.106 is again a simple scalar multiple,

$$\begin{aligned} & n_1 n_2 k_0^3 B \\ &= \tilde{\sigma}_q \tilde{\sigma}_z^e \sin^2\theta \,(n_2 \cos\theta_i + n_1 \cos\theta_t) + 4 n_1 n_2 \tilde{\sigma}_z^e \sin^2\theta + 4\tilde{\sigma}_q \cos\theta_i \cos\theta_t + 4 n_2 \cos\theta_i + 4 n_1 \cos\theta_t. \end{aligned} \tag{2.114}$$

Chapter 3

Conservation of energy and momentum

The conservation of energy and linear momentum, while something of a textbook problem, remains an extremely useful tool for analyzing physical systems, especially ones as idealized as an infinite flat interface occupied by a 2D material. In addition, calculations of the momentum transfer to such structures are relevant for applications in, for example, nano-optomechanical devices and sensors. In performing these calculations for energy conservation, we shall study the losses in 2D materials in order to:

- verify how evanescence modifies losses,
- identify how the out-of-plane response condition contributes to losses,
- identify how surrounding dielectrics modify losses,
- confirm the form of reflectance, transmittance and absorption in light of out-of-plane contributions,

while for the conservation of linear momentum, we shall study the surface forces on the 2D material in order to,

- identify how evanescent fields contribute to surface forces,
- identify how surrounding media contribute to surface forces,
- identify how the out-of-plane response contributes to surface forces,

- identify what stress tensor is appropriate for use with surrounding media through the vacuum gap method.

This last objective is somewhat controversial as it touches on the century-old Abraham-Minkowski controversy. The Abraham-Minkowski controversy is a debate over the correct form for electromagnetic momentum in media and has been ongoing for more than a century. Broadly speaking, the controversy can be summarized as follows. In vacuum, any momentum associated with an electromagnetic wave is possessed by that wave; in matter, an electromagnetic wave has some amount of momentum intrinsic to itself, but there is also a contribution from the reaction of the surrounding material. It is the correct dispensation of total momentum between field and material contributions that remains controversial [58]. The different proposals for the "correct" momentum are generally accompanied by an electromagnetic stress-energy tensor. The most famous of these are the Abraham and Minkowski tensors [59], though others exist [60]. Here we will not delve too deeply into the details of this debate. We will, however, use the techniques developed throughout this work to identify what stress tensor satisfies conservation of linear momentum in this specific case. Also important to note is that in the following calculations, we are considering purely real fields modelled as the real part of the complex fields,

$$\mathbf{E}_r = \frac{1}{2}(\mathbf{E}_c + \mathbf{E}_c^*). \tag{3.1}$$

3.1 Basic equations

In differential form, conservation of electromagnetic energy associated with the singular distribution of charges induced at the interface is given by [61]

$$-\mathbf{J}^s(\mathbf{r},t)\cdot\mathbf{E}^{av}(\mathbf{r},t) = \nabla\cdot\mathbf{S}(\mathbf{r},t) + \frac{\partial u}{\partial t}(\mathbf{r},t), \tag{3.2}$$

where $\mathbf{S}$ is the Poynting vector,

$$\mathbf{S}(\mathbf{r},t) = \mathbf{E}(\mathbf{r},t)\times\mathbf{H}(\mathbf{r},t), \tag{3.3}$$

u is the total energy density and is defined in vacuum by

$$u(\mathbf{r},t) = \frac{1}{2}(\epsilon_0\mathbf{E}(\mathbf{r},t)\cdot\mathbf{E}(\mathbf{r},t) + \mu_0\mathbf{H}(\mathbf{r},t)\cdot\mathbf{H}(\mathbf{r},t)), \tag{3.4}$$

$\mathbf{J}^s$ is the singular induced current in the 2D material, defined by

$$\mathbf{J}^s(\mathbf{r},t) = \mathbf{J}^{2D}(\mathbf{r}_\parallel,t)\delta(z) = \begin{pmatrix} J_q(\mathbf{r},t) \\ J_\tau(\mathbf{r},t) \\ J_z^e(\mathbf{r},t) \end{pmatrix} \delta(z), \tag{3.5}$$

and $\mathbf{E}^{av}$ is the total field at the interface ($z = 0$), modelled by the arithmetic mean of the fields on each side. Note that the out-of-plane current is the effective screened quantity defined in equation 2.47. This is necessary to satisfy conservation of energy, which we will verify numerically in the following analysis. The dependencies on position and time variables will be omitted in the integral expressions for concision. To consider the interface as a whole, we will average in time and integrate in space over a Gaussian pillbox with volume Ω,

$$\frac{1}{T}\int_{-T/2}^{T/2} dt \iiint_\Omega d^3\mathbf{r}\ (-\mathbf{J}^s \cdot \mathbf{E}^{av}) = \frac{1}{T}\int_{-T/2}^{T/2} dt \iiint_\Omega d^3\mathbf{r}\left[\nabla\cdot\mathbf{S} + \frac{\partial u}{\partial t}\right], \tag{3.6}$$

where the time derivative of the energy density u goes to zero in the average. To the remaining Poynting vector term on the right-hand side, we can apply divergence theorem,

$$\frac{1}{T}\int_{-T/2}^{T/2} dt \iiint_\Omega d^3\mathbf{r}\ (\nabla\cdot\mathbf{S}) = \frac{1}{T}\int_{-T/2}^{T/2} dt \iint_{\partial\Omega} dS\ (\mathbf{S}\cdot\hat{n})\,. \tag{3.7}$$

If we then consider the pillbox Ω to have a large extent in the in-plane direction, presumably covering the interface D, then the surface $\partial\Omega$ can be approximated by two parallel planes with spatial extents defined by D,

$$\frac{1}{T}\int_{-T/2}^{T/2} dt \iint_{\partial\Omega} dS\ (\mathbf{S}\cdot\hat{n}) \approx \frac{1}{T}\int_{-T/2}^{T/2} dt \iint_D d^2\mathbf{r}_\parallel \left(\mathbf{S}\cdot\hat{z}\big|_{z_1}^{z_2}\right), \tag{3.8}$$

where $z_{1/2}$ are the positions of the parallel planes relative to the interface. As before, we will define the polarization of the 2D material as a singular current density related to the electric field response function by equation 1.28, described here as a conductivity. We are only considering local response, so in the frequency domain, this relationship takes the form of a vector Ohm's law,

$$\mathbf{J}^s(\mathbf{r},\omega) = \mathbf{J}^{2D}(\mathbf{r}_\parallel,\omega)\delta(z) = \overleftrightarrow{\sigma}(\omega)\mathbf{E}^{av}(\mathbf{r}_\parallel,\omega)\,\delta(z), \tag{3.9}$$

where the total field, modelled as the arithmetic mean, is the same as that which acts on the singular current, as was discussed in section 2. Inserting equation 3.9 into the left-hand

side of equation 3.6,

$$\frac{1}{T}\int_{-T/2}^{T/2} dt \iiint_{\Omega} d^3\mathbf{r}\ \left(-\mathbf{J}^s \cdot \mathbf{E}^{av}\right) = \frac{1}{T}\int_{-T/2}^{T/2} dt \iint_{D} d^2\mathbf{r}_{\parallel}\ \left(-\mathbf{J}^{2D} \cdot \mathbf{E}^{av}\right). \tag{3.10}$$

Equation 3.10 and 3.8 can then be equated to recreate the integral form of conservation of energy for an interface containing a singular current sheet,

$$\frac{1}{T}\int_{-T/2}^{T/2} dt\, \frac{1}{L_q L_\tau} \iint_{D} d^2\mathbf{r}_{\parallel}\ \left(-\mathbf{J}^{2D} \cdot \mathbf{E}^{av}\right) = \frac{1}{T}\int_{-T/2}^{T/2} dt\, \frac{1}{L_q L_\tau} \iint_{D} d^2\mathbf{r}_{\parallel}\ \left(\mathbf{S} \cdot \hat{z}|_{z_1}^{z_2}\right), \tag{3.11}$$

where we divided each integral by the area of the region D, defined by the length scales L_q, and L_τ. This is necessary because we are specifically interested in electromagnetic plane waves, and due to their infinite extent, we can only work in average quantities. Integration over products of purely real plane waves, such as we have here, can be equivalently represented by the real part of conjugate products of complex plane waves in the Fourier domain,

$$\frac{1}{T}\int_{-T/2}^{T/2} dt \frac{1}{L_q L_\tau} \iint_{D} d^2\mathbf{r}_{\parallel}\ \left(A_i(\mathbf{r}_{\parallel}, t) B_j(\mathbf{r}_{\parallel}, t)\right) = \frac{1}{2}\Re(f_{0i}(\mathbf{q}_0, \omega_0) g^*_{0j}(\mathbf{q}_0, \omega_0)), \tag{3.12}$$

when the real and complex fields are related by,

$$\mathbf{A}(\mathbf{r}_{\parallel}, t) = \frac{1}{2}(\mathbf{f}(\mathbf{r}_{\parallel}, t) + \mathbf{f}^*(\mathbf{r}_{\parallel}, t)), \tag{3.13}$$

and,

$$\mathbf{B}(\mathbf{r}_{\parallel}, t) = \frac{1}{2}(\mathbf{g}(\mathbf{r}_{\parallel}, t) + \mathbf{g}^*(\mathbf{r}_{\parallel}, t)), \tag{3.14}$$

where $f_{0i}(\mathbf{q}, \omega)$ and $g_{0j}(\mathbf{q}, \omega)$ are the amplitudes in the Fourier domain of the complex monochromatic plane waves $\mathbf{f}$ and $\mathbf{g}$, respectively, in cartesian directions i and j. These plane waves are defined in the Fourier domain as,

$$\mathbf{f}(\mathbf{q}, \omega) = (2\pi)^3 \mathbf{f}_0(\mathbf{q}, \omega)\delta(\mathbf{q} - \mathbf{q}_0)\delta(\omega - \omega_0)e^{ik_{zf}z}, \quad \mathbf{g}(\mathbf{q}, \omega) = (2\pi)^3 \mathbf{g}_0(\mathbf{q}, \omega)\delta(\mathbf{q} - \mathbf{q}_0)\delta(\omega - \omega_0)e^{ik_{zg}z}, \tag{3.15}$$

which corresponds to monochromatic plane waves in the real domain, defined by

$$\mathbf{f}(\mathbf{r}, t) = \mathbf{f}_0(\mathbf{q}_0, \omega_0)e^{i(\mathbf{q}_0 \cdot \mathbf{r}_{\parallel} - \omega_0 t)}e^{ik_{zf}z}, \qquad \mathbf{g}(\mathbf{r}, t) = \mathbf{g}_0(\mathbf{q}_0, \omega_0)e^{i(\mathbf{q}_0 \cdot \mathbf{r}_{\parallel} - \omega_0 t)}e^{ik_{zg}z}. \tag{3.16}$$

Going forward, the 0 subscript will be left off of the wave vector and frequency components. The integral relationship to Fourier domain amplitudes is derived in detail in Appendix

B. Applying equation 3.12 to equation 3.11 transforms the integral expression for energy conservation into

$$-\frac{1}{2}\Re\left(\mathbf{J}_0^{\mathrm{2D}}(\mathbf{q},\omega)\cdot\mathbf{E}_0^{av*}(\mathbf{q},\omega)\right)=\frac{1}{2}\Re\left(\mathbf{E}_0(\mathbf{q},\omega)\times\mathbf{H}_0^{*}(\mathbf{q},\omega)\right)\cdot\hat{z}\Big|_{z_1}^{z_2}, \tag{3.17}$$

where the subscript 0 indicates that these quantities are only the amplitudes of the full fields. Strictly speaking, the dependency on $\mathbf{q}$ could be omitted, as non-locality is not being considered. However, this expression would hold if non-locality was being considered.

We can apply this same principle to the conservation of linear momentum. In terms of real field components, it reads, in the integral form,

$$\frac{1}{T}\int_{-T/2}^{T/2}dt\iiint_{\Omega}d^3\mathbf{r}\left[\rho\mathbf{E}^{av}+\mathbf{J}^{s}\times\mathbf{B}^{av}\right]=\frac{1}{T}\int_{-T/2}^{T/2}dt\iiint_{\Omega}d^3\mathbf{r}\left[\nabla\cdot\overleftrightarrow{T}+\epsilon_0\mu_0\frac{\partial\mathbf{S}}{\partial t}\right], \tag{3.18}$$

where $\mathbf{S}$ is, again, the Poynting vector, and $\overleftrightarrow{T}$ is the electromagnetic stress tensor, with $\nabla\cdot\overleftrightarrow{T}$ representing the momentum flux density. The specific form of $\overleftrightarrow{T}$ is somewhat controversial, and determining it will form a component of the following analysis.

We can follow the same arguments as in the energy conservation equation to transform the volume integrals to surface integrals using divergence theorem and a singular current. However in this case we also have a charge density per unit volume, ρ. We can represent the charge density in terms of the current using charge continuity,

$$\nabla\cdot\mathbf{J}^{s}(\mathbf{r},t)=\nabla_{\parallel}\cdot\mathbf{J}_{\parallel}(\mathbf{r}_{\parallel},t)\delta(z)+J_z^{e}(\mathbf{r}_{\parallel},t)\delta'(z)=-\frac{\partial\rho}{\partial t}(\mathbf{r},t), \tag{3.19}$$

where $\nabla_{\parallel}$ is the divergence in the in-plane coordinates, and $\mathbf{J}_{\parallel}$ is the in-plane component of the induced current in the 2D material, defined in terms of polarization in equation 2.2. Again, the out-of-plane current is the screened quantity defined in equation 2.47. Both the charge density and the current density are singular, however, the charge density also has second-order singularities in the form of a derivative of the Dirac delta distribution,

$$\rho(\mathbf{r},t)=\rho_0(\mathbf{r}_{\parallel},t)\delta(z)+\rho_1(\mathbf{r}_{\parallel},t)\delta'(z), \tag{3.20}$$

where, after converting to the Fourier domain in time ($t\to\omega$), $\rho_0(\mathbf{r}_{\parallel},\omega)=-(i/\omega)\nabla_{\parallel}\cdot\mathbf{J}_{\parallel}(\mathbf{r}_{\parallel},\omega)$, and $\rho_1(\mathbf{r}_{\parallel},\omega)=-(i/\omega)J_z^{e}(\mathbf{r}_{\parallel},\omega)$. Notably, $\rho_0(\mathbf{r}_{\parallel},\omega)$ is a charge density per unit area, while $\rho_1(\mathbf{r}_{\parallel},\omega)$ is the density of a layer of perpendicularly oriented dipoles per unit area. Inserting equation 3.20 into equation 3.18 will collapse the volume integrals to surface integrals over D, while in the time average, the time derivative of the Poynting vector

will disappear. The second-order singularity, $\delta'(z)$, will also introduce a derivative at the interface that needs to be handled carefully. The term with the second order singularity takes the form,

$$\frac{1}{T}\int_{-T/2}^{T/2} dt \iiint_D d^3\mathbf{r}\, \rho_1(\mathbf{r}_\parallel,\omega)\mathbf{E}(\mathbf{r},\omega)\delta'(z). \tag{3.21}$$

The electric field in this equation is the total field at the interface and is modelled, in vacuum, as the arithmetic mean of the fields on either side,

$$\mathbf{E}^{av} = \frac{1}{2}(\mathbf{E}_1 + \mathbf{E}_2). \tag{3.22}$$

Across a 2D material in vacuum, the electric field can be discontinuous in both tangential directions when one includes the out-of-plane response. This would imply that the derivative of the total field at the interface is singular. However, a singular field acting on the charge density would produce an infinite force, which is of course nonphysical. Instead, we will model the derivative at the interface as the arithmetic mean of the derivatives on either side. This is a common choice for non-singular field quantities that are discontinuous across an interface. However, in light of the singular nature of the derivative across the interface, a more careful argument is justified.

Without the out-of-plane response, the scalar potential is continuous across an interface. The electric field as, in part, the derivative of the scalar potential, experiences a finite jump. However, with out-of-plane response, the scalar potential itself experiences a jump across the interface [34]. As the derivative of this jump, the $\hat{z}$ component of the electric field would, in theory, be singular at the interface. Given the boundary condition due to the out-of-plane response defined in equation 2.44, a singular electric field in the perpendicular direction would imply through the boundary condition on the tangential directions that the electric fields experience an infinite jump,

$$\hat{z}\times\big(\mathbf{E}_2(\mathbf{r}_\parallel) - \mathbf{E}_1(\mathbf{r}_\parallel)\big) = -\frac{1}{\epsilon_0}\hat{z}\times\nabla P_z^e(\mathbf{r}_\parallel) = -\hat{z}\times\infty, \tag{3.23}$$

given the definition of P_z in terms of the electric field in equation 2.46. This is of course nonsense. Instead, there is experimental evidence to show that the appropriate definition for this seemingly singular field at the interface is still the arithmetic mean. In reference [3], a model for the reflectance of graphene was used to predict both in-plane (σ_q) and out-of-plane (σ_z) conductivity values by fitting to measurements. Their model is exactly the same as the one derived in 2.3, though they used a different screening on σ_z, and they predicted startlingly accurate conductivity values when compared to *ab initio* calculations

[2]. Given that our model uses the arithmetic mean for the total field in the $\hat{z}$ direction, the accurate conductivity predictions in [3] are evidence that the choice is accurate for the z component of the electric field, even though it would, in theory, be singular at the interface. So, experimental evidence supports the use of an arithmetic mean to model singular field quantities at interfaces.

While the choice to model the derivative of the total field at zero as the arithmetic mean may remain controversial, and certainly it is on less firm footing than the application of the same idea to the field itself, we will also show later through numerical verification that it does not violate conservation of linear momentum. Given that one of the primary justifications for the use of the arithmetic mean on the fields is that it satisfies the boundary conditions, the fact that it satisfies conservation of linear momentum when applied to the derivative of the field at the interface is a strong indication of its validity. We will therefore formally define the derivative of the total electric field at the interface as the arithmetic mean of the bulk values in the limit as they approach the interface at $z = 0$,

$$\left.\frac{\partial \mathbf{E}}{\partial z}\right|_{z=0} = \left.\frac{\partial \mathbf{E}^{av}}{\partial z}\right|_{z\to 0^{\pm}} = \frac{1}{2}\left[\left(\lim_{z_2\to 0^+}\left.\frac{\partial \mathbf{E}_2}{\partial z}\right|_{z=z_2}\right) + \left(\lim_{z_1\to 0^-}\left.\frac{\partial \mathbf{E}_1}{\partial z}\right|_{z=z_1}\right)\right]. \tag{3.24}$$

The second-order charge density term is, therefore,

$$-\frac{1}{T}\int_{-T/2}^{T/2} dt\, \frac{1}{L_q L_\tau}\iint_D d^2\mathbf{r}_\parallel\, \rho_1(\mathbf{r}_\parallel,\omega)\left.\frac{\partial \mathbf{E}^{av}(\mathbf{r},\omega)}{\partial z}\right|_{z\to 0^{\pm}}. \tag{3.25}$$

The rest of the equation has only standard Dirac deltas, and so no other special consideration is necessary,

$$\frac{1}{T}\int_{-T/2}^{T/2} dt\, \frac{1}{L_q L_\tau}\iint_D d^2\mathbf{r}_\parallel \left(\rho_0 \mathbf{E}^{av} - \rho_1 \left.\frac{\partial \mathbf{E}^{av}}{\partial z}\right|_{z\to 0^{\pm}} + \mathbf{J}^{\mathrm{2D}} \times \mathbf{B}^{av}\right) = \frac{1}{T}\int_{-T/2}^{T/2} dt\, \frac{1}{L_q L_\tau}\iint_D d^2\mathbf{r}\left(\overleftrightarrow{T}\cdot\hat{z}\Big|_{z_1}^{z_2}\right). \tag{3.26}$$

Finally, we can again apply equation 3.12 to transform the real domain integral equation into an expression in terms of the amplitudes of Fourier components,

$$\frac{1}{2}\Re\left(\rho_0(q,\omega)\mathbf{E}_0^{av*}(\mathbf{q},\omega) - \rho_1(\mathbf{q},\omega)\left.\frac{\partial \mathbf{E}_0^{av*}(\mathbf{q},\omega,z)}{\partial z}\right|_{z\to 0^{\pm}}\right) + \frac{1}{2}\Re\left(\mathbf{J}_0(\mathbf{q},\omega)\times\mathbf{B}_0^*(\mathbf{q},\omega)\right) = \frac{1}{2}\Re\left(\overleftrightarrow{T}(\mathbf{q},\omega,z)\right)\cdot\hat{z}\Big|_{z_1}^{z_2}, \tag{3.27}$$

where the 0 subscript indicates that these are the amplitudes of the corresponding complex monochromatic plane waves. The z derivative term is indicated as an amplitude, however, the derivative must be evaluated including the propagator defined by $e^{ik_z z}$. After evaluation of the derivatives and the limits, the field acting on the dipole density ρ_1 can be similarly written in terms of the amplitudes of Fourier components,

$$\left.\frac{\partial \mathbf{E}_0^{av*}(\mathbf{q},\omega,z)}{\partial z}\right|_{z\to 0^{\pm}} = \frac{1}{2}\left(-ik_{z1}\mathbf{E}^*_{I0}(\mathbf{q},\omega) + ik_{z1}\mathbf{E}^*_{R0}(\mathbf{q},\omega) - ik_{z2}\mathbf{E}^*_{T0}(\mathbf{q},\omega)\right), \tag{3.28}$$

where I, R, and T, indicate the incident, reflected, and transmitted fields, respectively. A more detailed exploration of the effect the derivative in z has on the conversion between integral and Fourier amplitude representations can be found in Appendix B.2.

3.2 Vacuum gap, revisited

In order to include the effects of surrounding dielectric materials, we will again apply the vacuum gap method. The application of this method allows us to separate the behaviour of the 2D material from the surrounding dielectrics. This means that the momentum calculations will not include any forces on the surrounding dielectrics. For a brief discussion of forces on dielectric interfaces and why they remain controversial, along with a supporting comparison between the Minkowski and Maxwell stress tensors, see Appendix C.1.

Both of the conservation equations, defined in 3.27 and 3.17, follow the general structure of a comparison between what is happening directly at the interface, and some combination of fields evaluated at observation planes away from the interface. Using the vacuum gap method makes it possible to isolate both the 2D material and the observation planes while maintaining the influence of surrounding materials through how they modify the fields. The method is the same as that which was used in section 2.3, however in this context we do not use transfer matrices.

The vacuum gap method turns the single interface into three interfaces as shown in figure 2.3. Then, in the limit that the gap closes, the surrounding dielectric interfaces can be considered pressed directly against the central 2D material from above and below. This means that the boundary conditions on the dielectric interfaces become equations that directly relate the fields acting on the central 2D material in vacuum, to the fields inside the dielectrics. Given that the total electric and magnetic fields are being modelled as the arithmetic mean of the fields above and below, this means that the total field acting on the 2D material, in the limit that the vacuum gap closes, can be directly related through the boundary conditions on the pure dielectric interfaces to the fields in the dielectric media.

The boundary conditions on the dielectric interfaces are defined in equations 1.63-1.66. In the vacuum gap configuration, these equations give rise to the transfer matrices defined in 2.50 and 2.51, from which we can extract a set of linear equations to relate field amplitudes on either side of the two dielectric interfaces surrounding the 2D material. However, in the ultimately transmitted medium, there is only a single upward-propagating field. As such, the conditions give the relationships between the central upward (u) and downward (d) propagating fields in the vacuum gap, to the incident (a), reflected (r), and transmitted (t) fields in the surrounding dielectrics as

$$u_{p2} = \frac{\cos\theta n_2 + \cos\theta_t}{2\cos\theta} t_p, \qquad u_{s2} = \frac{\cos\theta_t n_2 + \cos\theta}{2\cos\theta} t_s, \tag{3.29}$$

$$d_{p2} = \frac{\cos\theta n_2 - \cos\theta_t}{2\cos\theta} t_p, \qquad d_{s2} = \frac{-\cos\theta_t n_2 + \cos\theta}{2\cos\theta} t_s, \tag{3.30}$$

$$u_{p1} = \frac{\cos\theta n_1 + \cos\theta_i}{2\cos\theta} a_p + \frac{\cos\theta n_1 - \cos\theta_i}{2\cos\theta} r_p, \quad u_{s1} = \frac{\cos\theta_i n_1 + \cos\theta}{2\cos\theta} a_s + \frac{-\cos\theta_i n_1 + \cos\theta}{2\cos\theta} r_s, \tag{3.31}$$

$$d_{p1} = \frac{\cos\theta n_1 - \cos\theta_i}{2\cos\theta} a_p + \frac{\cos\theta n_1 + \cos\theta_i}{2\cos\theta} r_p, \quad d_{s1} = \frac{-\cos\theta_i n_1 + \cos\theta}{2\cos\theta} a_s + \frac{\cos\theta_i n_1 + \cos\theta}{2\cos\theta} r_s, \tag{3.32}$$

where the subscripts s and p indicate that the amplitude corresponds to s and p-polarization, respectively.

For the fields evaluated at the observation planes, we simply choose their location to be fixed at some distance less than, but proportional to, the vacuum gap thickness d. This ensures the planes are inside the vacuum gap region and that they remain in the vacuum gap as it closes. For simplicity, we can say the observation planes are fixed at half the distance between the 2D material and the surrounding dielectrics, as shown in configuration two of figure 3.1. This means that in the limit as $d \to 0$, the observation planes similarly end up pressed against the central interface, though technically still in the vacuum region. The conditions 3.29 and 3.31 therefore become applicable at both the central interface and the observation planes. This way, we can use the well-accepted energy and momentum conservation equations for vacuum, and then introduce the effect of material surroundings through the boundary conditions on the dielectric interfaces. In the case of momentum conservation, it would seem that this is in fact the only legitimate way of performing this calculation for the case of 2D materials surrounded by media if one is interested specifically in the forces exerted on the 2D material itself. If one places the observation planes explicitly inside the surrounding media instead of in a vacuum gap, like

configuration one of figure 3.1, then the forces on the surrounding dielectrics are also being captured.

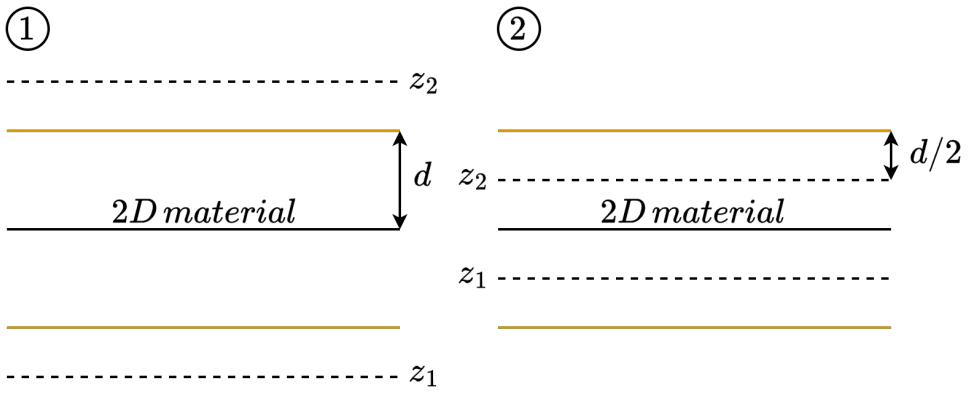


Figure 3.1: Observation plane configurations for application of the vacuum gap method. Only configuration (2) is applied in this section.

3.3 Conductivity models

For both energy and momentum conservation, two different cases of 2D materials will be considered. One case will be assumed to exhibit in-plane anisotropy, as in phosphorene, but no out-of-plane response, given by a sheet conductivity of the form,

$$\overleftrightarrow{\sigma} = \begin{bmatrix} \sigma_q & \sigma_c & 0 \\ \sigma_c & \sigma_\tau & 0 \\ 0 & 0 & 0 \end{bmatrix}. \tag{3.33}$$

The other will be described by a sheet conductivity that is isotropic in-plane, as in graphene, but includes out-of-plane response,

$$\overleftrightarrow{\sigma} = \begin{bmatrix} \sigma_q & 0 & 0 \\ 0 & \sigma_\tau & 0 \\ 0 & 0 & \sigma_z \end{bmatrix}. \tag{3.34}$$

To confirm that the derived equations uphold energy and momentum conservation, both with and without out-of-plane conductivity, we will evaluate the difference between

the two sides of each conservation equation numerically for a full range of incident angles and arbitrarily defined conductivity functions. The conductivity will be given by a set of arbitrary Drude-Lorentz models. We will define the in-plane longitudinal conductivity σ_q as,

$$\sigma_q(\omega) = \frac{i}{\pi}\frac{\omega'_{Fq}}{\omega + i\tau_f^{-1}} + \frac{i}{\pi}\frac{\omega S_{bq}}{\omega^2 - \omega_{bq}^2 + i\omega\tau_f^{-1}}, \tag{3.35}$$

the in-plane transverse conductivity σ_τ as,

$$\sigma_\tau(\omega) = \frac{i}{\pi}\frac{\omega'_{F\tau}}{\omega + i\tau_f^{-1}} + \frac{i}{\pi}\frac{\omega S_{b\tau}}{\omega^2 - \omega_{b\tau}^2 + i\omega\tau_f^{-1}}, \tag{3.36}$$

the in-plane anisotropic conductivity σ_c as,

$$\sigma_c(\omega) = \frac{i}{\pi}\frac{\omega'_{Fc}}{\omega + i\tau_f^{-1}} + \frac{i}{\pi}\frac{\omega S_{bc}}{\omega^2 - \omega_{bc}^2 + i\omega\tau_f^{-1}}, \tag{3.37}$$

and finally, the out-of-plane conductivity σ_z as,

$$\sigma_z(\omega) = \frac{i}{\pi}\frac{\omega S_{bz1}}{\omega^2 - \omega_{bz1}^2 + i\omega\tau_f^{-1}} + \frac{i}{\pi}\frac{\omega S_{bz2}}{\omega^2 - \omega_{bz2}^2 + i\omega\tau_f^{-1}}, \tag{3.38}$$

where $S_{bq} = 20\sigma_0/\hbar$, $\omega'_{Fq} = 10\sigma_0/\hbar$, $\omega_{bq} = 17/\hbar$, $S_{b\tau} = 10\sigma_0/\hbar$, $\omega'_{F\tau} = 8\sigma_0/\hbar$, $\omega_{bq} = 14/\hbar$, $S_{bc} = 5\sigma_0/\hbar$, $\omega'_{Fc} = 6\sigma_0/\hbar$, $\omega_{bc} = 10/\hbar$, $S_{bz1} = 19\sigma_0/\hbar$, $\omega_{bz1} = 16/\hbar$, $S_{bz2} = 10\sigma_0/\hbar$, $\omega_{bz2} = 7/\hbar$, $\sigma_0 = \pi\alpha/z_0$, and $\tau_f = 1.5\hbar$. These conductivities are shown as a function of energy in figure 3.2.

3.4 Energy

All of the expressions in the following subsections have been derived using the symbolic algebra capabilities of Maple [62].

3.4.1 In-plane anisotropic, no out-of-plane

Consider a 2D material modelled by a sheet of in-plane conductivity, defined in equation 3.33. In this configuration, without any out-of-plane currents, the in-plane electric fields

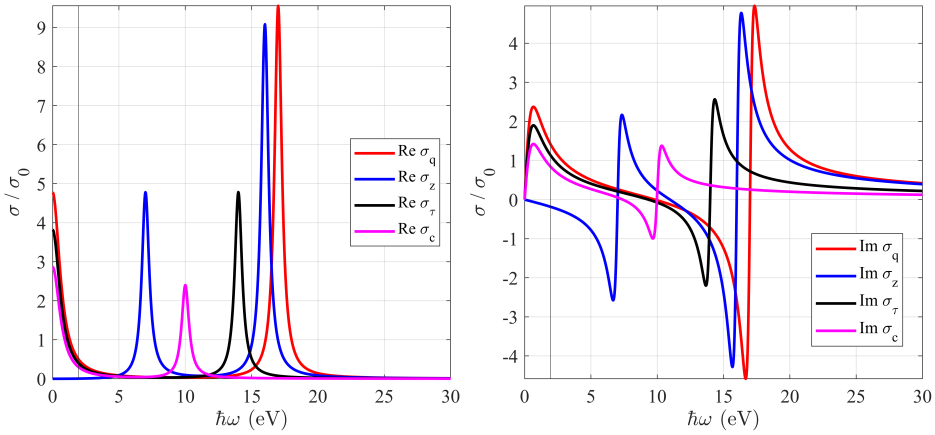


Figure 3.2: Artificial conductivities for testing the validity of derived conservation equations. $\sigma_0 = \pi\alpha/z_0$, where α is the fine structure constant.

remain continuous across the interface. This means that the total field can be represented in the in-plane direction as

$$\mathbf{E}_{\parallel}(\mathbf{r},t) = \frac{1}{2}\left(\mathbf{E}_{\parallel}^{(1)}(\mathbf{r},t) + \mathbf{E}_{\parallel}^{(2)}(\mathbf{r},t)\right) = \mathbf{E}_{\parallel}^{(1)}(\mathbf{r},t) = \mathbf{E}_{\parallel}^{(2)}(\mathbf{r},t). \tag{3.39}$$

First, we will examine the case of vacuum surroundings. In this scenario, all of the angles are made equal by Snell's law, so instead of incident and transmitted angles, a common vacuum angle θ is used. The complex amplitudes constituting the energy loss term given by the left-hand side of equation 3.17 are,

$$\mathbf{J}_0^{\mathrm{2D}}(q,\omega)\cdot\mathbf{E}_0^{av*}(q,\omega) = \begin{pmatrix}\sigma_q E_q + \sigma_c E_\tau \\ \sigma_c E_q + \sigma_\tau E_\tau \\ 0\end{pmatrix}\cdot\begin{pmatrix}E_q^* \\ E_\tau^* \\ E_z^*\end{pmatrix}, \tag{3.40}$$

$$= \sigma_q|E_q|^2 + \sigma_\tau|E_\tau|^2 + 2\sigma_c\Re\left(E_q E_\tau^*\right), \tag{3.41}$$

where the field quantities represent the total field at the interface in each direction. Next, we insert the vacuum field amplitudes. The standard forms of the Fresnel amplitudes were defined originally in equation 1.68. Here, though, as we are not dealing with fields inside a vacuum gap, we label the upward propagating field in region one (incident) as a, the downward propagating field in region one (reflected) as r, and the upward propagating field in region two (transmitted) as t, and we omit the downward propagating field in region two, giving

$$|E_q|^2 = E_q E_q^* = |t_p|^2\cos^2\theta, \tag{3.42}$$

$$|E_\tau|^2 = E_\tau E_\tau^* = |t_s|^2, \tag{3.43}$$

$$\Re\left(E_q E_\tau^*\right) = -\Re\left(t_p t_s^* \cos\theta\right), \tag{3.44}$$

where the total fields have been represented as the fields on side two as illustrated in equation 3.39. Inserting these results into the left-hand side of equation 3.17,

$$-\Re\left(\mathbf{J}_0^{\mathrm{2D}} \cdot \mathbf{E}_0^{av*}\right) = -\Re(\sigma_q)|t_p|^2\cos^2\theta + \Re(\sigma_\tau)|t_s|^2 - 2\Re(\sigma_c)\Re\left(t_p t_s^* \cos\theta\right), \tag{3.45}$$

where we have omitted the factor of $1/2$ that appears on both sides of equation 3.17.

Next, we can examine the Poynting vector terms on the right-hand side of equation 3.17,

$$\left(\mathbf{E}_0 \times \mathbf{H}_0^*\right) \cdot \hat{z} = E_q H_\tau^* - E_\tau H_q^*. \tag{3.46}$$

We can then insert the field amplitude components from the transmitted medium,

$$\Re\left(\mathbf{E}_0 \times \mathbf{H}_0^*\right) \cdot \hat{z}\big|_{z_2} = \Re\left(\frac{1}{z_0} t_p t_p^* \cos\theta e^{-2z_2\Im(k_{zt})} + \frac{1}{z_0} t_s \overline{u_s \cos\theta} e^{-2z_2\Im(k_{zt})}\right), \tag{3.47}$$

$$= \frac{1}{z_0}\left(|t_p|^2 + |t_s|^2\right)\cos\theta, \tag{3.48}$$

where the overbar indicates complex conjugation, and the exponential factor was dropped because, with vacuum surroundings, the fields can never go evanescent. Similarly, for the fields in the incident medium,

$$\begin{aligned}\Re\left(\mathbf{E}_0 \times \mathbf{H}_0^*\right) \cdot \hat{z}\big|_{z_1} = \Re\Bigg(&\frac{1}{z_0}(-a_p e^{ik_{zi}z_1} + r_p e^{-ik_{zi}z_1})\overline{(-a_p e^{ik_{zi}z_1} - r_p e^{-ik_{zi}z_1})}\cos\theta \\ &-\frac{1}{z_0}(a_s e^{ik_{zi}z_1} + r_s e^{-ik_{zi}z_1})\overline{(-a_s e^{ik_{zi}z_1} + r_s e^{-ik_{z1}z_1})\cos\theta}\Bigg)\end{aligned} \tag{3.49}$$

$$= \frac{1}{z_0}\left(\left(|a_p|^2 - |r_p|^2\right) - \left(|r_s|^2 - |a_s|^2\right)\right)\cos\theta, \tag{3.50}$$

where the exponential factors vanish because k_{zi} cannot be imaginary with vacuum surroundings. Equations 3.45, 3.48, and 3.50 yield the conservation of energy when substituted into equation 3.17, in terms of Fresnel field amplitudes,

$$\begin{aligned}-\left(\Re(\sigma_q)|t_p|^2\cos^2\theta_t + \Re(\sigma_\tau)|t_s|^2 - 2\Re(\sigma_c)\Re\left(t_p t_s^*\cos\theta_t\right)\right) = \\ \frac{1}{z_0}\left(|t_p|^2 + |t_s|^2\right)\cos\theta - \frac{1}{z_0}\left(|a_p|^2 - |r_p|^2 - |r_s|^2 + |a_s|^2\right)\cos\theta\end{aligned} \tag{3.51}$$

In this form, the standard expressions for reflectance and transmittance as the ratio of the squared magnitudes of the reflected and transmitted Fresnel amplitudes to the incident amplitude can be extracted along with an expression for the total absorbance. Equation 3.51 can be rearranged as

$$(|a_p|^2 - |t_p|^2 - |r_p|^2) + (|a_s|^2 - |t_s|^2 - |r_s|^2) = z_0 \left(\Re(\sigma_q)|t_p|^2 \cos\theta + \frac{\Re(\sigma_\tau)}{\cos\theta}|t_s|^2 - 2\Re(\sigma_c)\Re\left(t_p t_s^*\right) \right), \tag{3.52}$$

$$|a_p|^2(1 - T_p - R_p) + |a_s|^2(1 - T_s - R_s) = z_0 \left(\Re(\sigma_q)|t_p|^2 \cos\theta + \frac{\Re(\sigma_\tau)}{\cos\theta}|t_s|^2 - 2\Re(\sigma_c)\Re\left(t_p t_s^*\right) \right), \tag{3.53}$$

$$|a_p|^2 A_p + |a_s|^2 A_s = z_0 \left(\Re(\sigma_q)|t_p|^2 \cos\theta + \frac{\Re(\sigma_\tau)}{\cos\theta}|t_s|^2 - 2\Re(\sigma_c)\Re\left(t_p t_s^*\right) \right), \tag{3.54}$$

where $T_{p/s}$ is the transmittance, $R_{p/s}$ is the reflectance, and $A_{p/s}$ is the absorbance, each of their respective polarization, and we have used the definitions for A_p and A_a as,

$$A_p = 1 - T_p - R_p, , \tag{3.55}$$

$$A_s = 1 - T_s - R_s, \tag{3.56}$$

respectively. There is no influence from evanescence in this case, as without surrounding materials, there is no critical angle. It should be noted that the Fresnel field amplitudes t_p, t_s, r_p, and r_s each have contributions from both a_p and a_s as a result of the in-plane anisotropy. The anisotropy means that an incident field purely polarized in either s or p will generate reflected and transmitted fields with mixed polarization. The general expressions are given in equations 2.59-2.62 of section 2.3.

In cases of arbitrary linear polarization, one can define a polarization angle η, such that the incident s and p polarization amplitudes are $a_s = a\sin\eta$, and $a_p = a\cos\eta$. With these definitions, and for purely real incident amplitudes, the energy conservation relation shown in equation 3.53 takes the form,

$$a^2(1 - T_p - R_p)\cos^2\eta + a^2(1 - T_s - R_s)\sin^2\eta = z_0 \left(\Re(\sigma_q)|t_p|^2 \cos\theta + \frac{\Re(\sigma_\tau)}{\cos\theta}|t_s|^2 - 2\Re(\sigma_c)\Re\left(t_p t_s^*\right) \right), \tag{3.57}$$

$$a^2 A_p \cos^2\eta + a^2 A_s \sin^2\eta = z_0 \left(\Re(\sigma_q)|t_p|^2 \cos\theta + \frac{\Re(\sigma_\tau)}{\cos\theta}|t_s|^2 - 2\Re(\sigma_c)\Re\left(t_p t_s^*\right) \right), \tag{3.58}$$

Considering unit amplitude for the incident field ($a = 1$), we can write the total absorbance as,

$$A = A_p \cos^2\eta + A_s \sin^2\eta \tag{3.59}$$

$$= z_0 \left(\Re(\sigma_q)|t_p|^2 \cos\theta + \frac{\Re(\sigma_\tau)}{\cos\theta}|t_s|^2 - 2\Re(\sigma_c)\Re\left(t_p t_s^*\right) \right), \tag{3.60}$$

which we can alternatively relate to total transmittance and reflectance terms through equation 3.57,

$$A = (1 - T_p - R_p)\cos^2\eta + (1 - T_s - R_s)\sin^2\eta \tag{3.61}$$

$$= \cos^2\eta + \sin^2\eta - T_p\cos^2\eta - T_s\sin^2\eta - R_p\cos^2\eta - R_s\sin^2\eta \tag{3.62}$$

$$= 1 - T - R \tag{3.63}$$

where,

$$T = T_p\cos^2\eta + T_s\sin^2\eta, \tag{3.64}$$

and,

$$R = R_p\cos^2\eta + R_s\sin^2\eta. \tag{3.65}$$

Here we have recovered the common expression $1 = A + R + T$ for arbitrary linear polarization.

For material surroundings, the first step is to re-evaluate the conservation equation for vacuum surroundings; however, this time with four fields as defined in equation 1.68. There will be one upward and one downward propagating field in both regions around the 2D material as a result of internal reflections from the surrounding dielectrics. In this case, there will be an influence from evanescence also as a result of the surrounding dielectric interfaces. This means the out-of-plane components of the wave number (k_z), and any cosines of angles can become imaginary. Inside the vacuum gap, the energy loss term in the left-hand side of equation 3.17 therefore becomes,

$$-\Re\left(\mathbf{J}_0^{2\mathrm{D}} \cdot \mathbf{E}_0^{av*}\right) = -\Re(\sigma_q)|\cos\theta|^2(|u_{p2}|^2+|d_{p2}|^2-2\Re(u_{p2}d_{p2}^*)-\Re(\sigma_\tau)(|u_{s2}|^2+|d_{s2}|^2+2\Re(u_{s2}d_{s2}^*)) - \Re(\sigma_c)\Re((d_{p2}-u_p2)(d_{s2}^*+d_{s2}^*)\cos\theta), \tag{3.66}$$

where again, the average electric fields are represented as the field on just one side by exploiting the continuity of the tangential electric field components across the 2D material. Next, the relations in equations 3.29 and 3.31, derived from the dielectric boundary conditions, can be inserted to cast the vacuum gap energy loss in terms of field quantities in the surrounding dielectrics,

$$-\Re\left(\mathbf{J}_0^{2\mathrm{D}} \cdot \mathbf{E}_0^{av*}\right) = -\left(\Re(\sigma_q)|t_p|^2|\cos\theta_t|^2 + \Re(\sigma_\tau)|t_s|^2 - 2\Re(\sigma_c)\Re\left(t_p t_s^*\cos\theta_t\right)\right). \tag{3.67}$$

Next, the same is done for the Poynting vector terms,

$$\Re\left(\mathbf{E}_0 \times \mathbf{H}_0^*\right) \cdot \hat{z}\big|_{z_2} = -\frac{1}{z_0} e^{-2z_2 \Im(k_z)} \Re\left(\left(|d_{p2}|^2 - |u_{p2}|^2 - 2i\Im(u_{p2} d_{p2}^*)\right) \cos\theta \right.$$
$$\left. + \left(|d_{s2}|^2 - |u_{s2}|^2 - 2i\Im(u_{s2} d_{s2}^*)\right) \cos\theta^* \right), \quad (3.68)$$

and,

$$\Re\left(\mathbf{E}_0 \times \mathbf{H}_0^*\right) \cdot \hat{z}\big|_{z_1} = -\frac{1}{z_0} e^{-2z_1 \Im(k_z)} \Re\left(\left(|d_{p2}|^2 - |u_{p2}|^2 - 2i\Im(u_{p2} d_{p2}^*)\right) \cos\theta \right.$$
$$\left. + \left(|d_{s2}|^2 - |u_{s2}|^2 - 2i\Im(u_{s2} d_{s2}^*)\right) \cos\theta^* \right), \quad (3.69)$$

where products of the exponential factors go to one after the observation planes situated at z_1 and z_2 approach the interface in the limits $z_1 \to 0^-$ and $z_2 \to 0^+$. Now, again, inserting the conditions in equations 3.29 and 3.31 relating the vacuum field amplitudes to the amplitudes in the dielectrics,

$$\Re\left(\tilde{\mathbf{E}}_0 \times \tilde{\mathbf{H}}_0^*\right) \cdot \hat{z}\Big|_{z_2} = \frac{n_2}{z_0}(|t_p|^2 + |t_s|^2)\Re(\cos\theta_t), \quad (3.70)$$

and,

$$\Re\left(\tilde{\mathbf{E}}_0 \times \tilde{\mathbf{H}}_0^*\right) \cdot \hat{z}\Big|_{z_1} = \frac{n_1}{z_0}(|a_p|^2 + |a_s|^2 - |r_p|^2 - |r_s|^2)\cos\theta_i. \quad (3.71)$$

Taken together, equations 3.67, 3.70, and 3.71, when substituted into equation 3.17 constitute energy conservation for the case of dielectric surroundings,

$$-\left(\Re(\sigma_q)|t_p|^2|\cos\theta_t|^2 + \Re(\sigma_\tau)|t_s|^2 - 2\Re(\sigma_c)\Re\left(t_p t_s^* \cos\theta_t\right)\right) = \frac{n_2}{z_0}(|t_p|^2 + |t_s|^2)\Re(\cos\theta_t)$$
$$- \frac{n_1}{z_0}(|a_p|^2 + |a_s|^2 - |r_p|^2 - |r_s|^2)\cos\theta_i. \quad (3.72)$$

In this case, the form of the energy loss term is unchanged, however, the Poynting vector terms on the right-hand side of the above equation adopt scaling by the index of refraction in each region. Again, the standard forms for the reflectance, transmittance, and absorbance can be extracted by simply rearranging the terms in equation 3.72,

$$\left(|a_p|^2 - \frac{n_2\Re(\cos\theta_t)}{n_1\cos\theta_i}|t_p|^2 - |r_p|^2\right) + \left(|a_s|^2 - \frac{n_2\Re(\cos\theta_t)}{n_1\cos\theta_i}|t_s|^2 - |r_s|^2\right)$$
$$= \frac{z_0}{n_1\cos\theta_i}\left(\Re(\sigma_q)|t_p|^2|\cos\theta_t|^2 + \Re(\sigma_\tau)|t_s|^2 - 2\Re(\sigma_c)\Re\left(t_p t_s^*\cos\theta_t\right)\right), \quad (3.73)$$

$$|a_p|^2(1-T_p-R_p)+|a_s|^2(1-T_s-R_s)$$
$$=\frac{z_0}{n_1\cos\theta_i}\left(\Re(\sigma_q)|t_p|^2|\cos\theta_t|^2+\Re(\sigma_\tau)|t_s|^2-2\Re(\sigma_c)\Re\left(t_pt_s^*\cos\theta_t\right)\right), \quad (3.74)$$

$$|a_p|^2A_p+|a_s|^2A_s=\frac{z_0}{n_1\cos\theta_i}\left(\Re(\sigma_q)|t_p|^2|\cos\theta_t|^2+\Re(\sigma_\tau)|t_s|^2-2\Re(\sigma_c)\Re\left(t_pt_s^*\cos\theta_t\right)\right), \quad (3.75)$$

where again, the absorbance is defined as in equations 3.56 and 3.55.

So, the vacuum gap method has successfully recreated the appropriate angular dependence in the transmittance,

$$T_p=\frac{n_2\Re(\cos\theta_t)}{n_1\cos\theta_i}|t_p|^2, \quad (3.76)$$

as well as correctly accounting for the effect of evanescence. This expression represents the ratio of the normal components of the Poynting vector in the transmitted medium to the incident wave of unit amplitude. As was discussed in section A.1, evanescent fields propagate no energy into the media that bear their extent. In the above equation, the contribution to the energy conservation from the fields in the transmitted medium goes to zero in the evanescent regime. This is because, as was outlined in section A.1, in the evanescent regime, the cosine of the transmitted angle becomes imaginary.

3.4.2 In-plane isotropic, with out-of-plane

Now, we consider a 2D material modelled by a sheet conductivity that is isotropic in the plane but includes out-of-plane conductivity, defined in equation 3.34. This means that, according to the out-of-plane boundary condition 2.27, the electric fields in the $\hat{q}$ direction are no longer continuous. As a result, the total fields modelled as the arithmetic mean can no longer be reduced to the field on just one of the sides, the full average is required. Also of note is that the Poynting vector contributions to energy conservation are unchanged in form from the addition of out-of-plane response when compared to the Poynting vector contributions in the preceding subsection. This is because they are pure field quantities, evaluated away from the interface. Changing the interface only influences their behaviour in so far as it modifies the field magnitudes. Only the energy loss term changes visually, and even then only through the addition of a single extra term when compared to equation

3.41 with $\sigma_c = 0$,

$$\mathbf{J}_0^{\mathrm{2D}} \cdot \mathbf{E}_0^{av*} = \begin{pmatrix} \sigma_q E_q \\ \sigma_\tau E_\tau \\ \sigma_z^e E_z \end{pmatrix} \cdot \begin{pmatrix} E_q^* \\ E_\tau^* \\ E_z^* \end{pmatrix} \tag{3.77}$$

$$= \sigma_q |E_q|^2 + \sigma_\tau |E_\tau|^2 + \sigma_z^e |E_z|^2, \tag{3.78}$$

where all the field components represent the total field in their respective direction, modelled by the arithmetic mean. The process of casting this general form in terms of Fresnel field amplitudes is unchanged from subsection 3.4.1, and so will not be repeated here. As a summary, for vacuum surroundings, the Fresnel field amplitudes, which are defined generally in equation 1.68, are inserted into equation 3.78 with the substitutions $u_1 \to a$, $d_1 \to r$, $u_2 \to t$, and $d_2 \to 0$.

Considering first the case of vacuum surroundings with out-of-plane response, the total absorption is now

$$A = \frac{z_0}{4} \Big(\Re(\sigma_q)(|a_p|^2 + |r_p|^2 + |t_p|^2 - 2\Re(a_p r_p^* - a_p t_p^* + r_p t_p^*)) \cos\theta \\ + 4\frac{\Re(\sigma_\tau)}{\cos\theta}|t_s|^2 + \frac{\Re(\sigma_z^e)\sin^2\theta}{\cos\theta}(|a_p|^2 + |r_p|^2 + |t_p|^2 + 2\Re(a_p r_p^* + a_p t_p^* + r_p t_p^*)) \Big). \tag{3.79}$$

This expression is the energy loss term divided by $\cos\theta/z_0$. Again, the Poynting vector contribution is unchanged from the right-hand side of 3.51 with the addition of out-of-plane response. Only the absorption is modified.

Adding surrounding materials, the process again involves redoing the vacuum calculations with the full four fields in the central vacuum gap region and then applying the relations between the fields inside the vacuum gap to the fields in the surrounding dielectrics defined in equations 3.29 and 3.31. Following this process yields

$$A = \frac{z_0}{4n_1 \cos\theta_i} \Big(\Re(\sigma_q) \left((|a_p|^2 + |r_p|^2)\cos^2\theta_i + |t_p|^2 |\cos\theta_t|^2 + \Lambda_1 \right) \\ + 4\Re(\sigma_\tau)|t_s|^2 + \Re(\sigma_z^e) \left(n_1^4 (|a_p|^2 + |r_p|^2)\sin^2\theta_i + n_2^4 |t_p|^2 \sin^2\theta_t + \Lambda_2 \right) \Big), \tag{3.80}$$

where Λ_1 and Λ_2 are amplitude mixing terms coming from the products of total electric fields modelled as the arithmetic mean and are defined as

$$\Lambda_1 = -2\Re(a_p r_p^*)\cos^2\theta_i + 2\Re(a_p t_p^* \cos\theta_i \cos\theta_t^*) - 2\Re(r_p t_p^* \cos\theta_i \cos\theta_t^*), \tag{3.81}$$

$$\Lambda_2 = 2n_1^4 \Re(a_p r_p^*)\sin^2\theta_i + 2n_1^2 n_2^2 (\Re(a_p t_p^*) + \Re(r_p t_p^*))\sin\theta_i \sin\theta_t. \tag{3.82}$$

The total absorption in this case is defined by the interfacial loss term of energy conservation divided by $n_1 \cos\theta_i / z_0$. This solution indicates that including surrounding dielectric materials through the vacuum gap method has significant consequences for the absorption characteristics of the out-of-plane response. All of the out-of-plane conductivity terms are scaled by terms to the fourth order in the indices of the surrounding dielectrics, though after the dielectric screening in equation 2.47, the scaling will be to the second order in the indices. As a consequence, analysis of the losses in a 2D material like graphene could present an avenue for verifying the physical validity of the vacuum gap method, along with harmonic mean screening, as losses have a component that should increase in proportion to the surrounding dielectric materials. In particular, based on the dielectric screening by the harmonic mean of the surrounding dielectric constants, the incident and reflected terms will be scaled by n_1^2/n_2^2 and the transmitted by n_2^2/n_1^2. This indicates that an experiment may benefit from being designed to maximize the influence of surrounding materials by considering $n_2 > n_1$ and taking measurements around the Brewster angle, as defined in Appendix A.2, because this will maximize the transmittance.

The absorptions defined in equations 3.79, and 3.80 can be combined with the same Poynting vector contributions for the in-plane case, defined in equations 3.48, and 3.50 for vacuum, and equations 3.70, and 3.71 for material, to construct the full energy conservation equations.

3.4.3 Numerical validation

In general, conservation of energy is described in terms of Fourier amplitudes of monochromatic plane waves by equation 3.17. The energy conservation equation consists of a comparison between the energy losses at the interface and the difference between the Poynting vector contributions above and below the interface.

Here, we will verify that neither the Fresnel amplitudes defined in equations 2.59-2.62, nor the vacuum gap method violate conservation of energy. We will do so by evaluating the conservation equations that were derived in terms of Fresnel amplitudes in the preceding subsection numerically using the artificially constructed conductivities shown in figure 3.2, and the Fresnel amplitudes shown in equations 2.59-2.62. Then we will evaluate the difference between the loss terms and the Poynting vector flux differences, corresponding to the left and right sides of equation 3.17, for each configuration to ensure that they are satisfied,

$$\Delta E = L.S. - R.S. \tag{3.83}$$

If the derived equations satisfy conservation of energy, then the difference should be zero.

First will be the case with no out-of-plane response ($\sigma_z = 0$), in vacuum surroundings ($n_1 = n_2 = 1$). Energy conservation in this case was described in terms of Fresnel amplitudes prior to any rearranging by equation 3.51, and the difference between the energy loss term and the Poynting vectors is shown in figure 3.3 (a). For vacuum surroundings with

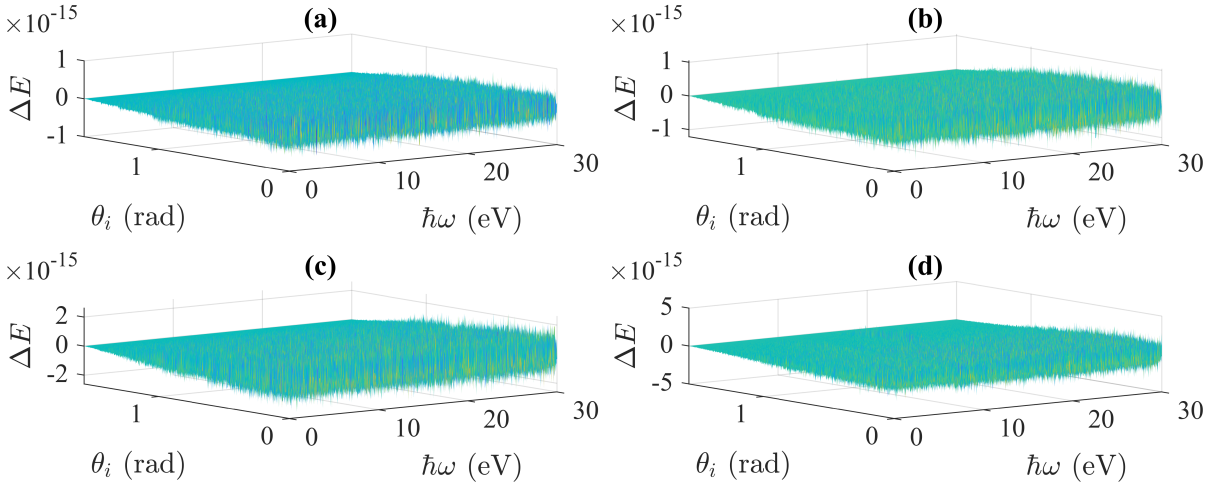


Figure 3.3: Numerical validation of the conservation of energy equations for (a) $\sigma_z = 0$ and $n_1 = n_2 = 1$, (b) $\sigma_z \neq 0$ and $n_1 = n_2 = 1$, (c) $\sigma_z = 0$ and $n_1 = 1.5, n_2 = 2$ (d) $\sigma_z \neq 0$ and $n_1 = 1.5, n_2 = 2$. $\Delta E = L.S. - R.S.$ of the energy conservation equation.

out-of-plane response included, the losses at the interface are described by equation 3.79, while the Poynting vector contribution is described by the difference between equations 3.48 and 3.50. The difference in this case is shown in figure 3.3 (b). For material surroundings ($n_1 = 1.5$, $n_2 = 2$), in the case without out-of-plane response, energy conservation is described by equation 3.72. This case is shown in figure 3.3 (c). For material surroundings with out-of-plane response, the losses at the interface are described by equation 3.80, while the Poynting vector contribution is described by equations 3.67 and 3.70. The difference in this case is shown in figure 3.3 (d).

In each case, the difference is apparently stochastic, and qualitatively identical. The magnitude of the difference never exceeded roughly 10^{-15}, which we attribute to numerical imprecision. So, the derived equations are self-consistent under the application of the Fresnel field amplitudes derived in equations 2.59-2.62 of section 2.3. It also confirms that the inclusion of material influence through the vacuum gap method does not violate the energy conservation equation, as well as the fact that the energy conservation equation, and by association the standard forms of reflectance and transmittance, appropriately

takes into account the effect of out-of-plane response. It further confirms in general that the Fresnel amplitudes themselves appropriately incorporate the effect of out-of-plane, or at least that they do it in a way that does not violate conservation of energy.

3.5 Linear momentum

All of the expressions in the following subsections have been derived using the symbolic algebra capabilities of Maple [62].

The linear momentum conservation equation (3.27) is used for numerical comparison, just like the energy conservation equation, between something that is happening at the central interface, to some combination of fields evaluated at external observation planes. In this case, the combination of fields in the right-hand side of equation 3.27 is defined by the electromagnetic stress tensor $\overleftrightarrow{T}$. In vacuum, there is no debate over the correct form for this tensor. It is called Maxwell's stress tensor,

$$\overleftrightarrow{T} = \epsilon_0 \mathbf{E}\mathbf{E} + \mu_0 \mathbf{H}\mathbf{H} - \frac{1}{2}\overleftrightarrow{I}\left(\epsilon_0 \mathbf{E}\cdot\mathbf{E} + \mu_0 \mathbf{H}\cdot\mathbf{H}\right), \tag{3.84}$$

and its derivation can be found in any electromagnetism textbook [41]. To account for the influence of materials, the vacuum gap method is being applied. As such, this well-accepted vacuum stress tensor will be used throughout this section, and any modifications for material surroundings will follow from the application of the conditions 3.29 and 3.31.

3.5.1 In-plane anisotropic, no out-of-plane

Considering a 2D material modelled by a sheet of in-plane conductivity, equation 3.33. The charge density term of the Lorentz force component of momentum conservation, defined in equation 3.27, for vacuum surroundings becomes,

$$\rho_0(q,\omega)\mathbf{E}_0^{av*}(q,\omega) = \frac{q}{\omega} J_q \mathbf{E}_0^{av*}(q,\omega), \tag{3.85}$$

$$= \left(\frac{q}{\omega}(\sigma_q E_q + \sigma_c E_\tau)\right)\begin{pmatrix} E_q^* \\ E_\tau^* \\ E_z^* \end{pmatrix}, \tag{3.86}$$

$$= \frac{q}{\omega}\left(\sigma_q \begin{pmatrix} |E_q|^2 \\ E_q E_\tau^* \\ E_q E_z^* \end{pmatrix} + \sigma_c \begin{pmatrix} E_\tau E_q^* \\ |E_\tau|^2 \\ E_\tau E_z^* \end{pmatrix}\right). \tag{3.87}$$

The process of casting this equation in terms of Fresnel field amplitudes is again identical to that shown in subsection 3.4.1. As such, only the final result will be shown. Beginning with vacuum surroundings, the Lorentz force contribution on the right-hand side of equation 3.27 takes the form

$$\begin{aligned}
&\Re\left(\rho_0(q,\omega)\mathbf{E}_0^{av*}(q,\omega)\right) + \Re\left(\mathbf{J}_0(q,\omega)\times\mathbf{B}_0^{av*}(q,\omega)\right) \\
&= \frac{k_0}{2\omega}\begin{pmatrix} 2\Re(\sigma_q)|t_p|^2\cos^2\theta\sin\theta + 2\Re(\sigma_\tau)|t_s|^2\sin\theta \\ 0 \\ \Re(\sigma_q)|t_p|^2\cos^3\theta + \Re(\sigma_\tau)|t_s|^2\cos\theta + \Re\left(\sigma_q(t_p r_p^* + t_p a_p^*)\cos^3\theta + \sigma_\tau(t_s a_s^* - t_s r_s^*)\cos\theta\right) \end{pmatrix} \\
&\qquad - \frac{k_0\cos^2\theta}{2\omega}\begin{pmatrix} 4\Re(\sigma_c)\Re(t_p t_s^*)\tan\theta \\ 0 \\ 2\Re(\sigma_c)\Re(t_p t_s^*) + \Re(\sigma_c t_s(a_p^* + r_p^*)) + \Re(\sigma_c t_p(a_s^* - r_s^*)) \end{pmatrix}, \quad (3.88)
\end{aligned}$$

where the transverse component of the force has canceled. This indicates that on an anisotropic 2D material suspended in vacuum, plane waves can only impart longitudinal and out-of-plane forces.

Next comes the stress tensor contribution to conservation of linear momentum in vacuum. Based on the standard Maxwell stress tensor in equation 3.84, this contribution can be written in terms of general field amplitudes as

$$\begin{aligned}
\overleftrightarrow{T}\cdot\hat{z} &= \left(\epsilon_0 E_q E_z^* + \mu_0 H_q H_z^*\right)\hat{q} + \left(\epsilon_0 E_\tau E_z^* + \mu_0 H_\tau H_z^*\right)\hat{\tau} \\
&\quad + \frac{1}{2}\left(\epsilon_0(|E_z|^2 - |E_q|^2 - |E_\tau|^2) + \mu_0(|H_z|^2 - |H_q|^2 - |H_\tau|^2)\right)\hat{z}. \quad (3.89)
\end{aligned}$$

Inserting the Fresnel amplitudes into this expression expands its size greatly. However, by simultaneously using the substitution $z_0 = \sqrt{\mu_0/\epsilon_0}$, the electric and magnetic field amplitudes can be collected together. For the transmitted side,

$$\overleftrightarrow{T}\cdot\hat{z}\Big|_{z_2} = -\epsilon_0\cos\theta\begin{pmatrix} (|t_p|^2 + |t_s|^2)\sin\theta \\ 2i\Im(t_p t_s^*)\tan\theta \\ (|t_p|^2 + |t_s|^2)\cos\theta \end{pmatrix}, \quad (3.90)$$

and for the incident side,

$$\overleftrightarrow{T}\cdot\hat{z}\Big|_{z_1} = -\epsilon_0\cos\theta\begin{pmatrix} \left(|a_p|^2 - |r_p|^2 + |a_s|^2 - |r_s|^2 + 2i\Im((a_s r_s^* + a_p r_p^*)e^{2ik_z z_1})\right)\sin\theta \\ 2i\Im(r_p r_s^* + a_p a_s^* + (a_p r_s^* - a_s r_p^*)e^{2ik_z z_1})\tan\theta \\ (|a_p|^2 + |a_s|^2 + |r_p|^2 + |r_s|^2)\cos\theta \end{pmatrix}. \quad (3.91)$$

Inserting these results into the stress tensor component in the right-hand side of equation 3.27,

$$\Re(\overleftrightarrow{T})\cdot\hat{z}\Big|_{z_1}^{z_2} = -\epsilon_0\cos\theta\begin{pmatrix}(|t_p|^2+|t_s|^2)\sin\theta-(|a_p|^2-|r_p|^2+|a_s|^2-|r_s|^2)\sin\theta\\0\\(|t_p|^2+|t_s|^2)\cos\theta-(|a_p|^2+|a_s|^2+|r_p|^2+|r_s|^2)\cos\theta\end{pmatrix}. \tag{3.92}$$

Taking the real part has eliminated the transverse component of the force, bringing this side into alignment with the Lorentz force contribution. This expression can be equivalently represented in terms of the reflectance, transmittance, and absorbance,

$$\Re(\overleftrightarrow{T})\cdot\hat{z}_2-\Re(\overleftrightarrow{T})\cdot\hat{z}_1 = \epsilon_0\cos\theta\begin{pmatrix}|a_p|^2(1-T_p-R_p)\sin\theta+|a_s|^2(1-T_s-R_s)\sin\theta\\0\\|a_p|^2(1-T_p+R_p)\cos\theta+|a_s|^2(1-T_s+R_s)\cos\theta\end{pmatrix}, \tag{3.93}$$

$$= \epsilon_0\cos\theta\begin{pmatrix}|a_p|^2A_p\sin\theta+|a_s|^2A_s\sin\theta\\0\\|a_p|^2(A_p+2R_p)\cos\theta+|a_s|^2(A_s+2R_s)\cos\theta\end{pmatrix}, \tag{3.94}$$

where $A_p = 1-T_p-R_p$, and $A_s = 1-T_s-R_s$. In this form, we can glean some physical insight into the process. The in-plane force is fully described by the absorption at the interface, while the out-of-plane force has an additional reflectance contribution. This could be a result of the direction change of the incident light. Force is equal to changing momentum, and to reflect the motion of anything, the momentum of that thing must change by twice its total magnitude. This fact may be reflected here in the additional reflectance contribution.

To consider material surroundings, we again repeat the vacuum gap derivation with the full set of four fields, as outlined in the preceding section. Then, the conditions in 3.29 and 3.31 are applied to find the influence of material surroundings. For an example of the interim step of repeating the vacuum derivation with four fields, see subsection 3.4.1. This step is not shown here as the resulting expressions are too large to be useful. Following

through this process, equation 3.88 becomes, for dielectric surroundings,

$$\begin{aligned}
&\Re\left(\rho_0(q,\omega)\mathbf{E}_0^{av*}(q,\omega)\right) + \Re\left(\mathbf{J}_0(q,\omega)\times\mathbf{B}_0^{av*}(q,\omega)\right) \\
&= \frac{k_0}{2\omega}\begin{pmatrix} 2\Re(\sigma_q)|t_p|^2|\cos\theta_t|^2\sin\theta + 2\Re(\sigma_\tau)|t_s|^2\sin\theta \\ 0 \\ n_2\Re(\sigma_q\cos\theta_t)|t_p|^2\cos^2\theta + n_2\Re(\sigma_\tau\cos\theta_t^*)|t_s|^2 + n_1\Re(\sigma_q t_p(a_p^*+r_p^*)\cos\theta_t)\cos^2\theta + n_1\Re(\sigma_\tau t_s(a_s^*-r_s^*))\cos\theta_i \end{pmatrix} \\
&\quad -\frac{k_0}{2\omega}\begin{pmatrix} 4\Re(\sigma_c)\Re(t_p t_s^*\cos\theta_t)\sin\theta \\ 0 \\ \Re(\sigma_c t_p(n_2 t_s^*\cos\theta_t^* + n_1(a_s^*-r_s^*)\cos\theta_i)\cos\theta_t) + \Re(\sigma_c t_s(n_2 t_p^* + n_1(a_p^*+r_p^*)))\cos^2\theta \end{pmatrix}.
\end{aligned} \tag{3.95}$$

While this expression is also cumbersome enough to have little use, it does reveal an interesting consequence of evanescence. In the $\hat{z}$ direction there are the evanescent switching terms. Whereas with vacuum surroundings the contributions from real or imaginary parts of the conductivity are in a sense fixed, here terms like $\Re(\sigma\cos\theta_t)$ will switch between the real and imaginary part of σ when $\cos\theta_t$ is itself real or imaginary.

From the expanded form of the Lorentz force contribution to momentum conservation in equations 3.88 and 3.95, a much simpler form can be derived. This is done by converting back into representation by total fields,

$$\Re\left(\rho_0(q,\omega)\mathbf{E}_0^{av*}(q,\omega)\right) + \Re\left(\mathbf{J}_0(q,\omega)\times\mathbf{B}_0^{av*}(q,\omega)\right) = \begin{pmatrix} \frac{q}{\omega}\Re(J_q E_q^* + J_\tau E_\tau^*) \\ 0 \\ \Re(J_q B_\tau^*\cos^2\theta - J_\tau B_q^*) \end{pmatrix}. \tag{3.96}$$

This result holds for both the case with and without material surroundings.

Now considering the stress tensor side of momentum conservation, by applying the vacuum gap method to consider material surroundings, equation 3.90 becomes,

$$\Re(\overleftrightarrow{T})\cdot\hat{z}\Big|_{z_1} = -\frac{\epsilon_0}{2}\begin{pmatrix} 2n_2(|t_p|^2+|t_s|^2)\sin\theta\Re(\cos\theta_t) \\ 0 \\ (|\cos\theta_t|^2 + n_2^2\cos^2\theta)|t_p|^2 + (n_2^2|\cos\theta_t|^2 + \cos^2\theta)|t_s|^2 \end{pmatrix}, \tag{3.97}$$

and equation 3.91,

$$\begin{aligned}
\Re(\overleftrightarrow{T})\cdot\hat{z}\Big|_{z_2} &= -\frac{\epsilon_0}{2}\begin{pmatrix} 2n_1(|a_p|^2 - |r_p|^2 + |a_s|^2 - |r_s|^2)\sin\theta\cos\theta_i \\ 0 \\ (n_1^2\cos^2\theta + \cos^2\theta_i)(|a_p|^2+|r_p|^2) + (n_1^2\cos^2\theta_i + \cos^2\theta)(|a_s|^2+|r_s|^2) \end{pmatrix} \\
&\quad + \epsilon_0\begin{pmatrix} 0 \\ 0 \\ \Re(a_s r_s^*)(n_1^2\cos^2\theta_i - \cos^2\theta) + \Re(a_p r_p^*)(\cos^2\theta_i - n_1^2\cos^2\theta) \end{pmatrix}.
\end{aligned} \tag{3.98}$$

The inclusion of material surroundings modifies the in-plane component through simple scaling by the refractive index, while in the out-of-plane direction, only a subset of the terms are scaled by the refractive indices.

It is somewhat difficult to interpret by just looking at the field amplitude components, but this result is actually different than the Minkowski stress tensor that is often used for dielectric surroundings. The Minkowski tensor takes the form,

$$\overleftrightarrow{T}_{Mink} = \mathbf{DE} + \mu_0 \mathbf{HH} - \frac{1}{2}\overleftrightarrow{I}\left(\mathbf{D}\cdot\mathbf{E} + \mu_0 \mathbf{H}\cdot\mathbf{H}\right). \tag{3.99}$$

However, the above result, based on the vacuum gap method, suggests a stress tensor that instead takes the form,

$$\overleftrightarrow{T}_{vGap} = \epsilon_0 \begin{bmatrix} E_q \\ E_\tau \\ \frac{D_z}{\epsilon_0} \end{bmatrix} \otimes \begin{bmatrix} E_q \\ E_\tau \\ \frac{D_z}{\epsilon_0} \end{bmatrix} + \mu_0 \mathbf{HH} - \frac{1}{2}\overleftrightarrow{I}\left(\epsilon_0 \begin{bmatrix} E_q \\ E_\tau \\ \frac{D_z}{\epsilon_0} \end{bmatrix} \cdot \begin{bmatrix} E_q \\ E_\tau \\ \frac{D_z}{\epsilon_0} \end{bmatrix} + \mu_0 \mathbf{H}\cdot\mathbf{H}\right). \tag{3.100}$$

This new tensor predicts the exact same forces in the in-plane direction, however in the out-of-plane direction it predicts a stronger influence from the properties of the surrounding materials. The vacuum gap method is used to isolate the forces on the 2D material from the forces on the surrounding dielectrics. As such, the resulting vacuum gap stress tensor is distinct from the Minkowski tensor in that it predicts zero force when the 2D material is removed. The Minkowski tensor, on the other hand, will predict a non-zero force on an interface with no 2D material, because it includes the forces on the dielectrics themselves.

3.5.2 In-plane isotropic, with out-of-plane

When we add out-of-plane conductivity to this model, the only changes occur in the Lorentz force term on the left-hand side of equation 3.27. Just as in the energy conservation case, the terms evaluated off of the interface involve only field components and so are unchanged in form when we modify the interface itself. Here we are considering a sheet modeled by a conductivity tensor, defined in equation 3.34. With the out-of-plane response, the electric fields in the $\hat{q}$ direction become discontinuous, as indicated in equation 2.44, and so must be modelled as the average of the fields on either side. The conservation of momentum equation (3.27) when considering out-of-plane response includes a derivative in the out-of-plane direction. This derivative is applied to all three components of the total electric field at the interface. This necessitates that the in-plane transverse ($\hat{\tau}$) electric field is modeled as the average,

$$E_\tau = \frac{1}{2}(E_\tau^{(1)} + E_\tau^{(2)}), \tag{3.101}$$

even though the electric field in the $\hat{\tau}$ direction is continuous across the interface, because the derivative is not. In this case, the charge density term, defined in equation 3.20, of the Lorentz force component of momentum conservation, defined in equation 3.27, becomes for vacuum surroundings,

$$\left(\rho_0(q,\omega)\mathbf{E}_0^{av*}(q,\omega) - \rho_1(q,\omega)\left.\frac{\partial \mathbf{E}_0^{av*}(q,\omega,z)}{\partial z}\right|_{z\to 0^{\pm}}\right) = \frac{q}{\omega}J_q\mathbf{E}_0^{av*}(q,\omega) - \frac{i}{\omega}J_z^e\left.\frac{\partial \mathbf{E}_0^{av*}(q,\omega,z)}{\partial z}\right|_{z\to 0^{\pm}}, \tag{3.102}$$

$$= \frac{q}{\omega}\sigma_q\begin{pmatrix}|E_q|^2\\ E_qE_\tau^*\\ E_qE_z^*\end{pmatrix} - \frac{i}{\omega}\sigma_z^e\begin{pmatrix}E_zE_{q,z}^*\\ E_zE_{\tau,z}^*\\ E_zE_{z,z}^*\end{pmatrix}, \tag{3.103}$$

where the comma notation $E_{x,y}$ indicates the y derivative of the x component of $\mathbf{E}$. The current density contribution takes the form,

$$\mathbf{J}_0(q,\omega)\times\mathbf{B}_0^*(q,\omega) = \begin{pmatrix}J_q\\ J_\tau\\ J_z^e\end{pmatrix}\times\begin{pmatrix}B_q^*\\ B_\tau^*\\ B_z^*\end{pmatrix}, \tag{3.104}$$

$$= \begin{pmatrix}J_\tau B_z^* - J_z^eB_\tau^*\\ J_z^eB_q^* - J_qB_z^*\\ J_qB_\tau^* - J_\tau B_q^*\end{pmatrix}, \tag{3.105}$$

where all field amplitudes represent the total field at the interface modelled as the arithmetic mean.

The process of expansion into the Fresnel field amplitudes of the kind given in equations 1.68 and 1.69 has been covered extensively in section 3.4.1. Here, only the final results will be presented, though the process remains the same. In this case, the Lorenz force contribution to conservation of momentum, represented in terms of the Fresnel field amplitudes

is,

$$\Re\left(\rho_0(q,\omega)\mathbf{E}_0^{av*}(q,\omega)-\rho_1(q,\omega)\left.\frac{\partial\mathbf{E}_0^{av*}(q,\omega,z)}{\partial z}\right|_{z\to 0^{\pm}}\right)+\frac{1}{2}\Re\left(\mathbf{J}_0(q,\omega)\times\mathbf{B}_0^{*}(q,\omega)\right)$$
$$=\frac{k_0\sin^2\theta}{4\omega}\begin{pmatrix}\Re(\sigma_z^e)(|a_p|^2+|r_p|^2+|t_p|^2+2\Re(a_pt_p^*+a_pr_p^*+t_pr_p^*))\sin\theta\\0\\\Re(\sigma_z^e)(|a_p|^2-|r_p|^2+|t_p|^2+2\Re(a_pt_p^*))\cos\theta+2\Im(\sigma_z^e)\Im(t_pr_p^*+a_pr_p^*)\cos\theta\end{pmatrix}$$
$$+\frac{k_0}{4\omega}\begin{pmatrix}\Re(\sigma_q)(|a_p|^2+|r_p|^2+|t_p|^2+2\Re(a_pt_p^*-a_pr_p^*-t_pr_p^*))\cos^2\theta\sin\theta\\0\\\Re(\sigma_q)(|a_p|^2-|r_p|^2+|t_p|^2+2\Re(a_pt_p^*))\cos^3\theta-2\Im(\sigma_q)\Im(a_pr_p^*+t_pr_p^*)\cos^3\theta\end{pmatrix}$$
$$+\frac{k_0}{4\omega}\begin{pmatrix}4\Re(\sigma_\tau)|t_s|^2\sin\theta\\0\\\Re(\sigma_\tau)(|a_s|^2-|r_s|^2+|t_s|^2+2\Re(a_st_s^*))\cos\theta+2\Im(\sigma_\tau)\Im(a_sr_s^*+t_sr_s^*)\end{pmatrix}. \quad (3.106)$$

This is again a monstrous equation with little practical use, though we present it here as a confirmation that the inclusion of out-of-plane response does not introduce any in-plane transverse forces. To include the influence of surrounding dielectrics, the process again involves redoing the vacuum derivation with four total fields, and then applying the conditions 3.29 and 3.31 to relate the vacuum fields to those in the surrounding dielectrics. This process results in an expression far too large to be useful, so it will not be presented here. However, it can again be simplified by representation in terms of total fields. This yields,

$$\Re\left(\rho_0(q,\omega)\mathbf{E}_0^{av*}(q,\omega)-\rho_1(q,\omega)\left.\frac{\partial\mathbf{E}_0^{av*}(q,\omega,z)}{\partial z}\right|_{z\to 0^{\pm}}\right)+\frac{1}{2}\Re\left(\mathbf{J}_0(q,\omega)\times\mathbf{B}_0^{*}(q,\omega)\right)$$
$$=\begin{pmatrix}\frac{q}{\omega}\Re(J_z^eE_z^*+J_qE_q^*+J_\tau E_\tau^*)\\0\\-\frac{q}{\omega}\Re(J_z^eE_q^*)+\Re(J_qB_\tau^*\cos^2\theta-J_\tau B_q^*)\end{pmatrix}. \quad (3.107)$$

3.5.3 Numerical validation

To confirm that the derived equations uphold linear momentum conservation, we will again use the conductivity functions defined in equations 3.35-3.38 to ensure both sides of each equation produce the same results. We will do so in analogy to equation 3.83 by taking the difference between the result from the Lorentz force contribution (L.S.) and the Stress tensor difference (R.S.). The Fresnel field amplitudes used can be found in equations 2.59-2.62. In each case, we will only show the result for the out-of-plane force, but all

components were validated. First will be the case with no out-of-plane response ($\sigma_z = 0$), in vacuum surroundings ($n_1 = n_2 = 1$). To maintain momentum conservation in this case, the left-hand sides of equations 3.88 and 3.92 must be equal. To verify this, the difference between their right-hand sides is shown in figure 3.4 (a). For vacuum surroundings with out-of-plane response included, momentum conservation is described by the equality of the right-hand sides of equations 3.106 and 3.92. The difference in their right-hand sides is shown in figure 3.4 (b). For material surroundings ($n_1 = 1.5$, $n_2 = 2$), without out-of-plane response ($\sigma_z = 0$), the Lorentz force contribution to momentum conservation is described by equation 3.95, while the stress tensor contribution is described by the difference between equations 3.97, and 3.98. The difference between the Lorentz and stress tensor contributions for this configuration is shown in figure 3.4 (c). For material surroundings ($n_1 = 1.5$, $n_2 = 2$), with out-of-plane response, the equation for the Lorentz force contribution to momentum conservation was not written explicitly in terms of Fresnel amplitudes, though it is given implicitly in equation 3.107. The Lorentz force component of momentum conservation in this case is therefore described by equation 3.107, with the stress tensor component described by the difference between 3.97, and 3.98. The difference for this final case is shown in figure 3.4 (d). In each of these cases, the force is represented in terms of the vacuum permittivity ϵ_0. This appears as a natural choice given both the stress tensor difference and the Lorentz force have a common factor of ϵ_0. So, just as with the energy conservation equations, the linear momentum conservation equations are self-consistent under application of the Fresnel field amplitudes derived in section 2.3. This is quite significant. It confirms that the vacuum gap method, and the stress tensor that results from it, satisfy conservation of linear momentum. It also confirms that the standard vacuum Maxwell stress tensor properly captures the forces as a result of the out-of-plane response and that the choice to model the z derivative of the electric field at the interface as the arithmetic mean does not violate conservation of momentum. While the fact that the vacuum gap stress tensor satisfies conservation of linear momentum is encouraging for the physical validity of the vacuum gap method as a whole, without experimental evidence to compare force calculations against, it is not enough to be conclusive.

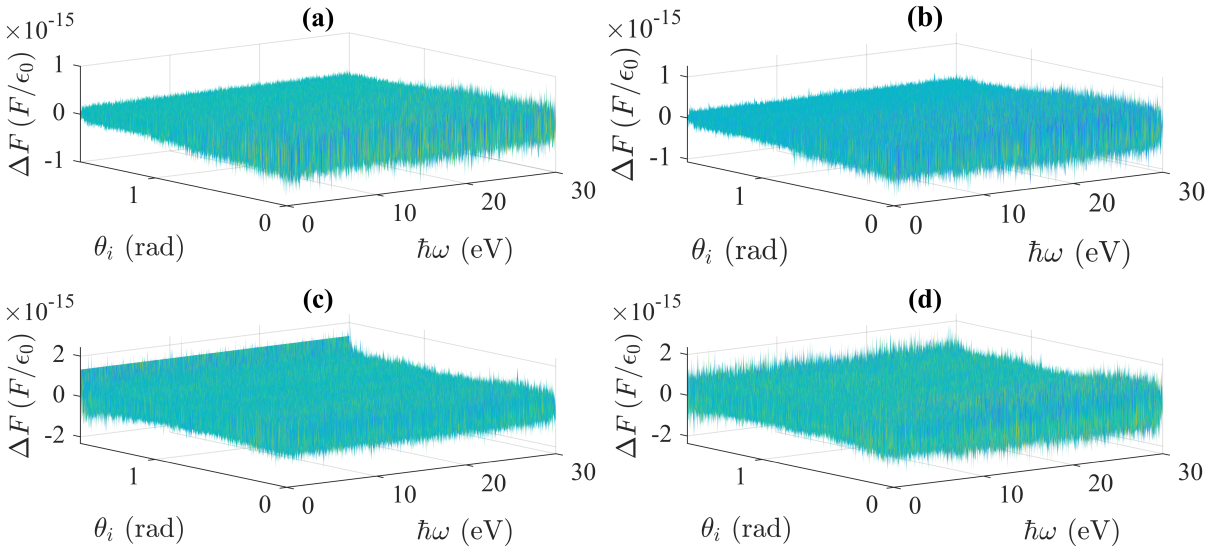


Figure 3.4: Numerical validation of the conservation of momentum equations for (a) $\sigma_z = 0$ and $n_1 = n_2 = 1$, (b) $\sigma_z \neq 0$ and $n_1 = n_2 = 1$, (c) $\sigma_z = 0$ and $n_1 = 1.5$, $n_2 = 2$, (d) $\sigma_z \neq 0$ and $n_1 = 1.5$, $n_2 = 2$. $\Delta F = L.S. - R.S.$ of the momentum conservation equation.

Chapter 4

Results for graphene

In the long wavelength limit, graphene is isotropic in the plane. However, as was indicated in section 1.6, when non-locality is considered, the in-plane longitudinal and transverse directions become distinct. While we are not considering this distinction, we have left the conductivity components distinct in all equations derived for graphene so that they are similarly applicable in the non-local case. Though again, when applying actual conductivity data, we will be considering in-plane isotropy given by $\sigma_\tau(\omega) = \sigma_q(\omega)$.

In this chapter, we will investigate the influence of out-of-plane response on the optical behaviour of graphene. Undoped graphene will be modelled by an *ab initio* conductivity response function digitized from [2], while doped graphene will be captured by a Drude model.

Even in the case of non-local analysis, graphene is modelled by a conductivity tensor defined as in equation 3.34. This means the Fresnel coefficients derived in section 2.3 can be simplified by setting the off-diagonal component to zero ($\sigma_c = 0$). This results in a set of simplified Fresnel coefficients that are valid for graphene,

$$t_p = -\frac{2n_1 \cos\theta_i f_3}{f_4 + 4f_1} a_p, \tag{4.1}$$

$$t_s = \frac{2n_1 \cos\theta_i}{f_2} a_s, \tag{4.2}$$

$$r_p = \left(1 - \frac{8n_1 \cos\theta_t + 2n_1 \tilde{\sigma}_z^e \sin^2\theta (\tilde{\sigma}_q \cos\theta_t + 4n_2)}{f_4 + 4f_1}\right) a_p, \tag{4.3}$$

$$r_s = \left(-1 + \frac{2n_1 \cos\theta_i}{f_2}\right) a_s, \tag{4.4}$$

where to simplify the expressions, we defined a set of functions,

$$f_1 = n_1 \cos\theta_t + n_2 \cos\theta_i + \tilde{\sigma}_q \cos\theta_t \cos\theta_i, \tag{4.5}$$
$$f_2 = n_1 \cos\theta_i + n_2 \cos\theta_t + \tilde{\sigma}_\tau, \tag{4.6}$$
$$f_3 = \sin^2\theta \sigma_q \tilde{\sigma}_z^e - 4 \tag{4.7}$$
$$f_4 = \sin^2\theta((n_2 \cos\theta_i + n_1 \cos\theta_t)\tilde{\sigma}_q + 4n_1 n_2)\tilde{\sigma}_z^e. \tag{4.8}$$

In each of the above equations, $\tilde{\sigma}$ indicates that the conductivity has absorbed a factor of z_0, and $\tilde{\sigma}_z^e = \epsilon_0 \tilde{\sigma}_z / \epsilon_\perp$ indicates that the conductivity is divided by the harmonic mean of relative dielectric constants of the surrounding media according to equation 2.47.

4.1 Undoped graphene

The *ab initio* response function used to model undoped graphene is shown in figure 4.1.

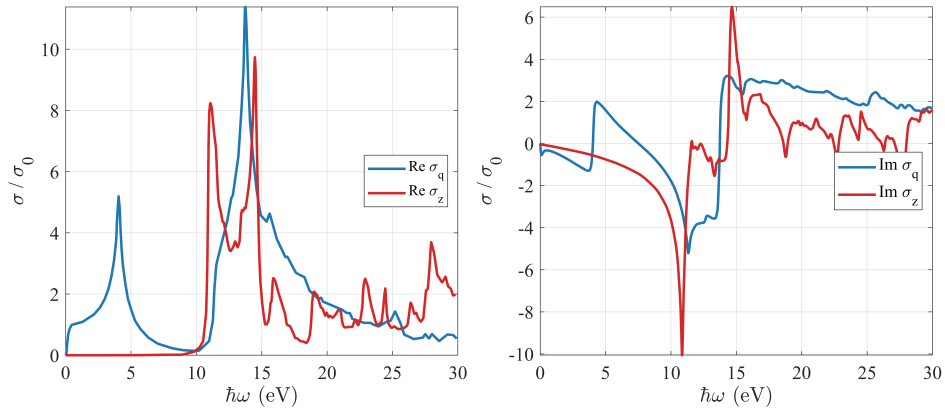


Figure 4.1: *Ab initio* response function of undoped graphene, digitized from [2]. $\sigma_0 = \pi\alpha/z_0$, where $\alpha = e^2/(\hbar c) \approx 1/137$ is the fine structure constant.

The *ab initio* conductivity response function for undoped graphene is computed up to $\hbar\omega = 30$ eV. This does not pose a problem for vacuum surroundings, as the energy of the incident radiation would have to be astronomical to disrupt the properties of the surroundings. For dielectric surroundings on the other hand, the approximation of a purely real, isotropic, and frequency-independent index of refraction becomes more difficult to

justify. In general, dielectrics have frequency-dependent optical properties. This frequency dependence can be modelled by the Sellmeier equation [63],

$$n^2(\omega) = 1 + \Sigma_i \frac{A_i}{B - C_i\omega^2}, \tag{4.9}$$

where A_i and C_i are constants determined by experiment, and $B = (2\pi c)^2$. C_i represents a squared resonant wavelength for the material, making the product $C_i\omega^2$ a kind of resonant wave speed. It cannot be said in general that any given material will have no resonant frequencies $(\mathrm{c}/\sqrt{C_i})$ across the entire $\hbar\omega = 0 - 30$ eV range. In this work, we will not consider the frequency dependence of the surrounding materials, so any results derived for the entire frequency range with dielectric surroundings do not necessarily correspond to any real surrounding material. They could, however, be locally accurate for materials with the appropriate index in the appropriate frequency range. While this makes broad spectrum comparisons to any given material impossible, the results can still be used for qualitative analysis of the influence of out-of-plane response with material surroundings.

It must also be noted that the frequency range $\hbar\omega = 0-30$ eV corresponds to a vacuum wavelength range of $\infty - 41$ nm. The validity of the infinitesimal sheet model rests on the assumption that the wavelength of the incident light is much longer than the thickness of the 2D material. Defining the thickness of graphene is more of a convention than a measurement, however, it is often taken to be $d = 0.34$ nm [24]. This number comes from the inter-layer spacing of bulk graphite. At this thickness, the ratio between the wavelength and the thickness is, at $\hbar\omega = 30$ eV, $\lambda/d \approx 120$. Whether or not this ratio is sufficient to use the sheet conductivity approximation for graphene would have to be determined through comparison to experiment. In this work, we will assume it is sufficient and use the sheet conductivity model for the whole range of energies.

4.1.1 Reflectance, transmittance, and absorption

We can see from the Fresnel coefficients in equations 4.1-4.4 that the out-of-plane conductivity only appears in the p-polarized amplitudes. So, in comparing the optical properties with and without out-of-plane contributions, we will only consider p-polarized light. This means the reflectance and transmittance can be defined simply, for unit incident amplitude $(a_p = 1)$, as,

$$R = \left| \frac{\left(n_2\tilde{\sigma}_z^2\tilde{\sigma}_q \sin^2\theta + 4\tilde{\sigma}_q\cos\theta_t + 4n_2\right)\cos\theta_i - \left((\tilde{\sigma}_z^e\tilde{\sigma}_q\sin^2\theta + 4)\cos\theta_t + 4n_2\tilde{\sigma}_z^e\sin^2\theta\right)n_1}{\left(n_2\tilde{\sigma}_z^2\tilde{\sigma}_q \sin^2\theta + 4\tilde{\sigma}_q\cos\theta_t + 4n_2\right)\cos\theta_i + \left((\tilde{\sigma}_z^e\tilde{\sigma}_q\sin^2\theta + 4)\cos\theta_t + 4n_2\tilde{\sigma}_z^e\sin^2\theta\right)n_1} \right|^2, \tag{4.10}$$

$$T = \frac{n_2 \Re(\cos\theta_t)}{n_1 \cos\theta_i} \times \left| \frac{2n_1 \cos\theta_i \left(\tilde{\sigma}_z^e \tilde{\sigma}_q \sin^2\theta - 4\right)}{\left(n_2 \tilde{\sigma}_z^2 \tilde{\sigma}_q \sin^2\theta + 4\tilde{\sigma}_q \cos\theta_t + 4n_2\right)\cos\theta_i + \left(\left(\tilde{\sigma}_z^e \tilde{\sigma}_q \sin^2\theta + 4\right)\cos\theta_t + 4n_2 \tilde{\sigma}_z^e \sin^2\theta\right) n_1} \right|^2, \tag{4.11}$$

from which the absorbance is derived as $A = 1 - R - T$. First, we shall examine the difference between the cases with and without out-of-plane response for each material configuration across the entire $\hbar\omega = 0 - 30$ eV frequency range. There are three possible material configurations using the simple non-magnetic, isotropic, lossless dielectrics, $n_1 = n_2$, $n_1 < n_2$, and $n_1 > n_2$. The first case, $n_1 = n_2 = 1$, is shown in figure 4.2.

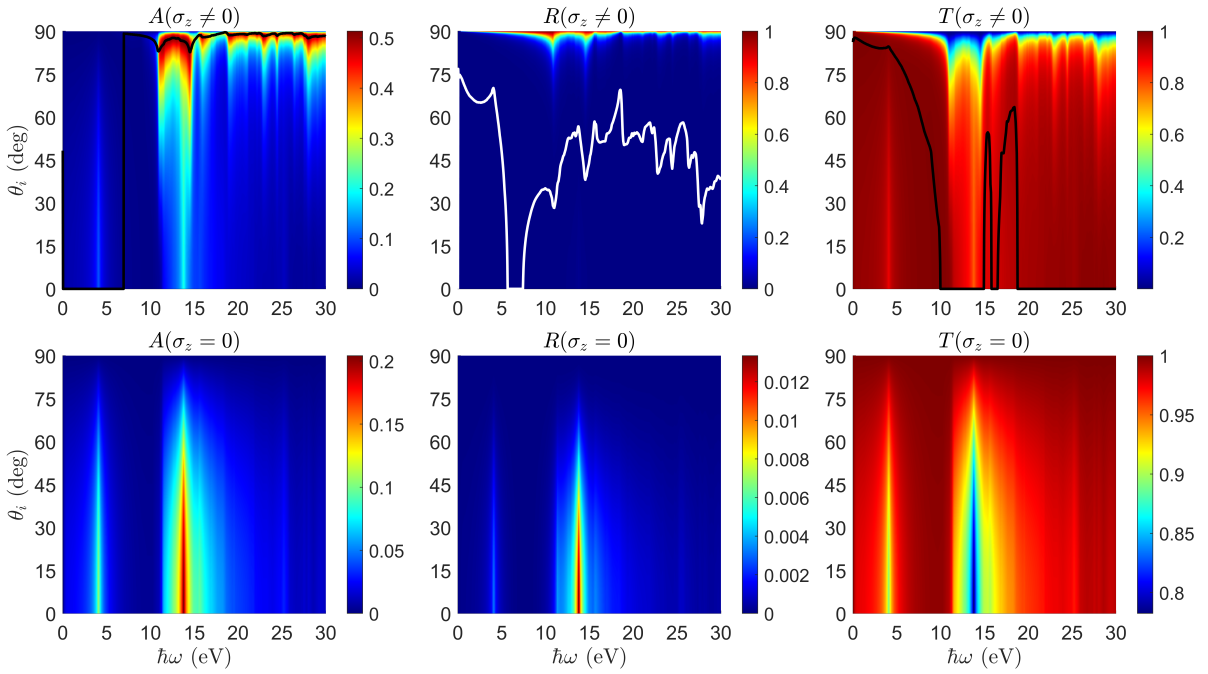


Figure 4.2: Absorbance, reflectance, and transmittance of graphene considering **TOP**: $\sigma_z \neq 0$, $\sigma_q \neq 0$ and **BOTTOM**: $\sigma_z = 0$, $\sigma_q \neq 0$. All cases considered with $n_1 = n_2 = 1$. Black lines indicate the maximum of a given spectra, and white lines indicate a minimum.

With vacuum surroundings, the introduction of out-of-plane conductivity produces a response that is qualitatively very different than the in-plane-only response. The response

of the in-plane-only case is most significant near $\theta_i = 0$, while the introduction of out-of-plane conductivity pulls the most prominent behaviour near $\theta_i = \pi/2$. This is likely because, for p-polarized light at normal incidence, the incident light is polarized perfectly in-plane, while for grazing incidence it is polarized perfectly out-of-plane. Interestingly, the out-of-plane conductivity does not pull the maximum absorption to the point where the electric field is maximally polarized in the out-of-plane direction ($\theta_i = \pi/2$); instead, it appears at a slightly lower angle. This occurs because the reflectance is invariably one at $\theta_i = \pi/2$, while the transmittance is zero. This ensures that the absorption is zero, and so the peak appearing slightly offset from the $\theta_i = \pi/2$ is a result of the balancing of this effect with the maximization of out-of-plane response from maximal out-of-plane polarization. The most significant change to the reflectance and transmittance is the creation of a ridge of perfect reflection near $\theta_i = \pi/2$. This ridge spans the entire frequency range, though it grows broader for larger conductivities, like near the peaks at 11 eV and 14.5 eV seen in the left panel of figure 4.1. This could be used to find the out-of-plane conductivity experimentally across a broad range of frequencies, as the in-plane only model predicts the reflectance will be nearly zero right up until $\theta_i = \pi/2$. An experiment of this kind could involve fitting reflectance measurements near $\theta_i = \pi/2$ to the reflectance function defined in equation 4.10, which when $n_1 = n_2$ simplifies to

$$R = \left| \frac{2\sigma_q \cos^2\theta_i - 2n^2\sigma_z \sin^2\theta_i}{(n\sigma_z \sin^2\theta_i + 2\cos\theta_i)(\sigma_q \cos\theta_i + 2n)} \right|^2 . \tag{4.12}$$

Alternatively, one could fit to a Brewster angle measurement. The addition of out-of-plane response creates a minimum in the reflectance where there is none with only in-plane response, as is evidenced by comparing the top and bottom middle panels in figure 4.2. This would potentially require a wider range of angle measurements if one does not already know where to look. Regardless, it would still be effective as the Brewster angle, like the reflectance ridge, is purely a product of the out-of-plane response. This method was used in [3] to measure the out-of-plane conductivity of graphene. It should be noted that with common dielectric surroundings $n_1 = n_2 = n$, the maximum of transmittance does not align with the minimum of reflectance, this is shown in figure 4.2. This is likely not a concern for measuring the Brewster angle to determine out-of-plane conductivity, but could be an important consideration when designing devices.

The next material configuration is $n_1 < n_2$, and is shown in figure 4.3. Similarly to the vacuum surroundings case, when $n_1 < n_2$, the maximum absorption is increased dramatically and drawn closer to $\theta_i = \pi/2$ in the presence of out-of-plane conductivity. Of note here is the difference in effect on the Brewster angle between the in-plane and out-of-plane conductivity. The reflectance calculations in figure 4.3 show that while large in-plane

conductivities serve to increase the Brewster angle, large out-of-plane conductivities serve to decrease the Brewster angle with respect to the value in the absence of a 2D material of $\theta_B \approx 56°$, which follows from equation A.5.

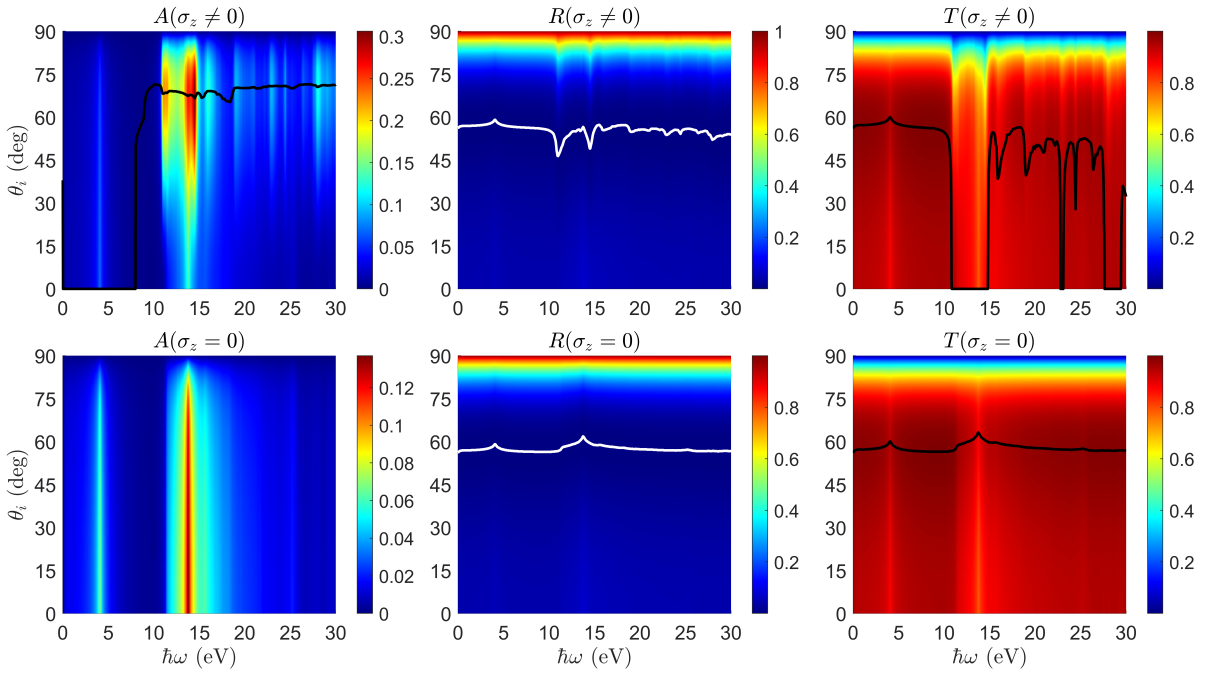


Figure 4.3: Absorbance, reflectance, and transmittance of graphene considering **TOP**: $\sigma_z \neq 0$, $\sigma_q \neq 0$ and **BOTTOM**: $\sigma_z = 0$, $\sigma_q \neq 0$. All cases considered with $n_1 = 1$, and $n_2 = 1.5$. Black lines indicate the maximum of a given spectra, and white lines indicate a minimum.

The final material configuration is $n_1 > n_2$, and is shown in figure 4.4. Besides the increase in absorption common across all three configurations, the most notable effect of the out-of-plane conductivity here is the maximum absorption appearing at the critical angle of $\theta_c \approx 41.8°$. The critical angle is defined in Appendix A.1, and it indicates the point past which the transmitted field becomes evanescent. However, exactly at the critical angle, the transmitted wave is not evanescent, but travelling along the interface. By travelling along the interface, a p-polarized transmitted wave is polarized perfectly out-of-plane. Theoretically, this would maximize the interaction between the transmitted wave and the out-of-plane conductivity, which could explain the maximum absorption at the critical angle. Also of note is how constant the maximum absorption remains across the entire range of in-plane conductivity values when $\sigma_z = 0$. While the absorption is entirely dependent on the presence of the sheet of conductivity at the interface, it would appear

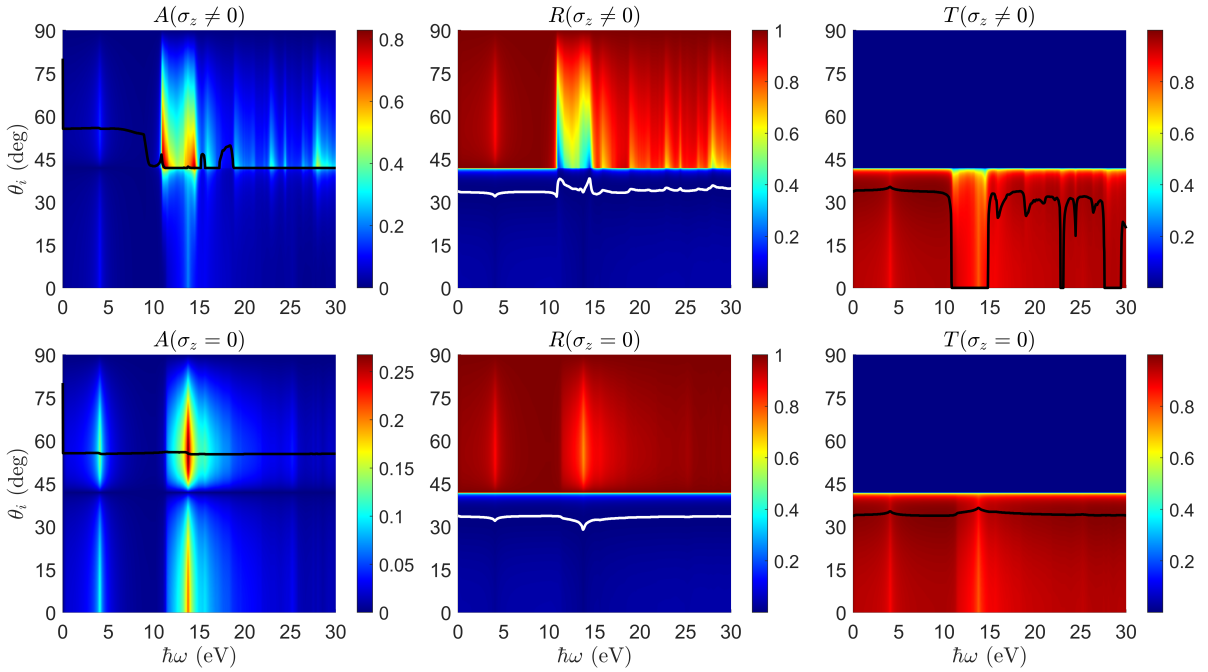


Figure 4.4: Absorbance, reflectance, and transmittance of graphene considering **TOP**: $\sigma_z \neq 0$, $\sigma_q \neq 0$ and **BOTTOM**: $\sigma_z = 0$, $\sigma_q \neq 0$. All cases considered with $n_1 = 1.5$, and $n_2 = 1$. Black lines indicate the maximum of a given spectra, and white lines indicate a minimum.

that the maximum absorption is more a consequence of the configuration of surrounding materials. In fact, Taylor expanding to the second order the absorbance when $\sigma_z = 0$, in terms of the in-plane conductivity, and solving for the extrema in terms of the incident angle yields a result that is totally independent of the conductivity,

$$\theta_{\max} = \arctan\left(\frac{n_2\sqrt{2n_1^2 - n_2^2 + \sqrt{8n_1^4 + n_2^4}}}{\sqrt{2n_1^4 + n_2^4 - n_2^2\sqrt{8n_1^4 + n_2^4}}}\right). \tag{4.13}$$

This equation predicts the maximum of absorption with $\sigma_z = 0$ to be $\theta_{\max} = 55.5^{\circ}$, which closely approximates the numerically derived value across the entire frequency range from $\hbar\omega = 0 - 30$ eV.

Also of note is the fact that the influence on Brewster angle from the in-plane and out-of-plane conductivities has reversed. In this configuration with $n_1 > n_2$, regions of large in-plane conductivity, shown in figure 4.1, can be mapped to decreases in the Brewster

angle as shown in the middle two panels of figure 4.4. Similarly, regions of large out-of-plane conductivity as shown in figure 4.1 can be mapped to increases in the Brester angle as shown in the middle two panels of figure 4.4. This has important consequences for any approximate expressions to the Brewster angle, as they would need to depend in some way on the difference between the two materials $(n_1 - n_2)$ so that the change in behaviour between the configurations could be captured.

4.1.2 Forces

Using the formalism developed in section 3.5 we can calculate optical forces on graphene with a variety of surrounding material configurations. We showed in section 3.5.3 that the Lorentz force and the stress tensor methods are equivalent under the application of the Fresnel amplitudes defined in equations 2.59-2.62. As such, all force calculations in this section will be based on the stress tensor method. This method involves evaluating the difference between the electromagnetic stress tensor on each side of the 2D material,

$$\mathbf{F} = \frac{1}{2}\Re\left(\overleftrightarrow{T}\cdot\hat{z}\Big|_{z_1}^{z_2}\right). \tag{4.14}$$

For vacuum surroundings, the standard Maxwell stress tensor will be used, which is defined in equation 3.84. For material surroundings, the vacuum gap stress tensor will be used, which is defined in equation 3.100.

Optical forces are generally very small, though they can still be an important consideration depending on the scale of the problem. The forces in the $\hat{z}$ and $\hat{q}$ directions for both the vacuum surroundings $(n_1 = n_2 = 1)$ and the substrate $(n_2 = 2, n_1 = 1)$ cases are shown in figure 4.5, both with and without out-of-plane response. Without the out-of-plane conductivity, there is almost no qualitative difference between the force profiles in the vacuum and substrate cases. The primary difference is a slight decrease in maximum amplitudes from the vacuum to the substrate cases for the force in the $\hat{z}$ direction of approximately 0.05 pPa. There is also a slight increase from the vacuum to the substrate cases for the force in the $\hat{q}$ direction, of again approximately 0.05 pPa. In terms of the difference between the cases with and without out-of-plane conductivity, the most significant effects are seen in the $\hat{q}$ direction. The force in the $\hat{q}$ direction, shown in the rightmost two columns of figure 4.5, exhibits the two new prominent force peaks that coincide with the positive peaks in the real part of the out-of-plane conductivity at approximately 11 eV and 14 eV, as shown in figure 4.1. It is clear that in both the vacuum and substrate cases, shown in figure 4.5, the in-plane forces are more strongly influenced by the introduction of out-of-plane conductivity.

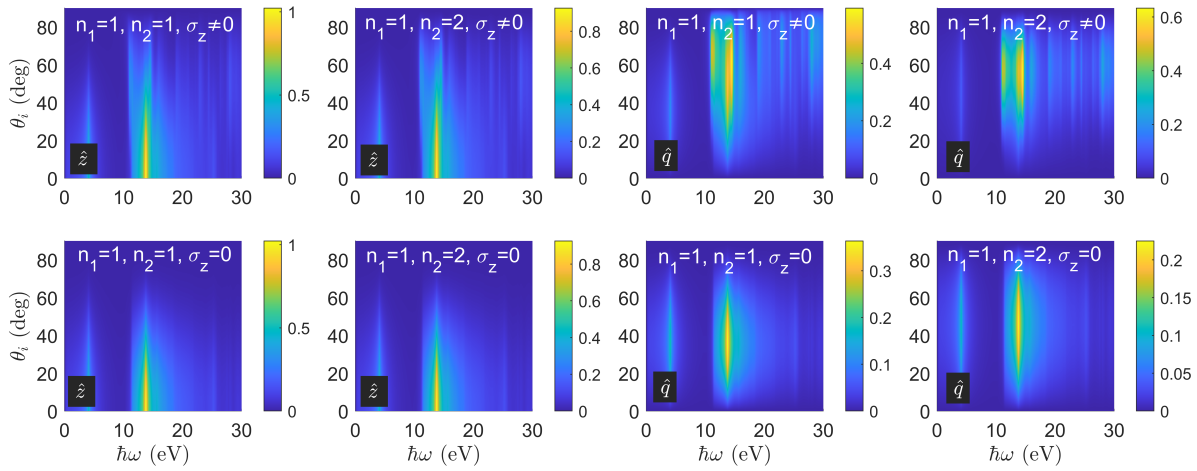


Figure 4.5: Forces in the $\hat{z}$ and $\hat{q}$ directions, measured in pPa, from p-polarized light on both $n_1 = n_2$ and $n_2 > n_1$ dielectric configurations both with and without out-of-plane conductivity.

The final material configuration is the case where $n_1 > n_2$, or specifically $n_1 = 2$ and $n_2 = 1$. In this configuration, the differences between the cases with and without out-of-plane conductivity are far more pronounced. In the $\hat{z}$ direction the most significant effect is the increase in maximum amplitude by a factor of approximately 6. This new peak coincides with peaks in both the real and imaginary part of the out-of-plane conductivity. The reason the 11 eV $\Re(\sigma_z)$ peak produces such a large force compared to the 14 eV peak is perhaps due to the fact that at 11 eV, $\Im(\sigma_z)$ has a negative peak, while at 14 eV $\Im(\sigma_z)$ is positive. It would appear, then, that force in the $\hat{z}$ direction is maximized in the evanescent regime by either negative peaks in the out-of-plane conductivity, or the combination $\Im(\sigma_z)\Re(\sigma_z) < 0$. For the force in the $\hat{q}$ direction the most notable change, besides a similar increase in amplitude of approximately a factor of three, is the shifting of the peak force to the critical angle. This is exactly what was shown to happen for the absorbance in figure 4.4. This effect can be understood by considering the force equation cast in terms of reflectance and absorbance. This equation was given originally in equation 3.94, and it states that for p-polarized light, the force on a 2D material in vacuum is given by,

$$\mathbf{F} = \frac{\epsilon_0}{2}\cos\theta \begin{pmatrix} |a_p|^2 A_p \sin\theta \\ 0 \\ |a_p|^2 (A_p + 2R_p)\cos\theta \end{pmatrix}. \tag{4.15}$$

This equation indicates that the force in the $\hat{q}$ direction is defined entirely by the ab-

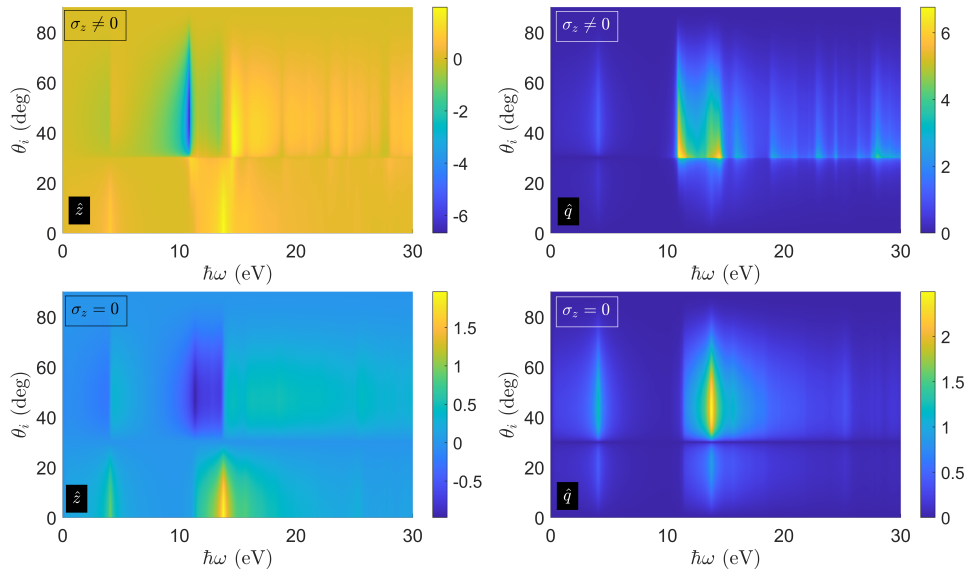


Figure 4.6: Forces in the $\hat{z}$ and $\hat{q}$ directions, measured in pPa, from p-polarized light and dielectric surroundings defined by $n_1 = 2$ and $n_2 = 1$, both with and without out-of-plane conductivity.

sorbance, hence the similar shifting of the peak to the critical angle. The same justification can then also be applied to the forces. It is possible that this shifting of the peak is a result of the p-polarized transmitted field propagating along the interface polarized perfectly out-of-plane. This out-of-plane polarization would maximize interaction with the out-of-plane conductivity.

4.1.3 Comparison to [1]

In [1], Fresnel coefficients were presented for 2D materials with in-plane anisotropy. In particular, strained graphene was being considered. However, also presented in the work were results for unstrained graphene at the universal conductivity of $\sigma_q = \sigma_0 = \pi\alpha/z_0$, or in Gaussian CGS coordinates, $\sigma_q = c\alpha/4 = v_B/4$, where v_B is the Borh speed. To help validate the models used in this work, and the results thereof, we present in figure 4.7 a comparison between the absorbance for graphene presented in [1], and the results from our model at the universal conductivity. This result does not include out-of-plane conductivity. The models in this work predict the same absorbance for graphene across the entire angular range.

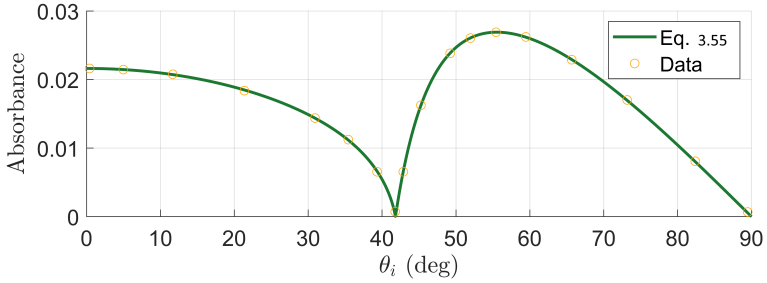


Figure 4.7: Comparison between the absorbance of graphene for p-polarized light, $\sigma_z = 0$, $\sigma_q = \pi\alpha/z_0$, and surrounding dielectrics defined by $n_1 = 1.5$ and $n_2 = 1$. Datapoints from [1]. Datapoints represent model predictions, not measurements.

As a further point of comparison for identifying the influence of out-of-plane conductivity, we can extend the results from [1]. We do so by evaluating our model with both in-plane (σ_q) and out-of-plane (σ_z) conductivities, defined in figure 4.1, at a frequency $\hbar\omega = 0.5$ eV. This frequency is chosen because at this point the *ab initio* response function of figure 4.1 predicts that $\Re(\sigma_q) \approx \pi\alpha/z_0$. The following analysis is then distinguished from [1] by the inclusion of $\sigma_z/\sigma_0 \approx 0 - 0.094i$ and $\Im(\sigma_q)/\sigma_0 \approx -0.331i$, making $\sigma_q/\sigma_0 \approx 1 - 0.331i$.

Figures 4.8, 4.9, and 4.10 show the difference between the optical response of undoped graphene at a frequency defined by $\hbar\omega = 0.5$ eV with out-of-plane conductivity, along with the deviation from the case without out-of-plane conductivity. The case with vacuum surroundings, shown in figure 4.8, is the most affected by the inclusion of out-of-plane conductivity. While the only significant deviation is near grazing incidence at $\theta_i = \pi/2$, it is multiple orders of magnitude larger than what is present in any other material configuration besides immersion ($n_1 = n_2 = n$), which is qualitatively identical to vacuum surroundings. In fact, across the entire angular range, and over the frequency range defined by $\hbar\omega = 0 - 1$ eV, the mean value of the absolute deviation between the reflectance with and without out-of-plane response, when $n_1 = n_2 = 1$, is $\langle|\Delta R|\rangle = 0.0016$, although if one omits the large deviation around $\theta_i = \pi/2$ by instead considering the angular range $\theta_i = 0 - 80\pi/180$, then for the $n_1 = n_2 = 1$ case, $\langle|\Delta R|\rangle = 3.3 \times 10^{-6}$. Among the other material configurations, deviations remain similarly small. When $n_1 = 1.5$, $n_2 = 1$, $\langle|\Delta R|\rangle = 2.7 \times 10^{-5}$, and for $n_1 = 1$, $n_2 = 1.5$, $\langle|\Delta R|\rangle = 2.3 \times 10^{-6}$. The final notable feature is the somewhat larger deviation of the $n_1 > n_2$ case shown in figure 4.10. This can be traced back to large deviations in the reflectance past the critical angle. This is indicative of the out-of-plane response being more influential in the evanescent regime.

On the whole, while there are regions where the inclusion of out-of-plane response can

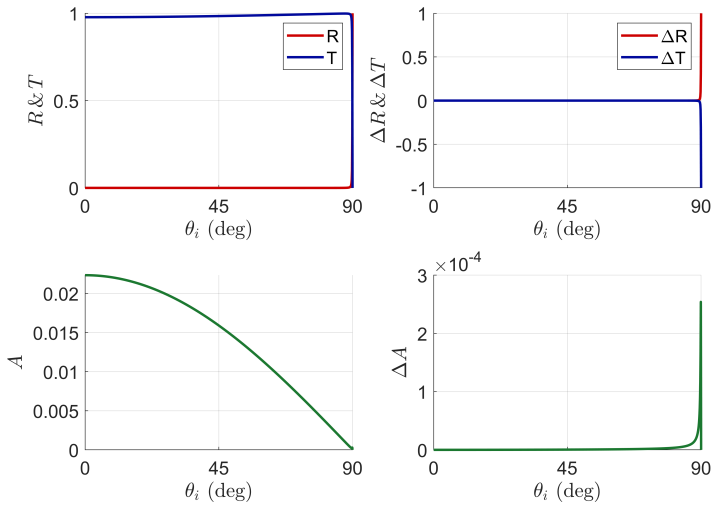


Figure 4.8: **LEFT**: Absorbance, reflectance, and transmittance of undoped graphene at a frequency defined by $\hbar\omega = 0.5$ eV. **RIGHT**: Difference between the absorbance, reflectance, and transmittance with and without out-of-plane response ($\Delta X = X(\sigma_z) - X(\sigma_z = 0)$). Each evaluated at $n_1 = 1$, $n_2 = 1$.

incite strong changes to the reflectance and transmittance, it is clear that in the frequency range defined by $\hbar\omega = 0-1$ eV, the commonly held assumption of out-of-plane conductivity being inconsequential is mostly true at the level of reflectance and transmittance. This is as long as one remains away from the large deviations around $\theta_i = \pi/2$.

4.1.4 Comparison to [2]

The same paper that provided the *ab initio* conductivity data shown in figure 4.1 also presented some absorbance calculations using their conductivity response function. We present here a brief comparison between the absorbance predicted by the model developed in this work, and those of [2]. The absorbance from [2] includes the effect of out-of-plane conductivity, so this comparison serves to confirm the form of our Fresnel amplitudes with out-of-plane conductivity. Figure 4.11 shows the comparison between the model developed in this work and that of [2] for vacuum surroundings and an incident angle $\theta_i = \pi/4$.

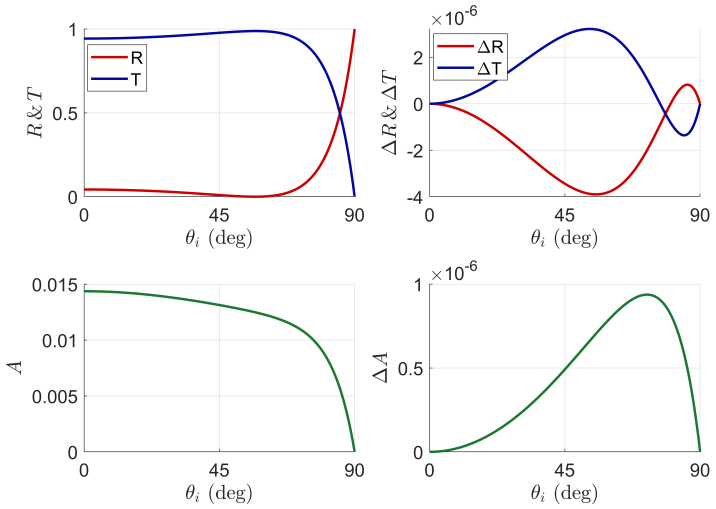


Figure 4.9: **LEFT**: Absorbance, reflectance, and transmittance of undoped graphene at a frequency defined by $\hbar\omega = 0.5$ eV. **RIGHT**: Difference between the absorbance, reflectance, and transmittance with and without out-of-plane response ($\Delta X = X(\sigma_z) - X(\sigma_z = 0)$). Each evaluated at $n_1 = 1$, $n_2 = 1.5$.

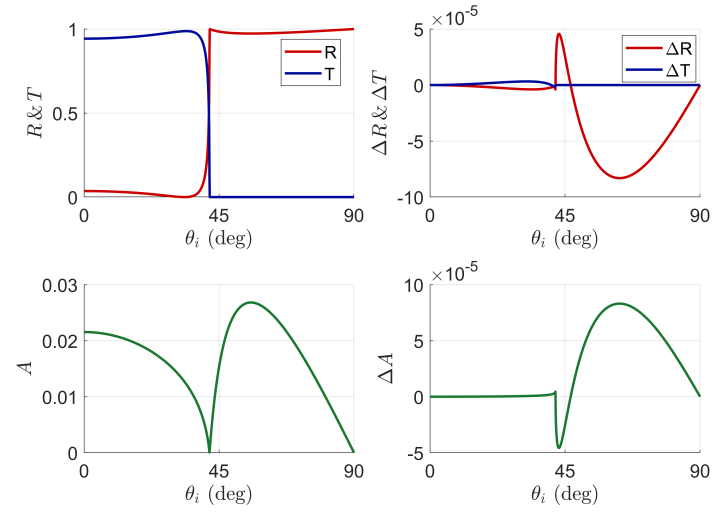


Figure 4.10: **LEFT**: Absorbance, reflectance, and transmittance of undoped graphene at a frequency defined by $\hbar\omega = 0.5$ eV. **RIGHT**: Difference between the absorbance, reflectance, and transmittance with and without out-of-plane response ($\Delta X = X(\sigma_z) - X(\sigma_z = 0)$). Each evaluated at $n_1 = 1.5$, $n_2 = 1$.

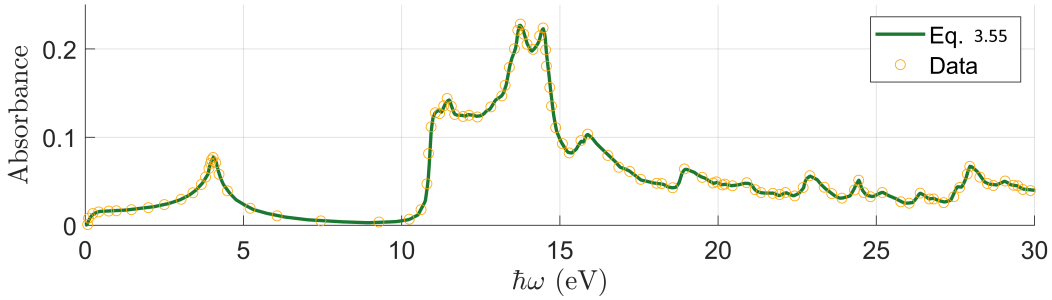


Figure 4.11: Continuous curve represents absorbance calculations from this work. Data points show the results from [2]. Both results for vacuum surroundings and $\theta_i = \pi/4$. Datapoints represent model predictions, not measurements.

4.1.5 Comparison to [3]

Research into the out-of-plane response of 2D materials is in its infancy, so there are few published works seeking measurements of out-of-plane conductivity. The only such case for single-layer graphene that the author is aware of is [3]. In this paper, an ellipsometer is used at a wavelength of 633 nm, or around $\hbar\omega = 1.95$ eV, to measure both the in-plane and out-of-plane conductivities. To ensure the out-of-plane response is well distinguishable from other influences, like the substrate, the graphene sample is fully emersed in a poly-dimethylsiloxane (PDMS) prism. The reasoning for this is that when fully immersed in a medium, the only reflection from the interface comes from the 2D material itself; if the 2D material was gone, there would be no interface. They further focus their measurements around the Brewster angle, which given the identical surrounding materials, is a direct product of the out-of-plane conductivity; this was shown using our model in figure 4.2.

Ellipsometry is a measurement technique that operates on the principle that most media influence s and p polarization differently. This can be seen in the different forms of the Fresnel amplitudes in the s and p directions derived in section 2.3. The method begins with polarizing some incident light source to a known state, say 45^o for equal contributions. The source is then reflected off of the sample and fed through another polarizer. The second polarizer will vary the intensity of the reflected light before measurement, encoding information about the polarization state of the reflected wave. There are a number of ways to extract the polarization information from the measured intensity, though one of the simplest is likely just rotating the second polarizer and taking multiple measurements [64].

The primary equation of ellipsometry is,

$$\tan\Psi\, e^{i\Delta} = \frac{r_p}{r_s}, \tag{4.16}$$

where $\tan\Psi$ is the amplitude, Δ is the phase angle, and r_p/r_s is the ratio of the reflected s and p Fresnel amplitudes. The parameters Ψ and Δ are extracted from the measurements, which can then be used to extract material parameters from the model-based Fresnel amplitudes.

In [3], a very similar model to the one developed in this work was used to calculate the Fresnel amplitudes. While it appears that in [3] the arithmetic mean of the polarizing electric field is not used directly, the Fresnel reflection coefficient that they quote for the case of graphene immersed in a homogeneous dielectric is equivalent to equation 4.3, when $n_1 = n_2 = n$, which we have developed using the arithmetic mean. The model they quote as having derived for the case of immersion is,

$$r_p = \frac{(ik_0\chi_\parallel + z_0\sigma_\parallel)\cos\theta}{(ik_0\chi_\parallel + z_0\sigma_\parallel)\cos\theta + 2n} - \frac{n(ik_0\chi_\perp + z_0\sigma_\perp)\sin^2\theta}{2\cos\theta + n(ik_0\chi_\perp + z_0\sigma_\perp)\sin^2\theta}, \tag{4.17}$$

where $\chi_\parallel$ and $\sigma_\parallel$ are real-valued parameters representing the in-plane response, and $\chi_\perp$ and $\sigma_\perp$ are real-valued parameters representing the out-of-plane response. They adopt a model for the sheet response that considers current and polarization separately, while we consider them to be interchangeable based on the general relationship between conductivity and susceptibility, $\sigma = -i\omega\epsilon_0\chi$. Our model, defined for graphene in equation 4.3, generates a reflected field amplitude for immersion in a homogeneous dielectric ($n_1 = n_2 = n$) of the form,

$$r_p = \frac{\tilde{\sigma}_q\cos\theta}{\tilde{\sigma}_q\cos\theta + 2n} - \frac{n\tilde{\sigma}_z\sin^2\theta}{2\cos\theta + n\tilde{\sigma}_z\sin^2\theta}. \tag{4.18}$$

The two models are identical when we express our normalized conductivities as $\tilde{\sigma}_q = z_0\sigma_\parallel + ik_0\chi_\parallel$ and $\tilde{\sigma}_z = z_0\sigma_\perp + ik_0\chi_\perp$, where $k_0 = -\omega/c$ because they used the sign convention $e^{i\omega t}$ for time dependence instead of $e^{-i\omega t}$. In other words, the real and imaginary parts of our conductivities $\sigma_{q/z}$ are proportional to their parameters $\sigma_{\parallel/\perp}$ and $\chi_{\parallel/\perp}$, respectively.

The equivalence between these two models for the case of full immersion is significant because, using their model, they were able to calculate very accurate conductivities for single-layer graphene, when compared to *ab initio* data. In particular, they reported $\Im(\tilde{\sigma}_z) = 0.006$ for the imaginary part of the normalized out-of-plane conductivity, which is almost exactly the value predicted by the *ab initio* data in figure 4.1. However, their methodology was insufficient for calculating the contribution from the real part of the

out-of-plane conductivity, as they stated it could not be distinguished from zero with their experimental error. The value they do quote for this parameter is larger than that predicted by *ab initio* calculations, but still small as expected.

Figure 4.12 shows a comparison between the reflectance model developed in this work, and that of [3], both using the conductivity parameters derived in the paper. The agreement between our model and theirs is nearly exact. The subtle differences that are present can be attributed to the process of digitizing the data from plots in [3].

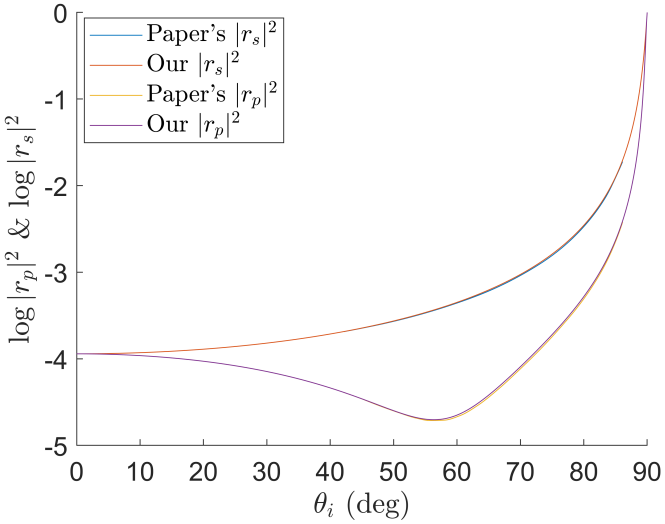


Figure 4.12: Comparison of s and p-polarized reflectances digitized from measurements presented in [3], and model predictions from equations 4.3 and 4.4. Data presented for immersion in a homogeneous dielectric defined by $n = 1.4233$. The model curves overlap with the measurement curves.

In this paper, they also quote a model derived for graphene on a substrate. Interestingly, while it is not mentioned in the paper, this model is equivalent to the model developed in [5], where the 2D material is ever so slightly immersed in one of the two materials at an interface. This would base the model from [3] on an out-of-plane boundary condition with screening by only the substrate (ϵ_0/ϵ_2), but also the total electric field modelled as the weighted average of the electric fields on both sides or the arithmetic mean of the electric displacement fields,

$$\big(\mathbf{E}_2(\mathbf{r}_\parallel,\omega) - \mathbf{E}_1(\mathbf{r}_\parallel,\omega)\big)\cdot\hat{q} = \frac{\sin\theta\tilde{\sigma}_z}{\epsilon_2} D_z^{av}, \tag{4.19}$$

where D_z^{av} is defined as in equation 2.10. This is somewhat strange, given that in [3] they list the Fresnel coefficients that they derive as valid in the case of dielectric substrates when they appear to be derived by considering immersion into one of the two materials at an interface.

Using equation 4.19 to calculate Fresnel amplitudes using the technique elaborated in section 2.3 does not, however, directly result in the amplitudes given in [3]. Instead, their model (r_p) is related to our version of their model (r'_p) by $r_p = -r'_p(\sigma_z = 0, \sigma_q = 0) + r'_p(\sigma_z = 0) + r'_p(\sigma_q = 0)$. This distinction likely comes about because the principle of superposition was used in their paper to separate the in-plane and out-of-plane responses and treat them independently. A comparison between our harmonic mean model, defined in equations 2.47, 4.3 and 4.4, the semi-immersed model based on equation 4.19 which is identical to the equation proposed in [5] (Felderhof), and the actual model based on the principle of superposition that was used in [3] (Merano) is shown in figure 4.13.

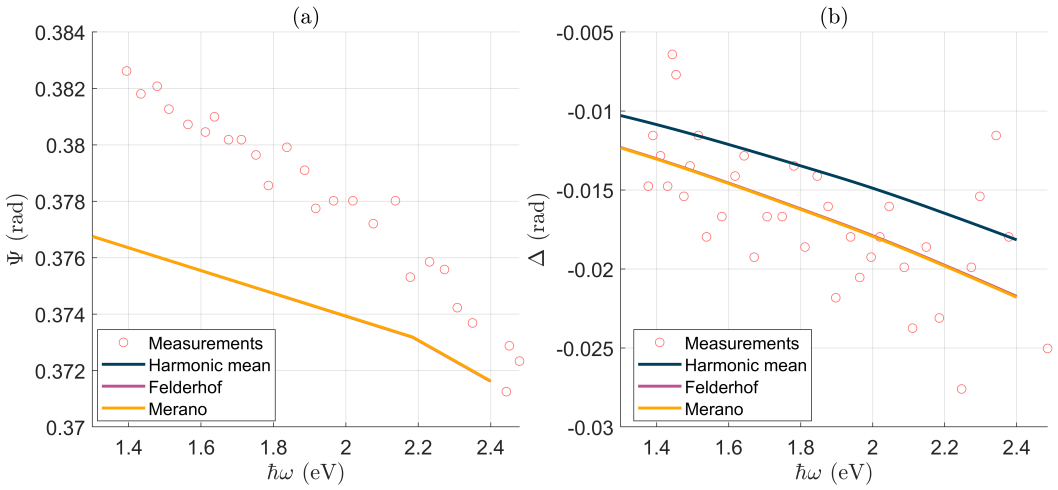


Figure 4.13: Comparison between ellipsometric measurements of undoped graphene on a substrate with index $n = 1.4233$ from [3], and the predictions by the models of various authors. All three models predict the same result in (a). The Felderhof and Merano models predict the same result in (b). Felderhof: [5]. Merano: [3]. The harmonic mean model is defined by equations 4.3 and 4.4 through equation 4.16.

All three models produce almost exactly the same ellipsometric amplitude Ψ, though there are significant differences in the phase Δ. Both our replication of the model in [3] based on the immersed boundary condition (equation 4.19), and their model based on the principle of superposition produce superior agreement for the phase when compared to the

harmonic mean model defined in equations 2.47, 4.3 and 4.4. This could indicate that the method of sample preparation resulted in the graphene sheet being slightly immersed into the substrate. Chemical vapour deposition was used to grow a graphene monolayer on a Cu foil, which was then transferred to a PDMS substrate. If this is not the case, then one would assume the graphene sheet, situated on top of the substrate, would not behave as if it were immersed. However, because it does seem to do so, this could mean that the interaction with the substrate is simply so much stronger than with air that even when not submerged it behaves as such. This seems unlikely as graphene exhibits only weak Van der Waals interactions out-of-plane. Of course, a final possibility is that this is proof of a flaw in the harmonic mean model. However, the model is based on the notion that surrounding dielectrics screen the out-of-plane polarization density, which air is incapable of doing. So this could serve as an indication that the harmonic mean model is only applicable when the 2D material is situated between particular dielectrics capable of providing screening. A replication of these ellipsometric tests with graphene sandwiched between distinct dielectrics could shine some light on this issue.

While this paper raises many questions in regard to the appropriate accounting of the influence of surrounding dielectrics, it remains strong evidence that the out-of-plane response, while weak at low frequencies, is experimentally accessible. There is a clear Brewster angle in the reflectance measurements, something that would not exist without the out-of-plane conductivity; and given the fitted out-of-plane conductivity values match *ab initio* calculations, the Brewster angle is not likely a result of inappropriate sample preparation.

4.2 Doped graphene

In this section, we will apply the models developed throughout this work to investigate some of the properties and behaviours of plasmons in graphene, which typically occur in the frequency range from the terahertz (THz) to the mid-infrared (MIR). In particular, we will identify the influence from out-of-plane conductivity and non-magnetic, isotropic, lossless dielectric material surroundings on both the dispersion relation, calculated in section 2.4, and surface forces, calculated in section 3.5.

To access the plasmonic regime we will implement a kind of shortcut. There are of course many ways to excite plasmons on surfaces, though the most easily describable by the classical models developed in this work are the configurations of Otto (a) and Kretschmann (b) shown in figure 4.14.

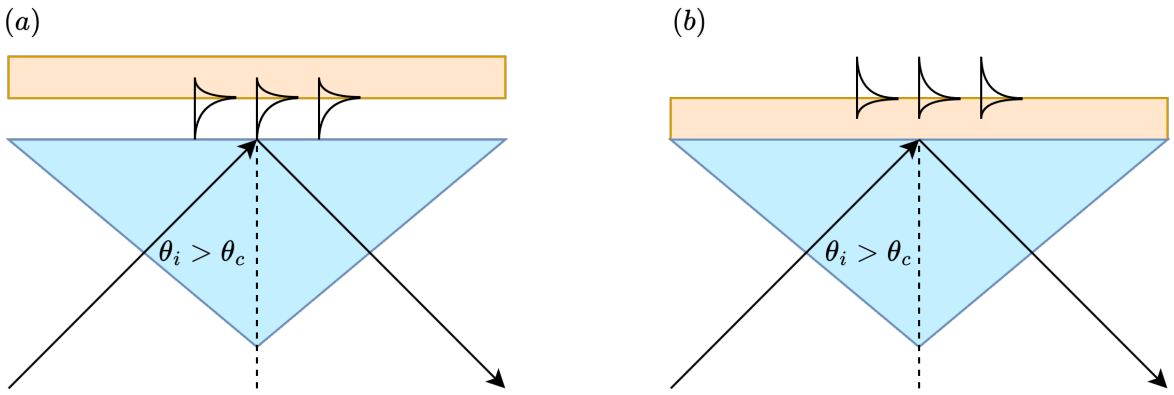


Figure 4.14: Schematic diagram of Otto (a) and Kretschmann (b) surface plasmon polariton excitation configurations. Blue represents some transparent dielectric, while orange represents a metal film.

Both configurations involve an incident beam past the critical angle which induces an evanescent field on the transmitted side. This evanescent field couples to the metal film, which in our case would be a 2D material, and excites surface modes with evanescent decay into both surrounding regions, otherwise known as surface plasmons.

These two geometries collapse to the same thing when considering 2D materials, but implementing it would involve extending the problem to multiple interfaces. However, this can be avoided by directly modifying the incident field. Each of these configurations uses an additional interface to turn the incident field into an evanescent field. This can instead be achieved directly by defining $\sin\theta_i = \xi$, and allowing ξ to be larger than one. Consider a standard incident plane wave,

$$\mathbf{E}_i = \begin{pmatrix} E_q \\ E_\tau \\ E_z \end{pmatrix} e^{i(k\xi x + k\sqrt{1-\xi^2}z - \omega t)}, \tag{4.20}$$

where k is the wave number in the incident medium. When ξ grows larger than one, the square root becomes imaginary,

$$\mathbf{E}_i = \begin{pmatrix} E_q \\ E_\tau \\ E_z \end{pmatrix} e^{-k\sqrt{\xi^2-1}z} e^{i(k\xi x - \omega t)}, \tag{4.21}$$

making the incident field evanescent, and replicating the effect of either evanescent coupling configuration in figure 4.14, without the need for multiple interfaces. This simplification

also has the added benefit of allowing direct control of the strength of the evanescent field coupling. The decay factor in the incident field is centred at the interface in which we are exciting plasmons, so the strength of coupling is controlled directly by the incident field amplitude, with no influence from decay during propagation between media.

By defining $\sin\theta_i = \xi > 1$, we are directly controlling the relative wavenumber between the induced plasmon in graphene and the vacuum,

$$\xi = \frac{q}{k} = \frac{qc}{\omega}, \tag{4.22}$$

where q is the in-plane wavenumber, and k is the total wavenumber. This means that when we vary ξ, we are actually varying the ratio of q and ω. Throughout this section, we will directly vary frequencies and wavenumbers, instead of working through the ratio ξ.

Plasmons can only form when there are sufficient free or quasi-free charge carriers to support collective motion. Undoped graphene cannot support plasmons as there are no electrons in its conduction band or holes in its valence band at zero temperature. This limits our investigation of plasmonic dispersion to doped graphene, and further to the low frequency range of the terahertz regime.

As was discussed in section 1.6, in this low-frequency regime, the in-plane conductivity is well described by a Drude model,

$$\tilde{\sigma}_q = \frac{i}{\pi}\frac{\omega'_F}{\omega + i\tau_f^{-1}}, \tag{4.23}$$

where $\omega'_F = 4\pi\alpha\omega_F$, $\omega_F = E_F/\hbar$, τ_f is the electron lifetime, and E_F is the Fermi energy. Unfortunately, there are as yet no published out-of-plane *ab initio* conductivity functions for doped graphene. The out-of-plane conductivity in undoped graphene is driven by high-frequency interband transitions, which are associated with localized electrons. With zero thickness in the out-of-plane direction, it is reasonable to assume that even with doping, the out-of-plane conductivity has to remain a result of localized electrons. As such, a reasonable first guess is to assume doping, and the resulting de-localized free and quasi-free electrons have little effect on the out-of-plane conductivity. Based on this, for investigations into plasmonic forces on graphene, we will use the Drude model for the in-plane conductivity, with $E_F = 0.316$ eV and $\tau_f = 500$ fs, and the *ab initio* data shown in figure 4.1 for the out-of-plane conductivity. We are only interested in the low-frequency regime, so the *ab initio* data can be approximated as having a zero real part and an imaginary part linear in frequency,

$$\sigma_z = im\omega, \tag{4.24}$$

where $m = -0.142\hbar\sigma_0$ with $\sigma_0 = \pi\alpha/z_0$, or in Gaussian CGS units, using $z_0 = 4\pi/c$, $m = -0.0512\,\text{nm}$. The numerical value -0.142 is the slope of the imaginary part of σ_z in figure 4.1, in the range $\hbar\omega = 0 - 3$ eV, and so has units of eV^{-1}. For material surroundings, the vacuum out-of-plane conductivity is replaced by an effective value resulting from interaction with the surrounding materials. As was established in section 2.2, we adopt screening on the out-of-plane conductivity by the harmonic mean, which is defined in equation 2.47.

4.2.1 Plasmon dispersion

In section 2.4, analytical relationships were derived for the dispersion relations of general 2D materials in vacuum and with material surroundings. Here we evaluate the dispersion relations for the particular case of graphene, with a focus on identifying the behaviour of the mode coupling between the σ_z and σ_q modes in the presence of distinct dielectrics. As such, only p-polarized plasmons will be considered, as s-polarization shows no coupling with out-of-plane. This means that the σ_τ mode will not be included in the dispersion relation.

In this work, we will focus on solutions to the dispersion relation in the limit of no losses in the conductivity functions. This is equivalent to considering an infinite electron lifetime $\tau_f \to \infty$. In general, solutions to the full dispersion relation with losses require that q be complex. Instead, working in the lossless limit, solutions can be found in terms of real wavenumbers. Having a finite electron lifetime primarily contributes to a broadening of the dispersion relation solution curves, so considering the lossless limit is still an effective way to find the central trajectory.

We can first verify that the model recreates the standard square root dispersion relation for graphene suspended in vacuum, defined in equation 2.99. This will be done by solving the full dispersion relation numerically in the lossless limit ($\tau_f \to \infty$). The full dispersion was derived in section 2.4, and is given by,

$$(\tilde{\sigma}_q k_z + 2k_0)(q^2\tilde{\sigma}_z + 2k_0 k_z) = 0, \tag{4.25}$$

for p-polarization. A comparison between the numerical solutions to equation 4.25, and the analytical square root dispersion defined in equation 2.99 is shown in figure 4.15.

There is qualitatively perfect agreement between the analytical square root dispersion relation, which was derived in the non-retarded limit, and the numerical results. This is a standard result [13], though it serves to confirm the validity of our formulation.

For material surroundings, the picture is more complicated. As was identified in section 2.4, the hybridization between in-plane and out-of-plane modes comes about as a result

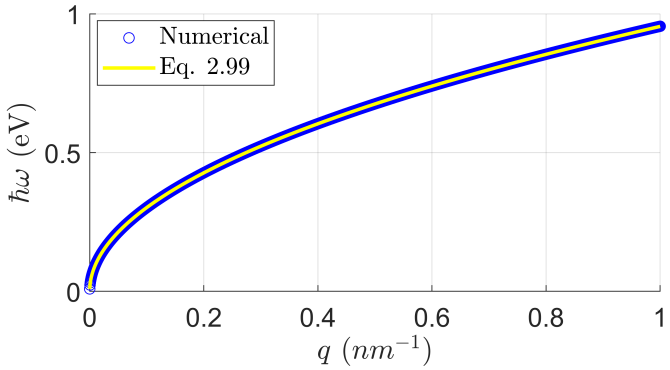


Figure 4.15: Comparison between the analytical square root dispersion for the in-plane plasmon mode in graphene (2.99), derived in the non-retarded limit, and the numerical solutions to the lossless dispersion relation defined in equation 4.25.

of the difference between surrounding materials. In that same vein, the standard in-plane dispersion relation for material surroundings, given by

$$k_{z1}k_{z2}\tilde{\sigma}_q + k_0(n_2^2 k_{z1} + n_1^2 k_{z2}) = 0, \tag{4.26}$$

deviates from the coupled dispersion relation,

$$q^2\tilde{\sigma}_q\tilde{\sigma}_z^e(n_2^2 k_{z1} + n_1^2 k_{z2}) + 4k_0(n_1^2 n_2^2 q^2\tilde{\sigma}_z^e + k_{z1}k_{z2}\tilde{\sigma}_q) + 4k_0^2(n_2^2 k_{z1} + n_1^2 k_{z2}) = 0, \tag{4.27}$$

more strongly as the difference between surrounding materials is increased. While direct solutions to the coupled dispersion relation are infeasible for the full retarded equation, in the non-retarded limit ($q \gg \omega/c$) they become far more tractable. In this limit, the lossless dispersion relation can be solved to find,

$$\omega = \sqrt{\frac{2v_B\omega_F q}{n_{AM}^2}}\sqrt{\frac{mqn_{AM}^2 + 2\epsilon_0}{mqn_{HM}^2 + 2\epsilon_0}}, \tag{4.28}$$

where v_B is the Bohr velocity, m is the slope defined in equation 4.24, ω_F is the Fermi frequency, n_{AM}^2 is the arithmetic mean of the squared indices, defined by,

$$n_{AM}^2 = \frac{n_1^2 + n_2^2}{2}, \tag{4.29}$$

and n_{HM}^2 is the harmonic mean of the squared indices, defined by,

$$n_{HM}^2 = \frac{2n_1^2 n_2^2}{n_1^2 + n_2^2}. \tag{4.30}$$

Figure 4.16 shows the numerical solutions to the hybridized dispersion relation for $n_1 = 1$ and $n_2 = 1 - 4$, as well as a comparison to equation 4.28. Qualitatively there

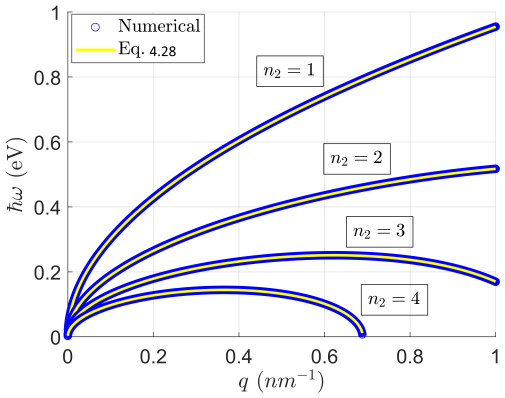


Figure 4.16: Comparison between the numerical solutions to the lossless hybridized dispersion relation defined in equation 4.27, and the analytical solution derived in the non-retarded limit defined in equation 4.28.

is no difference if n_1 and n_2 are swapped, so only the case of varying n_2 is shown. The coupling between the in-plane and out-of-plane surface modes is expressed in how the in-plane branch of the dispersion relation curls down to the x-axis. This termination at the x-axis represents a significant change over the case with only in-plane conductivity, which in theory extends to infinity in x. With out-of-plane conductivity, there appears to be a finite range of allowable plasmon wavenumbers in the low-frequency regime. In a sense, this means the out-of-plane conductivity serves as a kind of passband filter, preventing plasmon resonance outside the allowed set of frequencies and wavenumbers. In the context of metafilms with designer material properties, this could open an avenue for further tuning of plasmon resonance to specific allowed frequency ranges if one could control the out-of-plane conductivity.

A full investigation of the hybridized dispersion relation with a more accurate accounting of in-plane conductivity in the random phase approximation (RPA) is planned for the future [65][44]. However, there are a number of notable characteristics of the full complex dispersion relation with only the simple Drude model for in-plane conductivity. The complex lossy dispersion relation is not the focus here, but a brief discussion can be found in Appendix C.2.

4.2.2 Forces

All force calculations will again be based on the stress tensor method whereby the difference between the electromagnetic stress tensor on each side of the 2D material is evaluated as

$$\mathbf{F} = \frac{1}{2}\Re\left(\overleftrightarrow{T}\cdot\hat{z}\Big|_{z_1}^{z_2}\right). \tag{4.31}$$

For vacuum surroundings, the standard Maxwell stress tensor will be used, which is defined in equation 3.84. For material surroundings, the vacuum gap stress tensor will be used, which is defined in equation 3.100.

The enhancement of electric fields from plasmons greatly strengthens what are otherwise very weak forces. Enhanced plasmonic optical forces in graphene have already been widely investigated. They have been proposed for use in plasmonic tweezers for particle sorting, capture, and measurement [66][67], they have been investigated as platforms for straintronics and flexible optoelectronics [6][68], as well as for use in force sensors and actuators [69].

The focus in this section will again be on how the out-of-plane conductivity influences the well-established in-plane plasmon mode. In section 2.4 we showed that in vacuum, the surface plasmon modes are fully decoupled, so we can expect little to no influence on the in-plane surface mode forces from the inclusion of out-of-plane conductivity. However, we also identified that the in-plane and out-of-plane modes become coupled when there are surrounding dielectrics with distinct properties. We can therefore expect some changes to the forces from the in-plane plasmon mode from the out-of-plane conductivity in the presence of dielectrics.

The equations for force derived in section 3.5 are functions of frequency and wave number ($\mathbf{F}(q,\omega)$). As such, we will investigate forces in two ways, each shown schematically in figure 4.17, (a) scanning across the plasmon frequency, and (b) scanning along the plasmon frequency. Scanning across the plasmon frequency was the technique used in [6] to identify forces around plasmons. This technique involves fixing the frequency of the incident radiation and varying the wavenumber (q) across a region one knows to contain the plasmon resonance. Experimentally, varying q can be done by varying the incident angle in a configuration like those shown in figure 4.14, so it is a technique easily comparable to experimental observations. Scanning along the plasmon frequency is less commonly done, however, it offers a unique way to investigate simultaneously the forces from plasmons across broad regions of the dispersion relation. Using this technique, all forces can be attributed directly to those generated by surface plasmons, so it is a useful

tool in identifying regions along the dispersion relation that may exhibit unique behaviour and warrant further study.

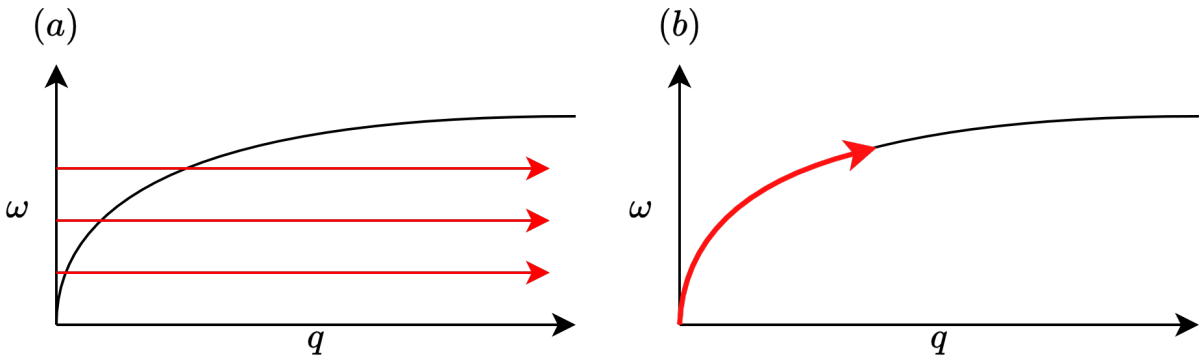


Figure 4.17: Frequency and wavenumber scans around the plasmon dispersion relation.

To begin with, we will confirm the validity of our model by recreating the results from [6]. It should be noted that while this paper does indicate that they divide the real part of the stress tensor difference by two, as we showed is necessary in section 3, our results end up being exactly a factor of 0.5 smaller than their results. In this paper graphene was modelled by a Drude conductivity with $\tau_f = 500$ fs, and a doping density $n = 7.36 \times 10^{16}\,\mathrm{m}^{-2}$, which is equivalent to a Fermi energy of $E = 0.3165$ eV. They also considered p-polarized incident light with an amplitude given by $|a_p| = 61378\,\mathrm{V/m}$. Figure 4.18 (a) shows the force in the $\hat{z}$ direction resulting from the model developed in this work for the parameters from [6], and correcting for the factor of 0.5. As far as can be determined from comparison to their figures, the agreement is exact. Figure 4.18 (b) and (c) show the forces using the same parameters, although (b) includes a substrate with $n_2 = 2$, and (c) includes the same substrate and out-of-plane conductivity.

The inclusion of a substrate causes significant changes; appearing to both focus the force into the direction of the substrate, as well as significantly increase the amplitude. On the other hand, the difference between the case with and without out-of-plane conductivity is imperceptible. It is clear that at these low frequencies, the influence of out-of-plane conductivity must be small. Along with these changes can be observed a shift in the wavenumber associated with each plasmon resonance. This happens because the inclusion of out-of-plane conductivity and a substrate changes the dispersion relation, and the dispersion relation defines where the resonances occur. This is shown in figure 4.19. The three horizontal lines indicate the iso-frequency scans at $\hbar\omega = 0.124$, 0.083, and 0.062 eV ($\lambda = 10$, 15, and 20 μm) that constitute the input to the force equations.

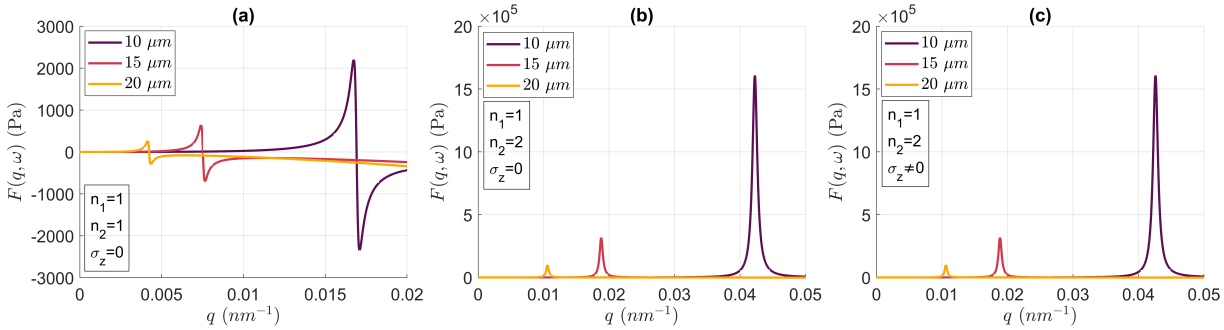


Figure 4.18: (a) Recreation of the iso-frequency force scans considered in [6], as well as an extension to the case with dielectric surroundings (b) and out-of-plane conductivity (c). The three considered wavelengths correspond to frequencies of $\hbar\omega = 0.124$, 0.083, and 0.062 eV. All forces are in the $\hat{z}$ direction.

While there is a difference between the dispersion relation with and without out-of-plane conductivity, at the low energies considered in [6], they are negligible. The most stark change is of course the elimination of the zero crossing at resonance. The existence of the zero crossing is explained in [6] as being the result of a rapid phase change around resonance. This phase change results in a resonant line shape that resembles the real part of a Lorentzian, while the line shape for material surroundings resembles the imaginary part. The Lorentzian character of these forces can be extracted directly from the force equation in the non-retarded limit ($q \gg \omega/c$). In the strict non-retarded limit, given by $c \to \infty$, the force diverges. To counteract the divergence, we will consider instead the limit that c grows large but remains finite. In this limit, the force in the $\hat{z}$ direction is directly proportional to c^2,

$$F_z = \frac{c^2}{2} \frac{\epsilon_0 q^3 \left(2n_{AM}^2 qm + 4\epsilon_0 n_1^2\right)\left(\Lambda_1 m + 4v_B\epsilon_0\omega_F\left(n_2^2\omega^2 - 2v_B\omega_F q\right)\right)}{\omega^4\left(n_{AM}^2 qm + 2\epsilon_0 n_{AM}^2\right)^2\gamma^2 + \left(\Lambda_2 m + 2\omega\epsilon_0\left(n_{AM}^2\omega^2 - 2v_B\omega_F q\right)\right)^2}, \tag{4.32}$$

where $\gamma = 1/\tau_f$ is the damping rate, n_{AM}^2 is defined in equation 4.29, n_{HM}^2 is defined in equation 4.30, and Λ_1 and Λ_2 are defined as

$$\Lambda_1 = -\omega^2 n_{HM}^2\left(2v_B\omega_F q - n_2^2(\omega^2+\gamma^2)\right), \tag{4.33}$$

$$\Lambda_2 = q\omega n_{AM}^2\left(\omega^2 - 2v_B\omega_F n_{HM}^2 q\right). \tag{4.34}$$

The same weak non-retarded limit can be applied to the force in the $\hat{q}$ direction,

$$F_q = \frac{c^2}{2n_1^2} \frac{\epsilon_0 v_B\omega_F q^3\left(2mn_{AM}^2 q + 4\epsilon_0 n_1^2\right)\gamma}{\omega^3\left(n_{AM}^2 qm + 2\epsilon_0 n_{AM}^2\right)^2\gamma^2 + \omega\left(\Lambda_3 m + 2\epsilon_0\left(n_{AM}^2\omega^2 - 2v_B\omega_F q\right)\right)^2}, \tag{4.35}$$

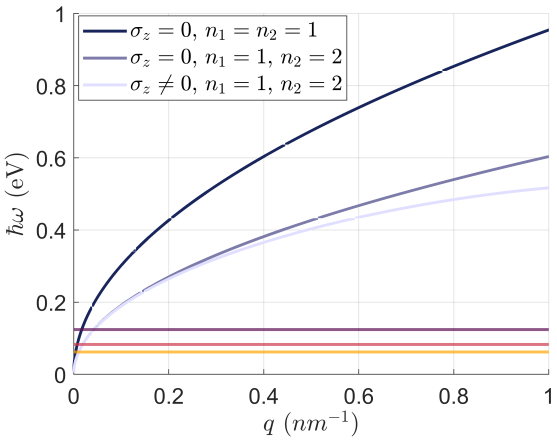


Figure 4.19: Dispersion relations for doped graphene at the material configurations used in figure 4.18. Iso-frequency scans corresponding to the three wavelengths considered in [6] are represented as horizontal lines at $\hbar\omega = 0.124$, 0.083, and 0.062 eV.

where Λ_3 is defined as

$$\Lambda_3 = q n_{AM}^2 \left(\omega^2 - 2 v_B \omega_F n_{HM}^2 q\right). \tag{4.36}$$

Based on the iso-frequency force scans shown in figure 4.18, we know that equation 4.32 exhibits a Lorentzian line shape. This Lorentzian character is made more obvious when one considers the case with $\sigma_z = 0$,

$$F_z = -\left(2c^2\epsilon_0 n_1^2 v_B \omega_F q^3\right) \frac{2 q v_B \omega_F - n_2^2 \omega^2}{\left(\omega n_{AM}^2 \gamma\right)^2 + \left(2 q v_B \omega_F - n_{AM}^2 \omega^2\right)^2}. \tag{4.37}$$

In this form, it is clear that the loss of zero crossing with the introduction of material surroundings, shown in figure 4.18, comes to pass because n_{AM}^2 in the denominator no longer coincides with n_2^2 in the numerator. This coincidence is restored when $n_1 = n_2 = n$, thus returning the zero crossing at resonance shown in figure 4.18 (a). The Lorentzian defined in equation 4.37 can be used to derive the locations of the positive and negative peaks shown in figure 4.18 (a) for the case where $n_1 = n_2 = n$. Doing so results in an equation for the positive and negative peaks given by,

$$q = \frac{n^2 \omega(\omega \pm \gamma)}{2 \omega_F v_B}. \tag{4.38}$$

Next, we will consider the same iso-frequency scan technique, but this time in a parameter regime that experiences a larger influence from the out-of-plane conductivity. For

all subsequent force calculations, we will present the results exactly as our model predicts and for unit incident amplitude. This means restoring the factor of 1/2 that was omitted to match results with those from [6], and using $|a_p| = 1$. However, we will continue to use the parameters for conductivity defined in that work. To highlight the effects of the out-of-plane conductivity, iso-frequency scans will be considered at $\hbar\omega = 0.1$, 0.15, 0.2, and 0.25 eV, with surrounding dielectrics defined by $n_1 = 1$ and $n_2 = 3$. The dispersion relation for this scenario is shown in figure 4.20.

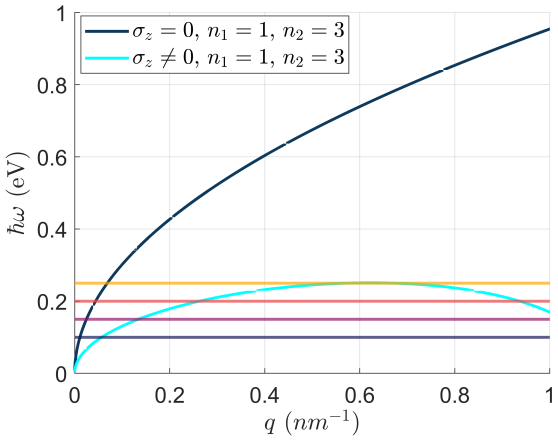


Figure 4.20: Dispersion relations of doped graphene for the material configurations used in the force scans of figure 4.21. The horizontal lines represent the iso-frequency scans at $\hbar\omega = 0.1$, 0.15, 0.2, and 0.25 eV.

The out-of-plane conductivity serves to curl the dispersion relation down to the x-axis. This curling effect results in significant deviations above 0.15 eV. Most significant is that out-of-plane conductivity makes the dispersion relation non-monotonic, which in turn introduces multiple valid solutions for each frequency. The force scans in the $\hat{z}$ direction for this dispersion relation are shown in figure 4.21 for both a substrate with $n_2 = 3$ and a superstrate with $n_1 = 3$, each is shown with and without out-of-plane conductivity.

The resonance peaks exhibit shifts in wavenumber according to the shift in the crossing point of the dispersion relation. The additional resonant peaks at higher wavenumbers are a result of the additional dispersion crossings coming from the non-monotonic dispersion relation. More interesting is what appears to be significant differences between the cases where $n_1 > n_2$ and $n_2 > n_1$. There is a clear reduction in amplitude near the maximum of the dispersion relation in the substrate case that is not reflected in the superstrate case. While this reduction in amplitude does appear to coincide with the maximum of the

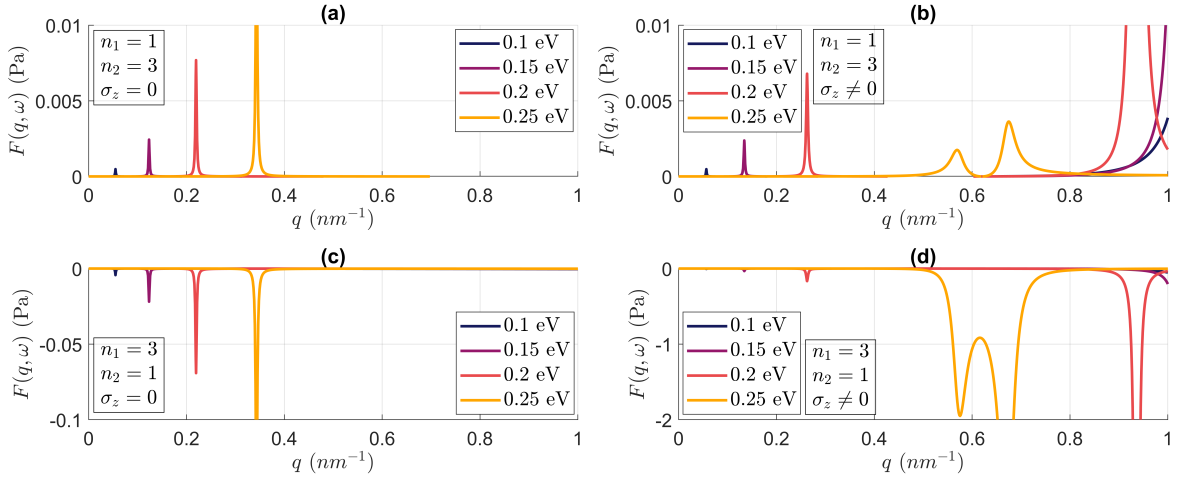


Figure 4.21: Comparison between the iso-frequency force scans both with (right) and without (left) out-of-plane conductivity, for both substrate (top) and superstrate (bottom) dielectric configurations. All forces are in the $\hat{z}$ direction.

dispersion relation, more clarity can be achieved by scanning along the dispersion relation rather than across.

To scan along the dispersion relation, the frequency is defined as a function of wave number through the dispersion relation, $\omega = \omega_p(q)$. This results in a force function that looks like $\mathbf{F}(q, \omega_p(q))$, where $\omega_p(q)$ indicates it is the plasmon frequency defined through the dispersion relation. In terms of implementation, the dispersion relation will be solved numerically, and the result fed directly into the force equations. The numerical solutions to the dispersion relation will be calculated in the lossless limit ($\tau_f \to \infty$). This limit simplifies what would otherwise be complex solutions to purely real frequencies and wavenumbers. However, the force equations themselves are evaluated with losses, it is only the dispersion relation that is evaluated as lossless. To begin, we will consider the decoupled vacuum case. In this case, we know the force exhibits a zero crossing at the resonance defined by the dispersion relation, as shown in figure 4.18 (a). If the splitting is symmetric, then one could assume scanning along the dispersion relation would simply yield zero force for the entire span. Instead, we will use the equation for the shift of the peak from the resonance point (4.38), to select out and scan along the positive peak rather than the central zero point. This involves simply subtracting a factor of $\omega\gamma/(2\omega_F v_B)$ from all of the q values inputted into the force equation. This shift was derived for the case with $\sigma_z = 0$, however, it can be expected to remain accurate in the vacuum case given that the σ_q and σ_z modes are fully

decoupled. This modifies the equation into something that looks like $\mathbf{F}(q - \Delta(q), \omega_p(q))$. Figure 4.22 shows the logarithms of the absolute value of the forces in the $\hat{z}$, (a), and $\hat{q}$, (b), directions, along with the unmodified forces to indicate direction (c). Figure 4.22 also shows the dispersion relation used to define the frequency in terms of wavenumber (d), along with the logarithm of the amplitude, (e), and phase, (f), spectrum of both the reflected and transmitted Fresnel components. The Fresnel amplitudes are of course also defined as functions of only the wavenumber, in the same way as the force, although the explicit dependencies are omitted in the plot to save space.

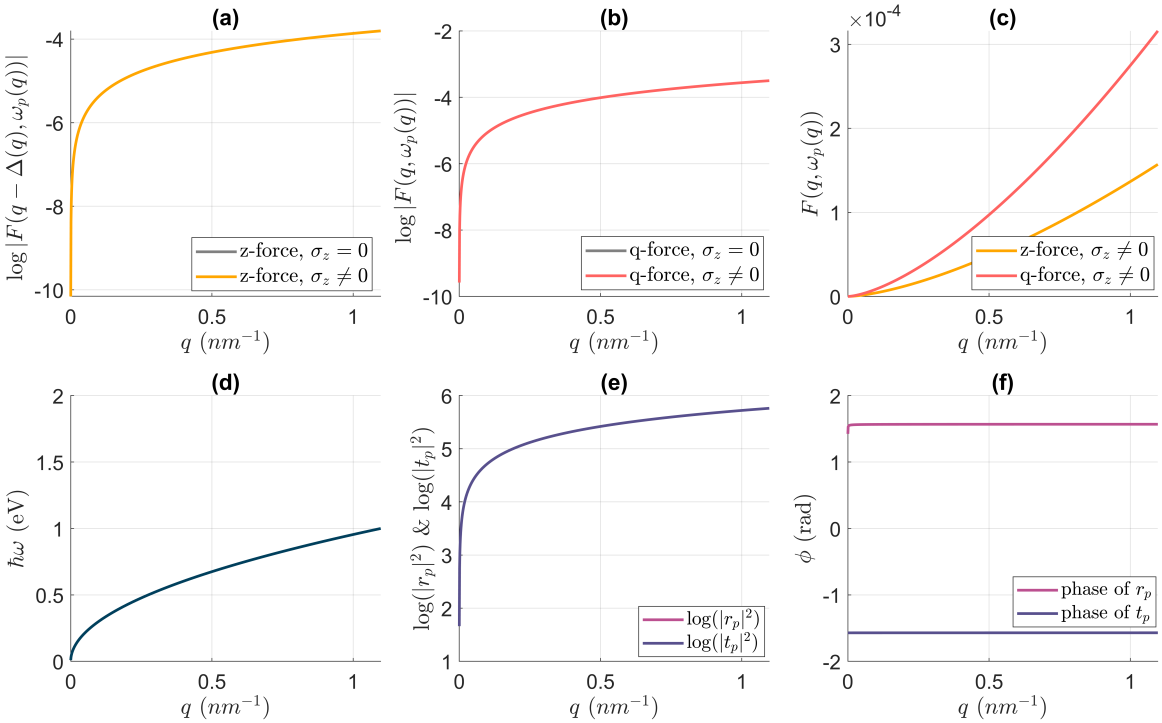


Figure 4.22: Dispersion scan plots of the (a) log of the absolute $\hat{z}$ force density, and (b) $\hat{q}$ force density, (c) force density with directions, (d) dispersion relation, (e) log of the absolute amplitude spectrum, and (f) phase spectrum. All are calculated with vacuum surroundings. Force is measured in Pascals, field amplitudes are measured in V/m.

Again, we are using the dispersion curve associated with the in-plane plasmonic mode to calculate these forces. This is why, as predicted based on the decoupled nature of the modes for vacuum surroundings, both the $\hat{q}$ and $\hat{z}$ components of the force are completely unchanged when the out-of-plane conductivity is set to zero.

Next, material surroundings will be considered. As predicted by the iso-frequency scan technique, there appears to be a significant deviation as a result of out-of-plane conductivity. Figure 4.23 shows the force, dispersion, and spectrum curves for the case where $n_1 = 2$ and $n_2 = 1$ in a manner analogous to that used to create figure 4.22.

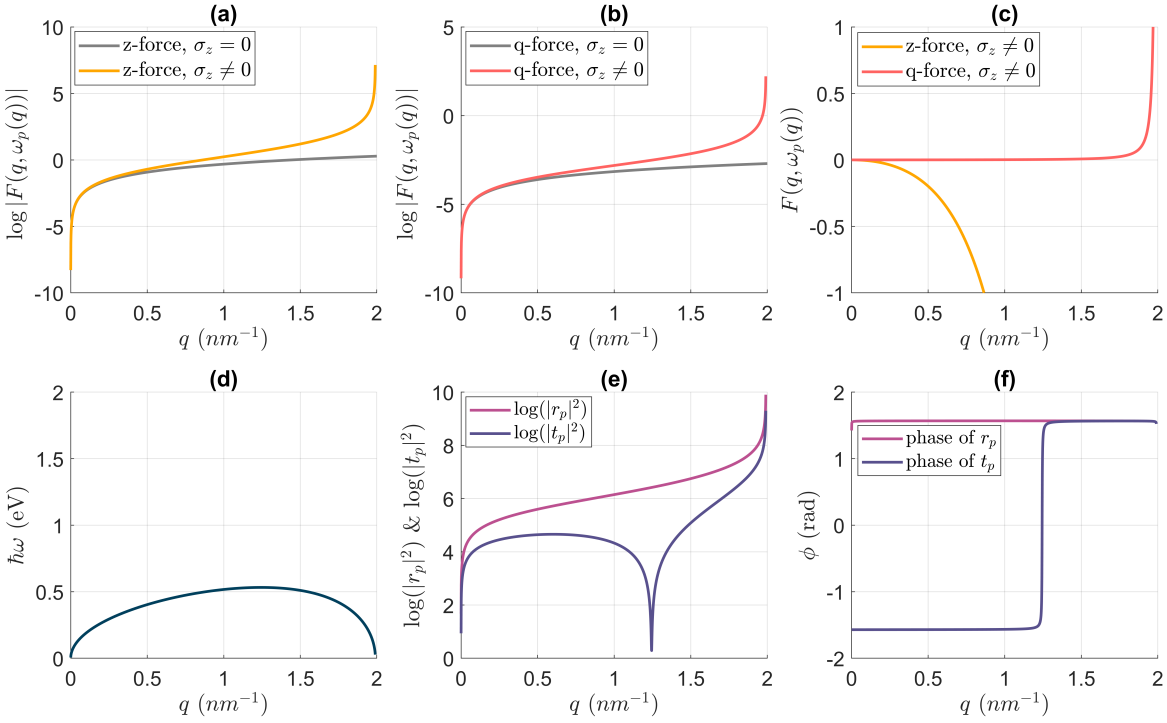


Figure 4.23: Dispersion scan plots of the (a) log of the absolute $\hat{z}$ force density, and (b) $\hat{q}$ force density, (c) force density with directions, (d) dispersion relation, (e) log of the absolute amplitude spectrum, and (f) phase spectrum. All are calculated with $n_1 = 2$, and $n_2 = 1$. Force is measured in Pascals, field amplitudes are measured in V/m.

With these distinct surrounding materials, the dispersion relation becomes finite in length. At the termination point there appears to be an additional resonance, indicating that plasmonic field amplification is enhanced in this low frequency, high wavenumber regime. While there is also a significant anti-resonance to the transmitted amplitude spectrum, it does not translate to differences in the force. This can be understood by recognizing that the force is a function of both the reflected and transmitted amplitudes. Even though the transmitted amplitude experiences what appears to be an anti-resonant response, with accompanying π shift in phase, because the reflected amplitude is multiple

orders of magnitude larger, any influence on the net force is overshadowed.

Next, we will look at the case when $n_2 > n_1$. Figure 4.24 shows the case where $n_2 = 2$ and $n_1 = 1$. Compared to the prior case, the magnitudes of the index of refraction for each material have been swapped, and the response changes dramatically.

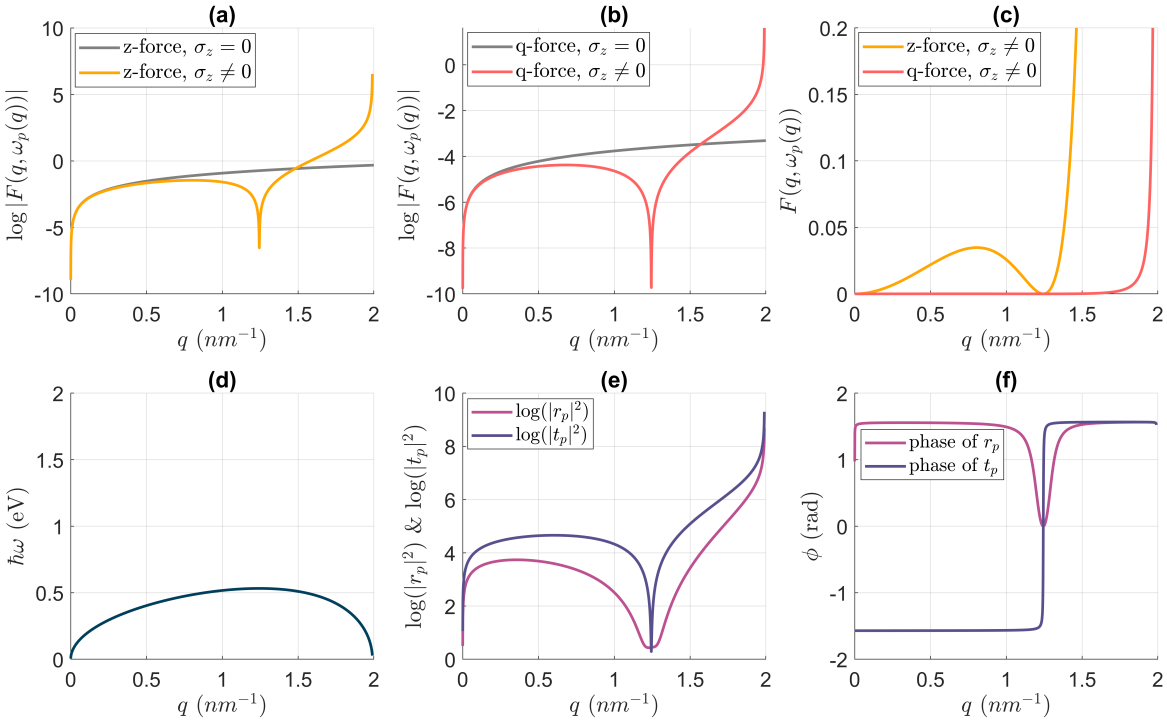


Figure 4.24: Dispersion scan plots of the (a) log of the absolute $\hat{z}$ force density, and (b) $\hat{q}$ force density, (c) force density with directions, (d) dispersion relation, (e) log of the absolute amplitude spectrum, and (f) phase spectrum. All are calculated with $n_1 = 1$, and $n_2 = 2$. Force is measured in Pascals, field amplitudes are measured in V/m.

In this case, the transmitted spectrum exhibits a similar anti-resonance and phase shift structure as in the previous case shown in figure 4.23, however now the transmitted amplitude is the dominant contribution, and the reflected amplitude also reaches a minimum. The result is that the force density exhibits a significant decrease in amplitude compared to the case without out-of-plane response. If this reduction in force remains significant when a more detailed model of conductivity and loss mechanisms is considered, then it could have significant consequences for the design of plasmonic nanostructures. Things

like plasmonic waveguides may benefit from tuning their operation to frequency ranges where the force is minimized to increase operational lifetimes.

Based on the results of scanning along the dispersion relation, it is apparent that, in general, the termination point of the finite hybridized dispersion relation corresponds to a resonance point in the force, and when $n_2 > n_1$, the maximum of the dispersion corresponds to an anti-resonance in the force. This explains the changes in amplitude observed in figure 4.21. It is also clear that the dominant Fresnel amplitude is always the one on the side of the higher index. This indicates that at the interface between two dielectrics, a surface plasmon exists primarily in the higher index medium.

We can again glean some analytical insights by working in the retarded limit ($q \gg \omega/c$). In this limit, the dispersion relation has a maximum at

$$q = -\frac{2\epsilon_0 n_{HM}^2}{m n_2^2}, \tag{4.39}$$

which we confirm to accurately predict the location of the anti-resonant force response when $n_2 > n_1$ and with the harmonic mean screening on the out-of-plane conductivity. The point where the force has its maximum, along with the point at which the dispersion relation intersects the x-axis is,

$$q = -\frac{2\epsilon_0 n_{HM}^2}{m n_{AM}^2}. \tag{4.40}$$

Both of the above points appear negative, however, the slope of the out-of-plane conductivity (m) is also negative, so the result is positive in both equations 4.39 and 4.40.

It is very important to note that while the differences between the cases with and without out-of-plane conductivity appear significant, it is likely that with a more accurate description of loss mechanisms and conductivity contributions, they would be significantly diminished. This is partly because the overwhelming majority of theoretical investigations of graphene treat it as if $\sigma_z = 0$, and if there were significant plasmonic effects from out-of-plane conductivity, it would seem likely that someone would have noticed the deviations from experiment. It is also true that the Drude model used here for the in-plane conductivity is only approximate, and in reality, there would be contributions from interband and intraband losses, along with optical phonons [44] which could significantly alter the plasmon dispersion. Regardless, at the level of Drude models, there is undeniably an effect, so it remains possible that even with more accurate conductivity models there would be regions in which the effect of out-of-plane conductivity on the in-plane plasmonic response would be measurable. Based on the force calculations in this section, it would seem that if these regions exist, they would coincide with either the maximum or the termination

point of the non-monotonic dispersion relation. Future experimental work in this direction should therefore focus on the regions around the wavenumbers defined by equations 4.39 and 4.40.

4.2.3 Comparison to [3]

Reference [3] is again the paper in which ellipsometric measurements of the reflectance of graphene were used to calculate both the in-plane and out-of-plane conductivities. The reflectance model used in the paper was equivalent to the one developed in this work for immersion, but not so when the surrounding dielectrics were distinct. The Fresnel reflected amplitude quoted in [3] is,

$$r_p = -\frac{n_2\cos\theta_i - n_1\cos\theta_t}{n_2\cos\theta_i + n_1\cos\theta_t} + \frac{n_2\cos\theta_i - n_1\cos\theta_t - n_1 n_2\tilde{\sigma}_z^e\sin^2\theta}{n_2\cos\theta_i + n_1\cos\theta_t + n_1 n_2\tilde{\sigma}_z^e\sin^2\theta} + \frac{n_2\cos\theta_i - n_1\cos\theta_t + \tilde{\sigma}_q\cos\theta_i\cos\theta_t}{n_2\cos\theta_i + n_1\cos\theta_t + \tilde{\sigma}_q\cos\theta_i\cos\theta_t}. \quad (4.41)$$

In the paper, this model was tooled specifically for the case of a dielectric substrate and used $\tilde{\sigma}_z^e = \tilde{\sigma}_z/n_2^2$ and $n_1 = 1$. Again, the general model in equation 4.41 (r_p) is related to our model (r_p') by $r_p = -r_p'(\sigma_z = 0, \sigma_q = 0) + r_p'(\sigma_z = 0) + r_p'(\sigma_q = 0)$. Equation 4.41 reduces to the model developed in this work when the surrounding dielectrics are identical ($n_1 = n_2$).

While all the measurements in the paper were taken for undoped graphene, the quoted model in equation 4.41, and its differences when compared to the model developed in this work, have important consequences for the behaviour of surface plasmons. The model from this work, derived in section 2.3, considered in-plane and out-of-plane response simultaneously. The model developed in [3] used the principle of superposition to consider the contributions to the electric and magnetic fields from the in-plane and out-of-plane response separately. As shown in figure 4.13, the consequences of this separation of responses are small outside the evanescent regime. However, the superposition method produces an equation with an inherently factored denominator, as shown in equation 4.41. This is significant because the denominator of the Fresnel coefficients is the dispersion relation of the associated surface plasmons. This was shown explicitly in section 2.4. Therefore, according to [3], the plasmon modes of doped graphene would be described by a dispersion

relation of the form $ABC = 0$, where,

$$A = n_2 \cos\theta_i + n_1 \cos\theta_t, \tag{4.42}$$
$$B = n_2 \cos\theta_i + n_1 \cos\theta_t + n_1 n_2 \tilde{\sigma}_z^e \sin^2\theta, \tag{4.43}$$
$$C = n_2 \cos\theta_i + n_1 \cos\theta_t + \tilde{\sigma}_q \cos\theta_i \cos\theta_t. \tag{4.44}$$

This dispersion relation can be cast equivalently in terms of wavenumbers by applying $n_1 k_0 \cos\theta_i = k_{z1}$, $n_2 k_0 \cos\theta_t = k_{z2}$, and $k_0 \sin\theta = q$,

$$A = n_2^2 k_{z1} + n_1^2 k_{z2}, \tag{4.45}$$
$$B = n_1^2 n_2^2 q^2 \tilde{\sigma}_z^e + n_2^2 k_0 k_{z1} + n_1^2 k_0 k_{z2}, \tag{4.46}$$
$$C = k_{z1} k_{z2} \tilde{\sigma}_q + n_2^2 k_0 k_{z1} + n_1^2 k_0 k_{z2}. \tag{4.47}$$

As a point of comparison, the dispersion relation on the hybridized plasmon modes derived in this work takes the form,

$$q^2 \tilde{\sigma}_q \tilde{\sigma}_z^e (n_2^2 k_{z1} + n_1^2 k_{z2}) + 4k_0 (n_1^2 n_2^2 q^2 \tilde{\sigma}_z^e + k_{z1} k_{z2} \tilde{\sigma}_q) + 4k_0^2 (n_2^2 k_{z1} + n_1^2 k_{z2}) = 0. \tag{4.48}$$

The superposition method of [3] destroys the coupling between the in-plane and out-of-plane plasmon modes that occurs when $n_1 \neq n_2$. The consequences of this are significant. With no coupling, the out-of-plane mode has no influence on the in-plane plasmon.

Here we will use the same Drude model for the in-plane conductivity, and linear approximation for the out-of-plane conductivity as established in section 4.2. Based on these conductivity models, there are no continuous solutions to B in the non-retarded limit ($q \gg \omega/c$). We have further confirmed numerically that the out-of-plane dispersion contribution supports no continuum of states besides those that follow the light line. The solutions to C, on the other hand, are the standard in-plane surface modes in the absence of out-of-plane conductivity. In the non-retarded limit this dispersion relation can be solved analytically to find,

$$\omega = \sqrt{\frac{4 v_B \omega_F}{(n_1^2 + n_2^2)}} \sqrt{q}, \tag{4.49}$$

where v_B is the Bohr speed and ω_F is the Fermi frequency. This reduces exactly to the vacuum solution shown in equation 2.99 when $n_1 = n_2 = 1$. Figure 4.25 shows a comparison between the non-retarded solution to the coupled dispersion relation, defined in equation 4.28, and the solution to the decoupled dispersion relation, defined in equation 4.49. The coupling between the in-plane and out-of-plane modes introduces a significant deviation from the pure root-like dispersion of the decoupled mode predicted by [3]. Verification

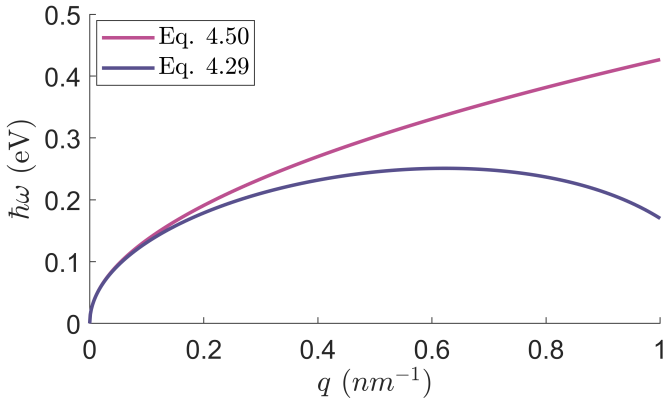


Figure 4.25: Comparison between non-retarded solutions to the coupled (4.28) and decoupled (4.49) dispersion relations for plasmon states in doped graphene.

of our model or theirs will come down to determining experimentally whether or not the out-of-plane mode truly does couple to the in-plane mode.

As a final note, A, the decoupled purely dielectric contribution, can be solved exactly in the fully retarded regime to find,

$$q = \frac{n_1 n_2}{\sqrt{n_1^2 + n_2^2}} \frac{\omega}{c}. \tag{4.50}$$

This predicts a light-line solution that corresponds to a medium given by half the harmonic mean of the surrounding dielectrics. Right away this must be nonphysical as half the harmonic mean can be less than one when both $n_1, n_2 > 1$. This would result in a light-line-like solution above the vacuum light-line.

Chapter 5

Results for phosphorene

In this section, we will evaluate the models developed throughout this work for phosphorene with an in-plane-only conductivity. Only in-plane conductivity is being considered, and as such, we will not be dedicating a section to an exploration of reflectance, transmittance, and absorption. These properties have been well established for anisotropic in-plane conductivity[1] [70] [71]. Further, we will only be considering results for doped phosphorene, with a focus on plasmonic effects.

Phosphorene has an in-plane anisotropic conductivity defined, in the material frame, by $\sigma_x(\omega)$ in the armchair (AC) crystal direction, and $\sigma_y(\omega)$ in the zigzag (ZZ) crystal direction. The presence of anisotropy in phosphorene means that the response will differ based on the polarization of the incident radiation. This was discussed in more detail in section 1.6, however, the result is that the conductivity response function, defined in equation 1.89 with $\sigma_z = 0$, as shown in equation 3.33, will have an angular dependence, $\overleftrightarrow{\sigma}(\omega, \phi)$, where ϕ represents the rotation angle of phosphorene's AC axis relative to the $\hat{q}$ direction, i.e., the in-plane direction of the incident light. This rotation introduces a set of effective conductivity values with angular dependence defined by

$$\sigma_q = \sigma_x(\omega)\cos^2\phi + \sigma_y(\omega)\sin^2\phi, \tag{5.1}$$

$$\sigma_\tau = \sigma_x(\omega)\sin^2\phi + \sigma_y(\omega)\cos^2\phi, \tag{5.2}$$

$$\sigma_c = (\sigma_y(\omega) - \sigma_x(\omega))\sin\phi\cos\phi. \tag{5.3}$$

With the additional dependence on the rotation angle compared to the isotropic case, polar coordinates, consisting of (q, ϕ), are a natural choice with which to describe the behaviour of phosphorene. However, we will primarily use a cartesian representation consisting of (q_x, q_y), where the coordinates are defined by $q_x = q\cos\phi$ and $q_y = q\sin\phi$. The cartesian

representation in a sense re-affixes the frame to the material itself, which can aid in the interpretation of results.

Without the out-of-plane conductivity contribution, the Fresnel coefficients derived in section 2.3 reduce to similar results to those derived in [1]. It is important to note that our derivation of Fresnel coefficients for in-plane anisotropy deviates from those derived in [1] by a negation of the σ_c term in the denominator, a negation of the mixing contribution to t_p, and r_p, and an extra cosine on all mixing contributions. The mixing contributions are the contributions from the incident s polarization to induced p polarization and vice versa. However, our formulation for anisotropic in-plane conductivity does agree with that derived in [72]. The Fresnel coefficients based on our derivation take the form,

$$t_p = \frac{2n_1 f_2 \cos\theta_i}{f_1 f_2 - \tilde{\sigma}_c^2 \cos\theta_i \cos\theta_t} a_p - \frac{2n_1 \tilde{\sigma}_c \cos^2\theta_i}{f_1 f_2 - \tilde{\sigma}_c^2 \cos\theta_i \cos\theta_t} a_s, \tag{5.4}$$

$$r_p = \left(1 - \frac{2n_1 f_2 \cos\theta_t}{f_1 f_2 - \tilde{\sigma}_c^2 \cos\theta_i \cos\theta_t}\right) a_p - \frac{2n_1 \tilde{\sigma}_c \cos\theta_t \cos\theta_i}{f_1 f_2 - \tilde{\sigma}_c^2 \cos\theta_i \cos\theta_t} a_s, \tag{5.5}$$

$$t_s = \frac{2n_1 f_1 \cos\theta_i}{f_1 f_2 - \tilde{\sigma}_c^2 \cos\theta_i \cos\theta_t} a_s + \frac{2n_1 \tilde{\sigma}_c \cos\theta_i \cos\theta_t}{f_1 f_2 - \tilde{\sigma}_c^2 \cos\theta_i \cos\theta_t} a_p \tag{5.6}$$

$$t_s \left(-1 + \frac{2n_1 f_1 \cos\theta_i}{f_1 f_2 - \tilde{\sigma}_c^2 \cos\theta_i \cos\theta_t}\right) a_s + \frac{2n_1 \tilde{\sigma}_c \cos\theta_i \cos\theta_t}{f_1 f_2 - \tilde{\sigma}_c^2 \cos\theta_i \cos\theta_t} a_p, \tag{5.7}$$

where we have defined, as in [1], the simplifying functions,

$$f_1 = n_1 \cos\theta_t + n_2 \cos\theta_i + \tilde{\sigma}_q \cos\theta_i \cos\theta_i, \tag{5.8}$$

$$f_2 = n_1 \cos\theta_i + n_2 \cos\theta_t + \tilde{\sigma}_\tau. \tag{5.9}$$

As shown in equations 5.4-5.7, the in-plane anisotropy of phosphorene serves to mix contributions from the incident polarization. To fully explore the behaviour of phosphorene, we therefore need to consider the full range of incident polarization states (restricted to linear polarization). To do so, we define a polarization angle η such that the incident Fresnel amplitudes a_p and a_s are related to a common incident amplitude a by $a_p = a\cos\eta$, and $a_s = a\sin\eta$. In all of the following work, the incident amplitude will be defined as $a = 1$.

As was established in section 1.6, the conductivity of doped phosphorene is well described by a Drude model at low frequencies; in particular, up to around $\hbar\omega = 1$ eV. The Drude model for phosphorene is, of course, anisotropic with distinct values in each crystal direction [73],

$$\tilde{\sigma}_j(\omega) = \frac{i}{\pi} \frac{\omega'_{Fj}}{\omega + i\tau_f^{-1}}, \tag{5.10}$$

where $j = x, y$. The Fermi frequencies in each direction can be defined in terms of the doping density and effective electron mass as $\omega'_{Fj} = 4\pi\alpha\omega_{Fj}$, with $\omega_{Fj} = \pi|n|/m^*_j$, where $m^*_x = 0.133m_0$ and $m^*_y = 1.119m_0$[73]. In this section we will consider a doping density $n = 10^{13}\,\mathrm{cm}^{-2}$, which corresponds to $\omega_{Fx} = 0.18/\hbar$, and $\omega_{Fy} = 0.021/\hbar$, along with $\tau_f = 500$ fs.

To access the plasmonic regime, we will again use the technique by which the incident beam is made evanescent by defining $\sin\theta_i > 1$. This technique is described in more detail in section 4.2.

5.1 Plasmon dispersion

Unlike the case with out-of-plane conductivity, the dispersion relation for in-plane anisotropic conductivity is well established. A detailed derivation of the anisotropic dispersion relation is given in [43]. Here we will simply state the result that follows from the formalism used in section 2.4, though it agrees exactly with the result from [43] when one assumes that the out-of-plane wavenumbers are purely imaginary. The dispersion relation for in-plane anisotropic conductivity is,

$$\tilde{\sigma}_c^2 = \left(\tilde{\sigma}_q + \frac{n_1^2 k_0}{k_{z1}} + \frac{n_2^2 k_0}{k_{z2}}\right)\left(\tilde{\sigma}_\tau + \frac{k_{z1}}{k_0} + \frac{k_{z2}}{k_0}\right). \tag{5.11}$$

The presence of the off-diagonal conductivity component σ_c couples together the two in-plane modes. Working in the non-retarded limit ($q \gg \omega/c$), it is easy to find an analytical solution given by,

$$\omega = \sqrt{\frac{2v_B q}{n_{AM}^2}\left(\omega_{Fx}\cos^2\phi + \omega_{Fy}\sin^2\phi\right)}, \tag{5.12}$$

where v_B is the Bohr speed, and n_{AM}^2 is defined in equation 4.29. Equation 5.12 is a standard result and is shown in [21] with an additional correction for interband transitions that are not being considered here. Due to the anisotropy, the dispersion relation depends on the material rotation angle ϕ along with the dielectric material parameters. Figure 5.1 shows a surface plot of the analytical dispersion relation defined in equation 5.12 in cartesian coordinates, along with iso-frequency level curves along the q_x-q_y plane.

There is a clear transition between elliptical and hyperbolic iso-frequency curves. This transition is characteristic of phosphorene and other anisotropic 2D materials [74]. The inclusion of in-plane anisotropy does not significantly modify the character of the dispersion

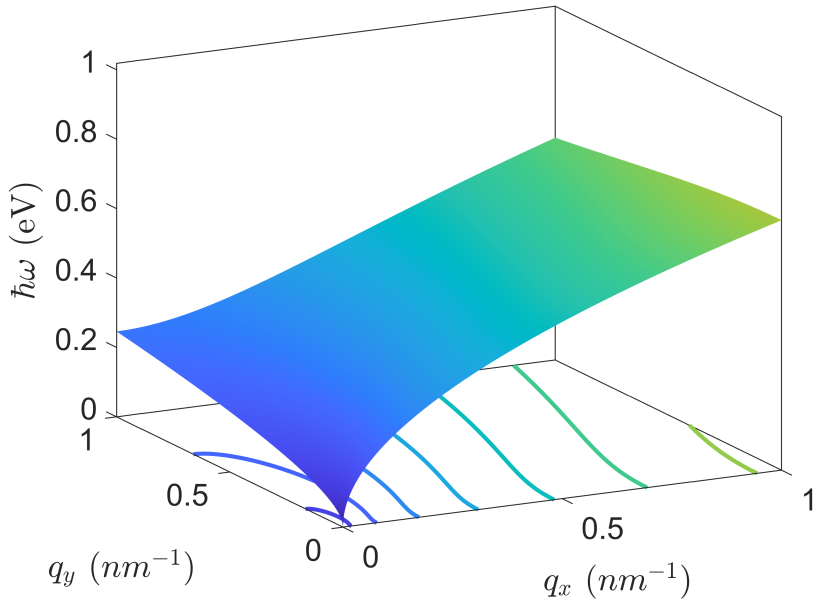


Figure 5.1: 3D dispersion surface for in-plane-only phosphorene surrounded by vacuum. Iso-frequency level curves are shown in the q_x-q_y plane.

relation at low energies, in comparison to how the out-of-plane conductivity modifies the dispersion of graphene. Variation of the associated parameters mostly serves to reduce the frequency while maintaining the root-like shape.

5.2 Forces

The forces will again be calculated using the stress tensor method, although only iso-frequency scans will be considered. For a more detailed explanation of this technique, see section 4.2.2. The scans along dispersion will not be considered for phosphorene because, over the parameter range explored in this work, there were no points of interest along the dispersion. The dispersion relation for phosphorene is monotonic and without inflection, so there is little additional information to be gained from scanning along the dispersion relation as all regions share essentially the same character.

The stress tensor method of calculating forces involves evaluating the difference between

the electromagnetic stress tensor on each side of the 2D material,

$$\mathbf{F} = \frac{1}{2}\Re\left(\overleftrightarrow{T}\cdot\hat{z}\Big|_{z_1}^{z_2}\right). \tag{5.13}$$

For vacuum surroundings, the standard Maxwell stress tensor will be used, which is defined in equation 3.84. For material surroundings, the vacuum gap stress tensor will be used, which is defined in equation 3.100.

We will start with iso-frequency scans at $\hbar\omega = 0.1$ eV. At this frequency, the iso-frequency curve of the dispersion relation will exhibit an elliptic character, as shown in figure 5.1. Vacuum surroundings will be considered initially, though the behaviour is qualitatively similar to the dielectric immersion case. Figure 5.2 shows the forces in the $\hat{z}$ and $\hat{q}$ directions for a series of iso-frequency scans with vacuum surroundings and p-polarization.

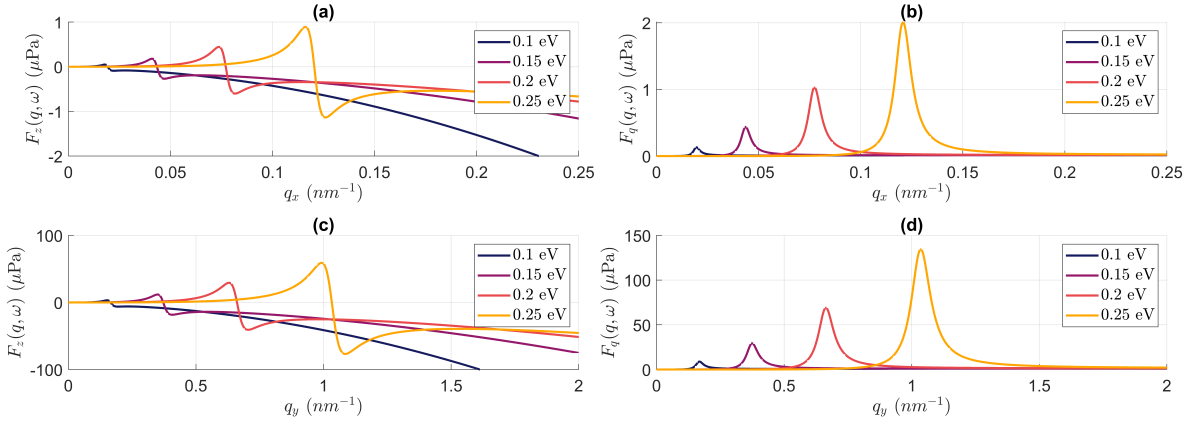


Figure 5.2: Iso-frequency $\hat{z}$ ((a), (c)), and $\hat{q}$ ((b), (d)) force plot. Polarization is defined by $\eta = 0$ and material rotation defined by $\phi = 0$ ((a), (b)), and $\phi = \pi/2$ ((c), (d)). All cases are calculated with vacuum surroundings.

These scans show a similar Lorentzian character to the scans for graphene, however, the switching peaks are more clearly asymmetric. There is also a significant difference in amplitude of almost two orders of magnitude between forces along q_x ($\phi = 0$, incident plane along the AC direction) and those along q_y ($\phi = \pi/2$, incident plane along the ZZ direction). With the additional polarization and rotation angular parameters in this case, more clarity is offered by considering density plots for broad ranges of angles. To cover the whole parameter space we will consider three polarization angles, $\eta = 0$ for p-polarization,

$\eta = \pi/4$ for even mixing, and $\eta = \pi/2$ for s-polarization. For each polarization angle, we will consider the range of material rotation angles $\phi = 0 - \pi/2$. Figure 5.3 (a) shows the iso-frequency scan force density plot for the $\hat{z}$ direction at $\hbar\omega = 0.1$ eV for p-polarization. As was shown in 5.2, across the entire range there is a zero crossing around resonance, however nearby $q = q_y$ ($\phi = \pi/2$), both the positive and negative amplitudes grow significantly. Figure 5.3 (b) shows the density plot with mixed polarization given by $\eta = \pi/4$. There is no qualitative difference between this setting and p-polarization, however there is a slight reduction in amplitude. This suggests forces are optimized in strength for pure p-polarization. Figure 5.3 (c) shows the iso-frequency density plot for s-polarization. In this case, there is a significant reduction in amplitude, along with a reversal to the direction of the limiting behaviour at $q = q_y$. For s-polarization, there is a positive linear increase in amplitude with wave number at $q = q_y$.

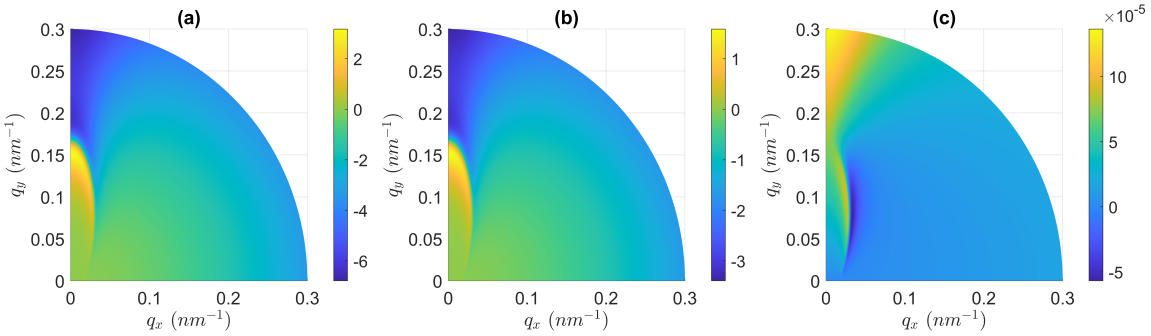


Figure 5.3: Iso-frequency $\hat{z}$ force density plot for $\hbar\omega = 0.1$ eV and polarization defined by (a) $\eta = 0$, (b) $\eta = \pi/4$, and (c) $\eta = \pi/2$. All cases are calculated with vacuum surroundings. Force density measured in μPa.

There are further changes to the forces in the $\hat{q}$ direction. Figure 5.4 (a) and (b) show the iso-frequency force density plot in the $\hat{q}$ direction at $\hbar\omega = 0.1$ eV for p-polarization, and mixed polarization with $\eta = \pi/4$, respectively. In both cases, the response exhibits a single positive peak around resonance, with the amplitude increasing towards a well-defined maximum at $q = q_y$ ($\phi = \pi/2$). This response is the imaginary Lorentzian counterpart to the real Lorentzian curve of the force in the $\hat{z}$ direction in the same regime. Figure 5.4 (c) shows a continuation of this trend, however with a suppression of the force at $q = q_y$, eliminating the well-defined maximum. In summary, for vacuum surroundings, or dielectric immersion, the $\hat{z}$ and $\hat{q}$ forces exhibit real and imaginary Lorentzian character, respectively. This is violated somewhat for s-polarization at $q = q_y$ ($\phi = \pi/2$) where the force in the $\hat{z}$ direction merges with a linear increase, and the force in the $\hat{q}$ direction is significantly

suppressed, eliminating the peak in both cases.

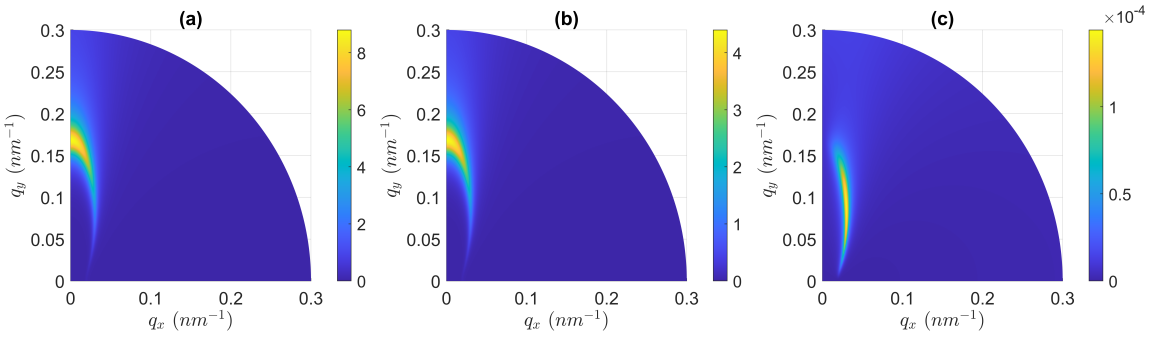


Figure 5.4: Iso-frequency $\hat{q}$ force density plot for $\hbar\omega = 0.1$ eV and polarization defined by (a) $\eta = 0$, (b) $\eta = \pi/4$, and (c) $\eta = \pi/2$. All cases are calculated with vacuum surroundings. Force density measured in μPa.

The Lorentzian nature of forces on phosphorene can be extracted analytically in the non-retarded limit. We will again consider the weak non-retarded limit such that c grows large but remains finite because the forces are all proportional to a factor of c^2. In the weak non-retarded limit, the $\hat{z}$ component of the force on phosphorene for arbitrary material rotation ϕ and polarization η is,

$$F_z = -\cos^2\eta\left(2c^2\epsilon_0 n_1^2 v_B \omega_{Fq}(\phi) q^3\right)\frac{2qv_B\omega_{Fq}(\phi) - n_2^2\omega^2}{\left(\omega n_{AM}^2\gamma\right)^2\omega^2 + \omega^2\left(2qv_B\omega_{Fq}(\phi) - n_{AM}^2\omega^2\right)^2}, \tag{5.14}$$

where n_{AM}^2 is defined in equation 4.29, v_B is the Bohr speed, and $\omega_{Fq}(\phi)$ is defined as,

$$\omega_{Fq}(\phi) = \omega_{Fx}\cos^2\phi + \omega_{Fy}\sin^2\phi. \tag{5.15}$$

The real Lorentzian character of the curve observed in figure 5.3 (a) and (b) is evident from the form of equation 5.14. Also reflected in equation 5.14 is the significant difference in amplitude between mixed or p-polarization and s-polarization shown in the right-most panel of 5.3. In the weak non-retarded limit, the force for s-polarization vanishes entirely.

Repeating this process for the $\hat{q}$ direction, the force in the weak non-retarded limit is,

$$F_q = \cos^2\eta\frac{2c^2\epsilon_0 n_1^2 v_B\omega_{Fq}(\phi)q^3\gamma}{\left(\omega n_{AM}^2\gamma\right)^2\omega + \omega\left(2qv_B\omega_{Fq}(\phi) - n_{AM}^2\omega^2\right)^2}, \tag{5.16}$$

where $\omega_{Fq}(\phi)$ is again defined as in equation 5.15. The imaginary Lorentzian character of the force in the $\hat{q}$ direction shown in figure 5.4 is revealed plainly in the weak non-retarded limit shown in equation 5.16.

Next, when considering distinct material surroundings we will only include numerical solutions for the $\hat{z}$ component of the force. This is because the $\hat{q}$ component remains qualitatively unchanged for the two cases $n_1 > n_2$ and $n_2 > n_1$, when compared to figure 5.4. To begin, figure 5.5 shows the iso-frequency force density scan at $\hbar\omega = 0.1$ eV for $n_1 = 1.5$, $n_2 = 1$.

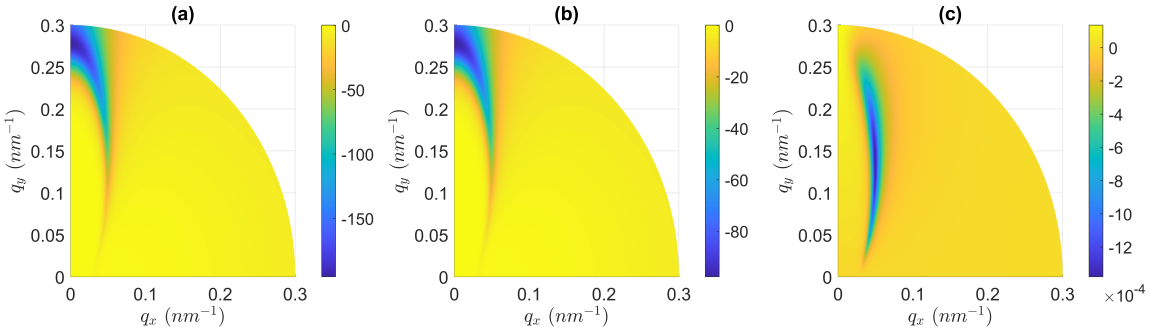


Figure 5.5: Iso-frequency $\hat{z}$ force density plot for $\hbar\omega = 0.1$ eV and polarization defined by (a) $\eta = 0$, (b) $\eta = \pi/4$, and (c) $\eta = \pi/2$. All cases are calculated with $n_1 = 1.5$, and $n_2 = 1$. Force density measured in μPa.

Similarly to the graphene case, once the surrounding dielectrics are distinct, all of the forces exhibit only one peak, either positive or negative depending on the material configuration. One notable feature is shown in figure 5.5 (c); the central linear trend at $\phi = \pi/2$ remains positive while the force at plasmon resonance is negative. Finally, figure 5.6 shows the iso-frequency force density scan at $\hbar\omega = 0.1$ eV for $n_1 = 1$, $n_2 = 1.5$. The same imaginary Lorentzian character is maintained, though in the opposite direction.

In each case explored here, the forces, be they in the $\hat{q}$ or $\hat{z}$ directions, are significantly diminished when the incident beam is s-polarized. In each case, the s-polarized force is around five orders of magnitude smaller than the forces for mixed or p-polarization. Across all of the configurations considered for phosphorene in the elliptic iso-frequency regime, the most prominent features in the force profiles appeared at the dispersion crossing when $q = q_y$ ($\phi = \pi/2$). For mixed or p-polarization $q = q_y$ corresponds to the largest plasmonic forces, while for s-polarization this point corresponds to highly suppressed forces.

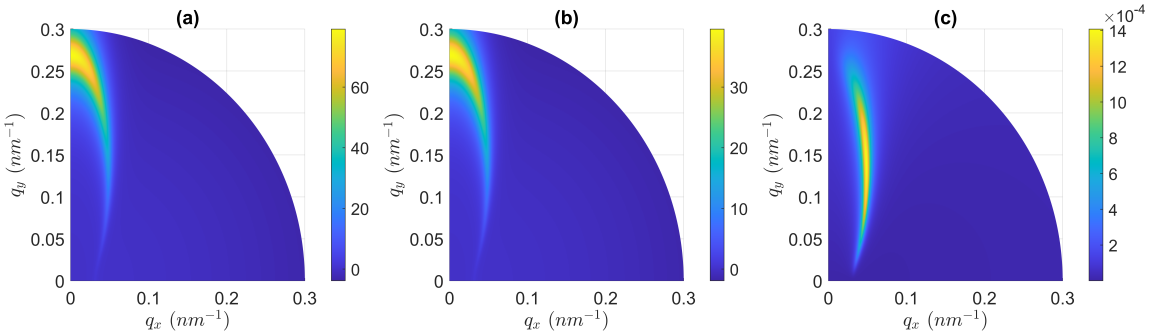


Figure 5.6: Iso-frequency $\hat{z}$ force density plot for $\hbar\omega = 0.1$ eV and polarization defined by (a) $\eta = 0$, (b) $\eta = \pi/4$, and (c) $\eta = \pi/2$. All cases are calculated with $n_1 = 1$, and $n_2 = 1.5$. Force density measured in μPa.

For completeness, we will also consider an iso-frequency force scan in the hyperbolic regime, corresponding to a frequency $\hbar\omega = 0.4$ eV. The force density profile for the $\hat{z}$ direction in this case is shown in figure 5.7. For this frequency, we only consider the

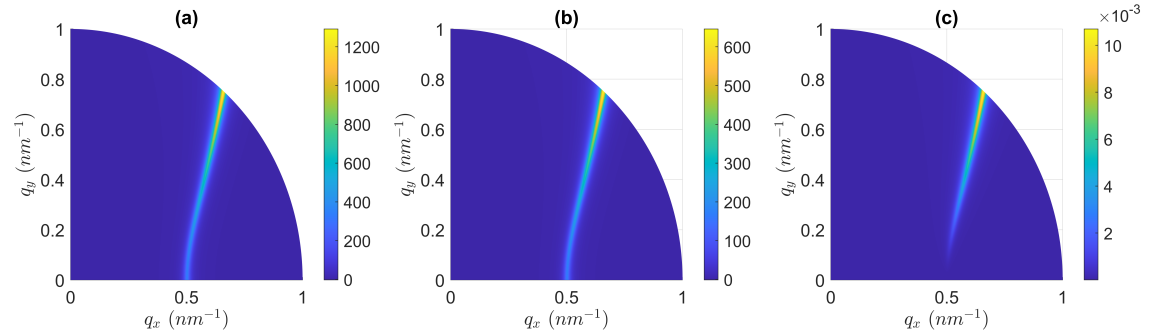


Figure 5.7: Iso-frequency $\hat{z}$ force density plot for $\hbar\omega = 0.4$ eV and polarization defined by (a) $\eta = 0$, (b) $\eta = \pi/4$, and (c) $\eta = \pi/2$. All cases are calculated with $n_1 = 1$, and $n_2 = 1.5$. Force density measured in μPa.

substrate case because the behaviour across all material configurations is broadly the same. In each case, including $n_1 = n_2$, $n_1 > n_2$, and $n_2 > n_1$, with p or mixed polarization the resonant ridge extends all the way to the q_x-axis, while for s-polarization there is an apparent suppression at the q_x-axis.

Chapter 6

Conclusion

It is critical that we further our understanding of optical interactions with 2D materials if we want to exploit the great potential of 2D material plasmonics. Towards that end, we have developed and applied a simple but flexible model based on Fresnel field amplitudes that takes into account the often ignored out-of-plane response. Chapter 1 formed the foundation of this investigation into optical interactions with 2D materials by establishing the formalism and introducing necessary concepts such as the Hertz vector, and material response functions.

Chapter 2 built upon this foundation by deriving the boundary conditions associated with the out-of-plane of 2D materials immersed in non-magnetic, isotropic, lossless, homogeneous dielectric environments. The work addressed the challenges associated with distinct dielectric surroundings through the introduction of screening by the harmonic mean of the dielectric permittivities of the surrounding media, which does not follow directly from the formalism, though it is supported by the work of other authors [36]. It further demonstrated the equivalence between the normal component of the electric field and the displacement field at the interface and showed derivations for the generalized Fresnel field amplitudes in cases involving both in-plane anisotropy and out-of-plane response. This led to the identification of the hybridization of the in-plane longitudinal (σ_q) and out-of-plane (σ_z) plasmon modes in the presence of distinct dielectric surroundings.

In Chapter 3, the integral conservation laws of energy and linear momentum were expressed directly in terms of field amplitudes in the Fourier domain for singular current sheets. By employing the vacuum gap method, the forces acting on the 2D material were isolated from those on surrounding dielectrics, and a non-standard stress tensor was derived, motivated by the vacuum gap method. Numerical verification of these conservation

equations proved that the vacuum gap method and associated stress tensor satisfy conservation of linear momentum.

Chapter 4 and 5 saw these theoretical developments applied to real materials such as undoped and doped graphene, as well as doped phosphorene. The analysis of undoped graphene revealed that while the out-of-plane influence is negligible at low frequencies in terms of reflectance (R), transmittance (T), and absorption (A), it becomes significant at higher frequencies and within the evanescent regime. Notably, new features in the reflectance appeared when including the out-of-plane response for matched dielectric surroundings ($n_1 = n_2 = n$). In particular, the emergence of a Brewster angle and a ridge of high reflectance near grazing incidence. Furthermore, the hybridization of surface modes in doped graphene resulted in a non-monotonic dispersion relation with a distinctive arch shape. The corresponding force profiles along the plasmon dispersion relation with out-of-plane response exhibited significant asymmetry with respect to the surrounding dielectrics. While the dispersion relation itself is unchanged under inversion of the dielectrics, the forces exhibited an anti-resonant feature at the maximum point of the non-monotonic dispersion relation when $n_2 > n_1$ that is not present when $n_1 > n_2$. In doped phosphorene, the well-known transition from elliptic to hyperbolic isofrequency curves was recreated, and polarization-dependent force amplification and suppression were observed. Along the zigzag (ZZ) crystal direction there was significant force amplification near plasmon resonance for p-polarization, while for s-polarization forces were heavily suppressed overall.

While much of this work is built systematically from well-accepted base principles, there are a number of key assumptions. Through comparison to the experimental results of [3], it appears certain that the out-of-plane response of 2D materials must be screened in some way by the surrounding dielectrics. Precisely how this screening appears in the boundary conditions remains an open question. Screening in classical electromagnetism is dictated by the background medium against which charges are defined. With the 2D materials defined precisely between two distinct dielectrics modelled as Heavisides, there is no unique way to define the screening. It was further assumed in this work that the forces on 2D materials at interfaces can be separated from the forces on the interfaces themselves. While the mathematical formulation is self-consistent, it is unclear how these results map to reality. Certainly, it is valid in the mathematical universe where surrounding dielectrics are truly abrupt and perfectly ridged. As such, how well the true forces experienced by 2D materials at interfaces match with the predictions in this work may depend on how well the surrounding materials can be approximated as abrupt and rigid. The most interesting result of this work is certainly the arch-shaped dispersion relation of graphene with the out-of-plane response. However, this result is based both on the assumption that doping

does not influence the out-of-plane conductivity and that the in-plane conductivity is well described by a Drude model. The true way to account for out-of-plane conductivity with doping is simply not known, but in terms of in-plane conductivity, it is certain that the Drude model is only an approximation. In reality, the notable non-monotonic behaviour could be destroyed through interaction with the continuum of intraband single-particle excitations that the Drude model does not capture [65]. Finally, it is very likely that phosphorene has a stronger out-of-plane response than graphene, making all of the work based solely on the in-plane conductivity incomplete.

The results of this investigation, combined with the myriad limitations, suggest a number of pertinent future research directions. Of course, it is important to identify if forces on 2D materials can be truly separated from the surrounding dielectrics. An experimental exploration of optical forces on 2D materials is therefore warranted. However, with forces outside the plasmonic regime measured in pico-Newtons, such things would be difficult to access experimentally. Static single-layer graphene has been used in force sensors before, however, the forces being measured were on the order of kilo-Newtons [75]. A perhaps more immediately accessible direction is the confirmation of the appropriate dielectric screening on the out-of-plane response. Reflectance measurements from a simple experiment involving a sample of graphene sandwiched between two distinct dielectrics could be compared to the reflectance models in this work to determine what screening is necessary. This experiment could be accompanied by a theoretical investigation of the boundary condition using a retarded Green's function derived for piecewise continuous media, as this may be able to predict the appropriate screening. Finally, a theoretical investigation into the full complex dispersion relation of graphene with out-of-plane response and a model of the in-plane conductivity that includes interband transitions, Pauli-blocking, and an intraband continuum of single-particle excitations is necessary to truly establish the plasmonic influence of out-of-plane conductivity [44][65].

References

[1] Maurice Oliva-Leyva and G Gonzalez De la Cruz. Unveiling optical in-plane anisotropy of 2d materials from oblique incidence of light. *Journal of Physics: Condensed Matter*, 31(33):335701, 2019.

[2] Lars Matthes, Olivia Pulci, and Friedhelm Bechstedt. Influence of out-of-plane response on optical properties of two-dimensional materials: First principles approach. *Physical Review B*, 94(20):205408, 2016.

[3] Zhemi Xu, Davide Ferraro, Annamaria Zaltron, Nicola Galvanetto, Alessandro Martucci, Luzhao Sun, Pengfei Yang, Yanfeng Zhang, Yuechen Wang, Zhongfan Liu, et al. Optical detection of the susceptibility tensor in two-dimensional crystals. *Communications Physics*, 4(1):215, 2021.

[4] JM Pitarke, VM Silkin, EV Chulkov, and PM Echenique. Theory of surface plasmons and surface-plasmon polaritons. *Reports on progress in physics*, 70(1):1, 2006.

[5] BU Felderhof and G Marowsky. Electromagnetic radiation from a polarization sheet located at an interface between two media. *Applied Physics B*, 44:11–17, 1987.

[6] Mohammad Mahdi Salary, Sandeep Inampudi, Kuan Zhang, Ellad B Tadmor, and Hossein Mosallaei. Mechanical actuation of graphene sheets via optically induced forces. *Physical Review B*, 94(23):235403, 2016.

[7] Richard R Hartmann, Junichiro Kono, and Mikhail E Portnoi. Terahertz science and technology of carbon nanomaterials. *Nanotechnology*, 25(32):322001, 2014.

[8] K S Novoselov, Artem Mishchenko, Alexandra Carvalho, and AH Castro Neto. 2d materials and van der waals heterostructures. *Science*, 353(6298):aac9439, 2016.

[9] Sh Das Sarma, Shaffique Adam, EH Hwang, and Enrico Rossi. Electronic transport in two-dimensional graphene. *Reviews of modern physics*, 83(2):407–470, 2011.

[10] Yu Li, Ziwei Li, Cheng Chi, Hangyong Shan, Liheng Zheng, and Zheyu Fang. Plasmonics of 2d nanomaterials: properties and applications. *Advanced science*, 4(8):1600430, 2017.

[11] Yexin Deng, Zhe Luo, Nathan J Conrad, Han Liu, Yongji Gong, Sina Najmaei, Pulickel M Ajayan, Jun Lou, Xianfan Xu, and Peide D Ye. Black phosphorus–monolayer mos2 van der waals heterojunction p–n diode. *ACS nano*, 8(8):8292–8299, 2014.

[12] Liang Li, Wei Han, Lejing Pi, Ping Niu, Junbo Han, Chengliang Wang, Bin Su, Huiqiao Li, Jie Xiong, Yoshio Bando, et al. Emerging in-plane anisotropic two-dimensional materials. *InfoMat*, 1(1):54–73, 2019.

[13] Yu V Bludov, Aires Ferreira, Nuno MR Peres, and Mikhail I Vasilevskiy. A primer on surface plasmon-polaritons in graphene. *International Journal of Modern Physics B*, 27(10):1341001, 2013.

[14] Stefan A Maier. Plasmonic field enhancement and sers in the effective mode volume picture. *Optics Express*, 14(5):1957–1964, 2006.

[15] Hyun Seok Lee, Min Su Kim, Youngjo Jin, Gang Hee Han, Young Hee Lee, and Jeongyong Kim. Selective amplification of the primary exciton in a mo s 2 monolayer. *Physical review letters*, 115(22):226801, 2015.

[16] Serkan Butun, Sefaattin Tongay, and Koray Aydin. Enhanced light emission from large-area monolayer mos2 using plasmonic nanodisc arrays. *Nano letters*, 15(4):2700–2704, 2015.

[17] Markus A Huber, Fabian Mooshammer, Markus Plankl, Leonardo Viti, Fabian Sandner, Lukas Z Kastner, Tobias Frank, Jaroslav Fabian, Miriam S Vitiello, Tyler L Cocker, et al. Femtosecond photo-switching of interface polaritons in black phosphorus heterostructures. *Nature Nanotechnology*, 12(3):207–211, 2017.

[18] Nicholas R Glavin, Rahul Rao, Vikas Varshney, Elisabeth Bianco, Amey Apte, Ajit Roy, Emilie Ringe, and Pulickel M Ajayan. Emerging applications of elemental 2d materials. *Advanced Materials*, 32(7):1904302, 2020.

[19] AM Albano, D Bedeaux, and J Vlieger. On the description of interfacial properties using singular densities and currents at a dividing surface. *Physica A: Statistical Mechanics and its Applications*, 99(1-2):293–304, 1979.

[20] E. Hecht. *Optics*. Pearson, 5th ed. edition, 2017.

[21] Zoran L Mišković, Milad Moshayedi, Maria Rosa Preciado Rivas, Josip Jakovac, Ivan Radović, and Vito Despoja. Modeling of the interband transitions in the optical conductivity of doped two-dimensional materials in the terahertz to the infrared frequency range: the case studies of graphene and phosphorene. *Radiation Effects and Defects in Solids*, 178(1-2):54–71, 2023.

[22] S.L. Chuang. *Physics of Photonic Devices*. Wiley Series in Pure and Applied Optics. Wiley, 2009.

[23] Vito Despoja, Tijana Djordjević, Lazar Karbunar, Ivan Radović, and Zoran L Mišković. Ab initio study of the electron energy loss function in a graphene-sapphire-graphene composite system. *Physical Review B*, 96(7):075433, 2017.

[24] Yilei Li and Tony F Heinz. Two-dimensional models for the optical response of thin films. *2D Materials*, 5(2):025021, 2018.

[25] Dick Bedeaux and Jan Vlieger. *Optical properties of surfaces*. Imperial College Press, 2004.

[26] Tobias Stauber, Numo MR Peres, and Andre K Geim. Optical conductivity of graphene in the visible region of the spectrum. *Physical Review B—Condensed Matter and Materials Physics*, 78(8):085432, 2008.

[27] Tianrong Zhan, Xi Shi, Yunyun Dai, Xiaohan Liu, and Jian Zi. Transfer matrix method for optics in graphene layers. *Journal of Physics: Condensed Matter*, 25(21):215301, 2013.

[28] L Matthes, O Pulci, and F Bechstedt. Optical properties of two-dimensional honeycomb crystals graphene, silicene, germanene, and tinene from first principles. *New Journal of Physics*, 16(10):105007, 2014.

[29] Xin-Hua Deng, Jiang-Tao Liu, Ji-Ren Yuan, Qing-Hua Liao, and Nian-Hua Liu. A new transfer matrix method to calculate the optical absorption of graphene at any position in stratified media. *Europhysics Letters*, 109(2):27002, 2015.

[30] M Shoufie Ukhtary, Eddwi H Hasdeo, Ahmad RT Nugraha, and Riichiro Saito. Fermi energy-dependence of electromagnetic wave absorption in graphene. *Applied Physics Express*, 8(5):055102, 2015.

[31] C Strachan. The reflexion of light at a surface covered by a monomolecular film. In *Mathematical Proceedings of the Cambridge Philosophical Society*, volume 29, pages 116–130. Cambridge University Press, 1933.

[32] M Idemen and A Hamit Serbest. Boundary conditions of the electromagnetic field. *Electronics Letters*, 13(23):704–705, 1987.

[33] Thomas BA Senior and John L Volakis. Sheet simulation of a thin dielectric layer. *Radio Science*, 22(07):1261–1272, 1987.

[34] Julius Adams Stratton. *Electromagnetic Theory*. McGraw-Hill Companies (New York), 1 edition, 1941. The URL and misc. info are for a re-issue published in 2007 by Wiley-IEEE Press.

[35] Ron Atkinson and NF Kubrakov. Boundary conditions in the simplest model of linear and second harmonic magneto-optical effects. *Physical Review B*, 65(1):014432, 2001.

[36] Mohamed Abed Mohamed, Edward F Kuester, Melinda Piket-May, and Christopher L Holloway. The field of an electric dipole and the polarizability of a conducting object embedded in the interface between dielectric materials. *Progress In Electromagnetics Research B*, 16:1–20, 2009.

[37] Vadim A Markel. External versus induced and free versus bound electric currents and related fundamental questions of the classical electrodynamics of continuous media: discussion. *JOSA A*, 35(10):1663–1673, 2018.

[38] Max Born and Emil Wolf. *Principles of Optics: Electromagnetic Theory of Propagation, Interference and Diffraction of Light (7th Edition)*. Cambridge University Press, 7th edition, 1999.

[39] Lukas Novotny and Bert Hecht. *Principles of Nano-Optics*. Cambridge University Press, 2 edition, 2012.

[40] Mithat Idemen. Universal boundary relations of the electromagnetic field. *Journal of the Physical Society of Japan*, 59(1):71–80, 1990.

[41] David J Griffiths. *Introduction to electrodynamics*. Pearson, 2013.

[42] Oleg V Kotov and Yu E Lozovik. Hyperbolic hybrid waves and optical topological transitions in few-layer anisotropic metasurfaces. *Physical Review B*, 100(16):165424, 2019.

[43] Vl A Margulis and EE Muryumin. Theory for surface polaritons supported by a black-phosphorus monolayer. *Physical Review B*, 98(16):165305, 2018.

[44] Marinko Jablan, Hrvoje Buljan, and Marin Soljačić. Plasmonics in graphene at infrared frequencies. *Physical Review B—Condensed Matter and Materials Physics*, 80(24):245435, 2009.

[45] Galina L Klimchitskaya and Vladimir M Mostepanenko. The casimir force between two graphene sheets: 2d fresnel reflection coefficients, contributions of different polarizations, and the role of evanescent waves. *Physics*, 5(4):1013–1030, 2023.

[46] Zoran L Mišković, Kamran Akbari, Silvina Segui, Juana L Gervasoni, and Néstor R Arista. Relativistic effects in the energy loss of a fast charged particle moving parallel to a two-dimensional electron gas. *Nuclear Instruments and Methods in Physics Research Section B: Beam Interactions with Materials and Atoms*, 422:18–23, 2018.

[47] A Principi, Marco Polini, and Giovanni Vignale. Linear response of doped graphene sheets to vector potentials. *Physical Review B—Condensed Matter and Materials Physics*, 80(7):075418, 2009.

[48] Evdokia Dremetsika and Pascal Kockaert. Enhanced optical kerr effect method for a detailed characterization of the third-order nonlinearity of two-dimensional materials applied to graphene. *Physical Review B*, 96(23):235422, 2017.

[49] Philippe Tassin, Thomas Koschny, and Costas M Soukoulis. Effective material parameter retrieval for thin sheets: Theory and application to graphene, thin silver films, and single-layer metamaterials. *Physica B: Condensed Matter*, 407(20):4062–4065, 2012.

[50] Bruno Majérus, Evdokia Dremetsika, Michaël Lobet, Luc Henrard, and Pascal Kockaert. Electrodynamics of two-dimensional materials: Role of anisotropy. *Physical Review B*, 98(12):125419, 2018.

[51] Edward F Kuester, Mohamed A Mohamed, Melinda Piket-May, and Christopher L Holloway. Averaged transition conditions for electromagnetic fields at a metafilm. *IEEE Transactions on Antennas and Propagation*, 51(10):2641–2651, 2003.

[52] JL Cheng, JE Sipe, Nathalie Vermeulen, and C Guo. Nonlinear optics of graphene and other 2d materials in layered structures. *Journal of Physics: Photonics*, 1(1):015002, 2018.

[53] Masud Mansuripur. Radiation pressure and the linear momentum of the electromagnetic field. *Optics Express*, 12(22):5375–5401, 2004.

[54] P Guyot-Sionnest, W Chen, and YR Shen. General considerations on optical second-harmonic generation from surfaces and interfaces. *Physical Review B*, 33(12):8254, 1986.

[55] Zoran L Mišković, Silvina Segui, Juana L Gervasoni, and Néstor R Arista. Energy losses and transition radiation produced by the interaction of charged particles with a graphene sheet. *Physical Review B*, 94(12):125414, 2016.

[56] Xiaoguang Luo, Teng Qiu, Weibing Lu, and Zhenhua Ni. Plasmons in graphene: recent progress and applications. *Materials Science and Engineering: R: Reports*, 74(11):351–376, 2013.

[57] Sergey G Menabde, Jacob T Heiden, Joel D Cox, N Asger Mortensen, and Min Seok Jang. Image polaritons in van der waals crystals. *Nanophotonics*, 11(11):2433–2452, 2022.

[58] Robert NC Pfeifer, Timo A Nieminen, Norman R Heckenberg, and Halina Rubinsztein-Dunlop. Colloquium: Momentum of an electromagnetic wave in dielectric media. *Reviews of Modern Physics*, 79(4):1197–1216, 2007.

[59] David J Griffiths. Resource letter em-1: Electromagnetic momentum. *American Journal of Physics*, 80(1):7–18, 2012.

[60] BA Kemp. Resolution of the abraham-minkowski debate: Implications for the electromagnetic wave theory of light in matter. *Journal of Applied Physics*, 109(11), 2011.

[61] Timothy H Boyer. Illustrations of maxwell's term and the four conservation laws of electromagnetism. *American Journal of Physics*, 87(9):729–738, 2019.

[62] Maplesoft, a division of Waterloo Maple Inc.. Maple.

[63] Sellmeier. Zur erklärung der abnormen farbenfolge im spectrum einiger substanzen. *Annalen der Physik*, 219(6):272–282, 1871.

[64] TWH Oates, Herbert Wormeester, and Hans Arwin. Characterization of plasmonic effects in thin films and metamaterials using spectroscopic ellipsometry. *Progress in Surface Science*, 86(11-12):328–376, 2011.

[65] EH Hwang and S Das Sarma. Dielectric function, screening, and plasmons in two-dimensional graphene. *Physical Review B—Condensed Matter and Materials Physics*, 75(20):205418, 2007.

[66] M Ghorbanzadeh, S Darbari, and MK Moravvej-Farshi. Graphene-based plasmonic force switch. *Applied Physics Letters*, 108(11), 2016.

[67] Jung-Dae Kim and Yong-Gu Lee. Graphene-based plasmonic tweezers. *Carbon*, 103:281–290, 2016.

[68] Brahim Guizal and Mauro Antezza. Light-induced optomechanical forces in graphene waveguides. *Physical Review B*, 93(11):115427, 2016.

[69] Peng Zhang, Nian-Hai Shen, Thomas Koschny, and Costas M Soukoulis. Surface-plasmon-mediated gradient force enhancement and mechanical state transitions of graphene sheets. *Acs Photonics*, 4(1):181–187, 2017.

[70] In-Ho Lee, Luis Martin-Moreno, Daniel A Mohr, Kaveh Khaliji, Tony Low, and Sang-Hyun Oh. Anisotropic acoustic plasmons in black phosphorus. *ACS photonics*, 5(6):2208–2216, 2018.

[71] Vl A Margulis, EE Muryumin, and EA Gaiduk. Optical reflection, transmission and absorption properties of single-layer black phosphorus from a model calculation. *Journal of Optics*, 18(5):055102, 2016.

[72] Muzamil Shah, Azizeh Alidoust Ghatar, Aamir Hayat, Omid Akhavan, and Dariush Jahani. Surface plasmon resonances in anisotropic strained graphene. *Journal of the Optical Society of America B*, 40(9):2315–2320, 2023.

[73] Milad Moshayedi, Maria Rosa Preciado Rivas, and Zoran L Mišković. Stopping and image forces on a charged particle moving parallel to an anisotropic two-dimensional material. *Physical Review B*, 105(7):075429, 2022.

[74] Kamran Akbari and Zoran L Mišković. Directional effects in plasmon excitation and transition radiation from an anisotropic 2d material induced by a fast charged particle. *Nanoscale*, 14(13):5079–5093, 2022.

[75] Sungwoo Chun, Youngjun Kim, Hyeongki Jin, Eunsuk Choi, Seung-Beck Lee, and Wanjun Park. A graphene force sensor with pressure-amplifying structure. *Carbon*, 78:601–608, 2014.

[76] A.K. Ghatak and K. Thyagarajan. *Contemporary Optics*. Mathematical Concepts and Methods in Science and Engineering. Springer US, 1978.

[77] Rémi H. Renard. Total reflection: A new evaluation of the goos–hänchen shift. *J. Opt. Soc. Am.*, 54(10):1190–1197, Oct 1964.

[78] AI Mahan and CV Bitterli. Total internal reflection: a deeper look. *Applied Optics*, 17(4):509–519, 1978.

[79] Meguya Ryu, Soon Hock Ng, Vijayakumar Anand, Stefan Lundgaard, Jingwen Hu, Tomas Katkus, Dominique Appadoo, Zoltan Vilagosh, Andrew W Wood, Saulius Juodkazis, et al. Attenuated total reflection at thz wavelengths: prospective use of total internal reflection and polariscopy. *Applied Sciences*, 11(16):7632, 2021.

[80] Shane Zhu, Anthony Yu, D. Hawley, and Rajarshi Roy. Frustrated total internal reflection: A demonstration and review. *American Journal of Physics - AMER J PHYS*, 54:601–607, 07 1986.

[81] Akhlesh Lakhtakia. Would brewster recognize today's brewster angle. *Optics News*, 15(6):14–18, 1989.

[82] Bruno Majérus, Mirko Cormann, Nicolas Reckinger, Matthieu Paillet, Luc Henrard, Philippe Lambin, and Michaël Lobet. Modified brewster angle on conducting 2d materials. *2D Materials*, 5(2):025007, 2018.

[83] SY Kim and K Vedam. Analytic solution of the pseudo-brewster angle. *JOSA A*, 3(11):1772–1773, 1986.

[84] Reginald Victor Jones and JCS Richards. The pressure of radiation in a refracting medium. *Proceedings of the Royal Society of London. Series A. Mathematical and Physical Sciences*, 221(1147):480–498, 1954.

[85] R. V. Jones and B. P. Leslie. The measurement of optical radiation pressure in dispersive media. *Proceedings of the Royal Society of London. A. Mathematical and Physical Sciences*, 360:347–363, 1978.

APPENDICES

Appendix A

Applications of Fresnel's formulas

A.1 Total internal reflection

When an electromagnetic wave crosses an interface to a material with a higher phase velocity (lower index of refraction), its trajectory is pulled toward the interface. This is a relationship well described by Snell's law, defined in equation 1.71. Between 0 and $\pi/2$, $\sin\theta$ is a function that increases from 0 to 1, so when $n_1 > n_2$, to maintain the equality, any angle θ_t has to be larger than the angle θ_i. This relationship reaches a breaking point at an incident angle $\theta_c = \sin^{-1}\frac{n_2}{n_1}$, when $\sin\theta_t$ reaches its maximum of one. To satisfy equation 1.71 past this point, θ_t must become complex. This results in $\sin\theta_t > 1$ and an imaginary value for the cosine given by,

$$\cos\theta_t = \sqrt{1-\sin^2\theta_t} = i\sqrt{\sin^2\theta_t - 1}. \tag{A.1}$$

At the critical angle $\cos\theta_t = 0$, and so the transmitted field is travelling parallel to the interface. However, past the critical angle the transmitted field is replaced by an evanescent field,

$$\mathbf{E}_t = \mathbf{E}_0 e^{i(\mathbf{q}\cdot\mathbf{r}_\parallel + k_z z - \omega t)}, \tag{A.2}$$

$$= \mathbf{E}_0 e^{i(\mathbf{q}\cdot\mathbf{r}_\parallel + k_2\cos\theta_t z - \omega t)}, \tag{A.3}$$

$$= \mathbf{E}_0 e^{-zk_2\sqrt{\sin^2\theta_t - 1}} e^{i(\mathbf{q}\cdot\mathbf{r}_\parallel - \omega t)}, \tag{A.4}$$

with an exponential decay into the second medium. For infinite plane waves, past the critical angle, the reflected field also receives a small phase shift called the Goos-Henchen

shift [34]. For finite beams, however, this shift is a physical shift, on the order of a wavelength, from the spot illuminated by the incident beam [76].

This new evanescent field exhibits no net flow of energy into the second medium, hence the name total internal reflection [34]. However, as shown in equation A.4, these fields do propagate along the interface, and they carry energy with them [34]. This would appear to violate the totality of reflection. The apparent violation is merely a consequence of the infinite extent of plane waves. For finite fields it has been shown that the evanescent wave propagating along the interface carries the exact amount of energy to produce the shift in the beam [77]. This indicates that the light is incident on the surface, converted into an evanescent field that propagates a distance given by the Goos-Henchen shift and is re-emitted as the reflected field. This picture has been corroborated by investigations of energy flow in these situations. In [78], it was shown that under conditions of TIR, electromagnetic energy propagates into and along the second medium, and then is re-emitted as the reflected field. In spite of this, the totality of reflection is more of an exception than a rule. Because energy is propagated through the interface and the second medium, if either is lossy, the reflected field will be attenuated. This is referred to as attenuated total internal reflection (ATR)[79]. Further, if there are obstructions in the second medium that interact with the evanescent field, for example, another interface, then the reflected field can also be attenuated. This is called frustrated total internal reflection (FTR)[80].

A.2 Brewster angle

The Brewster angle has seen numerous definitions throughout history [81]. Initially, it was known as the angle at which un-polarized light incident on an interface is reflected as linearly polarized. In these cases, it was often referred to as the polarizing angle. In modern times it is more commonly known as the angle at which p-polarized light is perfectly transmitted, and so is often defined as the angle θ when $R_p = |r_p|^2 = 0$, where r_p is the reflected Fresnel amplitude of p-polarized light. This distinction only becomes important when the interface or the surrounding media have complex optical behaviour like chirality. In these cases, it is possible to have a polarizing angle that does not coincide with $R = |r_p|^2 = 0$ [81]. In this work, no such cases are considered.

We will define the Brewster angle as the incident angle at which the reflectance of p-polarized light is zero. For a flat interface between two isotropic, non-magnetic, lossless

dielectrics, the zero reflectance Brewster angle is given by

$$\theta_b = \tan^{-1} \frac{n_2}{n_1}. \tag{A.5}$$

However, this definition is no longer applicable when a sheet of conductivity is introduced into the interface. For example, a singular isotropic in-plane current sheet at an interface results in a reflectance given by, [82]

$$R_p = \left| \frac{n_1 \cos\theta_t - n_2 \cos\theta_i - \sigma \cos\theta_i \cos\theta_t}{n_1 \cos\theta_t + n_2 \cos\theta_i + \sigma \cos\theta_i \cos\theta_t} \right|^2, \tag{A.6}$$

where σ is the in-plane sheet conductivity. When σ is real, the angle at which $R_p = 0$ no longer coincides with equation A.5. Instead, a solution to $R_p(\theta_i) = 0$ must be solved for numerically after the application of Snell's law to cast the equation only in terms of the incident angle [82]. The situation grows further complicated when σ is complex. In this case, R_p no longer goes to zero [82]. However, we can still define a pseudo-Brewster angle given by the minimum of the reflectance R_p [83]. It should be noted that this definition is highly dependent on absorption, so the minimum reflectance may not coincide with the maximum transmittance of p-polarized light.

Appendix B

Additional derivations for conservation relations

B.1 Conservation equations in the Fourier domain

Electromagnetic energy and momentum conservation are generally only physically meaningful when they involve purely real fields. With real fields, the differential form of energy conservation is defined in equation 3.2. However, the same relationship is often taken to be true for complex fields when the products are replaced with half the real part of conjugate products. Here we will show that this is in fact true for the integral form of both energy conservation and momentum conservation.

Consider two real fields $\mathbf{A}$ and $\mathbf{B}$ that are defined with respect to two complex fields $\mathbf{f}$ and $\mathbf{g}$,

$$\mathbf{A}(\mathbf{r}_\parallel, t) = \frac{1}{2}(\mathbf{f}(\mathbf{r}_\parallel, t) + \mathbf{f}^*(\mathbf{r}_\parallel, t)), \tag{B.1}$$

and,

$$\mathbf{B}(\mathbf{r}_\parallel, t) = \frac{1}{2}(\mathbf{g}(\mathbf{r}_\parallel, t) + \mathbf{g}^*(\mathbf{r}_\parallel, t)), \tag{B.2}$$

where we are assuming for simplicity in this section that the fields only have in-plane spatial dependence defined by $\mathbf{r}_\parallel$. The results will remain applicable to the case with z dependence because the Fourier analysis applied in this section only involves the in-plane spatial coordinates ($\mathbf{r}_\parallel$), and time (t). In this section, we also consider the full in-plane wavevector defined by $\mathbf{q} = q\hat{q} + \tau\hat{\tau}$.

Both the electromagnetic energy and momentum conservation equations can be broken down into terms that look like products of real field components, perhaps with some constant multiplier from the application of a derivative or multiplication by a conductivity,

$$\frac{1}{T}\int_{-T/2}^{T/2} dt \frac{1}{L_q L_\tau} \iint_D d^2\mathbf{r}_\parallel \, A_i B_j, \tag{B.3}$$

where A_i and B_j are components of electromagnetic fields, and D is a rectangular in-plane region defined by the side lengths L_q and L_τ. We can express the product in the integrand in terms of the complex fields,

$$A_i B_j = \frac{1}{4}(f_i g_j + f_i g_j^* + f_i^* g_j + f_i^* g_j^*), \tag{B.4}$$

where f_i and g_j are the cartesian components of the fields $\mathbf{f}$ and $\mathbf{g}$, respectively. What we will see in the following analysis is that the non-conjugate and conjugate-conjugate products go to zero for monochromatic plane waves. Consider first the product of un-conjugated field components,

$$\frac{1}{T}\int_{-T/2}^{T/2} dt \frac{1}{L_q L_\tau} \iint_D d^2\mathbf{r}_\parallel \, f_i g_j. \tag{B.5}$$

The first step is representing the real domain fields in terms of their Fourier domain counterpart as

$$\mathbf{f}(\mathbf{r}_\parallel, t) = \frac{1}{(2\pi)^3}\int_{\mathbb{R}} d\omega \iint_{\mathbb{R}^2} d^2\mathbf{q}\, \mathbf{f}(\mathbf{q},\omega) e^{i\left(\mathbf{q}\cdot\mathbf{r}_\parallel - \omega t\right)}, \tag{B.6}$$

and,

$$\mathbf{g}(\mathbf{r}_\parallel, t) = \frac{1}{(2\pi)^3}\int_{\mathbb{R}} d\omega \iint_{\mathbb{R}^2} d^2\mathbf{q}\, \mathbf{g}(\mathbf{q},\omega) e^{i\left(\mathbf{q}\cdot\mathbf{r}_\parallel - \omega t\right)}. \tag{B.7}$$

Then we insert equations B.6 and B.7 into equation B.3,

$$\frac{1}{T}\int_{-T/2}^{T/2} dt \frac{1}{L_q L_\tau} \iint_D d^2\mathbf{r}_\parallel \left(\frac{1}{(2\pi)^3}\int_{\mathbb{R}} d\omega \iint_{\mathbb{R}^2} d^2\mathbf{q}\, f_i(\mathbf{q},\omega) e^{i\left(\mathbf{q}\cdot\mathbf{r}_\parallel - \omega t\right)}\right) \left(\frac{1}{(2\pi)^3}\int_{\mathbb{R}} d\omega' \iint_{\mathbb{R}^2} d^2\mathbf{q}'\, g_j(\mathbf{q}',\omega') e^{i\left(\mathbf{q}'\cdot\mathbf{r}_\parallel - \omega' t\right)}\right). \tag{B.8}$$

The exponential factors in position and time can then be collected with their respective

integrals,

$$\frac{1}{(2\pi)^6}\int_{\mathbb{R}} d\omega \iint_{\mathbb{R}^2} d^2\mathbf{q}\, f_i(\mathbf{q},\omega)\int_{\mathbb{R}} d\omega' \iint_{\mathbb{R}^2} d^2\mathbf{q}'\, g_j(\mathbf{q}',\omega') \left(\frac{1}{T}\int_{-T/2}^{T/2} dt\, e^{-i(\omega+\omega')t}\right)\left(\frac{1}{L_qL_\tau}\iint_D d^2\mathbf{r}_\parallel\, e^{i(\mathbf{q}+\mathbf{q}')\cdot\mathbf{r}_\parallel}\right). \quad \text{(B.9)}$$

If one takes the factors T, L_q, and L_τ to be very large, corresponding to an average over a very large area and a very long time, then the collected terms simplify to Kronecker deltas,

$$\frac{1}{L_qL_\tau}\iint_D d^2\mathbf{r}_\parallel\, e^{i(\mathbf{q}+\mathbf{q}')\cdot\mathbf{r}_\parallel} = 4\frac{\sin\left(\frac{L_q(q'+q)}{2}\right)}{L_q(q'+q)}\frac{\sin\left(\frac{L_\tau(\tau'+\tau)}{2}\right)}{L_\tau(\tau'+\tau)} \approx \delta_{\mathbf{q},-\mathbf{q}'}, \quad \text{(B.10)}$$

and,

$$\frac{1}{T}\int_{-T/2}^{T/2} dt\, e^{-i(\omega+\omega')t} = \frac{2\sin\left(\frac{T(\omega'+\omega)}{2}\right)}{T(\omega'+\omega)} \approx \delta_{\omega,-\omega'}, \quad \text{(B.11)}$$

where the Kronecker delta terms are defined as

$$\delta_{\mathbf{q},-\mathbf{q}'} = \begin{cases} 0, & \text{when } \mathbf{q} \neq -\mathbf{q}' \\ 1, & \text{when } \mathbf{q} = -\mathbf{q}' \end{cases}, \quad \text{(B.12)}$$

and,

$$\delta_{\omega,-\omega'} = \begin{cases} 0, & \text{when } \omega \neq -\omega' \\ 1, & \text{when } \omega = -\omega' \end{cases}. \quad \text{(B.13)}$$

Inserting equation B.10 and B.11 into the equation B.9 results in

$$\frac{1}{(2\pi)^6}\int_{\mathbb{R}} d\omega \iint_{\mathbb{R}^2} d^2\mathbf{q}\, f_i(\mathbf{q},\omega)\int_{\mathbb{R}} d\omega' \iint_{\mathbb{R}^2} d^2\mathbf{q}'\, g_j(\mathbf{q}',\omega')\delta_{\mathbf{q},-\mathbf{q}'}\delta_{\omega,-\omega'} \quad \text{(B.14)}$$

Let us now choose to focus specifically on monochromatic plane waves. We will define these waves backwards in a sense, by asserting their frequency form first, and allowing the real space to follow,

$$\mathbf{f}(\mathbf{q},\omega) = (2\pi)^3\mathbf{f}_0(\mathbf{q},\omega)\delta(\mathbf{q}-\mathbf{q}_0)\delta(\omega-\omega_0), \quad \mathbf{g}(\mathbf{q},\omega) = (2\pi)^3\mathbf{g}_0(\mathbf{q},\omega)\delta(\mathbf{q}-\mathbf{q}_0)\delta(\omega-\omega_0). \quad \text{(B.15)}$$

Then, through equations B.6 and B.7, the real domain forms are defined as

$$\mathbf{f}(\mathbf{r}_\parallel, t) = \mathbf{f}_0(\mathbf{q}_0, \omega_0) e^{i(\mathbf{q}_0 \cdot \mathbf{r}_\parallel - \omega_0 t)}, \qquad \mathbf{g}(\mathbf{r}_\parallel, t) = \mathbf{g}_0(\mathbf{q}_0, \omega_0) e^{i(\mathbf{q}_0 \cdot \mathbf{r}_\parallel - \omega_0 t)}. \tag{B.16}$$

The subscript "0" is used here to both indicate amplitudes, and distinguish between the intrinsic frequency and wavenumber of the system, $(\omega_0, \mathbf{q}_0)$, and the free Fourier domain coordinates $(\omega, \mathbf{q})$. This labelling is omitted for the frequency and wavenumber terms when applying the results of this derivation in section 3. The fields are defined this way to allow their amplitudes to be influenced by temporal and spatial frequency dependence while recognizing that there is no dispersion or non-locality in the bulk where they propagate. Inserting the Fourier domain field definitions from equation B.15 into equation B.14 collapses all of the remaining integrals and leaves

$$f_{0i}(\mathbf{q}_0, \omega_0)\, g_{0j}(\mathbf{q}_0, \omega_0)\, \delta_{\mathbf{q}_0, -\mathbf{q}_0}\, \delta_{\omega_0, -\omega_0}. \tag{B.17}$$

The Dirac delta distributions have collapsed the integrals and selected the solution where $\mathbf{q} = \mathbf{q}_0$, and $\omega = \omega_0$. The result is that equation B.17 must be zero because the Kronecker delta is zero when the indices do not match, and no number can match its own negative. This same reasoning is obviously also true for the term with both fields conjugated. This reduces equation B.3 to

$$\frac{1}{T}\int_{-T/2}^{T/2} dt \frac{1}{L_q L_\tau} \iint_D d^2\mathbf{r}_\parallel\, A_i B_j = \frac{1}{T}\int_{-T/2}^{T/2} dt \frac{1}{L_q L_\tau} \iint_D d^2\mathbf{r}_\parallel\, \frac{1}{4}(f_i g_j^* + f_i^* g_j). \tag{B.18}$$

We can examine how these new terms behave by first looking at the product $f_i g_j^*$. If we conjugate the $\mathbf{g}$ field,

$$\mathbf{g}^*(\mathbf{r}_\parallel, t) = \frac{1}{(2\pi)^3} \int_{\mathbb{R}} d\omega \iint_{\mathbb{R}^2} d^2\mathbf{q}\, \mathbf{g}^*(\mathbf{q}, \omega) e^{-i\left(\mathbf{q}\cdot\mathbf{r}_\parallel - \omega t\right)}, \tag{B.19}$$

then equation B.9 becomes,

$$\frac{1}{(2\pi)^6} \int_{\mathbb{R}} d\omega \iint_{\mathbb{R}^2} d^2\mathbf{q}\, f_i(\mathbf{q}, \omega) \int_{\mathbb{R}} d\omega' \iint_{\mathbb{R}^2} d^2\mathbf{q}'\, g_j^*(\mathbf{q}', \omega') \left(\frac{1}{T}\int_{-T/2}^{T/2} dt\, e^{-i(\omega-\omega')t}\right) \left(\frac{1}{L_q L_\tau} \iint_D d^2\mathbf{r}_\parallel\, e^{i(\mathbf{q}-\mathbf{q}')\cdot\mathbf{r}_\parallel}\right). \tag{B.20}$$

The Kronecker deltas are therefore changed from $\delta_{\mathbf{q},-\mathbf{q}'}$ and $\delta_{\omega,-\omega'}$, which are defined in equations B.12 and B.13, to $\delta_{\mathbf{q},\mathbf{q}'}$ and $\delta_{\omega,\omega'}$. Following the same procedure that produced equation B.17 for this case with g_j^* results in a final expression of

$$f_{0i}(\mathbf{q}_0, \omega_0)\, g_{0j}^*(\mathbf{q}_0, \omega_0)\, \delta_{\mathbf{q}_0, \mathbf{q}_0}\, \delta_{\omega_0, \omega_0} = f_{0i}(\mathbf{q}_0, \omega_0)\, g_{0j}^*(\mathbf{q}_0, \omega_0), \tag{B.21}$$

where both Kornecker deltas evaluate to one. So, when considering monochromatic plane waves, the original integral expression defined in equation B.3 can be represented in terms of Fourier components as

$$\frac{1}{T}\int_{-T/2}^{T/2} dt \frac{1}{L_q L_\tau}\iint_D d^2\mathbf{r}_\parallel \frac{1}{4}(f_i(\mathbf{r}_\parallel,t)g_j^*(\mathbf{r}_\parallel,t)+f_i^*(\mathbf{r}_\parallel,t)g_j(\mathbf{r}_\parallel,t)) \tag{B.22}$$

$$=\frac{1}{4}\left(f_{0i}(\mathbf{q}_0,\omega_0)\,g_{0j}^*(\mathbf{q}_0,\omega_0)+f_{0i}^*(\mathbf{q}_0,\omega_0)\,g_{0j}(\mathbf{q}_0,\omega_0)\right)=\frac{1}{2}\Re\left(f_{0i}(\mathbf{q}_0,\omega_0)\,g_{0j}^*(\mathbf{q}_0,\omega_0)\right). \tag{B.23}$$

Alternatively, one can say that the spatiotemporal average of the product of real plane-wave field components is equal to the spatiotemporal average of half the real part of the conjugate product of complex plane-wave field components,

$$\frac{1}{T}\int_{-T/2}^{T/2} dt \frac{1}{L_q L_\tau}\iint_D d^2\mathbf{r}_\parallel\, A_i(\mathbf{r}_\parallel,t)B_i(\mathbf{r}_\parallel,t)=\frac{1}{T}\int_{-T/2}^{T/2} dt \frac{1}{L_q L_\tau}\iint_D d^2\mathbf{r}_\parallel \frac{1}{2}\Re(f_i(\mathbf{r}_\parallel,t)g_i^*(\mathbf{r}_\parallel,t)), \tag{B.24}$$

when the real and complex fields are related by equations B.1 and B.2.

B.2 A note on charge densities

In certain instances, the fields in the integration might instead be field-like quantities. For example, charge densities. To ensure that the results of section B.1 do not change, these are explored here. Consider first a charge density defined by a purely in-plane current through continuity as,

$$-\frac{\partial}{\partial t}\rho=\nabla_\parallel\cdot\mathbf{J}_\parallel(\mathbf{r}_\parallel,t)\delta(z). \tag{B.25}$$

Then converting to the Fourier domain, the charge density can be isolated as,

$$\rho=\frac{\mathbf{q}\cdot\mathbf{J}_\parallel(\mathbf{q},\omega)}{\omega}\delta(z), \tag{B.26}$$

where the imaginary terms from each derivative have been cancelled. For quantities like this, the method established in section B.1 is unchanged because there are no extra imaginary quantities to be acted upon by the conjugates, and the additional factors of $\mathbf{q}$ and ω will simply collapse to the intrinsic values associated with the monochromatic fields once the Dirac delta distributions defined in equation B.15 collapse the remaining integrals in

equation B.14. Consider next the higher-order contribution to charge density that appears as a result of an out-of-plane current,

$$-\frac{\partial}{\partial t}\rho = \nabla_{\parallel} \cdot \mathbf{J}_{\parallel}(\mathbf{r}_{\parallel}, t)\delta(z) + J_z(\mathbf{r}_{\parallel}, t)\delta'(z). \tag{B.27}$$

Then converting to the Fourier domain, the charge density can be isolated as

$$\rho = \frac{\mathbf{q} \cdot \mathbf{J}_{\parallel}(\mathbf{q}, \omega)}{\omega}\delta(z) - \frac{J_z(\mathbf{q}, \omega)}{i\omega}\delta'(z). \tag{B.28}$$

In this case, there is not only an additional imaginary contribution, but also a derivative in z, which is a coordinate not included in the Fourier transforms. To identify what changes this may cause, we will briefly consider the process established in section B.1 using

$$f(\mathbf{q}, \omega) = -(2\pi)^3\delta(\mathbf{q} - \mathbf{q}_0)\delta(\omega - \omega_0)\frac{f_0(\mathbf{q}, \omega)}{i\omega}\frac{\partial}{\partial z}, \tag{B.29}$$

and,

$$g(\mathbf{q}, \omega, z) = (2\pi)^3 g_0(\mathbf{q}, \omega)\delta(\mathbf{q} - \mathbf{q}_0)\delta(\omega - \omega_0)e^{ik_z z}, \tag{B.30}$$

to examine the behaviour of a product of a field-line quantity and the dipole density term defined in equation B.28.

It is immediately clear that the terms with matched conjugation will still go to zero because the Kronecker deltas, defined in equations B.10 and B.11, are unchanged. This would again leave only the terms with mixed conjugation,

$$\frac{1}{T}\int_{-T/2}^{T/2} dt \frac{1}{L_q L_\tau}\iint_D d^2\mathbf{r}_{\parallel}\,\frac{1}{4}(fg^* + f^*g). \tag{B.31}$$

Considering the first term in the integrand, following process established in section B.1 results in

$$\frac{1}{(2\pi)^6}\int_{\mathbb{R}} d\omega \iint_{\mathbb{R}^2} d^2\mathbf{q}\, f(\mathbf{q}, \omega)\int_{\mathbb{R}} d\omega' \iint_{\mathbb{R}^2} d^2\mathbf{q}'\, g^*(\mathbf{q}', \omega', z)\delta_{\mathbf{q},\mathbf{q}'}\delta_{\omega,\omega'} \tag{B.32}$$

Now inserting equations B.29 and B.30 and evaluating the Dirac delta distributions,

$$\left(-\frac{f_0(\mathbf{q}_0, \omega_0)}{i\omega_0}\frac{\partial}{\partial z}\right)\left(g_0^*(\mathbf{q}_0, \omega_0)e^{-ik_z^* z}\right)\delta_{\mathbf{q}_0,\mathbf{q}_0}\delta_{\omega_0,\omega_0} = \frac{k_z^*}{\omega_0}f_0(\mathbf{q}_0, \omega_0)g_0^*(\mathbf{q}_0, \omega_0)e^{-ik_z^* z}. \tag{B.33}$$

Next, we can repeat the preceding steps for the second term of the integrand in equation B.31,

$$\left(\frac{f_0^*(\mathbf{q}_0, \omega_0)}{i\omega_0}\frac{\partial}{\partial z}\right)\left(g_0(\mathbf{q}_0, \omega_0)e^{ik_z z}\right)\delta_{\mathbf{q}_0,\mathbf{q}_0}\delta_{\omega_0,\omega_0} = \frac{k_z}{\omega_0}f_0^*(\mathbf{q}_0, \omega_0)g_0(\mathbf{q}_0, \omega_0)e^{-ik_z z}. \tag{B.34}$$

This result is identical to that of equation B.23, only this time with an additional scalar multiple given by the frequency and out-of-plane wavenumber k_z. So, the higher order singularity term in the charge density for out-of-plane response behaves exactly the same as the other field quantities in the integration.

Appendix C

Additional discussion

C.1 Forces on purely dielectric interfaces

All of the stress tensors derived in section 3 for material surroundings are based on the vacuum gap method. Using this method, the forces on the 2D material itself are separated from the forces on the surrounding dielectrics. This is possible because the observation planes remain in the vacuum gap even as the thickness goes to zero, as shown in case (2) of figure 3.1. A consequence of this method is that if one were to apply the vacuum gap stress tensor to an interface with no 2D material, the result would always be zero net force. To account for the forces on the dielectrics themselves, the observation planes need to be inside the dielectrics, as shown in case (1) of figure 3.1, necessitating a dielectric stress tensor. The appropriate form of such a tensor has been the subject of sporadic debate for more than a century. The modern understanding of the problem is that truly only the full stress-energy tensor is fundamental, and the confusion is only in how one proportions the contributions to the total tensor between matter and electromagnetics. Here we are not attempting to make another contribution to this debate. Forces on dielectrics are not the focus of this work. Here we only seek to give context and highlight some of the issues with calculating forces on dielectrics by making a brief comparison between the force predictions from the standard Maxwell stress tensor,

$$\overleftrightarrow{T}_{\text{max}} = \epsilon_0 \mathbf{EE} + \mu_0 \mathbf{HH} - \frac{1}{2}\overleftrightarrow{I}\left(\epsilon_0 \mathbf{E}\cdot\mathbf{E} + \mu_0 \mathbf{H}\cdot\mathbf{H}\right), \tag{C.1}$$

and the Minkowski stress tensor,

$$\overleftrightarrow{T}_{\text{mink}} = \mathbf{DE} + \mu_0 \mathbf{HH} - \frac{1}{2}\overleftrightarrow{I}\left(\mathbf{D}\cdot\mathbf{E} + \mu_0 \mathbf{H}\cdot\mathbf{H}\right). \tag{C.2}$$

We make comparison to the Minkowski tensor because it is the most common choice for calculating forces in dielectrics from linearly polarized plane waves. To be truly confident in any stress tensor, it must satisfy conservation of linear momentum. This entails the existence of some charge and current density upon which the Lorentz force is identical to the stress tensor prediction. Consider a purely dielectric interface between two isotropic, non-magnetic, lossless materials defined by $\epsilon_1 = n_1^2\epsilon_0$ and $\epsilon_2 = n_2^2\epsilon_0$. At such an interface, there is an accumulated bound charge from the polarization in the normal direction. This bound charge takes the form,

$$\sigma_b = -(\mathbf{P}_2 - \mathbf{P}_1) \cdot \hat{z}. \tag{C.3}$$

Only this bound surface charge appears in the standard electromagnetic boundary conditions, no other charges or currents contribute to the field discontinuities at a lossless dielectric interface. While one can define a polarization current at the interface as the time derivative of the bulk polarization densities, only the bound surface charge is singular, and only singular contributions survive integration of the Lorentz force over a pillbox in the limit that the pillbox height goes to zero. This limit is taken to isolate the forces on the interface itself from those on the bulk materials. All of this taken together indicates that perhaps to calculate forces on a dielectric interface, one only needs to calculate the force on the bound surface charge. In fact, conservation of linear momentum is satisfied by the Lorentz force on the bound surface charge and the standard Maxwell stress tensor,

$$\frac{1}{2}\Re\left(\sigma_b(q,\omega)\mathbf{E}_0^{av*}(q,\omega)\right) = \frac{1}{2}\Re\left(\overleftrightarrow{T}_{\max}(q,\omega,z)\right) \cdot \hat{z}\Big|_{z_1}^{z_2}. \tag{C.4}$$

However, even though this combination does satisfy conservation of linear momentum, it predicts non-zero forces in the $\hat{q}$ and $\hat{\tau}$ directions, which other published works have claimed do not exist [60]. Regardless of whether or not this is true, the Maxwell stress tensor result is certainly incomplete given that it predicts zero force at normal incidence .

If the Maxwell stress tensor is insufficient, then the common next choice for plane wave interactions is the Minkowski stress tensor. Now, unlike the Maxwell stress tensor, the Minkowski tensor predicts zero force in the $\hat{q}$ and $\hat{\tau}$ directions. However, now it is not clear what equivalent charge and current densities satisfy conservation of linear momentum through the Lorentz force. It is possible to define a current density associated with the surface charge in the Fourier domain as

$$J_x = \frac{\omega}{q}\sigma_b. \tag{C.5}$$

However, this change alone is insufficient to satisfy conservation. While it is possible that some surface polarization could be defined to satisfy conservation with the Minkowsi tensor, the appropriate form is not evident, and this is not the only problem.

A monochromatic plane wave normally incident from a dielectric onto a perfect reflector produces a time-averaged optical pressure of $F_z = \epsilon_1 |a_p|^2 = \epsilon_0 n_1^2 |a_p|^2$, where a_p is the incident amplitude [59]. The force in the case of a lossless reflection should be entirely due to the reflection of the momentum of the incident beam. So, in theory, the force from a perfect reflection should form the upper limit of possible optical forces in these configurations. We can use this as a reference point for comparing the Minkowski and Maxwell force predictions on a lossless dielectric interface by considering the limit that $n_2 \to \infty$. In this limit, the reflection should be perfect, and in theory, the force should be at the maximum of $F_z = \epsilon_0 n_1^2 |a_p|^2$ regardless of the angle of incidence.

As stated previously, the Maxwell prediction is zero force at normal incidence, even in the limit $n_2 \to \infty$. The Minkowski prediction, on the other hand, approaches the theoretical maximum, though with the opposite direction,

$$\lim_{n_2 \to \infty} \mathbf{F}_{\text{mink}}(\theta_i = 0) = -\epsilon_0 n_1^2 |a_p|^2 \hat{z}. \tag{C.6}$$

This is a promising result, however it does not hold for oblique incidence.

For arbitrary non-zero incident angle θ_i, the Maxwell stress tensor method no longer predicts zero force. In fact, in the limit $n_2 \to \infty$, the in-plane components of the Maxwell force prediction go to zero, giving a result only along the $\hat{z}$ direction,

$$\lim_{n_2 \to \infty} \mathbf{F}_{\text{max}}(\theta_i \neq 0) = F_z^{\text{max}}(\theta_i) \hat{z}. \tag{C.7}$$

By comparing this result to that of the Minkowski tensor, we find,

$$\lim_{n_2 \to \infty} \mathbf{F}_{\text{mink}}(\theta_i \neq 0) = \left[-\epsilon_0 n_1^2 |a_p|^2 + n_1^2 F_z^{\text{max}}(\theta_i) \right] \hat{z}. \tag{C.8}$$

In the limit of total reflection, the Minkowski force prediction consists of one constant component given by the predicted maximum, along with another contribution that is the same as the Maxwell prediction scaled by the incident dielectric constant. Because the Maxwell prediction is also negative, this means the Minkowski tensor predicts a force greater in magnitude than the theoretical maximum at oblique incidence.

All of this is not to say that the Minkowski tensor is invalid, as there are studies that claim to verify Minkowski force predictions [84][85]. There simply remain questions regarding precisely when any given electromagnetic stress tensor is valid. For instance, the Minkowski stress tensor appears to be derivable from the Lorentz force on a material consisting of only free charges [59]. If this is truly the only way to satisfy conservation of linear momentum with the Minkowski tensor through the Lorentz force, then perhaps it is not a valid choice for calculating forces on lossless dielectric interfaces, and the alternative is not clear. In any case, we sidestep all of these issues in this work through the application of the vacuum gap method. No forces on dielectrics are considered.

C.2 Complex Dispersion

Here we will briefly consider solutions to the full complex dispersion relation with finite electron lifetime shown in figure C.1. Along the first half of the arch, the action of including

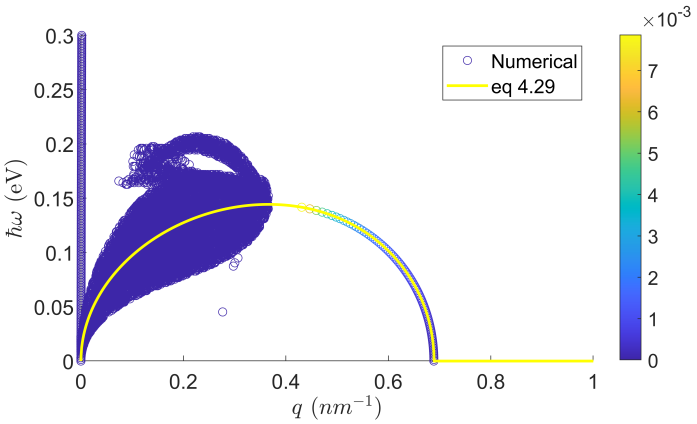


Figure C.1: Real part of q from the full complex solution to the hybridized dispersion relation shown in equation 4.27. The colour bar indicates the magnitude of the corresponding imaginary part in nm^{-1}. Calculated for the substrate case, with $n_2 = 4$ and $n_1 = 1$. Yellow line is the solution to the hybridized plasmon mode in the non-retarded limit.

losses through the finite electron lifetime is essentially only to broaden the dispersion curve. Nearly all of these states have zero or near zero imaginary contributions. Along the second half of the arch, the inclusion of losses acts in the exact opposite way as the first. The second half of the arch remains narrowly peaked around the analytical solution, however with comparatively much larger imaginary contributions. Curiously, the imaginary part of the in-plane wavenumber q also changes sign along the second half of the arch. This change of sign in the imaginary part corresponds to exponential growth, which could indicate that these solutions are not physically valid. However, along the second half of the arch, the group velocity, as the q-derivative of the dispersion relation when solved for ω ($v_g = \partial\omega/\partial q$), also changes direction. This could mean that the change in sign of the imaginary contribution that would otherwise indicate exponential growth instead indicates decay in the other direction. So, there are certainly questions regarding the physical validity of solutions along the second half of the hybridized dispersion relation. In this work, with the focus on the purely real, lossless dispersion relation, we consider solutions along the entire arch. However, the identification of whether or not the second half represents physically allowable states will be a focus of future investigations.